Search for New Physics in events with 4 top quarks in the ATLAS detector at the LHC

Daniela Paredes Hernández

DU 2375 PCCF T 1305

UNIVERSITÉ BLAISE PASCAL
U.F.R Sciences et Technologies

ÉCOLE DOCTORALE DES SCIENCES FONDAMENTALES
N^o 758

THÈSE

pour obtenir le grade de

DOCTEUR D'UNIVERSITÉ

SPÉCIALITÉ : PHYSIQUE DES PARTICLES

présentée et soutenue par

Daniela Paredes Hernández

Recherche de Nouvelle Physique dans les événements à quatre quarks top avec le détecteur ATLAS du LHC

Thèse soutenue publiquement le 13 Septembre 2013
devant la commission d'examen:

Président:	Dominique PALLIN	- CNRS (LPC Clermont-Ferrand)
Rapporteurs:	Stephane WILLOCQ	- University of Massachusetts
	Roberto CHIERICI	- CNRS (IPNL Lyon)
Examinateurs:	Henri BACHACOU	- CEA (IRFU, Saclay)
	Ana HENRIQUES	- CERN
	Farvah MAHMOUDI	- Université Blaise Pascal
Directeur de thèse:	David CALVET	- CNRS (LPC Clermont-Ferrand)

UNIVERSITE
BLAISE PASCAL
CLERMONT-FERRAND
UBP

DU 2375 PCCF T 1305

UNIVERSITÉ BLAISE PASCAL
U.F.R Sciences et Technologies

ÉCOLE DOCTORALE DES SCIENCES FONDAMENTALES
N^o 758

THESIS

to obtain the title of

Ph.D. of Science
SPECIALITY : PARTICLE PHYSICS

defended by

Daniela Paredes Hernández

Search for New Physics in events with 4 top quarks in the ATLAS detector at the LHC

Defended on September 13^{th}, 2013

President:	Dominique PALLIN	- CNRS (LPC Clermont-Ferrand)
Raviewers:	Stephane WILLOCQ	- University of Massachusetts
	Roberto CHIERICI	- CNRS (IPNL Lyon)
Examinators:	Henri BACHACOU	- CEA (IRFU, Saclay)
	Ana HENRIQUES	- CERN
	Farvah MAHMOUDI	- Université Blaise Pascal
Supervisor:	David CALVET	- CNRS (LPC Clermont-Ferrand)

A mi familia, porque sólo ellos importan...

"... pero se dejó llevar por su convicción de que los seres humanos no nacen para siempre el día en que sus madres los alumbran, sino que la vida los obliga otra vez y muchas veces a parirse a sí mismos."

El amor en los tiempos del cólera, Gabriel García Márquez

Acknowledgments

The road to obtain my doctoral degree has been a long one, and many people have made this possible. I really thank all of them.

First, I would like to thank Alain Baldit and Alain Farvard for hosting me at the LPC for the realization of this thesis. I am specially grateful with Roberto Chierici and Stephane Willocq for accepting to be the referees of this document, and to Henri Bachacou, Ana Henriques, Nazila Mahmoudi and Dominique Pallin for accepting to be part of the jury.

My deepest gratitude goes to David Calvet, my advisor, for his availability, advice, and over all patience through these 3 last years, whenever doubts about how to move forward assailed me, for answering all my questions, for helping me to solve my technical problems when they arose, and for his guide and help in my arrival to Clermont-Ferrand: I leave here after having learned many things from you, the main one, the meticulosity.

I would like to thank the ATLAS-LPC group members: Dominique, Samuel, Emmanuel, Julien, Claudio, François, Djamel, Hongbo, Philippe, Christophe, Timothée, Geoffrey, Emmanuelle, Loïc, Dorian and Fabrice, for their comments, suggestions and physics discussions when needed.

Thanks also to the Top Fakes Group for estimating one of the most important background used in the analysis presented in this thesis, to the Saclay group for the estimation of the electron charge mis-identification rates at $\sqrt{s} = 7$ TeV, and to the members of the TOP/Exotics same-sign dilepton group for their comments, expertise and useful remarks during the realization of this analysis.

I have to give a special grateful to my licentiate's thesis advisor, Luis Núñez, for his personal advice, guidance and encouragement when needed all these years, for always being attentive during the last state of this thesis, and over all, for helping me to chose the right road in order to decide my future. To my master's thesis advisor, Sascha Husa, and his wife, Alicia Sintes, for being attentive and encourage me with the doctoral thesis, without the knowledge obtained under their supervision this success would not be possible.

Thanks to my venezuelan friends, Camila Rangel, Reina Camacho, Rebeca Ribeiro, Homero Martínez, Joany Manjarrés, Hebert Torres, Anais Moller, Bárbara Millán, Roger Naranjo and Jacobo Montaño, for sharing their experience and support when needed, for all the nice moments that we shared together either in Paris or Geneva. To all those Spanish-speaking people that were in some moment in Clermont-Ferrand: Diego Roa, Patricio Ceniceros, Jazmín Porras, Mónica Huertas, Pablo Fernández, Sergio Martínez, Varinia Bernales, Juan Petit and Ricardo

Silva, for sharing with me some moments, dinners and beers, especially to Dieguito, for all the discussions when most of the other people were already gone.

I also have to thank some university friends: Francisco Morales, Andrea Valdéz, Rossana Rojas and Zoylimar Fune, for the support and encouragement provided. Especially to Francisco, for always keeping in communication, and for showing me almost all Belgium in a weekend: I will never forget this trip! To my old high-school friends for keeping close in distance and always being there during the reencounters that I organized: Jonathan Belandria, Luisana Gando, Liliana Gando, Yoli Mora, José Ramón González, Ana María Colls, Rolando Carrero, and many others. I think that I have never laughed so much in my life as in these reencounters. A special grateful goes to Jonathan, for having demonstrated being a true friend, for always being there, for listening to me in the difficult times and helping me to overcome them.

Finally, I would like to thank my family, for all the encouragement provided during this thesis despite the distance. Especially to my parents, who with their work, effort and sacrifice have supported all my studies. A special grateful goes to my cousin Yoli, for helping me, encouraging and supporting me the day of my defense.

Thank you very much to all of you!

Résumé

Cette thèse a pour but la recherche de Nouvelle Physique dans les événements à quatre quarks top en utilisant les données collectées dans les collisions proton-proton par l'expérience ATLAS au LHC. L'ensemble des données correspond à celui enregistré pendant tout 2011 à $\sqrt{s} = 7$ TeV et une partie de l'année 2012 à $\sqrt{s} = 8$ TeV. L'analyse est concentrée sur un état final avec deux leptons (des électrons et des muons) avec la même charge électrique. Cette signature est expérimentalement privilégiée puisque la présence de deux leptons avec le même signe dans l'état final permet de réduire le bruit du fond qui vient des processus du Modèle Standard. Les résultats sont interprétés dans le contexte d'une théorie effective à basse énergie, qui suppose que la Nouvelle Physique peut se manifester à basse énergie comme une interaction de contact à quatre tops droits. Dans ce contexte, cette analyse permet de prouver un type de théorie au delà du Modèle Standard qui, à basse énergie, peut se manifester de cette manière. Les bruits du fond pour cette recherche ont été estimés en utilisant des échantillons simulés et des techniques axées sur les données. Différentes sources d'incertitudes systématiques ont été considérées. La sélection finale des événements a été optimisée en visant à minimiser la limite supérieure attendue sur la section efficace de production des quatre tops si aucun événement de signal n'est trouvé. La région du signal a été ensuite examinée à la recherche d'un excès d'événement en comparaison avec le bruit du fond prévu. Aucun excès d'événement n'a été observé, et la limite supérieure observée sur la section efficace de production de quatre quarks top a été calculée. Ceci a permis de calculer la limite supérieure sur la constante de couplage C/Λ^2 du modèle. Une limite supérieure sur la section efficace de production de quatre tops dans le Modèle Standard a été aussi calculée dans l'analyse à $\sqrt{s} = 8$ TeV.

En plus de l'analyse physique du signal de quatre tops, des études concernant le système d'étalonnage LASER du calorimètre Tile ont été présentées. Ces études sont liées au système des photodiodes utilisé pour mesurer l'intensité de la lumière dans le système LASER.

Mots clés: ATLAS, LHC, quark top, quatre tops, théorie effective, Nouvelle Physique, erreur de reconstruction de la charge des électrons, système d'étalonnage LASER, TileCal, photodiodes.

Daniela Paredes

Abstract

This thesis presents the search for New Physics in events with four top quarks using the data collected in proton-proton collisions by the ATLAS experiment at the LHC. The dataset corresponds to the one taken during all 2011 at $\sqrt{s} = 7$ TeV and a part of 2012 at $\sqrt{s} = 8$ TeV. The analysis focuses on a final state with two leptons (electrons and muons) with the same electric charge. This signature is experimentally favored since the presence of two same-sign leptons in the final state allows to reduce the background coming from Standard Model (SM) processes. The results are interpreted in the context of a low energy effective field theory, which assumes that New Physics at low energy can manifest itself as a four right-handed top contact interaction. In this context, this analysis allows testing a class of beyond-the-SM (BSM) theories which at low energy can manifest in this way. Backgrounds to this search have been estimated using simulated samples and data-driven techniques. Different sources of systematic uncertainties have been also considered. The final selection of events has been optimized by aiming at minimizing the expected upper limit on the four tops production cross-section in case of no signal events found. The signal region is then analyzed by looking for an excess of events with respect to the predicted background. No excess of events has been observed, and the observed upper limit on the four tops production cross-section has been computed. This limit is then translated to an upper limit on the coupling strength C/Λ^2 of the model. An upper limit on the four tops production cross-section in the SM has been also computed in the analysis performed at $\sqrt{s} = 8$ TeV.

In addition to the physics analysis of the four tops signal, some studies about the LASER calibration system of the ATLAS Tile calorimeter are presented. In particular, they are related to the photodiodes system used to measure the intensity of the laser light in the LASER system.

Keywords: ATLAS, LHC, top quark, four tops, effective field theory, New Physics, misidentification of the electron charge, LASER calibration system, TileCal, photodiodes.

Daniela Paredes

Contents

Introduction

The Standard Model (SM) [1, 2] of particle physics represents currently the most accurate and predictive description of nature, at least up to the scale of the weak interactions. It provides an almost complete picture of the interactions of matter through three of the four known forces: strong, weak and electromagnetic. Numerous precision measurements have validated its accuracy. However, there are still many open questions that the SM does not answer. This indicates that it is just a low-energy approximation of a more fundamental theory, valid at the currently understood energy scales, expected to break down at the TeV scale.

The interest of knowing the fundamental constituents of matter and their fundamental interactions has lead to the construction of particle accelerators each time more powerful. A new era started with the Large Hadron Collider (LHC) [3], which is capable to accelerate particles up to energies never reached by the humanity, and therefore, providing access to a yet unexplored energy regime. It has been built in order to provide an answer to the several shortcomings presented by the SM. Several detectors are located in the interaction points of the LHC ring. ATLAS is one of them [4]. It counts with an extremely rich program designed to study many different types of physics that might become detectable in the energetic collisions of the LHC. Together with the Compact Muon Solenoid (CMS) [5], it is expected to improve or confirm measurements of the Standard Model and to look for New Physics.

In the domain of the New Physics the top quark is expected to play a leading role. Its large mass, and therefore its big coupling to the Higgs boson makes it a natural candidate to look for new phenomena. Many new physical models are linked to the top quark. Many of them predict also an enhancement of the four tops production ($t\bar{t}t\bar{t}$) as compared to the SM, which is very small at the energies provided up to now by the LHC. This signal has been proposed in the past as a probe of the electroweak symmetry breaking [6, 7], or of the existence of a Universe with extra-dimensions [8, 9]. It is linked to models where the top quark is composite [10, 11], and also appears in supersymmetric models [12].

Given the rich physics potential of four top quarks events, this thesis presents an analysis of the data taken by the ATLAS experiment at the LHC looking for New Physics in events with four top quarks. The results are interpreted in the context of a low energy effective field theory [13], which assumes that New Physics at low energy can manifest itself as a four right-handed top contact interaction. Therefore, this analysis does not test a particular theory, but rather a class of beyond-the-SM (BSM) theories which at low energy can manifest in this way. The data used correspond to the ones taken during all 2011 at $\sqrt{s} = 7$ TeV, and a part of 2012 at $\sqrt{s} = 8$ TeV.

The analysis focuses on a final state with two charged leptons of the same electric charge.

In addition to the physics analysis of the four tops signal, some studies about the LASER calibration system [14] of the ATLAS Tile calorimeter are presented. In particular, they are related to the photodiodes system used to measure the intensity of the laser light in the LASER system.

This thesis is organized as follows: Chapter 1 gives an overview of the SM of particle physics, and those aspects that are relevant for the four tops production. Some BSM theories which can lead to experimental signatures involving four top quarks are also described in this chapter. The experimental setup of the LHC is briefly introduced in Chapter 2. The ATLAS detector, together with the data acquisition system that records the detector information is described in Chapter 3. This is followed by the studies of stability and linearity of the photodiodes of the LASER system of the ATLAS Tile calorimeter in Chapter 4. An overview of the four tops signal analysis is presented in Chapter 5. The data samples and event preselection are given in Chapter 6. The background processes and their estimation are discussed in Chapter 7. The final selection of events, the comparison of data with expected background, and the final limit on the four tops production cross-section are given in Chapter 8. Finally, the conclusions are presented.

Author's contribution

The author's contribution to the different topics presented in this thesis can be divided in three parts:

The TileCal Laser calibration system: The author was in charge of studying the stability of the photodiodes and their electronics in the LASER system of the Tile calorimeter. She studied all the data taken during the photodiodes calibration and linearity tests from February, 2011 to February, 2013. A new method was proposed in order to study the stability of the alpha response. She demonstrated that this new method is more precise than the default method used to study the stability of the alpha response (normalized mean value). The work's author can be found in Refs. [15, 16]

Mis-identification of the electron charge: The author estimated the background coming from the mis-identification of the electron charge in the analysis performed at $\sqrt{s} = 8$ TeV. She developed a new method which takes into account the dependence on the electron p_{T} of the mis-identification rates. She also redefined the $|\eta|$ binning to extract the rates, and the regions used by the side-band method to extract the background from the Z-peak: now it takes into account the shift of the same-sign invariant mass distribution to lower values with respect to the opposite-sign distribution. In addition, the author improved the computation of the systematic uncertainty on the mis-id rates.

This background corresponds to the official estimation done for the ATLAS TOP/Exotics same-sign dilepton group. It was used to set limits on the fourth-generation b' signal, same-sign top production, vector-like-quarks, four top quarks produced via sgluon decay, and the 2UED/RPP model. Currently, it is also used in the $t\bar{t}H$ studies. An internal note is being written in order to show these results. They can be also found in Ref. [17].

Four-top signal: The author performed the full analysis of the four-top signal in the Standard Model and in a beyond the Standard Model framework using the full dataset taken in 2011 and the partial dataset in 2012. She determined the final selection of events using an optimization procedure aiming at minimizing the expected upper limit on the production cross-section. This way, she computed the observed upper limit on the four-top quarks production cross-section in the Standard Model and the beyond Standard Model framework. The results of these studies can be found in Refs. [18, 17].

Chapter 1

Theoretical background

Contents

1.1 Introduction

One of the questions that has puzzled the mankind since a long time ago is "what is this world made of?". The idea that all matter is composed of elementary particles is the current answer to this question.

So far, experimental tests have proved that the ordinary matter is made of particles. Different models have been proposed to explain the properties of these particles and the interactions with each other. Up to now, all the observed phenomena can be explained in terms of four fundamental interactions: *strong, weak, electromagnetic* and *gravitational*, which are characterized by widely different ranges and strengths. The strong interaction, which is responsible for the existence and structure of the atomic nuclei, has a range of about 10^{-15} m, and a coupling constant, as measured at a typical energy scale of 1 GeV, $\alpha_S \approx 1$. The weak interaction, responsible for radioactive decay, has a range of 10^{-18} m, and a coupling of $\alpha_W \approx 10^{-6}$. The electromagnetic interaction that governs much of macroscopic phenomena has infinite range and strength

determined by the fine structure constant, $\alpha = 1/137$. The last interaction, gravity, also has infinite range, and it is around 10^{38} times weaker than the strong interaction. Therefore, its impact on fundamental particle processes at accessible energies is totally negligible. One of the goals of particle physics is to find the theory which unifies these four interactions.

Currently, the *Standard Model* of particle physics [1, 2] provides the best predictions and explanations for the behavior of elementary particles and their interactions. It unifies the description of the strong, weak and electromagnetic interactions in the language of quantum gauge field theories. It remains a landmark success of theoretical physics after numerous experimental tests and precision measurements, and no significant deviation from the theoretical predictions have been observed so far. Despite its success, many questions about the Universe remain unanswered. The SM does not include gravity and its validity upper scale is unknown. It also fails to explain the values of many of its parameters, and has several shortcomings to act as a "Theory of Everything". In order to solve one or more of these problems, a wide range of new physics models have been formulated over the years. These theories predict different types of new particles and interactions that could be observed at the Large Hadron Collider. Some of these models predict final states involving four top quarks ($t\bar{t}t\bar{t}$), which can be studied using same-sign dilepton events as an experimental signature. The search for new physics in events with 4 top quarks with this specific signature is the main goal of this thesis.

This chapter starts with a brief overview of the elements of the Standard Model in Section 1.2. This is followed by the description of the SM production of four top quarks in Section 1.3. The outstanding issues of the SM are detailed in Section 1.4. Finally, some beyond-the-SM models predicting the production of four top quarks are described in Section 1.5.

1.2 The Standard Model of particle physics

The SM is currently the most precise theoretical framework to describe the world of particle physics. It is a relativistic quantum field theory, formulated during the 1960s and 1970s, that incorporates the basic principles of quantum mechanics and special relativity. It represents a unified description of three of the four known interactions –electromagnetic, weak and strong– based on a combination of local gauge symmetries. In addition, the SM combines the weak and electromagnetic forces in a single electroweak gauge theory. This way, it describes the known fundamental particles together with their interactions. The elementary particles included by this model are presented in Section 1.2.1. The mathematical formulation of the SM is discussed in Section 1.2.2. Unless explicitly stated otherwise the information about the SM in this section has been extracted from references [1, 2, 19, 20, 21].

1.2.1 Elementary particles

The Standard Model describes the characteristics of the fundamental constituents of matter and their interactions in terms of point-like particles. The nature and the properties of the particles can be determined by their internal angular momentum called spin. This way, the particles can be classified in two categories: *fermions* and *bosons*. Fermions are particles with half-integral spin that obey Fermi-Dirac statistics, while bosons have integral spin and obey Bose-Einstein statistics. For fermions, the Pauli exclusion principle does not allow the occupation of any single quantum state by more than one particle of a given type, while for the bosons the occupation of a single quantum state by a large number of identical particles is possible. In the SM, the

fermions are the constituents of matter while the bosons are the particles responsible for their interactions.

The fermions are subdivided in two categories: *leptons*, interacting only weakly and electromagnetically, and *quarks*, sensitive to all three interactions. Leptons are further divided into electrically charged and neutral leptons. The charged leptons include the electron (e^-), muon (μ^-), and tau (τ^-), while the neutral leptons are their associated neutrinos ν_e, ν_μ and ν_τ, respectively. There are six *flavors* of quarks. They carry fractional electric charges and are categorized as up-type ($Q = +2/3$) and down-type ($Q = -1/3$) quarks. The up-type quarks include the up (u), charm (c), and top (t) quarks, while the down-type quarks include the down (d), strange (s), and bottom (b) quarks. Another important property of the quarks is that they have *color charge*. This last one can take one of three values or charges: red, green, or blue. Antiquarks carry anticolor charges.

	Generation				
	I	**II**	**III**	Q	Spin
Leptons	e	μ	τ	-1	$\frac{1}{2}$
mass [MeV]	0.511	105.7	1776.8		
	ν_e	ν_μ	ν_τ	0	$\frac{1}{2}$
	$< 2 \times 10^{-6}$	< 0.19	< 18.2		
Quarks	u	c	t	$+\frac{2}{3}$	$\frac{1}{2}$
mass [MeV]	$1.8 - 3.0$	1275	173500		
	d	s	b	$-\frac{1}{3}$	$\frac{1}{2}$
	$4.5 - 5.5$	95	4180		

Table 1.1: The SM divides the fermions in leptons and quarks. They are organized into three different generations. Each generation consists of one electrically charged lepton, one electrically neutral lepton, two quarks, and their respective antiparticles. Fermions in each generation have similar physical behavior but different masses. The electric charge Q is given in fractions of the proton charge. Mass values have been obtained from Ref. [22].

All fermions are organized in three generations or families. Fermions in each generation have similar physical behavior but increasing particle mass as shown in Table 1.1. So far, there is no explanation for this triple repetition of fermion families. Each family consists of two quarks (one up-type quark and one down-type quark), one electrically charged lepton and one electrically neutral lepton (neutrino). The first family includes the u and d quarks that are the constituents of nucleons as well as pions and other mesons responsible for nuclear binding. It also contains the electron with its corresponding neutrino. The quarks of the other families are constituents of heavier short-lived particles. These quarks and their companion charged leptons rapidly decay via the weak force to the quarks and leptons of the first family. Therefore, all stable matter is made of the first generation of particles described by the SM. Neutrinos of all generations do not decay and rarely interact with matter. The neutrino masses as assumed by the SM are zero[1]. Leptons can exist as free particles, while quarks are found only in combinations of integer electrical charge and colorless particles called *hadrons*.

[1]Neutrino experiments have demonstrated the neutrinos change flavor as they travel from the source to the detector [23, 24, 25, 26, 27]. This phenomenon is called neutrino oscillation. Its observation implies that the neutrino has a non-zero mass.

In the SM, elementary particles interact via exchanges of gauge bosons. They are the force carriers of the three fundamental interactions included in this theory. There are four kinds of gauge mediators in the SM: the photon (γ), the gluons (g), and the $W^{\pm}$ and Z^0 bosons. The electromagnetic interaction is mediated by the photon, a massless particle that carries no electric charge and generates an interaction of infinite range. It acts between all electrically charged particles. The strong interaction acts between quarks and gluons, and it is mediated by eight massless gluons which are electrically neutral but carry color charge. The $W^{\pm}$ and Z^0 bosons mediate the weak interaction which affects both neutral and charged particles. Local gauge invariance requires that they be massless, and they acquire mass through spontaneous symmetry breaking (discussed later). In Table 1.2, the gauge bosons are presented along with their mass, charge and the interaction type they correspond to. The last particle predicted by the SM is the Higgs boson, a neutral scalar particle which is a consequence of the mechanism introduced to give mass to the $W^{\pm}$ and Z^0 bosons, and to the fermions as required by experimental results. In contrast to the other particles proposed by the SM, the existence of the SM Higgs boson is still not fully corroborated. However, a Higgs-like particle was discovered by the ATLAS and CMS Collaborations in July 2012 [28, 29]. So far, the properties of this particle have not shown deviations with respect to the ones predicted for the SM Higgs boson.

Interaction	**Gauge boson**	Q	**Spin**	**Mass [GeV]**
Weak	W^+	$+1$	1	80.39
	W^-	-1	1	80.39
	Z^0	0	1	91.19
Electromagnetic	γ	0	1	0
Strong	g	0	1	0

Table 1.2: Force carrier particles for the three fundamental interactions included in the SM. The electric charge Q is given in fractions of the proton charge. Mass values have been extracted from Ref. [22]. The gluon and photon masses are the theoretical values.

For each one of the described particles –leptons, quarks, and the charged gauge bosons– there exists the corresponding antiparticle –nearly doubling the particle counting in the SM– with the same mass and lifetime as the corresponding particle but with opposite sign of charge and magnetic moment. The neutral gauge bosons are their own antiparticles. The antiparticles are denoted with the same symbol used for the particles but with a bar added over it, or by changing the sign of its electric charge.

1.2.2 Theoretical formulation

Gauge theories are field theories for which the Lagrangian is invariant under some set of local transformations. These transformations are known as gauge transformations and form a symmetry group of the theory.

The SM describes the electromagnetic, weak, and strong interactions as gauge theories,

each one of them with an associated symmetry group. It is a non-Abelian[2] gauge theory invariant under transformations of the type $SU(3)_C \otimes SU(2)_L \otimes U(1)_Y$, where $SU(3)_C$ is the symmetry group of the strong interaction and $SU(2)_L \otimes U(1)_Y$ of the electroweak interaction. The indices refer to the conserved quantity in each transformation: color charge (C), hypercharge (Y) and for $SU(2)$, although the weak isospin (I) is the conserved quantity, the L denotes the fact that it involves only left-handed fields. The generators of these gauge groups represent the force carriers, while the group eigenvectors represent particles with different couplings to the force carriers (quantum numbers or eigenvalues).

From the theoretical point of view, the SM is based on two main theories:

- *Quantum chromodynamics* (QCD), developed by Politzer [30, 31], Wilczek and Gross [32, 33], describing the strong interaction based on the $SU(3)_C$ gauge symmetry group; and,
- the *Electroweak model* (EW) developed by Glashow [34], Weinberg [35] and Salam [36] proposed to unify the electromagnetic and weak interactions based on the $SU(2)_L \otimes U(1)_Y$ symmetry group.

Both theories, QCD and EW, will be briefly discussed in the following sections.

The spontaneous breaking of the electroweak symmetry $SU(2)_L \otimes U(1)_Y$ generates mass terms for the gauge bosons $W^{\pm}$ and Z^0. The breaking of the symmetry is believed to be produced through the *Higgs mechanism* [37], which predicts a new boson via the introduction of a scalar doublet that is the Higgs field. The Higgs mechanism will be also discussed here.

1.2.2.1 Quantum chromodynamics

Quantum chromodynamics [38, 39] is a renormalizable theory describing the strong interaction between quarks via exchange of gluons, with a non-Abelian local gauge symmetry group $SU(3)_C$. In this representation the gluons are the gauge fields. The quantum number of the strong interaction is the color charge.

The quarks are represented as color triplets, while gluons are realized as an octet of linear combinations of the three (anti)color charges. Only colorless bound states are invariant under transformations of the symmetry group, meaning that only colorless bound states can be observed as hadrons. These last ones come in two different categories: mesons –particles composed of one quark and one antiquark–, and baryons –particles made up of three quarks.

The QCD Lagrangian density is

$$\mathcal{L}_{QCD} = \sum_q \bar{\psi}_{q,a}[i\gamma^\mu (D_\mu)_{ab} - m_q \delta_{ab}]\psi_{q,b} - \frac{1}{4} F^A_{\mu\nu} F^{A\ \mu\nu}, \tag{1.1}$$

where $\psi_{q,a}$ are the quark-field spinors for a quark flavor q and mass m_q, with a color-index a that runs over the three different color charges, and the γ^μ are the Dirac matrices. The covariant derivative D_μ, and the field tensor $F^A_{\mu\nu}$ are defined as follow:

$$(D_\mu)_{ab} = \partial_\mu \delta_{ab} + i g_s t^A_{ab} G^A_\mu, \tag{1.2}$$

$$F^A_{\mu\nu} = \partial_\mu G^A_\nu - \partial_\nu G^A_\mu - g_s f_{ABC} G^B_\mu G^C_\nu, \tag{1.3}$$

[2]That means that its symmetry group is non-commutative.

where G_μ^A correspond to the gluon fields, with A running from 1 to 8, since there are 8 kinds of gluons. Each of the eight gluon fields acts on the quark color through one of the eight generator matrices of the $SU(3)_C$ group, t_{ab}^A. They correspond to three-dimensional matrices and are defined as a function of the Gell-Mann matrices λ_A as $t_A = \lambda_A/2$. They also obey the commutation relations $[t^A, t^B] = if_{ABC}t^C$, where the real numbers f_{ABC} are the structure constants of the $SU(3)_C$ group. Finally, g_s is a parameter that can be expressed in terms of the strong coupling constant α_s as $g_s^2 = 4\pi\alpha_s$. The third term in Eq. 1.3 gives QCD its non-Abelian character, which allows self-interactions between gluons.

The most prominent properties of QCD are *asymptotic freedom* and *confinement*. Asymptotic freedom means that the effective coupling becomes a function of the transferred momentum squared q^2:

$$\alpha_s(q^2) \propto \frac{1}{\ln(q^2/\Lambda_{QCD}^2)}, \tag{1.4}$$

where Λ_{QCD} is the energy scale of QCD ($\sim$ 200 MeV). Thus α_s decreases for increasing p and vanishes asymptotically. Therefore, the strong interaction becomes very weak in processes at high energy (or small scales), meaning that the quarks can be described as free particles in this regime. On the contrary, the interaction strength becomes large at large distances or small transferred momenta. In fact, the hadrons are bound composite states of quarks, with compensating color charges so that they are overall neutral in color. This phenomenon is called color confinement. An explanation for this phenomenon is that the energy required to separate two quarks increases with distance until pairs of quarks and antiquarks are created from the vacuum. The process will repeat until the momenta separating the quarks have been transformed into a shower of hadrons. This is referred to as hadronization and produces *jets* of hadrons.

1.2.2.2 Electroweak theory

The Electroweak theory is based on the same principle of gauge invariance as QCD. It unifies the electromagnetic and weak interactions in only one theory. The electromagnetic interaction is mediated by the photon and acts on all charged particles, while the weak interaction is mediated by the Z^0 and $W^\pm$ bosons and acts on all fermions. This last one ($W^\pm$) is the only boson able to change the flavor of a quark or a lepton. The weak interaction has a very short range due to the fact that its gauge bosons are massive.

As said above, the electroweak interaction is described by the $SU(2)_L \otimes U(1)_Y$ gauge symmetry group. The $SU(2)_L$ group has three gauge fields, W_μ^A ($A = 1, 2, 3$), with the weak isospin I as the conserved quantity. The $U(1)_Y$ has one associated gauge field, B_μ, with the hypercharge Y as the conserved quantum number.

In the electroweak framework, fermions are described through their left-handed and right-handed components[3]:

$$\psi_L = P_L\psi = \frac{1}{2}(1 - \gamma^5)\psi, \tag{1.5}$$

$$\psi_R = P_R\psi = \frac{1}{2}(1 + \gamma^5)\psi, \tag{1.6}$$

[3] A massless fermion is identified as left-handed if the direction of motion and spin are opposite to each other, and as right-handed otherwise. The handedness of massive fermions is defined as the chirality, describing the behavior under right- and left-handed transformations.

where $P_{L,R}$ are the chirality operators and $\gamma^5 = i\gamma^0\gamma^1\gamma^2\gamma^3$, with γ^μ the usual Dirac matrices. Left-handed fields ψ_L form doublets

$$\begin{pmatrix} u \\ d \end{pmatrix}_L, \begin{pmatrix} \nu_e \\ e \end{pmatrix}_L, \quad \begin{pmatrix} c \\ s \end{pmatrix}_L, \begin{pmatrix} \nu_\mu \\ \mu \end{pmatrix}_L, \quad \begin{pmatrix} t \\ b \end{pmatrix}_L, \begin{pmatrix} \nu_\tau \\ \tau \end{pmatrix}_L, \tag{1.7}$$

and have $I = \frac{1}{2}$, while right-handed fields, ψ_R, form singlets

$$u_R,\ d_R,\ e_R, \quad c_R,\ s_R,\ \mu_R, \quad t_R,\ b_R,\ \tau_R, \tag{1.8}$$

with $I = 0$, and are invariant under the weak isospin transformations. There are no right-handed neutrinos in the SM. Only left-handed fermions (right-handed antifermions) interact with the $SU(2)_L$ gauge fields. That means that the Parity (P) symmetry is violated by the weak interaction.

The Lagrangian density of the electroweak interaction involving only the gauge fields and fermions is given by:

$$\mathcal{L}_{EW} = \bar{\psi}_L i\gamma^\mu D_\mu \psi_L + \bar{\psi}_R i\gamma^\mu D_\mu \psi_R - \frac{1}{4}F^A_{\mu\nu}F^{A\ \mu\nu} - \frac{1}{4}B_{\mu\nu}B^{\mu\nu}, \tag{1.9}$$

with the first two terms describing the interactions between particles, mediated by the gauge bosons, and the second two terms the interactions between the gauge fields themselves. The $F^A_{\mu\nu}$ and $B_{\mu\nu}$ tensors are gauge antisymmetric tensors constructed out of the gauge fields B_μ and W^A_μ. They are defined as:

$$F^A_{\mu\nu} = \partial_\mu W^A_\nu - \partial_\nu W^A_\mu - g\epsilon_{ABC}W^B_\mu W^C_\nu, \tag{1.10}$$

$$B_{\mu\nu} = \partial_\mu B_\nu - \partial_\nu B_\mu, \tag{1.11}$$

where ϵ_{ABC} are the group structure constants, which for $SU(2)_L$ coincide with the Levi-Civita tensor. The covariant derivative D_μ is given by

$$D_\mu = \partial_\mu + igI^A W^A_\mu + \frac{ig'}{2}YB_\mu, \tag{1.12}$$

where I^A and Y are the $SU(2)_L$ and $U(1)_Y$ generators, respectively. The $SU(2)_L$ generators must satisfy the commutation relations $[I^A, I^B] = i\epsilon_{ABC}I^C$. They can be expressed in terms of the Pauli matrices τ_A, as $I_A = \tau_A/2$. The hypercharge is connected to the electric charge generator Q and weak isospin by

$$Q = I_3 + \frac{Y}{2}, \tag{1.13}$$

where I_3 is the third component of the weak isospin. Finally, the variables g and g' describe the coupling constants of the $SU(2)_L$ and $U(1)_Y$, respectively. They are related via

$$\tan\theta_W = \frac{g'}{g}, \tag{1.14}$$

where θ_W is the weak mixing angle, which describes the mixing between $SU(2)_L$ and $U(1)_Y$. Using θ_W, the gauge bosons can be written as linear combinations of the gauge fields:

$$\gamma : A_\mu = \cos\theta_W B_\mu + \sin\theta_W W^3_\mu, \tag{1.15}$$

$$Z^0 : Z_\mu = -\sin\theta_W B_\mu + \cos\theta_W W^3_\mu, \tag{1.16}$$

$$W^\pm : W^\pm_\mu = \frac{1}{\sqrt{2}}(W^1_\mu \mp iW^2_\mu). \tag{1.17}$$

So far, all the gauge bosons introduced in the theory are massless due to the gauge invariance. However, the gauge bosons associated with the weak interaction are experimentally known to be massive. But, adding a mass component to the Lagrangian leads to violation of the gauge invariance. It indicates that the symmetry associated with this interaction has to be broken. In the SM, the breaking of the electroweak gauge symmetry is achieved via the Higgs mechanism.

1.2.2.3 Higgs mechanism

The Higgs mechanism was introduced by Brout, Englert [40] and Higgs [41], following a non relativistic treatment by Anderson [42], and applied to the weak interaction by Weinberg [35] and Salam. It introduces an additional $SU(2)_L$ isospin doublet of complex scalar fields with hypercharge $Y = 1$ defined as

$$\Phi = \begin{pmatrix} \phi^+ \\ \phi^0 \end{pmatrix}, \tag{1.18}$$

where the indices + and 0 will turn out to denote electric charges. They are defined as

$$\phi^+ = \frac{\phi_1 + i\phi_2}{\sqrt{2}}, \quad \text{and} \quad \phi^0 = \frac{\phi_3 + i\phi_4}{\sqrt{2}}. \tag{1.19}$$

The introduction of Φ adds an additional contribution to the SM Lagrangian of the form

$$\mathcal{L}_{Higgs} = (D_\mu \Phi)^\dagger (D^\mu \Phi) - V(\Phi^\dagger \Phi), \tag{1.20}$$

where D_μ is given by Eq. 1.12, and the potential term, $V(\Phi^\dagger\Phi)$, represents the Higgs potential defined as

$$V(\Phi^\dagger \Phi) = \mu^2 \Phi^\dagger \Phi + \lambda (\Phi^\dagger \Phi)^2. \tag{1.21}$$

The shape of the potential is determined by the choice of the parameters μ and λ. For $\mu^2 < 0$ and $\lambda > 0$, its shape is shown in Fig. 1.1. It has a minimum at $\Phi^\dagger\Phi = -\frac{\mu^2}{2\lambda}$. However, the ground state is infinitely degenerate. This way, one state can be chosen as the reference for the local gauge transformation. It is always possible to pick a gauge such that in the ground state $\phi_1 = \phi_2 = \phi_4 = 0$ and $\phi_3 = v$, thus:

$$\Phi_0 = \frac{1}{\sqrt{2}} \begin{pmatrix} 0 \\ v \end{pmatrix}, \quad \text{with} \quad v = \sqrt{\frac{-\mu^2}{\lambda}}, \tag{1.22}$$

where v is the vacuum expectation value. The choice of this particular direction of the space means that the system *spontaneously* breaks the symmetry. Spontaneous symmetry breaking means that the Lagrangian remains invariant, while the lowest energy state, the vacuum, is not invariant under the gauge symmetry.

The Higgs field fluctuations around the vacuum can be parametrized by four real fields, ξ_i $(i = 1, 2, 3)$, and H. Then, Φ can be redefined in terms of these fields:

$$\Phi = e^{\frac{i\xi_a(x)\tau^a}{2v}} \begin{pmatrix} 0 \\ \frac{v+H(x)}{\sqrt{2}} \end{pmatrix}. \tag{1.23}$$

The Lagrangian is locally invariant under $SU(2)_L$, and by using the freedom of gauge transformations, the $\xi_a(x)$ disappear from the Lagrangian. These three fields correspond to the

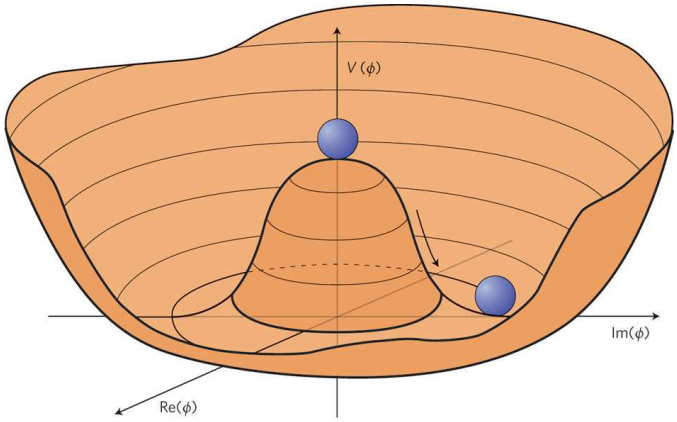

Figure 1.1: The Higgs potential as a function of Φ in the plane $\mathcal{R}(\Phi)$-$\mathcal{I}(\Phi)$ for $\mu^2 < 0$ and $\lambda > 0$ [43].

Nambu-Goldstone bosons, which are absorbed by the three gauge fields W_i^μ. The remaining field, $H(x)$, is the real scalar Higgs field –the Higgs boson. Thus, Φ is replaced by

$$\Phi = \frac{1}{\sqrt{2}} \begin{pmatrix} 0 \\ v + H(x) \end{pmatrix}. \tag{1.24}$$

This way, once the Higgs field acquires a vacuum expectation value, the gauge bosons gain mass by absorbing the Nambu-Goldstone bosons. Thus, the broken symmetry provides masses to the gauge bosons. The value of gauge bosons masses can be found by their coupling to the Higgs field:

$$m_{W^\pm} = \frac{gv}{2}, \tag{1.25}$$

$$m_{Z^0} = \frac{v}{2}\sqrt{g^2 + g'^2}, \tag{1.26}$$

while the photon remains massless. The relation between the mass of the bosons and the weak mixing angle is

$$m_{W^\pm} = m_{Z^0} \cos\theta_W. \tag{1.27}$$

The Higgs mechanism also provides mass to quarks and charged leptons in a similar procedure. These couplings between the fermions and the Higgs field are described by the Yukawa interactions. The procedure basically adds another term to the SM Lagrangian. Fermions acquire a mass proportional to the vacuum expectation value v, and are given by

$$m_f = \frac{\lambda_f}{\sqrt{2}} v, \tag{1.28}$$

where the Yukawa coupling constant λ_f becomes another parameter of the theory.

To finalize, as stated before, the weak interaction mediated by $W^\pm$ bosons is the only one able to change the flavor of a fermion. But, the mass eigenstates of fermions are not the same as the ones of the weak interaction. For quarks, the unitary transformation connecting the two bases of mass and weak eigenstates is represented by the Cabibbo-Kobayashi-Maskawa (CKM) matrix V_{CKM}[44, 45], while for leptons the mixing is described by the Pontecorvo-Maki-Nakagawa-Sakata matrix[4]. The V_{CKM} is a 3×3 unitary matrix, where the weak eigenstates q'

[4]This matrix is actually not a part of the SM, since it was introduced to explain the neutrino oscillations [46, 47].

of the down-type quarks connect to the mass eigenstates as

$$\begin{pmatrix} d' \\ s' \\ b' \end{pmatrix} = \begin{pmatrix} V_{ud} & V_{us} & V_{ub} \\ V_{cd} & V_{cs} & V_{cb} \\ V_{td} & V_{ts} & V_{tb} \end{pmatrix} \begin{pmatrix} d \\ s \\ b \end{pmatrix}. \tag{1.29}$$

The probability for a quark of flavor i to be transformed to a quark of flavor j, emitting a W boson is proportional to the component $|V_{ij}|^2$ of the CKM matrix. Each one of the mixing parameters has to be determined experimentally. They are valid only under the assumption of three generations of fermions. Their values (extracted from Ref. [22]) are:

$$V_{CKM} = \begin{pmatrix} V_{ud} & V_{us} & V_{ub} \\ V_{cd} & V_{cs} & V_{cb} \\ V_{td} & V_{ts} & V_{tb} \end{pmatrix} = \begin{pmatrix} 0.9743 & 0.2253 & 0.0035 \\ 0.2252 & 0.9734 & 0.0412 \\ 0.0087 & 0.0404 & 0.9991 \end{pmatrix}. \tag{1.30}$$

1.3 Four tops in the SM

In order to have a better understanding of the production and decay of four top quarks it is important to summarize some of the properties of the top quark itself.

The top quark is the heaviest particle described by the SM, and also the last quark discovered [48, 49]. It has a mass of 173.2 ± 0.9 GeV [50], which is close to the electroweak symmetry breaking scale. It is special not only due to its large mass, but also due to its short lifetime, which is around 5×10^{-25} s. Since the characteristic hadron formation time is around 3×10^{-24} s, it decays before hadronizing, i.e. there are no hadrons made of top quarks, and it has to be studied through its decay products. The fact that the top quark decays before hadronizing also allows to study the properties of the (anti)top quark itself.

The top quark properties are well determined by the SM, meaning that it provides a sensitive probe of the validity of the model. Since the Yukawa coupling to the Higgs boson is close to 1, it also provides a good opportunity to look for physics beyond the SM. This topic will be discussed in Section 1.5.

The production of the four top quarks in the SM as well as their decay modes is briefly described in the following section.

1.3.1 Production

Four top quarks are produced in hadron colliders via the strong interaction. At the LHC, at $\sqrt{s} = 7$ TeV, the dominant mechanism is the gluon-gluon fusion with a fraction of the total rate of 98%, followed by the quark-antiquark annihilation with a fraction of 2%. Both mechanisms are shown in Fig. 1.2. In both cases, two gluons are produced and the four top quarks are obtained via gluon splitting. The production cross-section of four top quarks via these processes at the LHC computed at leading order (LO) approximation is around 0.53 (resp. 11) fb at 7 (resp. 14) TeV [51].

1.3.2 Decay

In the SM, there are three possible top decays: $t \to Wb$, $t \to Ws$ and $t \to Wd$. The probability for each type of down-type quark to occur as decay product is proportional to the square of the

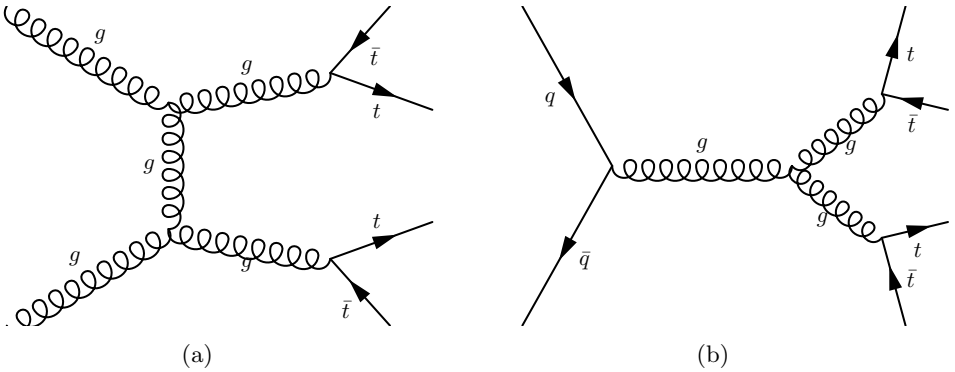

Figure 1.2: Production of four top quarks via gluon-gluon fusion (a) and quark-antiquark annihilation (b).

magnitude of the corresponding element of the CKM matrix, $|V_{tq}|^2$ with $q = b, s, d$, respectively. For the particular decay $t \to Wb$, this can be written in terms of the ratio of the branching fractions. Assuming that the CKM matrix is unitary and that there are three generations of quarks, this is given by

$$R_b = \frac{\mathcal{BR}(t \to Wb)}{\mathcal{BR}(t \to Wq)} = \frac{|V_{tb}|^2}{|V_{tb}|^2 + |V_{ts}|^2 + |V_{td}|^2} = 0.998, \tag{1.31}$$

which means that the top quark decays almost uniquely into a W boson and a b-quark.

For an event with four top quarks, the final state is determined by the decay of the W bosons. Each one of them can decay either leptonically, into a charged lepton-neutrino pair ($W \to \ell\nu_\ell$, with $\ell = e, \mu, \tau$), or hadronically, into a quark-antiquark pair ($u\bar{d}$ or $c\bar{s}$[5]). There are three possible combinations for the leptonic decay, while there are six possibilities for the hadronic one[6]. Each of the nine decay modes occurs almost at the same frequency. The branching fractions for these decays are shown in Table 1.3. As can be seen, each leptonic decay occurs more or less with the same probability making around 33% of the total.

Decay mode	**Branching fraction**
$e^+\nu_e$	$(10.75 \pm 0.13)\%$
$\mu^+\nu_\mu$	$(10.57 \pm 0.15)\%$
$\tau^+\nu_\tau$	$(11.25 \pm 0.20)\%$
$q\bar{q}'$	$(67.60 \pm 0.27)\%$

Table 1.3: Branching fractions of the different decay modes of the W boson [22].

There are 35 final states for four top quarks depending on the W decay –q, e, μ, τ. They can be grouped into five channels, each one with a different signature:

[5]This is referred to the weak interaction eigenstates rather than the Cabibbo rotated mass eigenstates.
[6]This is because of each pair is always color neutral and can be formed for the three different color combinations.

- **Fully hadronic:** events where the four W bosons decay hadronically. Their final state is composed of 12 jets, where 4 of them are coming from b-quarks.
- **Mostly hadronic:** events where three W bosons decay hadronically and one leptonically. The final state has one charged lepton, 6 light jets, 4 b-jets and missing transverse momentum.
- **Semi-leptonic/hadronic:** events where two W bosons decay leptonically and two hadronically. The experimental signature includes 2 charged leptons, 4 light jets, 4 b-jets and missing transverse momentum.
- **Mostly leptonic:** in this kind of events three W bosons decay leptonically. The signature in the detector consists of 3 charged leptons, 2 light jets, 4 b-jets and missing transverse momentum.
- **Fully leptonic:** events where all W bosons decay leptonically. They are composed of 4 charged leptons, 4 jets coming from b-quarks and missing transverse momentum.

Examples of each one of these final states are shown in Fig.1.3. The corresponding branching fractions are shown in Fig. 1.4. The four tops decay topology considered in this analysis corresponds to events with two isolated leptons (semi-leptonic/hadronic) with the same electric charge ($hh\ell^{\pm}\ell^{\pm}$ with $\ell^{\pm}\ell^{\pm} = e^{\pm}e^{\pm}$, $\mu^{\pm}\mu^{\pm}$, $e^{\pm}\mu^{\pm}$). The branching fraction for this topology (4.19%) is smaller than the one for the most-hadronic (40.04%). However, this analysis aims to look for New Physics and therefore, this signature is experimentally favored since the presence of two same-sign leptons in the final state allows to reduce the background coming from Standard Model processes, since this kind of events is rarely produced in the SM. It may have in particular large contributions from new phenomena.

1.4 Limitations of the Standard Model

The Standard Model has achieved considerable success in describing and predicting the physical processes observed in experiments. For example, the theory predicted the existence of the $W^{\pm}$ and Z bosons before they were discovered [52, 53]. Despite its success, there are still many open questions that do not have any answer in the SM, indicating that it may be a low-energy approximation of an underlying more fundamental theory. Some of its shortcomings are presented here.

- By construction, the SM does not include gravity. That limits the validation of the model to energy scales at which gravity is small compared to the other interactions. So far, there is not a successful theoretical framework capable of describing general relativity in terms of a quantum field theory. The effects of quantum gravity become important at high enough energies. This scale is quantified at first approximation by the Planck scale $M_{\text{Planck}} \approx 10^{19}$ GeV, beyond which the SM is not expected to be valid anymore.
- Latest studies from the Planck mission [54] indicate that ordinary matter is just 4.9% of the energy content of the Universe. Another 26.8% is *dark matter* [55]. Evidence of dark matter has been confirmed through the study of galactic rotation curves. Since dark matter has not been detected through electromagnetic or strong interactions, it is believed that it is

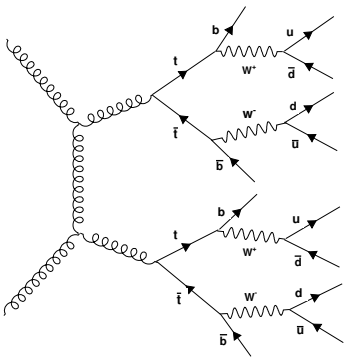

(a)

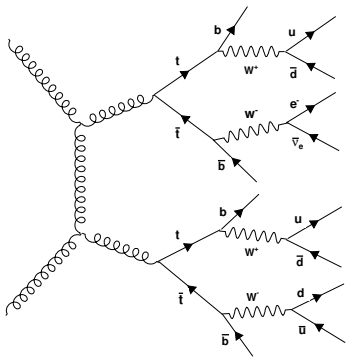

(b)

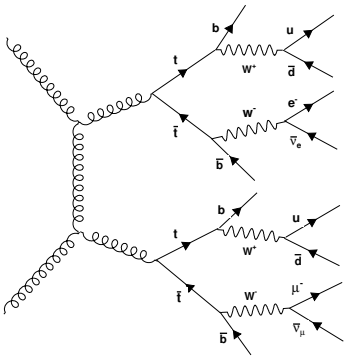

(c)

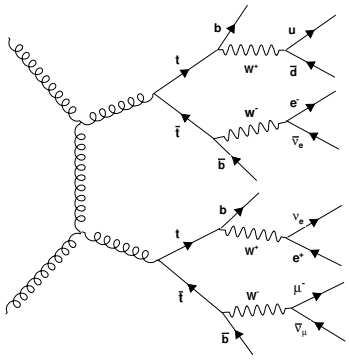

(d)

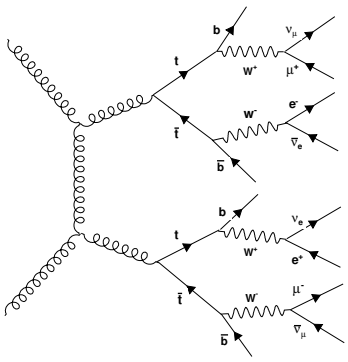

(e)

Figure 1.3: Feynman diagrams examples illustrating the different final states of four top quarks in the full-hadronic (a), most-hadronic (b), semi-leptonic/hadronic (c), most-leptonic (d) and full-leptonic channels (e).

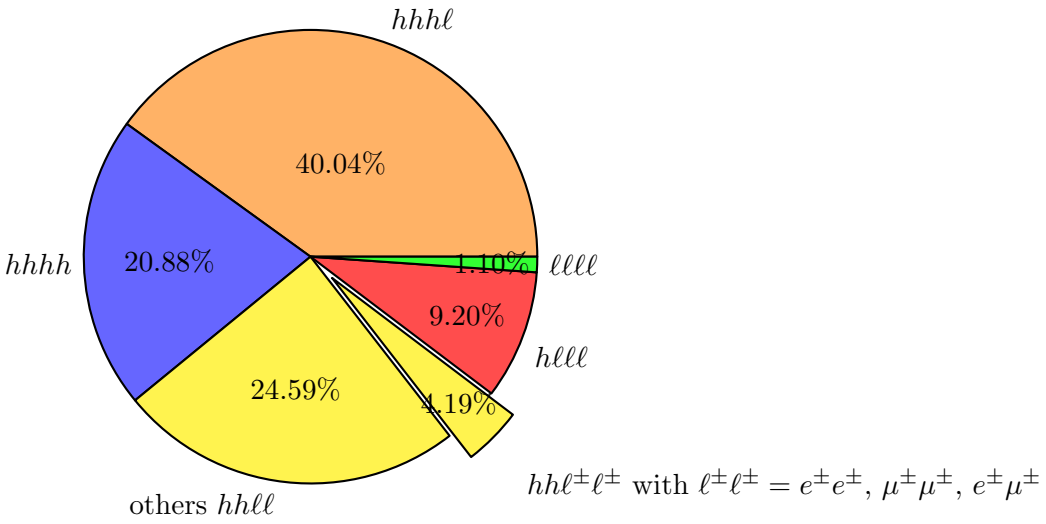

Figure 1.4: Branching fractions for the different decays of the four top quarks, depending on whether the W boson decays hadronically (h) or leptonically (ℓ).

composed of weakly interacting massive particles (WIMPs). The combination of ordinary matter and dark matter is still only 31.7%. The remaining 68.3% is called *dark energy* [56], which is inferred as responsible for accelerating the expansion of the Universe [57, 56]. The SM does not provide any candidate for dark matter and does not explain dark energy.

- In the SM there are three fundamental symmetries: C (charge conjugation), P (parity), and T (time-reversal). If all of them are respected there is no reason for the prevalence of matter with respect to antimatter observed in the Universe [58]. However, in the SM, there is no source of CP violation strong enough which can explain the matter-antimatter asymmetry [59].

- Neutrinos are proposed by the SM as massless particles. However, the observation of neutrino oscillations provides experimental evidence that neutrinos have mass [23, 24, 25, 26, 27]. Nevertheless, it can be easily accommodated in the SM.

- As stated before, quarks and leptons are grouped in three different families. The SM does not explain why there are three generations of particles nor its mass hierarchy. In addition, it does not explain why there are so many different types of quarks and leptons.

- In the SM with electroweak symmetry intact, all particles are massless. Explicit mass terms are forbidden in the Lagrangian due to gauge invariance. A new mechanism (Higgs) has to be introduced "by hand" in order to break the symmetry, and therefore, to generate the masses of the particles. The SM does not explain the origin of this mechanism.

- The *hierarchy problem* constitutes a major limit of the SM. Following renormalization, the Higgs mass at first order is given by

$$M_H^2 = (M_H^2)_{\text{bare}} - \frac{\lambda_f^2 \Lambda^2}{8\pi^2}, \tag{1.32}$$

where the first term corresponds to the bare Higgs mass squared and the second one to one-loop corrections. λ_f is the coupling constant to a fermion f, and Λ is interpreted as the scale above which the SM is no longer valid. If the scale is that of gravity –as said before–, then Λ is the Planck scale. If $M_H \sim 125$ GeV, in order to keep this value at the weak scale, two large numbers must cancel to an extremely high precision. This way, an unnatural fine-tuning is required to balance terms which can take values up to 10^{19} GeV. Thus, the hierarchy problem is just a consequence of the disparity between the strengths of the electroweak and gravitational interactions.

- In addition, the SM does not explain the particle quantum numbers, such as the electric charge Q, weak isospin I, hypercharge Y and colour C. It also contains at least 19 arbitrary parameters. These include three independent gauge couplings and a possible CP-violating strong-interaction parameter, six quark and three charged-lepton masses, three generalized Cabibbo weak mixing angles and the CP-violating Kobayashi-Maskawa phase, as well as two independent masses for weak bosons [60].

1.5 Four-top production in beyond the SM theories

The need to look for New Physics is motivated by the limitations presented by the SM. The top quark is the heaviest particle, with the largest coupling to the Higgs boson, making it a natural laboratory to explore New Physics. Many new physical models are linked to the top quark. Many of them predict an enhanced rate for events containing four top quarks with respect to the SM production, which is very small at the energies accessible for the Large Hadron Collider.

The four-top signal has been proposed in the past as a probe of the nature of the electroweak symmetry breaking [6, 7]. Moreover, this signal is enhanced in extended or modified electroweak symmetry breaking sectors beyond the SM in models of composite tops [10, 11] and supersymmetric models with light stops and gluinos [12]. Enhancement production of $t\bar{t}t\bar{t}$ events also appears in extra dimensional models, where the four-top signal is described as an important probe for low scale warped extra dimensions [8], or in specific models which provide a natural dark matter candidate [9]. Therefore, searching for events containing four top quarks could open a window on new physics phenomena.

This section briefly discusses some of the beyond the Standard Model (BSM) physics which can lead to experimental signatures involving four top quarks.

1.5.1 Models involving right-handed top quarks

This section describes the frameworks predicting four tops as a final state, but which involve only right-handed top quarks.

1.5.1.1 Randall-Sundum model

The Randall-Sundrum model [61] is a five-dimensional model which addresses the hierarchy problem without introducing a new energy scale in the fundamental theory. The fifth dimension is a slice of anti-de Sitter spacetime, strongly curved, and compactified on a S^1/Z^2 orbifold. In this model, the four dimensional metric is multiplied by the warp factor which is function of the additional dimension.

The full metric is given by

$$ds^2 = e^{-2kr_c\phi}\eta_{\mu\nu}dx^\mu dx^\nu + r_c^2 d\phi^2, \tag{1.33}$$

where k is a scale of order the Planck scale, $\eta_{\mu\nu}$ refers to the flat Minkowski metric, x^μ are the usual four dimension coordinates, and ϕ is the angular coordinate that parametrizes the fifth dimension satisfying $0 \leq \phi \leq \pi$, and whose size is set by r_c. This last one represents the radius of compactification of the extra dimension. The orbifold fixed points at $\phi = 0, \pi$ are taken as the location of two 3-branes, which extend in the x^μ-directions, so that they represent the boundaries of the five-dimensional spacetime. The boundary $\phi = 0$ is called the *Planck* or *UV* brane, while the one at $\phi = \pi$ is called the *TeV* or *IR* brane. The SM fields are constrained to the TeV brane, while gravitons exist in the full five-dimensional spacetime. The warp factor is represented by the exponential, which is the source of the large hierarchy between the observed Planck and weak scales. The model predicts a discrete spectrum of Kaluza-Klein (KK) excitations of the graviton, which couple to the SM fields with a coupling that is enhanced by the warp factor to be of the order of electroweak strength.

While in the original model the SM fields are constrained to the TeV brane, variations of the Randall-Sundrum model have been proposed in which the SM fermions and gauge bosons propagate throughout all five dimensions [62, 63, 64, 65, 66]. These versions have desirable features like the suppression of FCNC[7], generating the large mass hierarchies, and also allow gauge coupling unification at high energies. The interesting signal in this scenario is the production of KK excitations of the gauge bosons, and for the LHC, the production of KK gluons (g_{KK}).

The KK gluon couples strongly to the right-handed top quark. As a consequence, it decays predominantly to top pairs [67]. Four top quarks can be obtained via pair production of KK gluons or via their single production in association with a $t\bar{t}$ pair [8, 67, 68]. One example of the Feynman diagram is shown in Fig. 1.5.

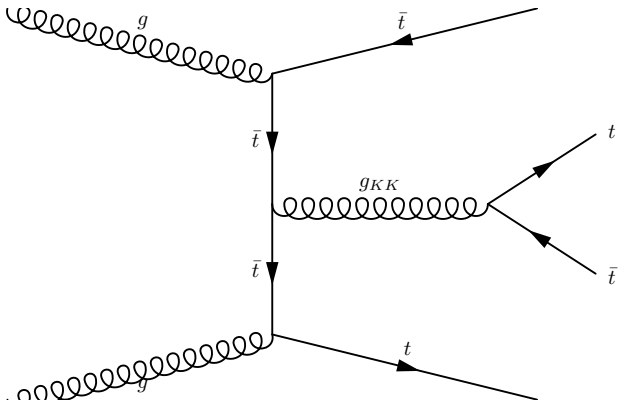

Figure 1.5: Feynman diagram example illustrating the production of four top quarks in an extended version of the Randall-Sundrum model.

[7]Flavor-Changing Neutral Current.

1.5.1.2 Top compositeness

Many models exist in which the top quark is composite [69, 70, 71, 72, 11]. In general, they are motivated by the large mass of the top quark.

In some of these theoretical frameworks, the standard search for compositeness looks for higher dimensional (non-renormalizable) operators, where only the right-handed component of the top is composite [72, 11]. The largest of these operators is a four-point interaction of t_R of the form:

$$(\bar{t}_R\gamma^\mu t_R)(\bar{t}_R\gamma_\mu t_R). \tag{1.34}$$

An example of this four-top quark contact interaction is shown in Fig. 1.6. In these models, the top quark is composed of some new constituent particles, called preons, which are bound together by a new confining force. Above the scale of confinement, there should exist a weakly coupled description in terms of its constituents. Below this scale, the physics should be described by an effective field theory which contains the bound states that result. The right-handed top quark should be the lightest of the bound states of this new sector. At the LHC, the energy should be high enough as to explore for top compositeness, where the operator given by Eq. 1.34 will lead to an enhancement of the $t\bar{t}t\bar{t}$ production rate.

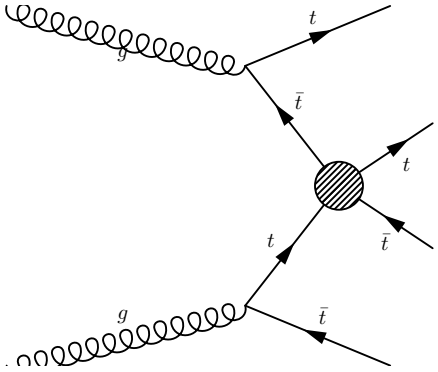

Figure 1.6: Feynman diagram example illustrating the production of four top quarks via contact interaction.

1.5.1.3 Low energy effective field theory

The low energy effective field theory assumes that the effects of new physics can be well captured by higher dimensional interactions among the SM particles, which respect all the symmetries of the SM.

In the framework given by Degrande et *al*. in Ref. [13], a model independent approach is presented. It includes operators which are not specific to a BSM theory, and therefore it can be used to test models where new physics can manifests itself as four-right-handed top contact interaction. This is the case of theories predicting new heavy vector particles strongly coupled to the right-handed top such as top compositeness [73, 72, 11] or Randall-Sundrum theories [67]. Due to the general character to test different new physics theories of this approximation, it would be the theoretical framework to look for New Physics in this thesis. This is described below.

The independent model approach presented in Ref. [13] considers only non-resonant *top-philic*[8] new physics, focusing on modifications from new physics to top pair production. All the symmetries of the SM are conserved by the new physics. Operators up to six-dimensions are considered. They correspond to the set of operators which affect the $t\bar{t}$ production at tree-level by interference with the SM amplitudes. At the LHC, the dominant SM amplitudes involve QCD via gluon-gluon fusion or quark-antiquark annihilation. Therefore, all new interactions which interfere only with SM weak processes are neglected. New interactions that would affect only the standard gluon vertices and operators affecting the decay of the top quark are also ignored. This leaves only two kinds of operators:

- Operators with a top and an antitop and one or two gluons:

$$\mathcal{O}_{gt} = [\bar{t}\gamma_\mu T^a D^\nu t]G^A_{\mu\nu}, \tag{1.35}$$
$$\mathcal{O}_{gQ} = [\bar{Q}\gamma^\mu T^A D^\nu Q]G^A_{\mu\nu}, \tag{1.36}$$
$$\mathcal{O}_{hg} = [(H\bar{Q})\sigma^{\mu\nu}T^A t]G^A_{\mu\nu}, \tag{1.37}$$

  where $Q = (t_L, b_L)$ represents the left-handed weak doublet of the third quark generation, t denotes the right-handed top quark, T^A are the generators of $SU(3)$ in the fundamental representations normalized to $tr(T^A T^B) = \delta^{AB}/2$.

- Four-fermion operators with a top and an antitop together with a pair of light quark and antiquark. They can be grouped depending on their chiral structures:

  – $\bar{L}L\bar{L}L$:

$$\mathcal{O}^{(8,1)}_{Qq} = (\bar{Q}\gamma^\mu T^A Q)(\bar{q}\gamma_\mu T^A q), \tag{1.38}$$
$$\mathcal{O}^{(8,3)}_{Qq} = (\bar{Q}\gamma^\mu T^A \sigma^I Q)(\bar{q}\gamma_\mu T^A \sigma^I q), \tag{1.39}$$

  – $\bar{R}R\bar{R}R$:

$$\mathcal{O}^{(8)}_{tu} = (\bar{t}\gamma^\mu T^A t)(\bar{u}\gamma_\mu T^A u), \tag{1.40}$$
$$\mathcal{O}^{(8)}_{td} = (\bar{t}\gamma^\mu T^A t)(\bar{d}\gamma_\mu T^A d), \tag{1.41}$$

  – $\bar{L}L\bar{R}R$:

$$\mathcal{O}^{(8)}_{Qu} = (\bar{Q}\gamma^\mu T^A Q)(\bar{u}\gamma_\mu T^A u), \tag{1.42}$$
$$\mathcal{O}^{(8)}_{Qd} = (\bar{Q}\gamma^\mu T^A Q)(\bar{d}\gamma_\mu T^A d), \tag{1.43}$$
$$\mathcal{O}^{(8)}_{tq} = (\bar{q}\gamma^\mu T^A q)(\bar{t}\gamma_\mu T^A t), \tag{1.44}$$

  – $\bar{L}R\bar{L}R$:

$$\mathcal{O}^{(8)}_{d} = (\bar{Q}T^A t)(\bar{q}T^A d), \tag{1.45}$$

  where σ^I are the Pauli matrices, which are normalized to $tr(\sigma^I\sigma^J) = 2\delta^{IJ}$. q, u and d represent respectively the left- and right-handed components of the first two generations.

[8] That means that the new physics manifests itself in the top sector.

The operator $(\bar{Q}T^A\gamma^\mu q_L)(\bar{Q}T^A\gamma^\mu q_L)$ as well as its $SU(2)$ triplet and color singlet analogues have been discarded since they are already constrained by flavor physics [74].

In composite models, and at energies below the resonances masses, the top sector can be described by the SM Lagrangian plus a few higher dimensional operators. This kind of model is characterized by a new strong interaction which is responsible for the electroweak symmetry breaking. It is parametrized by two parameters: g_ρ and m_ρ. The former represents a dimensionless coupling, while the latter is a mass scale associated to the heavy physical states. The decay constant of the Goldstones f is related to these parameters by

$$m_\rho = g_\rho f \tag{1.46}$$

where the coupling must satisfy $1 \lesssim g_\rho \lesssim 4\pi$. The size of these operators is controlled by simple rules referred to as Naive Dimensional Analysis (NDA) [75, 76]. Two classes of gauge-invariant operators are relevant for the top pair production:

- Operators containing only fields from the strong sector. This kind of operators is dominant since their coefficients scale like g_ρ^2. If only the right component of the top quark is composite the operator is given by

$$\mathcal{O}_R = (\bar{t}\gamma^\mu t)(\bar{t}\gamma_\mu t). \tag{1.47}$$

  If only the left handed is composite, there are two independent operators

$$\mathcal{O}_L^{(1)} = (\bar{Q}\gamma^\mu Q)(\bar{Q}\gamma_\mu Q), \tag{1.48}$$
$$\mathcal{O}_L^{(8)} = (\bar{Q}\gamma^\mu T^A Q)(\bar{Q}\gamma^\mu T^A Q). \tag{1.49}$$

  If both chiralities are composite, two additional operators should be considered

$$\mathcal{O}_S^{(1)} = (\bar{Q}t)(\bar{t}Q), \tag{1.50}$$
$$\mathcal{O}_S^{(8)} = (\bar{Q}T^A t)(\bar{t}T^A Q). \tag{1.51}$$

  However, none of these operators contribute at tree-level to the top pair production. But, they are relevant for the direct production of four top quarks.

- Operators contributing directly to $t\bar{t}$ production. This kind of operators is subdominant.

This way, if the top quark is not an elementary particle but rather a composite bound state, the dominant operators are the ones given in Eq. 1.47-1.51. Thus, the direct production of four top quarks would be a golden channel to study this dynamics. Usually, in most composite top models only its right handed component is composite, since left handed are already constrained by experimental results [77]. Thus, the final Lagrangian is given by

$$\mathcal{L} = \mathcal{L}_{SM} + \frac{C}{\Lambda^2}(\bar{t}_R\gamma^\mu t_R)(\bar{t}_R\gamma_\mu t_R), \tag{1.52}$$

where $\mathcal{L}_{SM}$ is the Standard Model Lagrangian, t_R is the right-handed top spinor, γ_μ are the Dirac matrices, C is a dimensionless constant and Λ is the new physics energy scale. An example of the four tops production via this four tops contact interaction operator is shown in Fig. 1.6.

1.5.2 Other models involved in the four-top production

This section describes only a couple of other models involved in the four-top production that are not studied in this thesis.

1.5.2.1 Universal extra dimensions (UED/RPP) model

This model is a Universal Extra Dimension (UED) model. It considers two extra dimensions which are compactified under the Real Projective Plane geometry (RPP) [78, 79, 9].

In the framework presented in [9], a UED on the flat RPP is considered. This geometry is the consequence of requiring the absence of fixed points/lines of the orbifold, together with the existence of chiral zero modes for fermions. This model provides a dark matter candidate which is a direct consequence of the geometry of the orbifold. It can be thought of as a rectangular patch of a torus with the opposite sides identified as twisted, in the way of a double Möbius strip. The Real Projective Plane can also be obtained from a sphere with identified antipodal points.

The lowest order Lagrangian is given by the SM Lagrangian, but extended to 6 dimensions. A tower of massive resonances corresponds to each SM field. The towers are organized in tiers, and labelled by the intergers k and l. They correspond to the discretization of the momenta along the extra directions. At leading order, the states in each tier are degenerate. Their masses are determined by the two integers

$$m_{l,k}^2 = \frac{l^2}{R_5^2} + \frac{k^2}{R_6^2}, \tag{1.53}$$

where $R_{5,6}$ are the radii of the two extra dimensions. The absence of fixed points in the orbifold ensures that the residual symmetry (after the compactification of the 6D space-time with its 6D Lorentz symmetry) is left unbroken. This symmetry forbids the decay of the lightest particle from tier $(1,0)$ (and tier $(0,1)$ in case of equal radii) to SM particles, thus allowing for a natural dark matter candidate.

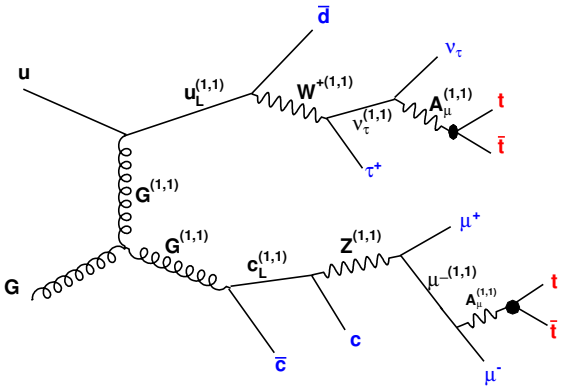

Figure 1.7: Feynman diagram example illustrating the four tops production in the UED/RPP model.

The four tops final state arises from particles of tier $(1,1)$. Particles from this tier are pair produced via bulk interactions. Once a heavy state of this tier is produced, it then chain

decays until the lightest state of this tier: the vector photon $A_\mu^{(1,1)}$. Soft SM particles are emitted during this process due to the small mass splitting within a given tier. The two heavy photons then decay via next-to-leading order processes into a pair of SM particles. As the top is the heaviest SM particle it is assumed to couple more strongly to the UV completion of the model. As the heavy states are pair produced, and under the assumption that the vector photon decays predominantly in $t\bar{t}$ pairs, the final state will contain four tops ($t\bar{t}t\bar{t}$) plus a few low energy SM particles. This process is illustrated in Fig. 1.7.

1.5.2.2 Scalar gluon (sgluon) pair production

The sgluon is a complex color-adjoint scalar, with a R-parity of 1. It can arise in supersymmetric models [80, 81], vector-like confining theories [82, 83], or extra-dimensions models [84].

If the gauge coupling of sgluon to gluons is allowed, the sgluon can be produced by QCD processes. Single sgluon production is also allowed but strongly suppressed. Below the top quark threshold the decay through gluons should be the dominant [85], while after the threshold, the sgluon mainly decays to top quarks. This way, four top quarks can be obtained by pair production of sgluons [86]. An example of this production is illustrated in Fig. 1.8. For very high mass sgluons, the decay to squarks and gluons is not negligible [81].

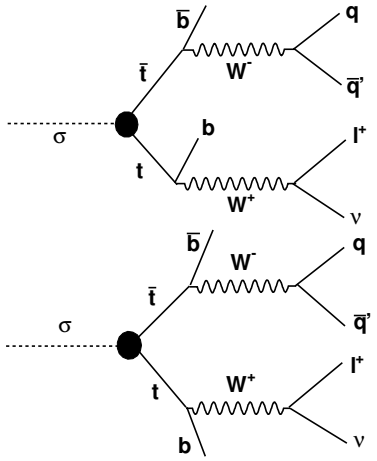

Figure 1.8: Feynman diagram example illustrating the production of four top quarks via pair production of sgluon.

Chapter 2

The Large Hadron Collider

Contents

2.1 Introduction

The collisions of particles allow to explore in the deepest of the matter, studying from the smallest to the biggest in the Universe. In particular, in this field, the interest resides in understanding Nature each time at smaller scales.

This need of knowing the last components of the matter started in 1911 when Rutherford and collaborators used alpha particles as projectiles to probe the theory proposed by Thompson. The study of the atomic structure gave rise to a new field in physics, whose experimental part was done *initially* by studying the collisions of the particles produced by radioactive sources against a fixed target. The need of creating new instruments capable of generating particles to be used as projectiles with the goal of obtaining a better understanding of atomic nucleus gave rise to the particle accelerators. Approximately 20 years after Rutherford's experiment, in England, Cockcroft and Walton managed to construct the first particle accelerator to produce a nuclear disintegration by generating a proton beam to bombard Lithium isotopes. During the same year, and in parallel to the creation of the Cockcroft-Walton generator, the first cyclotron was operated in Berkeley.

But for exploring the possible structure of protons and neutrons, energies much bigger were needed. After the construction of these first accelerators, other kind of accelerators such as synchrotrons and linear accelerators were created. A big advance was done during the second half of

the twentieth century with the development of accelerators each time more powerful, starting with the first large proton synchrotron, the Cosmotron at Brookhaven National Laboratory, which accelerated protons to about 3.3 GeV. Later, the Bevatron at Berkeley, the Synchrophasotron at Dubna, the Alternating Gradient Synchrotron (AGS) at Brookhaven, the Proton Synchrotron (PS) and the Super Proton Synchrotron (SPS) at CERN were built. The Stanford Linear Accelerator (SLAC) became operational in 1966 accelerating electrons up to 50 GeV, and it is still the world's longest linear accelerator. Tevatron, completed in 1983 with a ring of 6.4 km, and capable of accelerating protons and antiprotons to energies up to 1 TeV, ceased operations in 2011 as the second highest energy particle collider, almost 20 years after announcing what can be considered its biggest discovery: *the top quark* [48, 49]. The largest circular accelerator ever built has been the Large Electron-Positron (LEP) synchrotron at CERN with a circumference of 26.7 km, and which was intended to collide electrons and positrons to energies of up to 209 GeV. Many of the particles discovered in these accelerators were originally thought to be elementary. Now, most of them have since turned out to be composites of quarks.

Most of the objects of interest to the particle physicist today do not exist as free particles in Nature and they have to be created artificially. The progress in the understanding of these particles and the forces between them have been linked with the construction of accelerators more and more powerful. Currently, the highest energy collider is the *Large Hadron Collider* (LHC) [3].

By examining the collisions produced at LHC energies, it is possible to extract some information about the constituents of the matter. It is hoped that the LHC helps to clarify the questions not answered by the Standard Model, and thus it can point to the right direction in order to construct the Theory of Everything.

This chapter presents a summarized version about what is the LHC and its operation. It starts with a brief description of the LHC in Section 2.2, followed in Section 2.3 by a description of the chain of accelerators used to increase the energy of particle beams before injecting them to the LHC. The operation of the LHC is presented in Section 2.4. The main experiments installed around the LHC ring are described in Section 2.5. A summary of the LHC activity is given in Section 2.6. Finally, the pileup effect at the LHC is explained in Section 2.7.

2.2 Description

The Large Hadron Collider is a two-ring-superconducting-hadron accelerator and collider built by the European Organization for Nuclear Research (CERN). It is located beneath the Franco-Swiss border outside of Geneva, Switzerland, and lies between 45 m and 170 m underground on a plane inclined at 1.4% sloping towards Lake Geneva. It was installed in the existing 26.7 km tunnel that was constructed for the CERN LEP machine, making full use of its civil engineering structures[1].

Several parameters are used to define the physics potential of an accelerator. A large amount of energy is required to cross a new threshold of discovery, but the luminosity is also important. They are defined below:

- The center-of-mass energy ($\sqrt{s}$) is the total energy of a particle-particle system measured in the laboratory frame.

[1]The decision to build LHC at CERN was strongly influenced by the cost saving to be made by re-using the LEP tunnel and its injection chain. Even, LEP was closed in 2000 to liberate the tunnel for the LHC.

- The luminosity is defined in its simplest form as

$$\mathcal{L} = \frac{f_{rev} n_b N_p^2}{4\pi\sigma_x\sigma_y}, \tag{2.1}$$

where N_p is the number of particles per bunch, n_b the number of bunches, f_{rev} the revolution frequency, and σ_x and σ_y characterize the transverse beam profiles in the horizontal and vertical directions respectively.

Thus, the LHC has been designed to collide proton beams with a centre-of-mass energy of 14 TeV and an unprecedented luminosity of $10^{34}\text{cm}^{-2}\text{s}^{-1}$, making the LHC the world's largest and highest-energy particle accelerator. It can also collide heavy (Pb) ions with an energy of 2.8 TeV per nucleon and a peak luminosity of $10^{27}\text{cm}^{-2}\text{s}^{-1}$. In this thesis, the data used correspond to the ones taken during proton-proton collisions, and therefore the following description will be focused on that.

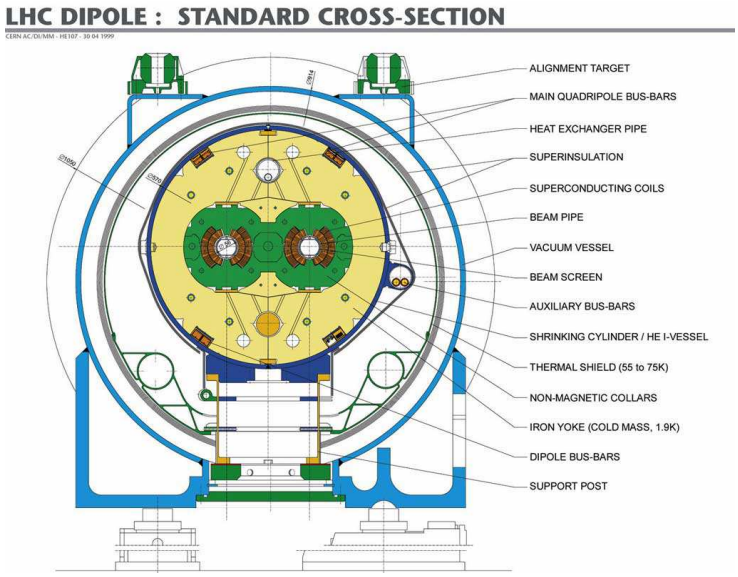

Figure 2.1: Cross-section of superconducting LHC dipole magnet placed throughout the LHC ring showing its main components.

The LHC design was driven keeping in mind the physical constraints imposed by LEP tunnel and to achieve its ambitious goals related to the beam energy and luminosity. This way, it was designed as a two-ring superconducting accelerator. Protons were chosen because the energy loss due to synchrotron radiation in circular accelerators is negligible in their case. The two proton beams circulate in separate vacuum tubes in the opposite direction along two rings crossing each other in eight points. In four of these intersections four experiments have been installed (see Section 2.5). The remaining four sections do not have beam crossings. The beam trajectory is bent by 1232 14.3 m long superconducting dipole magnets that surround the tubes. The overall design is based on a two-in-one dipole magnet as shown in Fig. 2.1. The superconducting elements are Niobium-Titanium (NbTi) coils cooled to 1.9 K through the use of 96 tons of superfluid liquid Helium, providing a maximum field strength of 8.33 T at a current

of around 11.7 kA. 392 quadrupoles magnets are used to focus the beams. Both rings share a cryogenic and mechanical structure. They are coupled magnetically, each ring having a magnetic flux equal in magnitude, but opposite in direction to the other.

2.3 Accelerator complex

The LHC is only the final stage of the CERN accelerator complex. Before reaching the LHC, the particles are accelerated by a series of accelerators that progressively increase their energy. This chain of accelerators is depicted in Fig. 2.2, where the most important links in the chains for both proton and ion beam production are shown. Several filling schemes have been defined for the LHC, each defined for different modes of operation. Detailed information about these filling schemes is given in Ref. [87]. The following explanation is focused in the chain acceleration of protons.

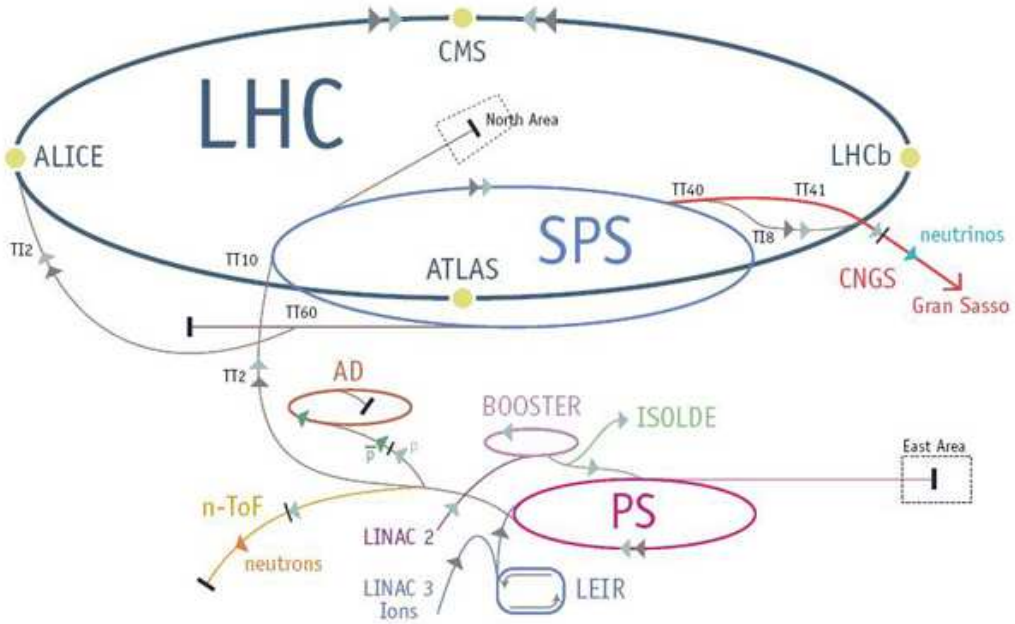

Figure 2.2: The LHC accelerator complex. Protons are accelerated by the LINAC 2, the BOOSTER, the PS, and the SPS accelerators prior to injection into the LHC.

Protons are created from hydrogen atoms that are ionized by an electric field in a duoplasmatron. They are first accelerated to 50 MeV using a linear accelerator: LINAC 2. Then, protons are injected into the first circular accelerator of the chain, the *Proton Synchroton Booster* (PSB or BOOSTER), which increases the protons' energy up to 1.4 GeV. The *Proton Synchroton* (PS) will raise the energy from 1.4 GeV to 25 GeV. From the PS, the proton beam is then injected to the *Super Proton Synchroton* (SPS), where the energy of the particles increases up to 450 GeV[2] to be finally injected at the LHC, in both, clockwise and counter-clockwise directions.

[2]This is the minimum energy at which the LHC can maintain a stable beam.

At the LHC, protons circulate around 20 minutes before reaching the maximum energy. In this last stage, the energy of the proton beam can be raised up to 7 TeV. More information about the injection chain of the LHC can be found in Ref. [88].

2.4 Operation

The proton injection from the SPS is performed in bunches. In the nominal conditions (i.e. for an operation with 25 ns bunch spacing and which has not been used so far), prior to injection, bunches are split into patterns of 72 bunches separated by 12 empty buckets, forming bunch trains. The radio frequency (RF) cavities of the LHC operating at approximately 400 MHz, capture, accelerate and store the beams. This results in around 35640 regions in the RF field where it is energetically favorable for the bunches to be located in the beam (called RF buckets). It corresponds to a spacing in time of 2.5 ns, but only one-tenth of these regions can be filled with protons. Thus, the LHC fills 2808 of the 3564 available regions per beam, making the resulting bunch spacing 25 ns. The remaining 742 stable regions are left for beam injection and abort system. The minimum distance between bunches is about 7 m. Each bunch has a maximum size of roughly 1.15×10^{11} protons, and orbits the ring with a frequency of 11 kHz. Bunch crossings occur at each of the interaction points at a frequency of 40.08 MHz.

After injection into the LHC, the beams are declared as stable once they have accomplished the desired energy. In this moment, the experiments start the data taking. Beams circulate and collide for a long period of time, which can take as long as 24 hours. Over this time, the instantaneous luminosity will degrade due to the loss of protons in the collisions, or through other factors, and the proton bunches slowly lose their integrity. When the quality of the beam is insufficient, the beam is directed out the accelerator, "dumped" into a large metal block where it is absorbed, and the magnets are ramped down to 0.54 T. Then the LHC is refilled before the magnets are ramped up again to 8.33 T starting a new cycle. This beam cycle is called a "fill". The LHC running conditions for the nominal design and during the data taking in 2011 and 2012 are shown in Table 2.1.

Parameter	**Nominal**	**June 2011**	**June 2012**
Beam energy [TeV]	7	3.5	4
Bunch spacing [ns]	25	50	50
Number of bunches	2808	1092	1380
Number of particles per bunch	1.15×10^{11}	1.25×10^{11}	1.48×10^{11}
Magnetic field on the dipoles [T]	8.33	4.16	4.76
Beam current [A]	0.582	0.236	0.369
Bunch length [cm]	7.55	≥ 8.7	≥ 9
Luminosity [$\mathrm{cm}^{-2}s^{-1}$]	10^{34}	1.2×10^{33}	6.8×10^{33}
Transverse beam size at the interaction point [μm]	16.7	34	19
Crossing angle at the interaction point [μrad]	285	240	290

Table 2.1: LHC running conditions for the nominal design and during the data taking in 2011 and 2012.

2.5 Main experiments

Four main experiments have been installed in four of the eight interaction points of the LHC ring: CMS [5], ATLAS [4], LHCb [89] and ALICE [90]. Each one of the detectors has been designed with a different proposal. Their locations around the LHC ring are depicted in Fig. 2.2. They are described below:

- **CMS (Compact Muon Solenoid):** It is one of the two large general purpose experiments. It was designed to improve or confirm measurements of the Standard Model and to look for New Physics.
- **ATLAS (A Toroidal LHC AparatuS):** As CMS, ATLAS is a large general purpose experiment designed to study many different types of physics that might become detectable in the energetic collisions of the LHC. Both experiments were designed to complement each other both to extend reach and to provide corroboration of their discoveries.
- **LHCb (Large Hadron Collider beauty experiment):** It is an experiment dedicated to heavy flavor physics. It is designed to look for indirect evidence of new physics in CP violation and rare decays of beauty and charm hadrons, which could help to explain the matter-antimatter asymmetry of the Universe.
- **ALICE (A Large Ion Collider Experiment):** It is an experiment focused on the study of heavy ion collisions at the LHC. It is designed to study the physics of strongly interacting matter and the quark-gluon plasma at extreme values of energy density and temperature, or, in a few words, to understand the matter confinement at the early time of Universe.

Other experiments as TOTEM (TOTal Elastic and diffractive cross section Measurement) [91], LHCf (Large Hadron Collider forward) [92], and MoEDAL (Monopole and Exotics Detector At the LHC) [93] have been also integrated to the LHC. TOTEM shares the intersection point with CMS and it aims to measure the total pp cross-section with the luminosity-independent method and study elastic and diffractive scattering at the LHC. LHCf is a special-purpose experiment designed to measure neutral particles emitted in the very forward region of collisions. It shares the intersection point with ATLAS. Finally, MoEDAL is dedicated to the search for the magnetic monopole and other highly ionizing stable massive particles at the LHC.

2.6 LHC activity

On September 10, 2008, the LHC successfully circulated its first proton beams. Nine days after starting operations, and before collisions were managed, the accelerator had to be taken out of operation due to a magnet quench occurred in about 100 bending magnets. On November 20, 2009, low-energy proton beams circulated in the LHC tunnel for the first time since the incident. Three days after that, the first pp collisions were finally recorded by all detectors at the injection energy of 450 GeV. Shortly after, on November 30, the LHC achieved 1.18 TeV per beam becoming the world's highest energy particle accelerator. Collisions at $\sqrt{s} = 2.36$ TeV were then recorded in mid-December 2009. A new record was broken by the LHC on March 19, 2010, when the beam energy was ramped up to 3.5 TeV, culminating in the first pp collisions at $\sqrt{s} = 7$ TeV on March 30, 2010. The main goal of the LHC during 2010 was to gain experience operating the machine, in particular in terms of injecting, ramping, squeezing and establishing

stable beams. The beam energy was kept at 3.5 TeV in whole 2011, and increased up to 4 TeV in 2012.

The analysis performed in this thesis uses proton-proton collision data from the LHC collected by the ATLAS detector during 2011 and 2012. The total integrated luminosity recorded by the ATLAS detector and delivered by the LHC during these years is shown in Fig. 2.3. It shows that the ATLAS detector was recording data with an efficiency of around 94%. In 2013 the LHC went into a long shutdown to prepare for higher-energy running starting in 2015.

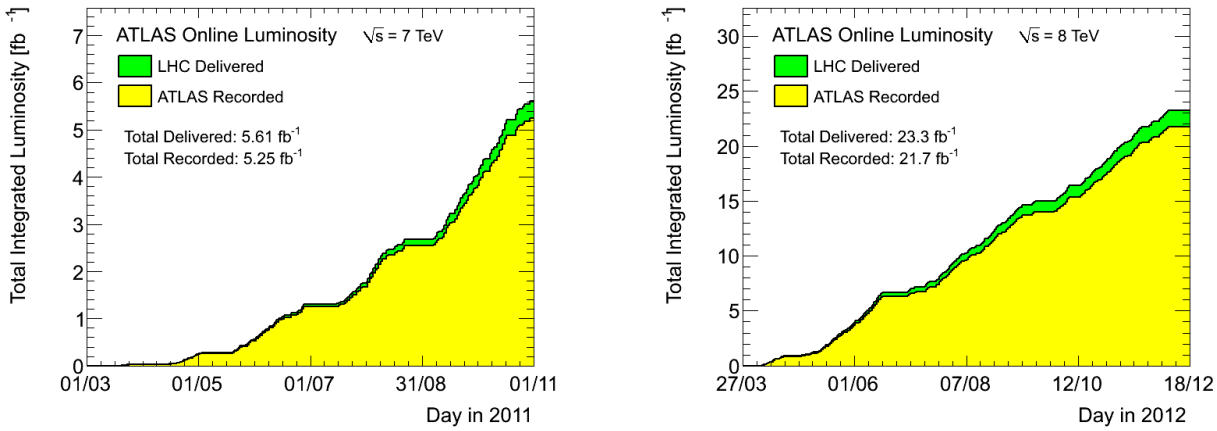

Figure 2.3: Total integrated luminosity delivered by the LHC and recorded by the ATLAS experiment during 2011 (left) and 2012 (right).

2.7 Pile-up effect at the LHC

As stated before, the luminosity is one of the main parameters that define the potential of an accelerator. Rare physics processes that could be produced at the LHC have a small expected cross-section, for that reason, a high luminosity is needed in order to produce them. As shown by the Equation 2.1, the luminosity depends on the number of particles per bunch, on the number of bunches, the revolution frequency and the transverse size of the beam. From the beginning of its operation, the LHC has experimented several distinct periods of configuration. This way, changes in the beam optics and proton bunch parameters resulted in clear changes in the delivered luminosity.

The luminosity permits to determine the rate of particle interactions. That means that as long as the luminosity increases, the possibility to have multiple *pp* interactions measured as only one event in the same bunch crossing increases proportionally. This phenomenon is known as *pileup*. Therefore, more *pp* collisions in a bunch crossing different from that which produced the collision of interest can therefore affect the measurement.

From the beginning of its operation, the instantaneous luminosity delivered by the LHC has increased continuously (see Fig. 2.4), augmenting the pileup of events. This phenomenon can really occur in two distinct forms:

- The large number of protons in colliding bunches gives rise to multiple collisions per bunch crossing. But even at the highest instantaneous luminosities, most bunch crossings will

contain only one hard interaction. Additional interactions in each crossing are referred to as *in-time pileup*, which typically comes from soft particles, which contribute with energy distributed homogenously throughout the detector. The best estimator of the in-time pileup is the number of reconstructed primary vertices.

- Though only one *pp* interaction happened in a given bunch crossing, *pp* interactions in a previous bunch crossing can also affect the measurement if the spacing between the bunches is shorter than the response time of the detectors. This way, additional collisions from different bunches are recorded simultaneously. This is referred to as *out-of-time pileup*, and it will become important as the LHC bunch spacing is decreased. The out-of-time pileup is estimated using the average number of *pp* collisions per bunch crossing at the time of the recorded event[3].

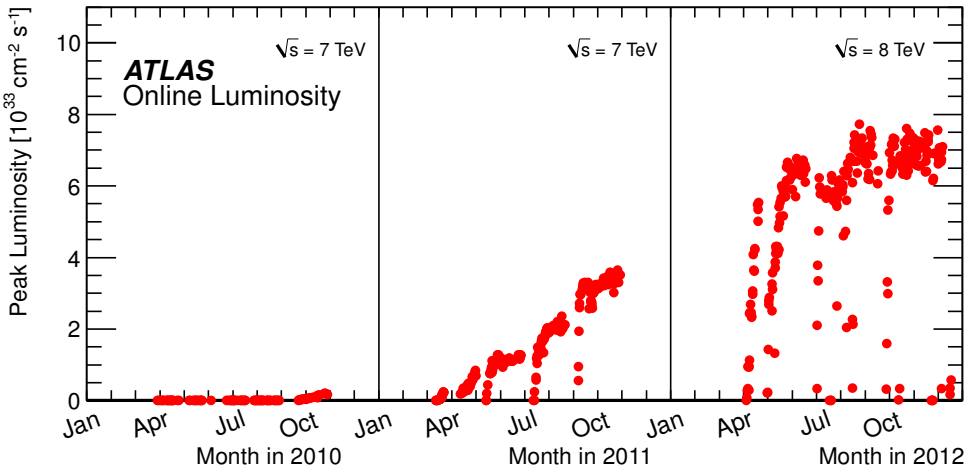

Figure 2.4: The peak instantaneous luminosity delivered to ATLAS per day versus time during the *pp* runs of 2010, 2011 and 2012.

In 2010, the maximum instantaneous luminosity delivered by the LHC was about $2.1 \times 10^{32}\text{cm}^{-2}\text{s}^{-1}$, and the bunch spacing was not smaller than 150 ns. In this low-luminosity running conditions, the average number of interactions per event was 2.2, with a maximum of 3.78, mostly arising from in-time pileup. The effect of the out-of-time pileup was small due to the big bunch spacing. In 2011, the bunch spacing was reduced to 50 ns with an instantaneous luminosity that reached values of $3.65 \times 10^{33}\text{cm}^{-2}\text{s}^{-1}$ increasing the out-of-time pileup. The average number of *pp* collisions per bunch crossing was between 3 and 8 until September technical stop, with an average of 6.3. It increased to reach values between 5 and 17 after that September, with an average of 11.6. In 2012, the bunch spacing was kept to 50 ns, and the luminosity reached a value of $7.73 \times 10^{33}\text{cm}^{-2}\text{s}^{-1}$ with a mean number of interactions per bunch crossing of 20.7. The maximum mean number of events per beam crossing versus day during the *pp* collisions runs of 2010, 2011 and 2012 is shown in Fig. 2.5. At the design luminosity and for a bunch spacing of 25 ns, it is expected to have around 23 interactions per bunch crossing.

[3]This number is computed using the average luminosity over a time period $\Delta t \gg 600$ ns, the total inelastic *pp* cross-section, the LHC revolution frequency and the number of colliding bunches.

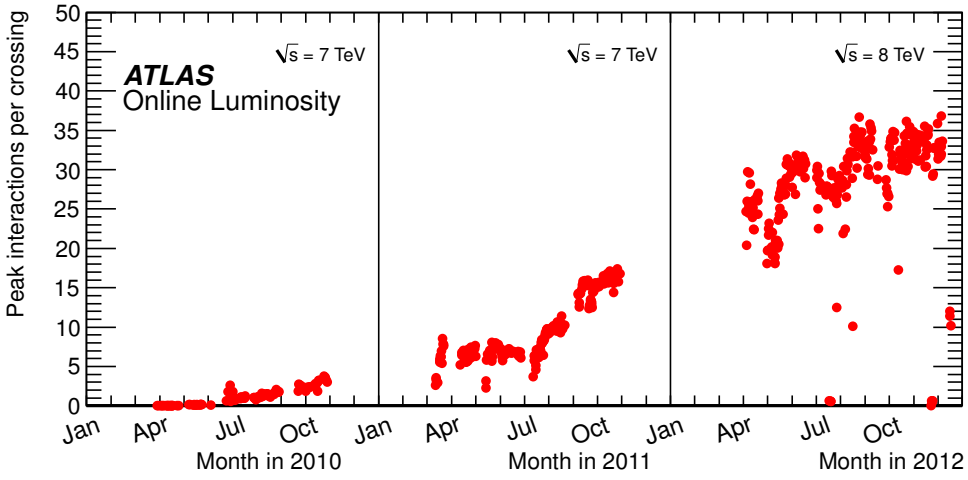

Figure 2.5: Maximum mean number of events per beam crossing versus day during the *pp* collisions runs of 2010, 2011 and 2012.

Chapter 3

The ATLAS detector

Contents

Daniela Paredes

3.1 Introduction

The ATLAS experiment was proposed in 1994 and approved in 1996. Currently this experiment groups more than 3000 scientists from 175 institutions in 38 countries, making it one of the largest collaborations ever formed in the world.

As mentioned in the previous chapter, ATLAS is one of the general purpose detectors constructed at the LHC, designed to improve or confirm measurements of the Standard Model and to look for New Physics. It is 45 m long, 25 m in diameter and weighs about 7000 tons. Its design requirements were driven by some of the most important signals for possible New Physics which could be observed, and to support the hard radiation environment.

The ATLAS detector consists of an ensemble of sub-detectors with cylindric shape placed around the interaction point where the proton beams from the LHC collide. From the interaction point outwards, these sub-detectors can be identified as: the *inner detector*, which is used for tracking of charged particles, the *calorimeters*, which surround the inner detector and are used for measuring the energies of the particles traversing them, and the *muon spectrometer*, which is the most external system and is used for identifying muons and measuring their momenta. A *magnet system* is used to bend the charged particles for momentum measurement. The overall ATLAS detector layout is shown in Fig. 3.1. Additional measurements can be done using the *forward detectors*. The detector has been designed as hermetic as possible, meaning that it must detect all particles produced with the exception of neutrinos. However, the neutrinos presence can be inferred by measuring a momentum imbalance among detected particles.

A *trigger system* has also been implemented, which has been designed to decide which events should be recorded in a very short time. Each aspect already mentioned will be discussed in this chapter, starting from a definition of the coordinate system and the basic quantities used in this thesis.

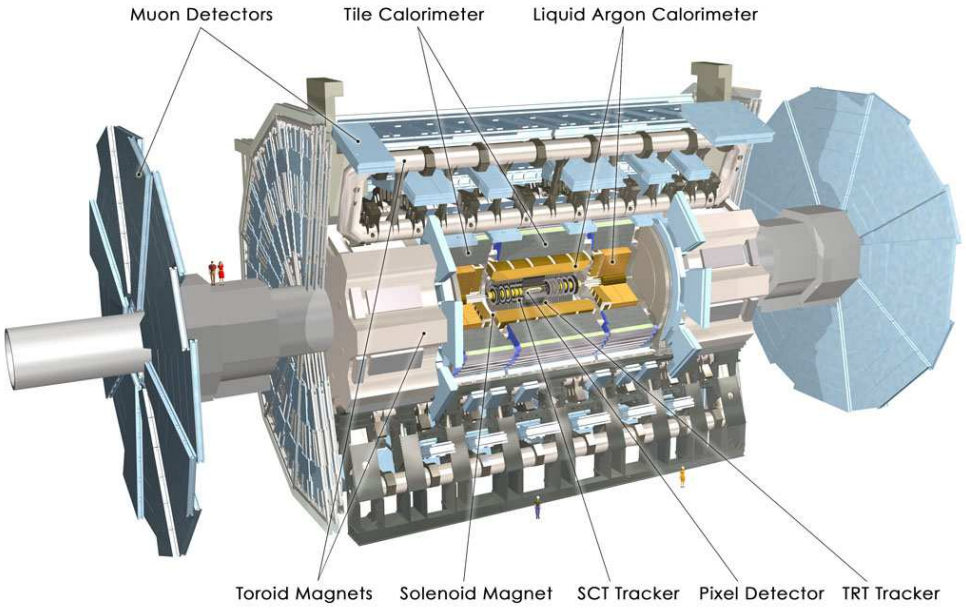

Figure 3.1: The Atlas detector.

3.2 The coordinate system and basic quantities

The coordinate system used to describe the ATLAS detector and the particles emerging from the collisions defines the origin at the nominal proton-proton interaction point, located in the geometrical center of the detector. The reference system is a Cartesian right-handed coordinate system, where the counter-clockwise beam direction defines the positive z-axis. The x-y plane is perpendicular to the z-axis, with the positive x-axis pointing from the interaction point to the center of the LHC ring and the y-axis points towards the surface, upwards from the interaction point. The detector is symmetric for positive and negative z, the part of the detector corresponding to $z > 0$ is called "Side A", while for $z < 0$ is called "Side C". Some subsystems of the detector are composed of a barrel portion with detecting elements parallel to the z-axis, and two endcap portions with detecting elements arranged in transversal planes to the beam axis. These endcaps can be referred as "Endcap-A" and "Endcap-C".

From this reference system, cylindrical and polar coordinates are defined in order to describe either the detecting elements, the trajectories of the particles through the detector, or some of the variables repeatedly used throughout this thesis. The azimuthal angle ϕ is measured in the x-y plane around the beam axis ($\phi = 0$ is defined along the positive x-axis), while the polar angle θ is taken with respect to the positive z direction. The radius r is defined as the perpendicular distance to the z axis.

In proton-proton collisions, the constituents partons carry unknown fractions of the proton momentum. A large fraction of the longitudinal momentum (z-axis) gives rise to hard processes which cannot be fully measured, and some of this momentum is lost in the remnants that escape down the beam pipe, thus the overall boost of the collision is unknown. For that reason, Lorentz invariant quantities are used in most analyses. Thus, the polar angle is rarely used and it is replaced by the rapidity

$$\mathrm{y} = \frac{1}{2}\ln[(E + p_z)/(E - p_z)], \tag{3.1}$$

with E representing the energy of the object, and p_z its momentum along the beam direction; or rather the pseudorapidity, which is equal to the rapidity in the ultrarelativistic approximation

$$\eta = -\ln[\tan(\theta/2)]. \tag{3.2}$$

Since η is a function only of the polar angle θ, it has a well-defined and mass-independent interpretation in the laboratory frame. It is also common to refer to the η-ϕ angle space, in which the surfaces of the cylindrical detectors appear as flat sheets, and where the ΔR cone is defined as

$$\Delta R = \sqrt{\Delta\eta^2 + \Delta\phi^2}. \tag{3.3}$$

In proton collisions, partons carry unknown fractions of the proton momentum. Some of that momentum is exchanged in the hard interaction, and some of it is lost to remnants that escape down the beam pipe. This way, the total momentum conservation can not be easily used to place constraints on the kinematics of an event. However, as protons approach each other with trajectories that are nearly along the z-axis, momentum is conserved in the plane perpendicular to the beam axis. Thus, in many cases, only the transverse component is used when describing object kinematics, as for example, $E_{\mathrm{T}} = E\sin\theta$ and $p_{\mathrm{T}} = p\sin\theta$, which are defined in the x-y plane. In this thesis, the pseudorapidity and the transverse components of the energy and momentum, are the kinematic variables which play a fundamental role in the analysis description.

3.3 Inner detector

The inner detector (ID) [94, 95] is the component of the ATLAS detector closest to the beam axis. It is designed to reconstruct the trajectories of charged particles traversing it, to provide excellent momentum resolution, and both primary and secondary vertex measurements for charged tracks with a $p_{\mathrm{T}} > 0.5$ GeV[1] covering the region $|\eta| < 2.5$ with full coverage in ϕ. It has a transverse momentum resolution $\sigma_{p_{\mathrm{T}}}/p_{\mathrm{T}} = 0.05\% p_{\mathrm{T}}$ GeV $\oplus\, 1\%$, and it also permits to identify electrons within $|\eta| < 2.0$ for energies between 0.5 GeV and 150 GeV [4].

The inner detector is contained within a cylinder envelope ± 3512 mm in length, with outer radius 1150 mm. It is immersed in a 2 T magnetic field generated by a superconducting solenoid magnet (described in Section 3.7.1), which is necessary to bend charged particles for momentum measurements[2].

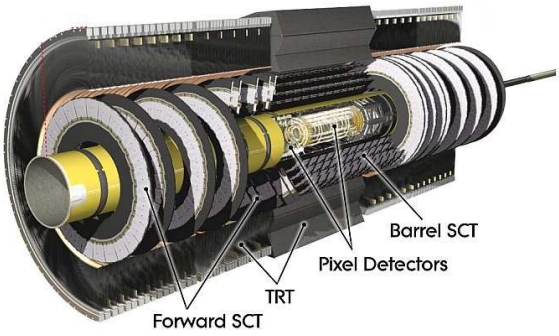

Figure 3.2: Cut-away view of the ATLAS inner detector showing each one of the sub-detectors.

In the collisions, a large amount of particles are created in the interaction point generating a large track density in the detector. In this way, a fine granularity of this part of the detector is needed. This is managed by means of the use of three high precision subsystems within the inner detector: the *Pixel Detector* (Pixel), which is the subsystem closest to the interaction point and is composed of silicon pixel sensors; the *SemiConductor Tracker* (SCT), which is just outside of the pixel detector; and the *Transition Radiation Tracker* (TRT), which is the outermost system. Their configuration is illustrated in Fig. 3.2. The first two sub-detectors (Pixel and SCT) use semiconductor technology and provide a small number of hits on track, while the TRT uses small drift tubes (straw tubes) providing a semi-continuous tracking out to large radii and the identification/separation of electrons and pions. Each of the sub-detectors is divided in a *barrel* region, where they are arranged in concentric cylinders around the beam line (see Fig. 3.3(a)); and an *endcap* region, where the detecting elements are mounted on disks orthogonal to the

[1] This value is nominal, but it can be as low as 0.1 GeV in some studies of measurements with minimum-bias events.

[2] The transverse momentum of the particle is determined by using the following relation $p_{\mathrm{T}}[\mathrm{GeV}] = 0.3 \times B[\mathrm{T}] \times R[\mathrm{m}]$, where B is the magnetic field and R the bending radius [96].

beam axis (Fig. 3.3(b)), and which are used to increase the detector coverage in η without a significant increase in detector surface.

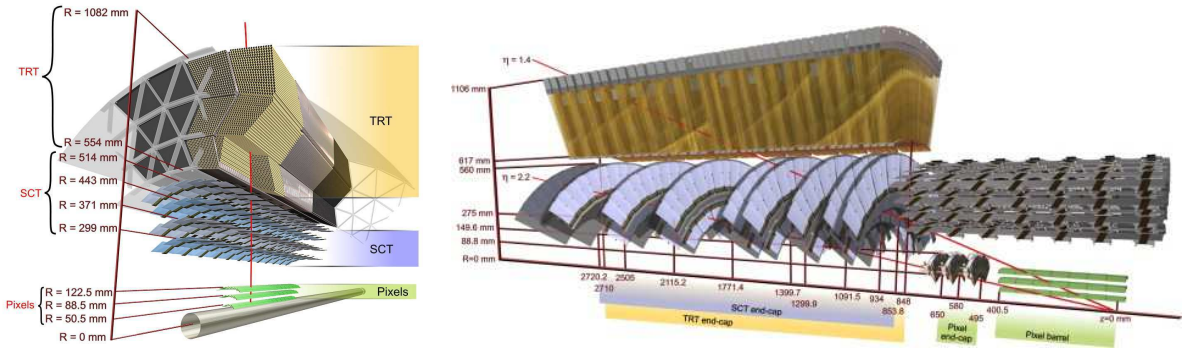

(a) ID Barrel (b) ID Endcap

Figure 3.3: The barrel (a) and endcap (b) tracking system of the ATLAS inner detector. The barrels of each sub-detector are arrayed in concentric cylinders around the beam line, while the endcaps are mounted on disks perpendicular to it.

Since all material between the interaction point and the calorimeters degrade the resolution of the measured energy, the three sub-detectors have to be designed with a structure so that it minimizes the quantity of matter to be crossed by the particles, and also to support the high-radiation conditions to which they are subjected for being the part of the detecter closest to the beam axis.

In this section, a brief description of each one of the subsystems of the inner detector is given. More details about the inner detector can be found in [94, 95].

3.3.1 The Pixel Detector

The innermost tracking subsystem of the ID is the semiconductor pixel detector [97]. It has the highest granularity detecting elements as close to the interaction point as possible, which provide the most accurate position measurements in ATLAS. The pixel detector consists of three concentric barrel layers[3] (called ID layers 0-2) placed at radii of 50.5, 88.5, and 122.5 mm around the beam axis covering the central region up to $|\eta| = 1.9$; and three endcap disks placed at $|z|$ positions of 495, 580 and 650 mm in each direction along the beam axis from the interaction point, extending the total coverage out to $|\eta| = 2.5$. This configuration is shown in Fig. 3.4.

Each layer or disk is segmented in modules, which form the basic unit of data acquisition. Each module has an active surface of 6.08×1.64 cm^2 and it is assembled primarily of a silicon sensor and 16 radiation-hard front-end chips [98] bump-bonded to the sensor, each with 2880 read-out channels, making the only mechanical connection between the sensors and the front-end electronics. Thus the pixel detector consists of 1744 sensor tiles of approximately 250 μm thick and external dimensions of 19×63 mm^2, using oxygenated n-type wafers with readout pixels on

[3]The innermost one –ID layer 0– is mechanically integrated with the beryllium beam pipe in order to provide the best possible vertex resolution, and it is also called *b*-layer due to its function in identifying *b*-quarks initiated jets.

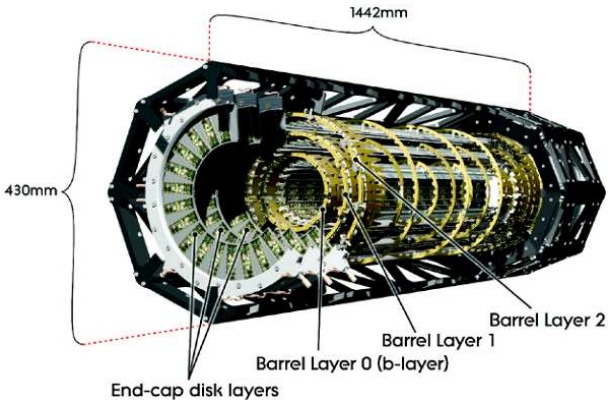

Figure 3.4: A schematic view of the active region of the pixel detector consisting of barrel and end cap layers.

the n^+-implanted side of the detector[4]. Each sensor tile contains 47232 bipolar diodes (or pixels), but for reasons of space there are four ganged pixels in each column of the front-end chip, leading to a 46080 readout channels, resulting in a total of 80.4 million pixels. The nominal pixel size is 50×400 μm^2 and it is dictated by the readout pitch of the front-end electronics[5].

A bias voltage is applied to the doped silicon sensors. This way, when a charged particle traverses the semiconductor, the electron-hole pairs created travel to the surface and produce the signal, which is collected if it exceeds a tunable threshold[6]. A charged particle originated at the interaction point typically traverses three layers, producing three pixel hits and permitting therefore determining the particle's position. The pixel detector is the most important detector used in the identification and reconstruction of secondary vertices from the decay of, for example, particles containing a b-quark or for b-tagging of jets. Moreover, it provides excellent spatial resolution for reconstructing primary vertices even in the presence of the multiple interactions in proton-proton collisions at the LHC design luminosity. Its intrinsic spatial resolution is 10 μm (r-ϕ) and 115 μm (z) in the barrel, and 10 μm (r-ϕ) and 115 μm (r) in the disks.

The pixel modules operate at a nominal voltage between 150 V and 600 V, which increases with their exposure to radiation. In order to reduce damage to the sensors due to the radiation, the silicon sensors must be kept at low temperature, between -5°C and -10°C. A more detailed description about the pixel electronic system is found in [97, 99].

3.3.2 The SemiConductor Tracker

The SCT [100] is located after the pixel detector, forming the middle part of the inner detector and it is based upon silicon microstrip detector technology. Similarly to the pixel detector, it is composed of a barrel and two endcap sections. The barrel has four coaxial cylindrical layers (called ID layers 3-6) at radii 299, 371, 443, and 514 mm around the beam axis in the radial direction, covering the central region up to $|\eta| = 1.1$. Each endcap region has nine disks of

[4]Highly oxygenated material increases the tolerance to the radiation to charged hadrons, while the n^+ implants allow the detector to work with good charge-collection efficiency.

[5]This size is for around 90% of the pixels, for the remaining ones the size is 50×600 μm^2 in the regions at the front-end chips on a module.

[6]This threshold was set at 3.5 ke$^-$ during the 2010 run.

different sizes located between 854 and 2720 mm from the interaction point along the beam axis, providing a total coverage out to $|\eta| = 2.5$.

The detector is segmented in 4088 modules: 2112 of rectangular shape in the barrel and 1976 trapezoidal in the endcap region. They are illustrated in Fig. 3.5 and 3.6, respectively. The modules are made of silicon-strip devices that arrange the strips parallel to the beam axis in the barrel and radially in the endcap, thus providing a precision measurement in (r-ϕ). They cover a total surface of 63 m^2 of silicon and provide almost hermetic coverage. The modules consist of one or two pairs of single-sided p-in-n microstrip sensors glued back-to-back at a 40 mrad stereo angle[7]. The sensors are divided into 768 AC-coupled strips (there are 1536 strips per module) of 12 cm in length, with a constant pitch of 80 μm in the barrel, while in the endcap it varies from 56.9 to 94.2 μm due to the trapezoidal shape. The intrinsic accuracies per module are 17 μm (r-ϕ) and 580 μm (z) in the barrel and 17 μm (r-ϕ) with 580 μm (r) for the endcap disks.

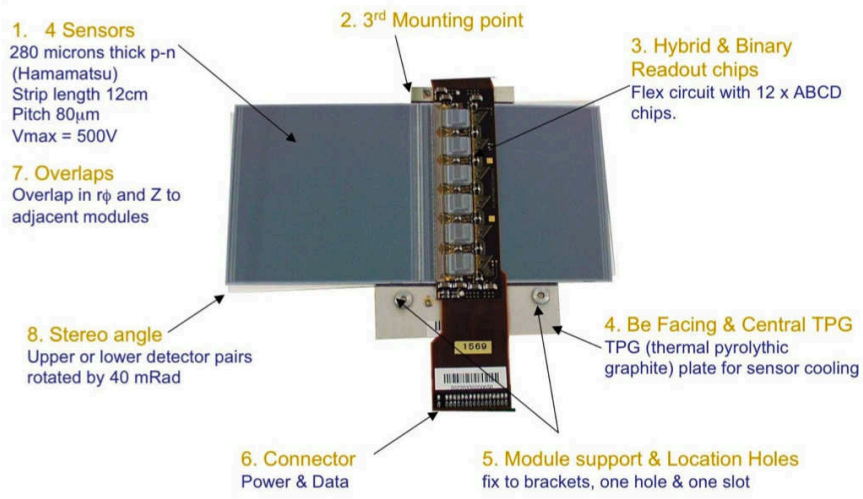

Figure 3.5: An SCT barrel module [101].

Many of the design considerations of this sub-detector, including the detection principle, are similar to those of the pixel detector. A charged particle originating from the interaction point typically crosses eight strip sensors, combining to form four space-point measurements, and contributing to the measurement of momentum, impact parameter and vertex position. A hit is registered only if the pulse height exceeds a preset threshold, which normally corresponds to a charge of 1 fC. The charge measured in the strip is stored for a period of ~3.2 μs and used for tracking if the trigger indicates that the event should be considered in more detail. Each module is read out by means of 12 identical 128-channel front-end ASICs[8], resulting approximately in 6.3 million readout channels [102].

The SCT operates under similar environmental conditions as the pixel detector, sharing the cooling system (based on C_3F_8) with it. The nominal voltage in the modules varies from ~150 V (bias voltage) up to 350 V during operation, but it can increase as much as 500 V as radiation damage accumulates. The SCT has been fully operational throughout all data taking

[7] This configuration gives the required space-point resolution in (r-ϕ) and r.
[8] Application-Specific Integrated Circuit.

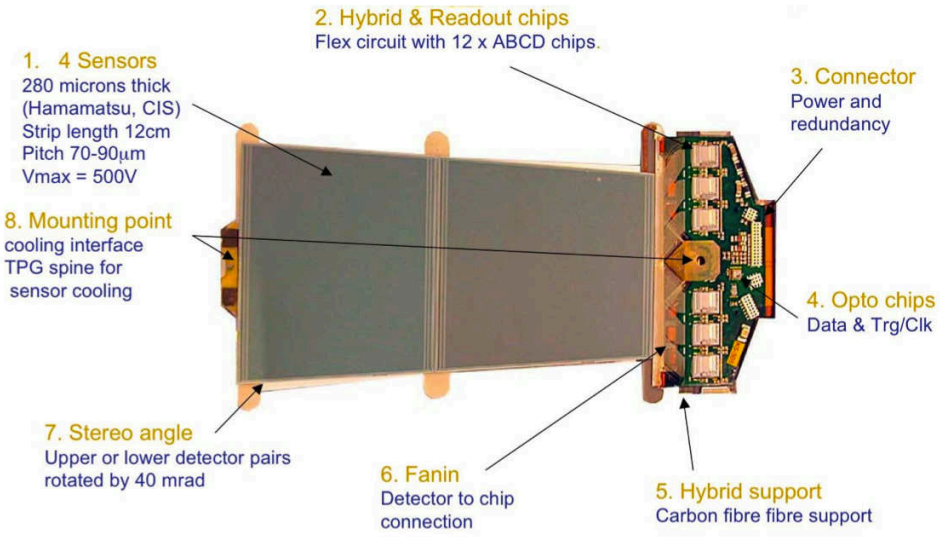

Figure 3.6: One of the types of SCT endcap modules [101].

periods, delivering high quality tracking data for 99.9% (2010), 99.6% (2011) and 99.3% (2012) of the delivered luminosity [103].

3.3.3 The Transition Radiation Tracker

The TRT surrounds the silicon detectors being therefore the outermost part of the inner detector. Its basic detector elements are polyimide drift tubes of 4 mm diameter denoted as straw tubes, filled with a gaseous mixture of 70% Xe, 27% CO_2 and 3% O_2, and mechanichally stabilized using carbon fibers. The straw tube wall was developed in order to have a minimal wall thickness, and specially good electrical and mechanical properties. Each tube is equipped with a 31 μm diameter tungsten wire plated with 0.5-0.7 μm gold. The wire is going through the center of the straw, supported at the straw end by an end-plug and it is directly connected to the front-end electronics.

As the other two sub-detectors, the TRT is composed of a barrel and two endcap sections. The barrel contains 73 layers of straws interleaved with polypropylene fibers forming an approximately uniform array parallel to the beam direction, with an average spacing of about 6.6 mm between centers radially and tangentially. It is divided into 96 modules of three types, arranged in three cylinders of 32 modules each one. The barrel spans the radius range from 56 cm up to 108 cm and has a sensitivity region of 144 cm in length along the beam axis, covering the region up to $|\eta| < 1$ [104]. Along the z-axis in each endcap there are 160 radial straw planes interleaved with polypropylene radiator foils[9], forming a uniform array in the azimuthal plane perpendicular to the beam axis, covering the backward and forward pseudorapidity region $1 < |\eta| < 2$. In the endcap region, the modules are referred as wheels because of their cylindrical shape and radial straws like spokes. Each endcap consists of two sets of independent wheels perpendicular to the

[9]The polypropylene radiator foils in the endcap region together with the polypropylene fibers in the barrel constitute the transition radiation material of the TRT.

beam direction, the set closer to the interaction point has 12 wheels, each with eight successive layers spaced 8 mm apart, while the outer set contains eight wheels, also with eight straw layers but spaced 15 mm apart [105]. There are 52544 straw tubes of 144 cm length in the barrel, while each endcap has 122880 straw tubes of 37 cm length, resulting in a total of 298304 straws, read out by 350848 channels of electronics.

Charged particles passing through the straws ionize the gas inside the tube. Because of the electric field created by the potential difference between the wire acting as the anode, and the wall of the tube playing the role of the cathode[10], the liberated electrons move towards the anode ionizing more the atoms in the gas, inducing therefore an avalanche of electrons that amplifies the signal at the wire. During normal operation the maximum electron collection time is ∼48 ns with a drift-time accuracy of 130 μm per straw. The straws only provide measurements in the bending plane, and no measurements along the straw direction.

The TRT is designed so that charged particles with $p_{\mathrm{T}} > 0.5$ GeV and $|\eta| < 2.0$ cross at least 36 straws, except in the barrel-endcap transition region ($0.8 < |\eta| < 1.0$), where this number decreases to at least 22 straws. This large number of tracking points allows almost continuous tracking that improves the precision of the momentum measurement. The TRT also provides electron/pion discrimination via transition radiation from the fibers interleaved between the straws in the barrel and the foils in the endcaps. When a relativistic particle pass between media with different dielectric constants, it emits energy in the form of photons. The total energy radiated by this particle is proportional to its Lorentz γ factor, which will be significantly larger for an electron with the same energy as a pion[11]. The emitted photons are absorbed by the Xenon gas, which increases the transition radiation and produce stronger signals. The amplitude of this signal will be higher when an electron traverses the transition material than when a pion does. Transition radiation photons yield much larger signals than minimum-ionizing charged particles. The distinction between transition radiation and tracking signals is obtained by using separate low and high thresholds in the front-end electronics[12]. Summarizing, the difference in the signal amplitude allows for particle identification by using transition radiation and tracking by using its ionization signals.

In contrast with the silicon detectors, the TRT is designed to operate at room temperature, but in order to avoid high-voltage discharges and pollution from diffusion of gas from the outside into the straws through their walls, or flush away any gas leakage from inside the straws, the modules have to be operated in an envelope of CO_2.

3.4 Calorimeters

The ATLAS calorimeter system is located outside the solenoid magnet that surrounds the inner detector. It consists of several non-compensating[13] sampling calorimeters which use different

[10] The wires are kept at ground potential, while the walls of the straws are kept at -1530 V to give a gain of 2.5×10^4 for the chosen gas mixture with 5-10 mbar over-pressure.

[11] $\gamma = E/mc^2$, where E is the energy of the particle and m its mass. For an electron with the same energy as a pion, the γ factor will be significately larger for an electron due to its mass being around 250 times smaller than the pion mass.

[12] The low-threshold is for ionization signals and it is set at $\approx$ 250 eV, while the high-threshold is for transition radiation and it is set at $\approx$ 6 keV.

[13] It refers to the fact that some energy released in nuclear collisions is lost to nuclear recoils and dissociation and it is not deposited in the active material.

technologies suited in order to study the different physics processes of interest, and to support the hard radiation environment. It has a full ϕ-symmetry and coverage around the beam axis spanning the pseudorapidity range up to $|\eta| < 4.9$, with a varying granularity in $\eta \times \phi$. Sampling calorimeters use alternating layers of absorber and active material. The incident particle interacts with the material in the calorimeter through several processes (they depend on the particle, its kinematics and the medium) producing a shower of particles that are detected in the active medium which measures the deposited energy on the material. In general, the absorber medium is chosen to be a dense material with a high stopping power so that particles in the energy range under study are contained in the calorimeter.

This way, the calorimeter system is designed to stop all the interacting particles emerging from the interaction point (except muons, which are not absorbed by the calorimeters since they are highly penetrating particles) measuring their energy and position. It provides electromagnetic and hadronic energy measurements. Thus, the ATLAS calorimeters can be classified corresponding to their design as *electromagnetic* and *hadronic* calorimeters. The electromagnetic (EM) calorimeter has a high granularity, which is needed for precision measurements of electrons and photons. It also contributes to measuring the energy of hadrons in jets. The hadronic calorimeter has a coarser granularity, but it is sufficient to satisfy the hadronic jets reconstruction and missing transverse energy measurements.

There are four calorimeters in ATLAS detector: the Liquid Argon (LAr) electromagnetic calorimeter, which covers the pseudorapidity region up to $|\eta| < 3.2$, the Tile hadronic calorimeter covering $|\eta| < 1.7$, the LAr hadronic endcap calorimeters covering $1.5 < |\eta| < 3.2$, and the LAr Forward calorimeter covering the region $3.1 < |\eta| < 4.9$. The overall system is depicted in Fig. 3.7, which indicates where the various calorimeters are installed. The ones closest to the interaction point are accommodated in three cryostats: one barrel and two endcaps. The barrel contains the LAr electromagnetic barrel calorimeter (EMB), while each one of the two endcap cryostats contains a LAr electromagnetic endcap (EMEC), a LAr hadronic endcap (HEC), situated behind the EMEC, and a forward calorimeter (FCal) covering the region closest to the beam axis. In all these calorimeters the active medium is liquid argon. The showers in the argon liberate electrons that are later collected and recorded. Liquid argon was chosen as the active medium due to its resistance to radiation, its linear behavior and its stability of response. The LAr calorimeters are housed in cryostats, which are cooled to a temperature of $\sim$89 K in order to maintain the argon in liquid state. Over the pseudorapidity range $|\eta| < 1.8$, the EM calorimeter is preceded by a presampler detector, which is installed behind the cryostat, and it is used to correct for the energy lost in the material upstream of the calorimeter [4].

The outer section of the calorimeter system is constituted by the Tile calorimeter. It consists of iron plates used as absorber material and scintillating plastic tiles used as active medium. Hadronic showers developing in the plates illuminate the tiles, the light thus produced is detected and recorded.

Hadronic and EM calorimeters provide separate event data for reconstruction. But, due to the fact that some energy can be deposited in the inactive region of the detector, they do not manage to measure the full energy of the original particle. The response of the calorimeter therefore refers to the fraction of energy of the incident particle that is measured. For that reason, calibrations need to be applied in order to properly measure the energy of the original particle.

In this section, a brief description of the electromagnetic and hadronic calorimeters is given. More information about the calorimeter system can be found in [4, 106, 107].

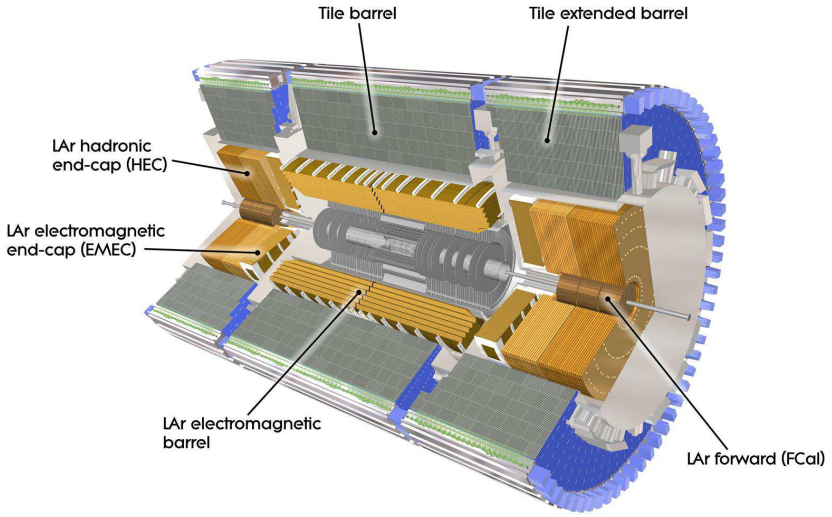

Figure 3.7: Cut-away view of the ATLAS calorimeter system. Calorimeters with LAr as active medium are situated in the inner section, while in the outer section the sampling medium consists of scintillator tiles [4].

3.4.1 The electromagnetic calorimeter

The EM calorimeter [108] provides precision measurements of electrons and photons, contributing also to measuring the energy of hadrons in jets. It is a lead-LAr detector with accordion-shaped kapton electrodes and lead absorber plates. The LAr is used as the active medium. The accordion geometry provides a full coverage in ϕ without azimuthal cracks, and a fast extraction of the signal at the rear or at the front of the electrodes. When a photon traverses the calorimeter, it interacts with the lead and produces an electron-positron pair. This pair also interacts with the material, producing Bremsstrahlung photons, which have the same effect that the incident photon creating an electromagnetic shower. Charged particles that traverse the active material ionize it, releasing ionization electrons which are collected as a current in the presence of an electric field by the electrodes mounted on the accordion plates. An electron passing through the LAr will produce the same reaction chain as a photon.

The accordion geometry of this calorimeter also allows it to have several active layers in depth. Thus the EM calorimeter is segmented in three longitudinal layers for the region up to $|\eta| < 2.5$. The first layer (at lowest r) is equipped with narrow strips in η with a pitch of $\sim$4 mm, and it has a depth of $\sim$6 radiation lengths (X_0) including dead material and presampler. It acts as a preshower detector, helping to identify particles and providing a precise position measurement in η. Only a small fraction of the energy of a particle is deposited there. The second (middle) layer is transversally segmented into square towers ($\Delta\eta \times \Delta\phi = 0.25 \times 0.25$, $\sim 4 \times 4$ cm^2 at $\eta = 0$), with a total thickness of the calorimeter up to the end of this section of $\sim 24 X_0$. Most of the energy is deposited in this layer. The last layer has a coarser granularity in η (twice with respect to the previous section), with a thickness between $2X_0$ and $12X_0$, and only contains the tails of the electromagnetic showers. For the region covering $|\eta| > 2.5$, the calorimeter is segmented

in two longitudinal layers, with a coarser lateral granularity than for the rest of the acceptance. The cells in the calorimeter point towards the interaction point over the complete η-coverage. As said before, the EM calorimeter is preceded by a presampler detector, installed behind the cryostat in the region where the amount of material exceeds $\sim 2X_0$, corresponding to $|\eta| < 1.8$. It consists of an active LAr layer of thickness 1.1 cm in the barrel and 0.5 cm in the endcap region. At the transition between the barrel and the endcap EM calorimeters, it is complemented by a scintillator slab inserted in the crack between the barrel and endcap cryostats. The presampler is designed to estimate and correct for losses of energy by electrons and photons through a particle's interaction with material upstream of the calorimeter. A large amount of material is situated in front of the EM calorimeter in the region $1.37 < |\eta| < 1.52$, for that reason, electrons and photons that fall within this region have reduced energy and position resolutions, and therefore are excluded in the analysis [107].

The EM calorimeter is divided into a barrel part covering the region up to $|\eta| < 1.475$ and two endcap components covering $1.375 < |\eta| < 3.2$, each housed in their own cryostat. The absorbers in the barrel have a thickness of 1.53 mm for $|\eta| < 0.8$ and 1.13 mm for $|\eta| > 0.8$, while in the endcaps their thickness is 1.7 mm for $|\eta| < 2.5$ and 2.2 mm for $|\eta| > 2.5$. The electrodes are located in the gaps between the lead absorbers, and consists of three copper layers, which are separated by insulating polyimide sheets. The inner layer is used to read out the signal by means of capacitive coupling, while the two outer ones are at high-voltage potential. As can be inferred, the LAr is located also in the gaps between the absorbers.

The full barrel cryostat is 6.8 m long, with an outer radius of 2.25 m, and an inner cavity radius of 1.15 m. The barrel consists of two identical half-barrels, separated by a gap of 4 mm at $z = 0$ [4]. The length of each barrel is 3.2 m along the z-axis, with an inner diameter of 2.8 m and an outer one of 4 m. Each half-barrel weighs around 57 tonnes and consists of 1024 absorbers, interleaved with readout electrodes. The electrodes are located in the middle of the gap by honeycomb spacers. The size of the drift gap on each side of the electrode is 2.1 mm, which at the nominal operating voltage of 2 kV gives an average drift time of $\sim$ 450 ns. Each half-barrel is divided into 16 modules. The total thickness of a module is at least $22X_0$, which increases to $30X_0$ between $|\eta| = 0$ and $|\eta| = 0.8$, and from $24X_0$ to $33X_0$ between $|\eta| = 0.8$ and $|\eta|$=1.3. One example of a barrel module is shown in Fig. 3.8(a).

Each endcap calorimeter is divided in two coaxial wheels: an outer wheel covering the range $1.375 < |\eta| < 2.5$, and an inner wheel covering $2.5 < |\eta| < 3.2$. The boundary between the inner and the outer wheel (located at $|\eta| = 2.5$) is mostly filled with low-density material, and is 3 mm wide. It matches the acceptance of the inner detector. Each endcap is housed in its cryostat (which is also shared with the hadronic wheels and the forward calorimeter). An example of an endcap cryostat is shown in Fig. 3.8(b). Each endcap wheel is divided into eight wedge-shaped modules and contains 768 absorbers interleaved with readout electrodes in the outer wheel and 256 absorbers in the inner one. As for the barrel, the electrodes are in the middle of the gaps, and are positioned by honeycomb spacers. The total active thickness of each endcap is greater than $24X_0$ (except for $|\eta| < 1.475$), and it increases to $38X_0$ as $|\eta|$ increases from 1.475 to 2.5 for the outer wheel, and from 26 to $36X_0$ as $|\eta|$ increases from 2.5 to 3.2 for the inner wheel.

The fine segmentation of the EM calorimeter allows detailed measurements of electrons and photons. Its energy resolution is $\sigma_E/E = 10\%/\sqrt{E} \oplus 0.7\%$ [4].

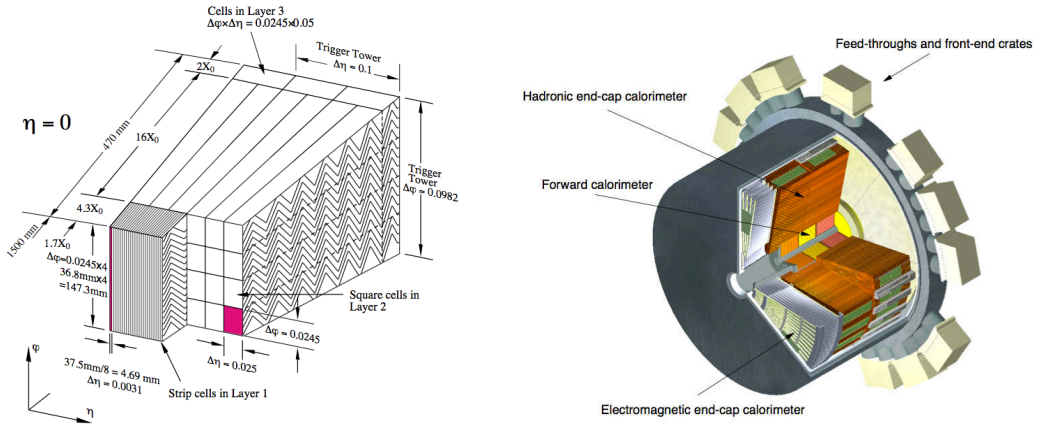

(a) (b)

Figure 3.8: a) One example of a barrel module of the EM calorimeter showing its three different layers, the granularity in η and ϕ of the cells of each of the three layers, the trigger towers, and its accordion structure. b) Cut-away view of an endcap cryostat showing the positions of the three endcap calorimeters [4].

3.4.2 The hadronic calorimeter

The hadronic calorimeter contributes to the hadronic jets reconstruction and missing transverse energy measurements. It has to provide good containment for hadronic jets and reduce punch-through into the muon spectrometer to a minimum. It has a total thickness of 11 interaction lengths (λ) at $|\eta| = 0$ including the outer support.

The hadronic calorimeter is realized with different techniques depending on the region: central and endcap. Thus it is composed of 2 independent sub-detectors: the Tile calorimeter (TileCal), instrumenting the central region up to $|\eta| < 1.7$ and the LAr hadronic endcap (HEC), covering the range $1.5 < |\eta| < 3.2$. This section describes each one of these sub-detectors.

3.4.2.1 The Tile calorimeter

The Tile calorimeter [109] is a sampling calorimeter which uses steel plates as absorber material and plastic scintillators as active medium. It consists of a cylindrical structure, placed behind the EM calorimeter and the solenoid coil, covering the pseudorapidity region up to $|\eta| < 1.7$. It extends in the radial direction from a inner radius of 2.28 m to an outer radius of 4.25 m, with a radial depth of approximately 7.4λ.

The Tile calorimeter is divided into a central barrel of 5.8 m in length covering the region up to $|\eta| < 1$, and two extended barrels of 2.6 m in length covering the range $0.8 < |\eta| < 1.7$. A cut-away view of the Tile calorimeter showing this configuration is illustrated in Fig. 3.9(a). The Tile calorimeter is segmented in depth in three layers of approximately 1.5, 4.1 and 1.8λ thick for the barrel, and 1.5, 2.6, and 3.3λ for the extended barrel. The total thickness at the outer edge of the tile-instrumented region is 9.7λ at $\eta = 0$. The barrels are divided azimuthally into 64 wedge-like modules of size $\Delta\phi \sim 0.1$. The assembled module forms a steel-scintillator structure, with the tiles oriented radially, and normal to the beam axis. This geometry is illustrated in

Fig. 3.9(b). The gaps between the central barrel and the extended barrels are instrumented with special modules which permit partially to recover the energy lost in the crack regions.

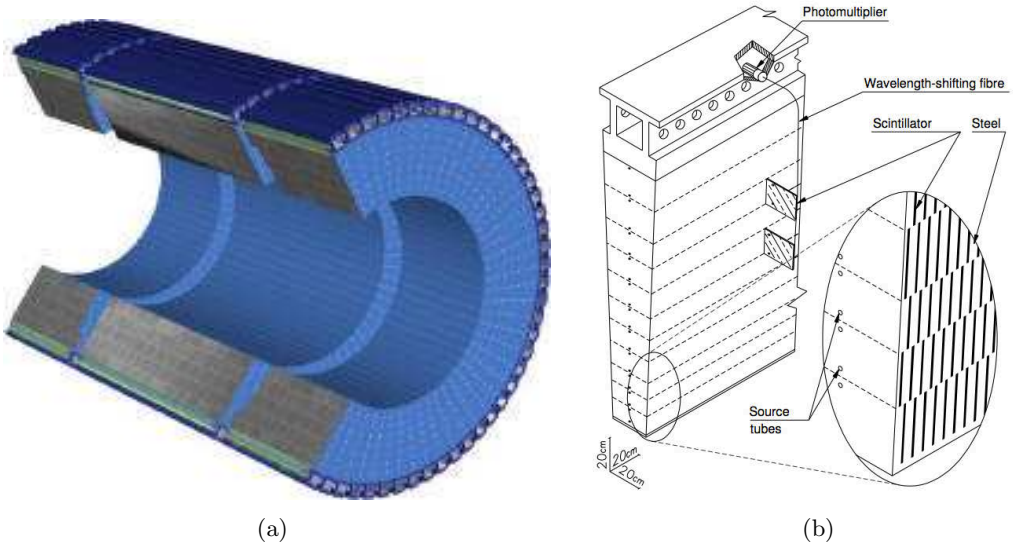

(a) (b)

Figure 3.9: a) Cut-away view of the Tile calorimeter. b) Structure of a module of the Tile calorimeter, showing the placement of the scintillator tiles, the steel plates and the readout components [4].

The tiles are 3 mm thick with radial lengths ranging from 97 mm to 187 mm, and azimuthal lengths ranging from 200 mm to 400 mm, while the basic element of the absorber structure consists of a master plate of 5 mm thick, onto which 4 mm thick spacer plates are glued in a staggered way to form the pockets in which the tiles are placed. Hadronic showers crossing the tiles induce the production of ultraviolet light in the base material (polystyrene). The light produced is collected and converted to visible light by wavelength shifting optical fibers, which are grouped together and coupled to the photomultiplier tubes (PMTs) housed at the outer edge of each module. The charge collected by each PMT is then digitized and transmitted to the ATLAS readout system. This information is reconstructed and summed up in order to measure the initial particle energy. The tiles orientation together with the fibres readout on the tile edges, permit an almost complete azimuthal coverage. The three-dimensional structure of the readout cell is defined by the previous fibre grouping, and provides in η an approximately projective geometry towards the interaction region. These cells have dimensions $\Delta\eta \times \Delta\phi = 0.1 \times 0.1$ in the first two layers, and 0.2×0.1 in the last layer. The segmentation in depth in η of the barrel and extended barrels is shown in Fig. 3.10.

The readout electronics is integrated with the mechanical structure. All the front-end electronics together with the PMTs are mounted in aluminum units (1.4 m long) called drawers, which are placed at the rear of each module.

The Tile calorimeter is essential for measuring the energy and direction of the hadrons produced in the collisions, and it also complements the energy measurement of the EM calorimeter for these hadrons. These appear in the detector as isolated hadrons, or jets of charged and neutral particles. The hadronic calorimeter hermeticity allows, in addition, to measure the missing transverse energy and therefore reconstructing particles that are escaping to the detection.

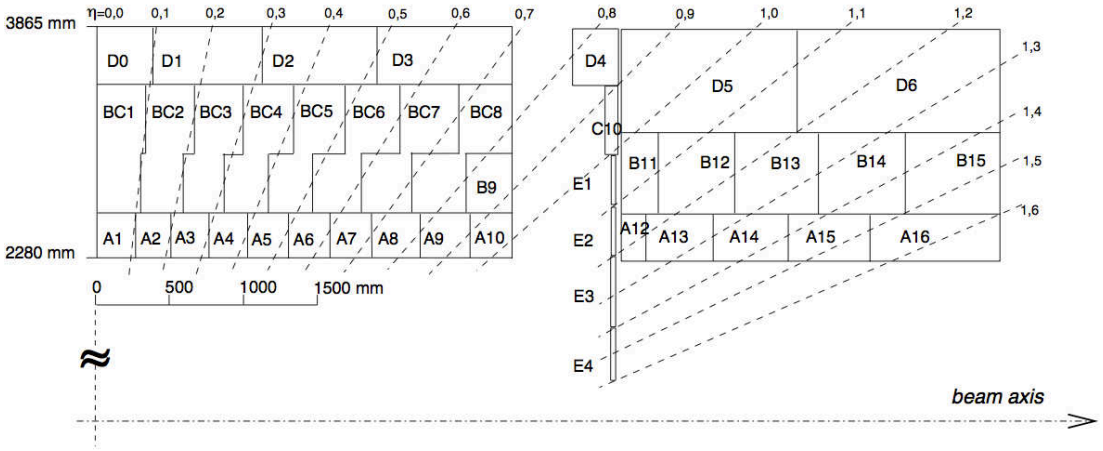

Figure 3.10: Segmentation in depth in η of the TileCal modules in the central (left) and extended (right) barrels [4].

The Tile calorimeter is also equipped with three hardware calibration systems: Cesium [110], LASER [14], and Charge Injection System [111]. Together, they provide a complete calibration of the hardware chain, from the active modules to the readout electronics. In particular, the LASER system is studied in Chapter 4.

The energy resolution of the Tile calorimeter is $\sigma_E/E = 50\%/\sqrt{E} \oplus 3\%$ [4].

3.4.2.2 The LAr hadronic endcap calorimeter

The hadronic calorimetry is extended in the pseudorapidity region $1.5 < |\eta| < 3.2$ by the HEC. This is a copper/LAr sampling calorimeter with a flat-plate design. The copper-plate acts as absorber, while the LAr does as active medium. LAr is used because of its higher radiation tolerance, which is required for the forward regions. The segmentation of the HEC in $\eta \times \phi$ is 0.1×0.1 up to $|\eta| < 2.5$, and 0.2×0.2 for the pseudorapidity region $2.5 < |\eta| < 3.2$.

The HEC consists of two independent wheels per endcap, which are located behind the EMEC sharing the same LAr cryostats. The wheels in each endcap have a cylindrical shape with an outer radius of 2030 mm, and they are placed one after the other along the beam direction. The wheels inside the cryostat are supported by two sliding rails, which form part of the mechanical structure. Each wheel contains two longitudinal sections (making a total of four layers per endcap), and is built of 32 identical wedge-shaped modules. One example of a module is shown in Fig. 3.11(a). The modules of the wheels closest to the interaction point are made of 24 copper plates of 25 mm thickness, plus a 12.5 mm thick front plate, while in the rear wheels, they are made of 16 plates of 50 mm thickness, plus a 25 mm thick front plate. The inner radius of the copper plates is 475 mm, except in the overlap region with the forward calorimeter where this radius becomes 372 mm. The copper plates are interleaved with 8.5 mm LAr gaps. These gaps are divided by three parallel electrodes into four separate drift zones of about 1.8 mm, as shown is Fig. 3.11(b). The middle electrode serves as the readout electrode and defines the lateral ($\eta \times \phi$) segmentation, while to the other two electrodes a high voltage is applied. The typical drift time for electrons in the drift zone is ∼430 ns for a nominal voltage of 1800 V.

The HEC overlaps with the forward calorimeter in the range $3.1 < |\eta| < 3.2$, and with the Tile calorimeter in the region $1.5 < |\eta| < 1.7$. Its energy resolution is the same as the Tile calorimeter.

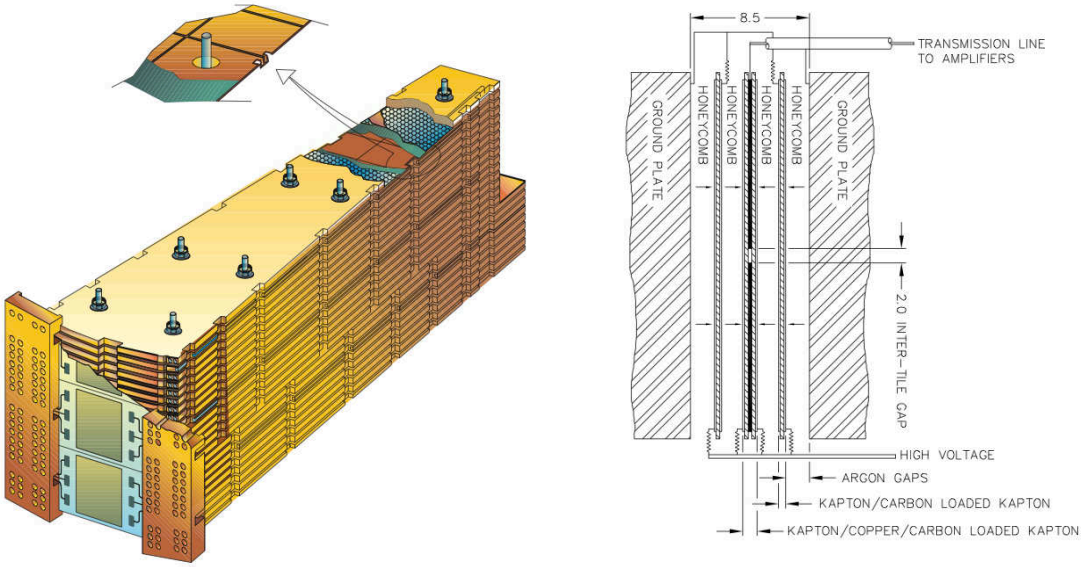

(a) (b)

Figure 3.11: a) Cut-away view of a HEC module. b) Arrangement of the HEC readout structure in a LAr gap [4].

3.4.3 The LAr forward calorimeter

The LAr forward calorimeter (FCal) consists of two cylindrical endcaps, with a front face placed at a distance of approximately 4.7 m from the interaction point along the beam axis. It uses LAr as the active medium covering the pseudorapidity region $3.1 < |\eta| < 4.9$. As mentioned before, it is integrated into the same cryostat as the endcap calorimeters.

The FCal has to accommodate at least 9λ of active detector in a short longitudinal space, and therefore making it a high density detector. Each FCal endcap is divided into three 45 cm deep modules: one electromagnetic and two hadronics. This configuration is illustrated in Fig. 3.12(a). The electromagnetic module is the closest to the interaction point, and in order to optimize the resolution, uses copper as absorber material. The hadronic modules are far away, and use tungsten as the absorber medium to limit the extension of the particle shower. In each module, the calorimeter consists of a metal matrix with regularly spaced longitudinal channels filled with the electrode structure, which consists of concentric rods centered in tubes parallel to the beam direction. One example of this arrangement for one hadronic module is shown in Fig. 3.12(b). LAr fills the gap between the rod and matrix. These gaps are 250 μm wide in the first module (electromagnetic module) and 375 (500) μm in the second (last) one (hadronic modules). These small LAr gaps are needed due to the high radiation environment in this region of the detector, also in order to avoid ion build-up problems and to provide at the

same time the highest possible density. They lead to a faster signal, with a drift time of 60 ns for the electromagnetic module, while for the hadronic ones it scales with the gap size. The rods are at positive high voltage while the tubes and matrix are grounded.

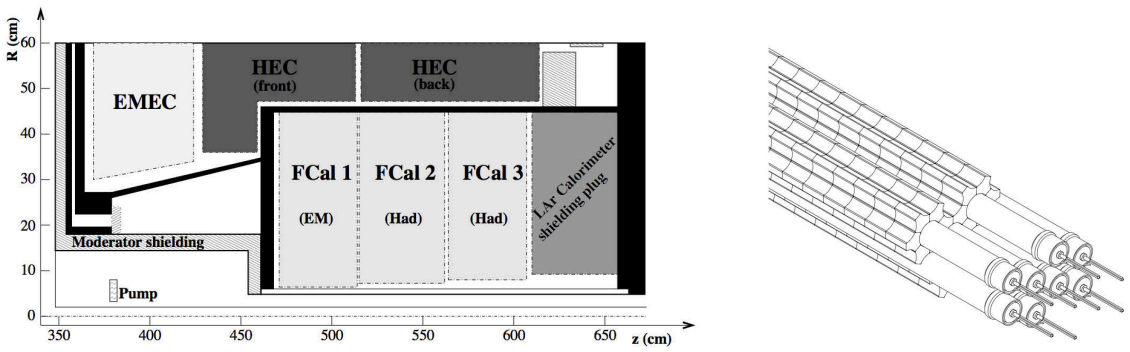

(a) (b)

Figure 3.12: a) Diagram showing the modules located in one endcap cryostat. The structural parts of the cryostat are shown in black. b) View of the FCal hadronic module absorber matrix [4].

The FCal provides uniformity coverage to the calorimeter, reducing the effects of the crack and dead space in the transition region (around $|\eta| = 3.1$). A shielding plug made of copper alloy located behind the last hadronic module reduces the radiation background levels to the muon spectrometer. Signals are read out through the front of the electromagnetic module and through the back of the two hadronic modules. The total number of readout channels is 3524. Its energy resolution is $\sigma_E/E = 100\%/\sqrt{E} \oplus 10\%$ [4].

3.5 Muon spectrometer

The Muon Spectrometer (MS) [112] is the outermost part of the ATLAS detector. It is designed to detect charged particles which manage to traverse the calorimeters, and to measure their momentum in the range $|\eta| < 2.7$. The MS allows identification of muons with momenta above 3 GeV, and the measurement of their momenta with a resolution between 3% and 4% for a range of 10 GeV $< p_{\mathrm{T}} <$ 500 GeV and better than 10% for p_{T}'s up to 1 TeV [113]. It is based on the magnetic deflection of muon tracks in the large superconducting air-core toroid magnets, which provides between 1 and 7.5 Tm of bending power. The magnetic field necessary to bend the particle trajectories in the pseudorapidity range up to $|\eta| < 1.4$ is provided by the large barrel toroid, while in the region $1.6 < |\eta| < 2.7$ muon tracks are bent by the smaller endcap magnets placed in both extremes of the barrel toroid. A combination of the barrel and endcap fields provides the magnetic deflection in the transition region $1.4 < |\eta| < 1.6$. The magnetic field provided by this magnet configuration is mostly orthogonal to the muon trajectories, minimizing the degradation of resolution due to the multiple scattering. The requirements to measure the curvature of high-p_{T} tracks dictate the size of the MS, and therefore also the dimensions of the ATLAS detector.

The MS is also designed to trigger on these particles traversing the calorimeters in the pseudorapidity region up to $|\eta| < 2.4$. It is instrumented with separate trigger and high-precision

tracking chambers. The chambers are arranged such that particles emerging from the interaction point can traverse three stations of chambers, which are situated so that they provide good hermeticity and optimum momentum resolution.

As for the other detectors in ATLAS, the MS is formed by a barrel and two endcap regions. The barrel chambers form three cylinders concentric with the beam direction, placed at radii of approximately 5 m, 7.5 m, and 10 m away from the beam, covering the pseudorapidity range up to $|\eta| < 1$. The chambers in the barrel are of rectangular shape with size of 2-10 m^2. In the two endcap regions, the chambers are arranged in four disks, located at $|z| \approx 7.4$ m, 10.8 m, 14 m, and 21.5 m from the interaction point, and concentric with the beam axis, covering the range $1 < |\eta| < 2.7$. The most of the endcap chambers are of trapezoidal shape with sizes ranging from 1-10 m^2. All chambers combined provide an almost full coverage, except in the region with $\eta \approx 0$, where a gap in the chamber coverage has been left open for the passage of cables and services of the inner detector, central solenoid, and the calorimeters. A 16-fold azimuthal segmentation has been chosen for both, the barrel and endcaps, which follows the eightfold azimuthal symmetry of the magnet structure. The chambers are arranged in small and large sectors. The small sectors cover the azimuthal range around the barrel toroid coils, while the large sectors cover the region between them. The barrel toroid structure supports all the barrel chambers and a part of the endcap chambers. The rest of the endcap chambers are supported on the service structures at the extremes of the experimental hall, and on special support frames.

The MS is equipped with four different kind of chambers: *Monitored Drift Tube* chambers (MDT), *Cathode Strip Chambers* (CSC), *Resistive Plate Chambers* (RPC) and *Thin Gap Chambers* (TGC). The first two are used for precision measurements of muon tracks, while the other two are used for the trigger and data acquisition system. They are illustrated in Fig. 3.13. The muon chambers are described in this section according to their function. Thus we have high-precision tracking chambers and trigger chambers.

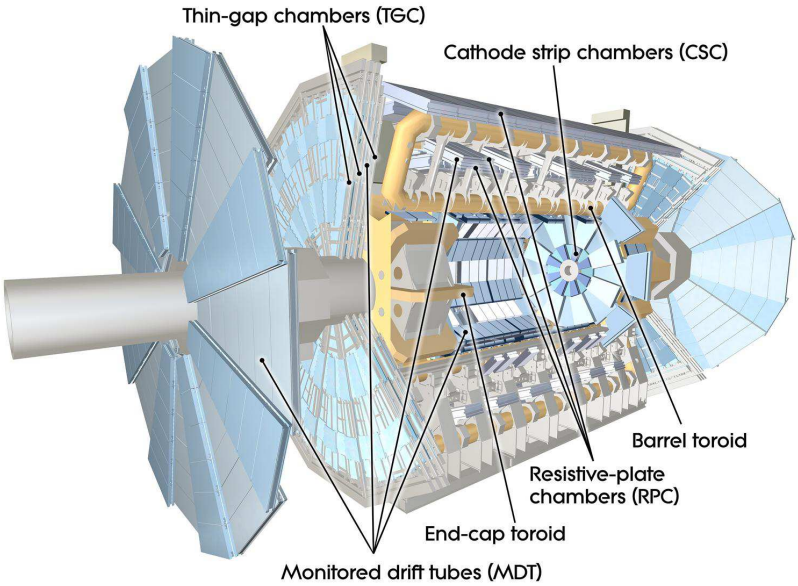

Figure 3.13: Cut-away view of the muon spectrometer showing the positions of the four different kind of chambers [4].

3.5.1 The high-precision tracking chambers

The tracking precision chambers determine the muon momenta from the deflection of the muon tracks in the magnetic field. They are built out of two kind of technologies: MDT and CSC. The MDT chambers perform the measurement of the muon trajectory up to $|\eta| < 2.7$, except in the forward region closest to the interaction point, where their coverage is limited up to $|\eta| < 2$. In this region, the particle fluxes and muon-track density are the highest and therefore the MDT chambers are replaced by CSC with higher granularity. The CSC cover the range $2 < |\eta| < 2.7$, and are used to sustain the demanding rate and background conditions in this region of the detector. The precision measurement of the muon tracks is made in the r-z projection, in a direction parallel to the bending direction of the magnetic field. The z coordinate is measured in the barrel, while the radial coordinate r is measured in the transition and endcap regions. A measurement of ϕ is also obtained by the CSC in the forward region.

The basic detection elements of the MDT chambers are pressurized aluminium drift tubes of 29.97 mm diameter and 400 μm wall thickness, with a 50 μm diameter central gold-plated W-Re wire. The wire is at a potential of 3080 V, and is held in position at the tube ends by a cylindrical end-plug, which guarantees the concentricity of the wire. The HV supply system and the signal transmission to the electronics are located at opposite ends. The tubes are operated with Ar/CO_2 gas (93/7) at 3 bar absolute pressure. This operating gas is selected because of the good aging properties. The electrons resulting from ionization caused by the muons traversing the tube are collected at the wire, resulting in a measurable signal. The maximum drift time from the wall to the wire in the tube is about 700 ns. There are 1088 MDT chambers with a total area of 5500 m^2. The regular chambers consists of two groups of tube layers (multilayers), which are separated by a mechanical spacer. In the innermost layer, each multilayer consists of 4 tube layers, while in the middle and outer layer, it consists of three tube layers only (in the innermost layer one extra layer of tubes is needed to enhance the pattern-recognition performance). The mechanical structure of a MDT chamber is shown in Fig. 3.14(a). The average resolution in z is about 80 μm per tube, or $\sim$35 μm per chamber. The MDT chambers are rectangular in the barrel and trapezoidal in the endcap region. Most of the tubes in the barrel are of identical length, while in the endcap chambers the tube lengths vary along r in steps of 24 tubes. The direction of the tubes in the barrel and in the endcap region is along ϕ.

The CSC system is formed by two disks with eight chambers each, segmented in ϕ into large and small chambers as shown in Fig. 3.14(b). It has 32 chambers with a total area of 65 m^2. The chambers are operated at a voltage of 1900 V and take up the radial space between 881 mm and 2081mm. The CSC are multiwire proportional chambers with the wires oriented in the radial direction, and sandwiched between the strip cathodes in a gas mixture of Ar/CO_2 (80/20). The anode wires are made of gold-plated tungsten with 3% rhenium and have a diameter of 30 μm. The cathodes planes are segmented into strips in orthogonal directions, which allows both coordinates to be measured: the cathode with the strips perpendicular to the wires provides the precision coordinate, while the one parallel to the wires provides the transverse coordinate. The resolution of a chamber is 40 μm in the bending plane and about 5 mm in the transverse plane. Each chamber has a similar configuration to the multilayer of the MDT system, with four wire planes but with a finer granularity, resulting in four independent measurements in η and ϕ along each track. A four layer chamber consists of five flat rigid panels, each made of sheet of polyurethane foam and two 0.82 mm thick copper-clad laminates, where the 17 μm thick copper cladding forms the cathodes. When a muon goes through the chamber, electron ion pairs

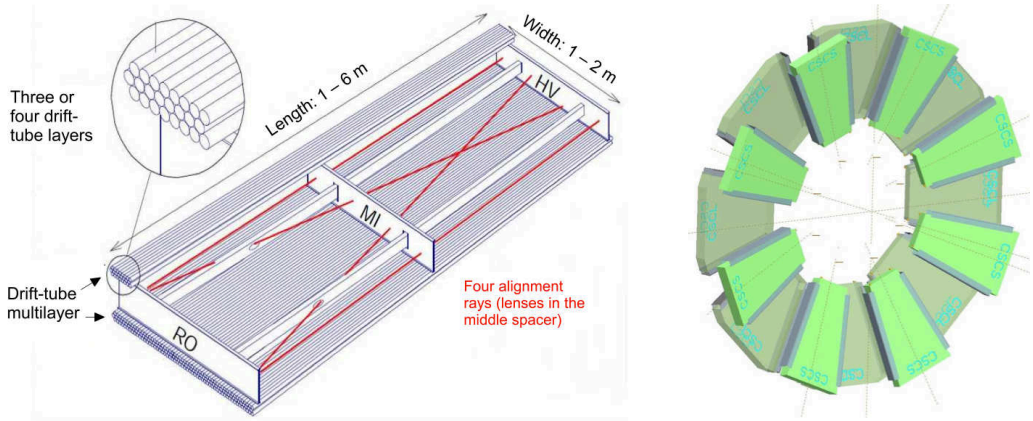

(a) (b)

Figure 3.14: a) Mechanical structure of a MDT chamber showing the multilayers and the alignment system. b) Layout of a CSC endcap showing the eight small and eight large chambers [4].

are created in the gas, and the signal is measured from the charged induced in the strips. The electron drift times are less than 40 ns, which results in a timing resolution of about 7 ns per plane. The total number of readout channels is 30700.

An internal chamber alignment system was implemented in order to monitor the potential deformations expected to occur in the various mounting positions in ATLAS. It consists of a combination of precision mechanical-assembly techniques and optical alignment systems implemented within and between muon chambers.

3.5.2 The trigger chambers

The trigger system covers the pseudorapidity region up to $|\eta| < 2.4$, over the full ϕ range. It complements the high-precision tracking chambers with a system of fast trigger providing information within a few tens of nanoseconds on muon tracks traversing the detector. The capability to trigger on muon tracks is one of the fundamental requirements of the muon system. It also has to provide bunch-crossing identification, discrimination of muon transverse momentum, robustness towards random hits due to n/γ-background, and the second coordinate measurement in the non-bending ϕ-projection to complement the MDT and CSC measurements. Actually, the trigger chambers measure both coordinates of the track, one in the bending (η) plane and one in the non-bending (ϕ) plane.

The trigger system uses RPC in the barrel and TGC in the endcap region. Three layers of trigger chambers are arranged in the barrel, while a fourth layer is added in the endcap region in order to increase the trigger robustness in case of higher backgrounds. In the barrel, the middle layer (BML) of the MDT is sandwiched by two layers of RPC, while the third RPC layer is placed close to the outer (BOL) MDT layer. In the endcap region, one TGC layer is in front of the second (EML) MDT wheel, while two layers are behind it. The fourth TGC layer of the endcap region is placed in front of the innermost tracking layer (EIL). This system is illustrated in Fig. 3.15. A system of fast coincidences between the three layers along the muon track generates the trigger information.

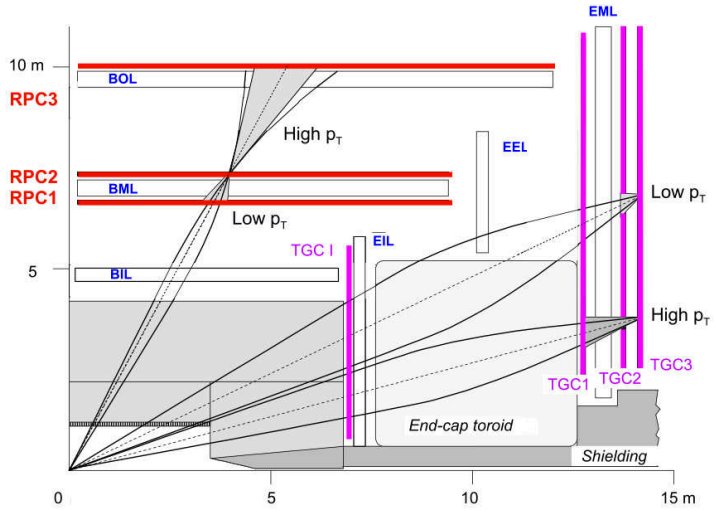

Figure 3.15: Schematics of the muon trigger system showing the positions of the RPC layers in the barrel and the TGC layers in the endcap region [4].

The RPC are a gaseous parallel electrode-plate detectors covering the region up to $|\eta| < 1.05$. A RPC chamber is formed by two rectangular units contiguous to each other. Each unit is composed of two independent detector layers filled with a gas mixture of $C_2H_2F_4$/Iso-C_4H_{10}/SF_6 in the proportions 94.7/5/0.3%, and readout by two orthogonal sets of pick-out strips. A detector layer (gas volume) consists in two resistive plates made of phenolic-melaminic plastic laminate, kept at a distance of 2 mm by insulating spacers. The electric field between the plates is 4.9 kV/mm. When a muon traverses the plates, the electric field between them allows to create an avalanche along the ionization tracks towards the anode. The signal is read out by two metallic strips, which provide a measurement in both the z and ϕ coordinates, with a spatial resolution of 10 mm for both. The time resolution is 1.5 ns.

The TGC are operated using the same principle as the multiwire proportional chambers, providing good time resolution to tag the beam-crossing and high rate capability. The readout channel granularity determines the spatial resolution, which provides a sufficient sharp cut-off in the momentum of triggering the muon. Seven layers of TGC arranged in one triplet and two doublets complement the middle layer of the MDT in the endcap region, while only two layers complement the inner layer. A chamber is formed by a detector layer containing a wire plane and two cathodes. The detector layer consists of a gas mixture of CO_2/n-pentane at proportions of 55/45%. The wire and the cathode are separated at a distance of 1.4 mm, while the distance between wires is 1.8 mm. The wires have a diameter of 50 μm and are kept at a potential of 2900 V, while the cathode planes consist of 1.6 mm thick FR4 (Flame Resistant 4) plates, grafite coated on the inside and copper cladding on the other side. The wires are placed parallel to the MDT tubes, while the cathode strips are arranged radially. The readouts from the anode wire and the cathode strip reconstruct the hit position of the muon track in the vertical direction with respect to the beam pipe (r) and in the azimuth angle (ϕ), respectively. The spatial resolution of the TGC is 2-6 mm in r, and 3-7 mm in ϕ. The timing resolution is of 4 ns.

The trigger chambers have overlap regions with contiguous chambers and between the barrel and endcap sections in order to assure full acceptance down to the low-momentum limit.

3.6 Forward detectors

The ATLAS detector includes several forward detector systems [114]: Mimimum Bias Trigger Scintillators (MBTS), the LUminosity measurement using Cerenkov Integrating Detector (LUCID), the Zero-Degree Calorimeter (ZDC), and the Absolute Luminosity For ATLAS (ALFA) Roman pots. Together they provide additional measurements for physics and monitoring purposes. Their locations relative to the ATLAS central detector is shown in Fig. 3.16. A very brief description of each one of these detectors is given in this section.

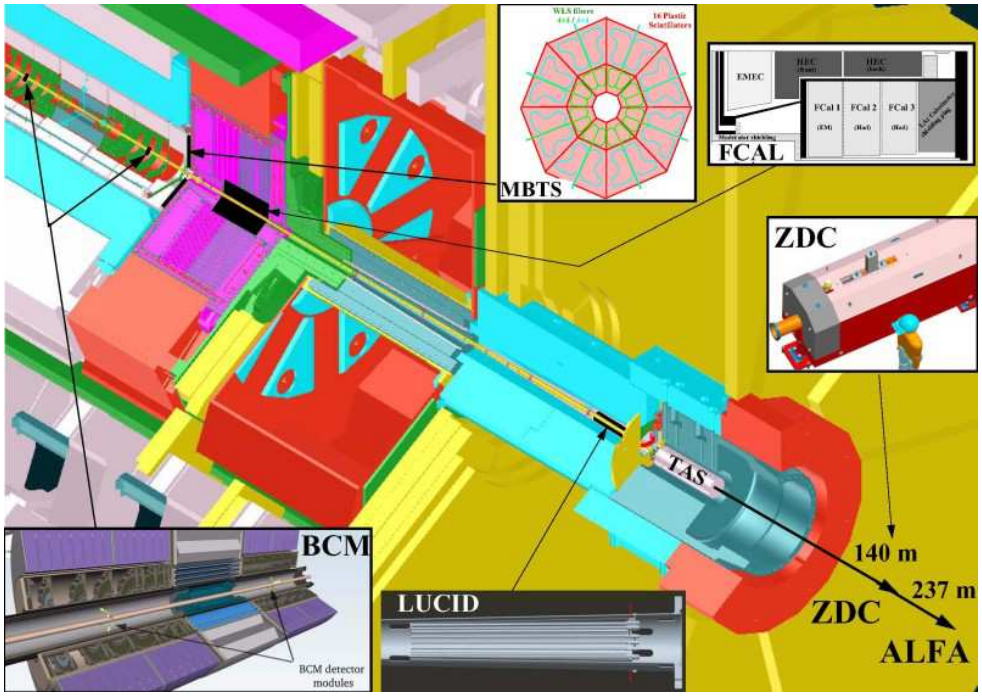

Figure 3.16: Schematics showing the positions along the beam axis of the forward detectors.

3.6.1 The MBTS

The ATLAS detector was equipped with segmented scintillator paddles with the main purpose of providing a Level 1 minimum bias trigger for the initial running period at low instantaneous luminosity ($< 10^{33}\text{cm}^{-2}\text{s}^{-1}$ [115]).

The MBTS system consists of thirty-two 2 cm thick scintillation paddles organized in two disks, one on each side of the interaction point of ATLAS. Each disk is separated into an inner and an outer ring, which are segmented in eight units in ϕ and two units in η. They are installed on the inner face of the endcap calorimeter cryostat at $|z| = 3.65$ m from the collision point, and cover the pseudorapidity range $2.09 < |\eta| < 3.84$. Wavelength-shifting optical fibers collect and guide the light emitted by each scintillator segment to a TileCal PMT. The MBTS signals, after being shaped and amplified, are fed into leading edge discriminators and sent to the Central Trigger Processor (CTP). A hit is defined if the signal is above a threshold of 50 mV.

3.6.2 The LUCID detector

The LUCID detector is a Cerenkov detector, located at a distance of $|z| = 17$ m from the interaction point and at a radial distance of 10 cm from the beam line, covering the pseudorapidity range $5.61 < |\eta| < 5.93$. It measures the integrated luminosity and provides online monitoring of the instantaneous luminosity and beam conditions by detecting inelastic p-p scattering. In order to determine the luminosity, the number of interactions per beam-crossing has to be well known. Thus the LUCID design is based on the concept that the number of interactions in a bunch-crossing is proportional to the number of particles detected.

The LUCID detector is composed of twenty aluminum tubes placed in a light-weight aluminum gas vessel and filled with C_4F_{10}. The tubes are 1.5 m long and 15 mm in diameter. They surround the beam-pipe and point toward the interaction point. When a particle traversing the tube emits Cerenkov light, it is reflected in the tube walls, and measured by the PMTs. The signal from the PMTs is used to measure the number of particles per tube, while the timing response provides measurements of individual bunch-crossings.

3.6.3 The ZDC

The main purpose of the ATLAS ZDC is to detect neutrons and photons with $|\eta| > 8.3$ in both p-p and heavy-ion collisions. It is a sampling calorimeter which contributes to minimum bias and diffractive physics in p-p collisions. It has also a key role in determining the centrality of heavy ion collisions. It resides in a slot in the TAN (Target Absorber Neutral) absorber, located at $|z| = 140$ m from the interaction point, exactly at the place where the straight-section beam-pipe is divided back into two independent beam-pipes. Its design is based on the radiation tolerance.

The ATLAS ZDC system consists of four modules on each arm: one electromagnetic (about $29X_0$ deep) followed by three hadronics (each about 1.14λ deep). The modules are composed of tungsten acting as absorber material with an embedded matrix of quartz rods, read out by PMTs. Two types of quartz fibers are used: vertical quartz strips for energy measurement and horizontal quartz rods for providing position information. It provides a time resolution of 100 ps, sufficient to locate the interaction point to about 3 cm in z, providing therefore a measurement of the vertex location. The ZDC is fully efficient for energies above ∼400 GeV [115].

3.6.4 The ALFA detector

The ALFA detector was installed about the middle of 2011, and is intended to measure the absolute luminosity at ATLAS during special high beta optics runs at low luminosity via elastic scattering at small angles in the Coulomb-Nuclear Interference region.

The system is constituted of four Roman pots stations[14], two on each side of the collision point separated by 4 m, each housing two vertically movable detectors. It is placed at $|z| = 240$ m away from the interaction point, and as close as 1-1.5 mm from the LHC beam. The Roman pots house scintillating fiber detectors, which provide a spatial resolution of about 30 μm [116]. Because the low instantaneous luminosity, no radiation-hard technology is required for this set of detectors. The effective area of the detector is smaller than 32×32 mm^2.

[14]The Roman pot concept is based upon a detector volume that is separated from the vacuum of the accelerator by a thin window but is connected with bellows to the beam-pipe, and can therefore be moved close to the beam.

3.7 Magnet system

The magnet system of the ATLAS detector provides the magnetic field for bending the trajectories of charged particles for momentum measurement, which is determined by means of the radius of curvature of the tracks left within the detector. It is 26 m long and 22 m in diameter, with a stored energy of 1.6 GJ. It provides a magnetic field over a volume of about 12000 m^3 via a hybrid system of four large superconducting magnets, which are cooled by forced flow of helium at 4.5 K through tubes welded on the casing of the windings.

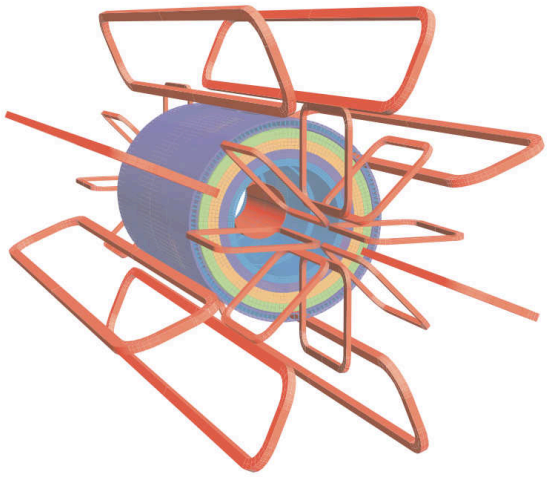

Figure 3.17: Geometry of magnet windings and Tile calorimeter steel. The solenoid magnet lies inside the calorimeter system. The eight barrel toroid coils interleaved with the endcap coils are also visible.

The four magnets are arranged in a central solenoid aligned on the beam axis and providing the inner detector with an axial magnetic field, surrounded by a system of three large air-core toroids generating a toroidal magnetic field for the muon spectrometer. This configuration is illustrated in Fig. 3.17. The characteristics of the central solenoid magnet and the toroid system are discussed in this section.

3.7.1 The solenoid magnet

The central solenoid is aligned on the beam axis and is designed to provide a 2 T axial magnetic field for the inner detector, with a peak magnetic field of 2.6 T. The flux of magnetic field is returned by the steel of the hadronic calorimeter and its girder structure. The solenoid is a layer coil made of a doped Al stabilized NbTi/Cu rectangular conductor wound on its thin edge, developed to achieve a high field optimizing the thickness, and inside a 12 mm thick Al support cylinder. It weights 5.4 tons and has an inner/outer diameter of 2.46/2.56 m with an axial length of 5.8 m. It operates at a nominal current of 7.73 kA and stores an energy of 40 MJ.

Since the solenoid magnet lies in front of the calorimeter system, a demanding requirement is that its presence must have a small impact on the energy measurement in the calorimeters. Thus it was designed to keep the material thickness as low as possible, contributing with a total of approximately $0.66X_0$ at normal incidence. As a consequence the solenoid shares a common vacuum vessel with the LAr calorimeter, thereby eliminating two vacuum walls.

3.7.2 The toroidal magnet system

The toroidal magnet system consists of one barrel and two endcap magnets. It provides a toroidal magnetic field of 0.5 T and 1 T for the muon spectrometer in the central and endcap regions, respectively. It lies outside the calorimeters and within the muon system. As for the solenoid, the conductor and coil-winding technology is based on winding a pure Al-stabilized Nb/Ti/Cu conductor.

The barrel consists of eight coils encased in individual racetrack-shaped, stainless-steel vacuum vessels filling the cylindrical volume surrounding the calorimeter system and both endcap toroids. It provides a peak magnetic field of 3.9 T. The coils are assembled radially ad symmetrically around the beam axis. It has an inner/outer diameter of 9.4/20.1 m with a length of 25.3 m. Its weight is 830 tons and it operates at a nominal current of 20.5 kA. The coils are kept in place by a set of 16 rings of struts positioned along them.

The endcap toroids are placed inside the barrel toroid at both ends of the central solenoid. They have an inner/outer diameter of 1.65/10.7 m with an axial length of 5 m, weighting about 478 tons. Each endcap is rotated by 22.5° with respect to the barrel toroid in order to provide the radial overlap and optimizing the bending power at the interface between the two coil systems. Each endcap toroid consists of a single cold mass built up from eight coils in a aluminum alloy housing. The endcap toroids are operated at a nominal current of 20.5 kA and provide a peak magnetic field of 4.1 T.

The barrel toroid provides bending power in the pseudorapidity range $|\eta| < 1.4$, and the endcap toroids in the region $1.6 < |\eta| < 2.7$. The bending power in the transition region $1.4 < |\eta| < 1.6$ is lower and is provided by the overlap of the magnetic field generated by the two magnets.

3.8 The trigger and data acquisition system (TDAQ)

In general, the interesting phenomena to be studied at the LHC have a small expected cross-section, thus high luminosity is needed in order to produce that kind of events. At the design luminosity of $10^{34}\text{cm}^{-2}\text{s}^{-1}$, starting from an initial bunch crossing frequency of 40 MHz and about 23 interactions per bunch crossing, the proton-proton interaction rate becomes approximately 1 GHz. Most of these events are not relevant for the studied processes and they also can correspond to minimum bias events[15]. In addition, the event data recording (based on technology and resource limitations) is limited to about 200 Hz for permanent storage in the design configuration. This limit requires an overall rejection factor of 5×10^6 against minimum-bias processes while maintaining maximum efficiency for keeping interesting events, which could lead to the discovery of new physics phenomena. This rejection is done by the ATLAS trigger system [117].

The ATLAS trigger system has been designed in order to use simple criteria to decide which events can be recorded in a very small fraction of time. It consists of three levels of event selection: *Level-1* (L1), *Level-2* (L2), and *Event Filter* (EF). The L2 and EF together form the *High-Level Trigger* (HLT). Each trigger level refines the decisions made at the previous level by applying progressively more selection criteria, leading to a final event size of approximately 1.3 Mbyte. The L1 is implemented in fast custom electronics boards and performs the event selection

[15]The total *pp*-cross-section can be split into an elastic and inelastic part. The inelastic cross-section is dominated by non-diffractive interactions producing many low-p_{T} particles. These non-diffractive events are usually referred as to minimum bias events, though the exact definition is made by the trigger system.

using limited hardware information from the calorimeters and muon detectors, while the HLT is implemented entirely in software using also the data provided by the calorimeters and the muon detector, as well as the data from the inner detector. An overview of the ATLAS trigger system is shown in Fig. 3.18. The characteristics of each trigger level are described in this section.

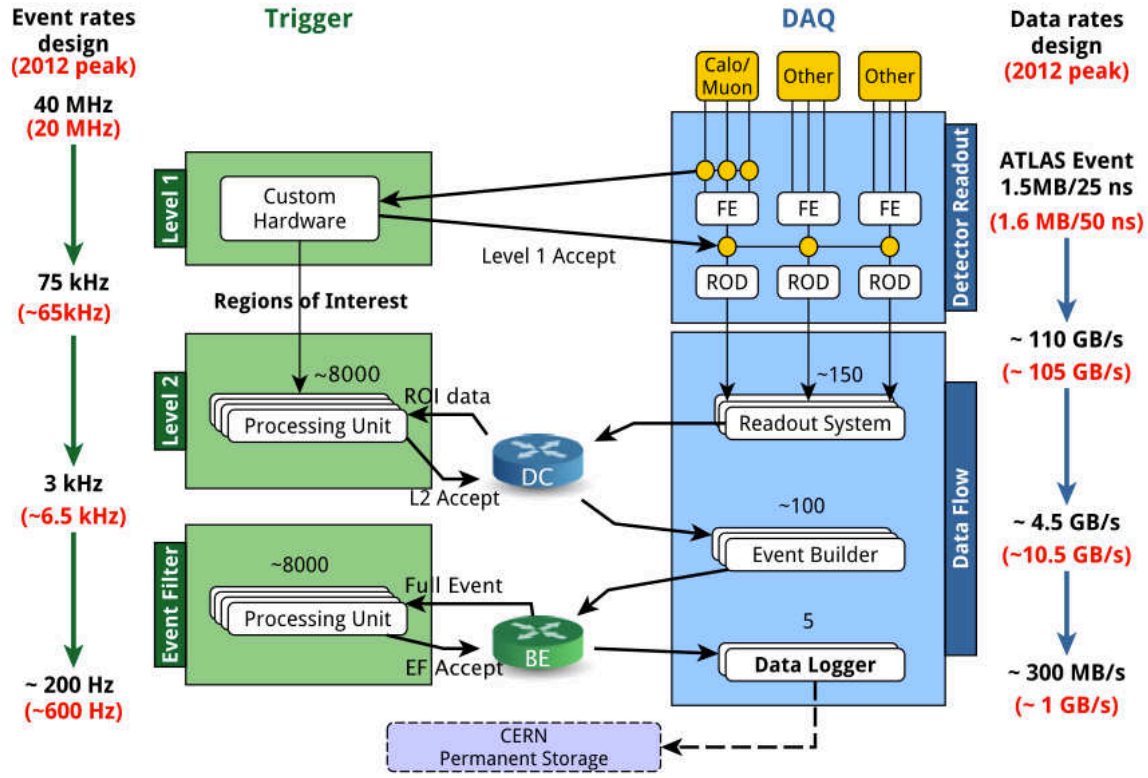

Figure 3.18: ATLAS trigger and data acquisition system [118].

3.8.1 The Level-1 trigger

The L1 is the responsible of performing the initial event selection looking for specific signatures based on reduced-granularity information provided by the calorimeters and the muon detector.

Information from all the calorimeters is used for the event selection. The L1 calorimeter trigger (L1Calo) is a pipelined digital system designed to work with about 7000 analogue trigger towers of reduced granularity (0.1×0.1 in $\Delta\eta \times \Delta\phi$ in most parts). It is intended to identify high-E_{T} objects such as electrons and photons, jets, and τ leptons decaying into hadrons. It also selects events with large missing transverse energy ($E_{\mathrm{T}}^{\mathrm{miss}}$) and large total transverse energy. It is located off-detector in the service cavern USA15, and sends the result for each LHC bunch-crossing to the Central Trigger Processor (CTP) approximately 1.5 μs after the event occurs, which results in a total latency of about 2.1 μs.

The L1 muon trigger is based on signals generated in finely segmented detectors: the trigger chambers. They are used for the identification of high p_{T} muons originating from the

interaction region, and have sufficient timing accuracy to provide unambiguous identification of the bunch-crossing containing the muon candidate.

The L1 muon and calorimeter triggers are processed by the CTP, which combines the information for different object types. The L1 trigger decision is based on the multiplicity of trigger objets. The information about the geometric location of these objects is used to define the Region(s) of Interest (RoI), which basically corresponds to the region of the detector in η-ϕ where the trigger has identified interesting features. The design of the trigger and front-end systems requires the L1 latency to be less than 2.5 μs, where about 1 μs of this time is accounted for by cable-propagation delays alone. It implies that the L1 decision must reach the front-end electronics within 2.5 μs after the bunch-crossing with which it is associated. This is managed by implementing the L1 trigger as a system of purpose-built hardware processors. For events accepted by L1, the RoIs are passed to L2. Meanwhile data on detector front-end electronics are sent to detector specific ReadOut Drivers (ROD) to be assembled and pushed to the dedicated memories on ReadOut System (ROS) PCs, which are in charge of keeping the data until L2 rejection or event building.

The L1 reduces the event rate to a maximum of 75 kHz due to limitations in the detector readout systems.

3.8.2 The Level-2 trigger

The L2 trigger is the second stage of the trigger system, and the first one of the ATLAS data acquisition system with access to data from the inner detector. It uses the full granularity and precision detector information associated with the RoI defined at the L1 trigger. As the L1, the event selection at L2 also uses inclusive criteria –as for example high-E_{T} objects above defined thresholds–, refining the selection done at L1. It uses complex object reconstruction algorithms to reduce the event rate to below 3.5 kHz, with an average event processing time of approximately 40 ms. For the events fulfilling the L2 selection criteria, the event-building is performed. The assembled events are then moved to the event filter for further analysis.

The main component of the L2 trigger is the L2 processing farm, where is executed the event selection. This system provides an event rejection factor of about 30, with an average throughput per farm node of about 200 Hz, using the data located in the RoI.

3.8.3 The Event Filter

The EF makes the final stage of the online event selection. It receives the events that have been selected by the L2 and processes the events with the full detector granularity, using offline analysis procedures on fully-built events. It uses much more complex algorithms than L2 to reduce the events rate to about 200 Hz[16], with an average event processing time of approximately 4 s.

In addition to the selection, the event filter classifies the selected events according to a predetermined set of event *streams* (muon, jet, electron/photon, minimum bias, etc.), which is added to the event structure. The chain of algorithms that defines a trigger object at each level is referred as a *trigger chain*. The name convention for a trigger chain is:

`[Level][N][Type(s)][Threshold][Isolation][Quality]`,

[16]The trigger can be configured to record events at a peak event rate of up to 400 Hz.

where `Level` is referring to the trigger level used, `N` indicates the object multiplicity, `Type(s)` is the object(s) candidate(s), `Threshold` is a number which corresponds to the transverse momentum (or energy) threshold applied to the object, `Isolation` indicates the object isolation and `Quality` refers to the rigor of requirements in the algorithm. For example, the trigger chain `EF_mu18_medium` triggers muons at the Event Filter level with a $p_{\mathrm{T}} > 18$ GeV and satisfying the medium requirements defined in the reconstruction algorithm used at the event filter level. More complex trigger chains can be obtained depending on the individual decisions. The ATLAS triggers are inclusive, which means that the same event can appear in more than one stream. The event streams are designed to help in the data analyses by separating interesting events for different analysis in different datasets. The final size of the event is approximately 1.3 Mbyte.

The events passing the criteria of the event filter are moved to the Data Loggers. Events not fulfilling any of the criteria are expunged from the system. Data flow between DAQ and trigger systems goes over two Gigabit Ethernet networks called data collection (DC) and back end (BE) networks. The DC network transfers data among L2, ROS and Event Builder (EB). The BE network transfers full event data from EB to EF and then from EF to data loggers [118].

The files are asynchronously transferred from the Data Loggers to the offline CERN permanent storage (Tier-0) [119]. At Tier-0, the data are processed, and then registered in the ATLAS Distributed Data Management system (DDM) [120]. DDM organizes, transfers and manages ATLAS data across more than a hundred individual grid sites that are part of the Worldwide LHC Grid [121].

The recorded data are classified by *runs*. A run is a time interval of data taking, which usually corresponds to a LHC fill. They are designated by a unique integer: the Run Number. The runs are subdivided into *luminosity blocks* (LB). A LB is the smallest unit of time over which luminosity is measured and data quality is assessed. It generally corresponds to 1 or 2 minutes of data taking, and it is designated by an integer ascending as the run progresses. Certain configurable quantities are allowed to change at LB boundaries, such as trigger prescales to regulate the output data taking rate for changing beam conditions. The runs are grouped at the same time into *periods*, which are usually denoted by letters (i.e. `A`, `B`...). Runs in the same period share the same general detector conditions, machine configuration and trigger menu.

Chapter 4

The TileCal Laser calibration system

Contents

4.1 Overview

As mentioned in Section 3.4.2.1, the Tile calorimeter is a large hadronic sampling calorimeter which consists of steel plates used as absorber material and scintillating plastic tiles used as active medium. Hadronic showers developing in the plates illuminate the tiles. The light produced is transmitted via optical fibers to the PMTs. The charge collected by each PMT is then digitized and transmitted to the ATLAS readout system. This information is reconstructed and summed up in order to measure the initial particle energy. TileCal is therefore essential for measuring

the energy and direction of the hadrons produced in the collisions. The hadronic calorimeter hermeticity allows, in addition, to measure the missing transverse energy and therefore to reconstruct particles that are escaping the detection. The understanding of the calorimeter response to hadrons and of their shower development is crucial to achieve the best possible performance of the energy measurement. In order to provide the best possible physics input, the difference between the true energy and the reconstructed shower energy has to be as small as possible. This is the main reason for which it is necessary to calibrate the system, a process which is done at two levels:

- **Hardware:** A good understanding of the TileCal response requires the monitoring and control of many parameters (such as electronic noise, PMT gain, among others) which can depend on time, temperature, and so on. These parameters must be known very precisely in order to interpret the collected data correctly. Therefore, it is necessary to develop specific calibration systems in order to monitor and control these variables.

- **Software:** Once the hardware parameters are under control, the right estimation of the shower energy has to be done. In hadronic showers, a significant amount of energy is not detected because of nuclear interactions. Also, the calorimeter finite granularity, as well as uninstrumented regions, will lead to a non-exact estimation of the shower energy, even with a perfect hardware calibration. This is corrected by using a software calibration.

The LASER system is one of the three hardware calibration systems of the Tile calorimeter. Its main role is to monitor the stability of the response of the PMTs and associated electronics used in the detector. In the LASER calibration, a known intensity of light emitted by the laser and monitored by photodiode sensors is incident on the photocathode of each PMT. Four photodiodes are used for the absolute measurement of this intensity. The stability and linearity of these photodiodes is therefore crucial to establish the performance of each PMT itself, and the first step towards the understanding of the LASER system. Before any use of the LASER system for calibration purposes, it is necessary to know if the photodiodes used for measuring the laser intensity are calibrated themselves. Naturally, this intrinsic calibration has to be independent from the laser light. An alpha radioactive source is used for the absolute calibration of the photodiodes system.

In order to monitor the stability of the photodiodes response over long periods of time, it is crucial to understand the behavior of their readout electronics, as well as the response of the photodiodes in presence of the alpha source (alpha response). The behavior of the readout electronics alone –when no energy is deposited in the photodiodes– can be quantified by two parameters, the average response, called mean pedestal, and the RMS of this response, which represents the noise of the system. In particular, it is important to check that the pedestal and the noise are the same whether there is some energy in the other photodiodes or not. The linearity of the photodiodes electronics is tested by injecting calibrated charges in it. These charges are measured in order to control the linearity of the readout electronics which is being used.

Before this study, the stability of the alpha response had been studied by simply computing the mean of the pedestal subtracted alpha spectra. Here, an alternative and more sensitive method has been proposed, the *scale factor*. Both methods will be compared in simulated data, including their sensitivity to variations of the pedestal or the noise. Then, these methods will be applied to the real data.

This chapter is dedicated to the study of the stability of the photodiodes and the linearity of their electronics from February 2011 to February 2013. The role of the LASER system in the hardware calibration chain of the Tile calorimeter is explained in Section 4.2. A brief description of the LASER system and its intrinsic calibration is presented in Section 4.3. Then, the results of the stability and linearity of the photodiodes electronics are shown in Sec. 4.5. This is followed by the studies of the stability of the alpha spectra, including the comparison between the scale factor and average methods in Section 4.6. Finally, the summary and conclusions are given in Section 4.7.

4.2 Hardware calibration of TileCal

The Tile calorimeter has three hardware calibration systems: Cesium [110], LASER [14], and Charge Injection System [111]. They provide a complete calibration of the hardware chain, from the active modules to the readout electronics. This process is illustrated in Fig. 4.1. It is carried out as follows.

The Cesium system provides the calibration of the main hardware chain: cells and PMTs, but not downstream electronics. The Cesium information is going through all the hardware chain, therefore, if it sees a drop in one cell efficiency, it could come from a change in the PMT gain, and not only from the cell.

In order to determine if the problem occurred before of after the PMT, laser light is sent via clear optical fibers to the PMTs: if the laser light intensity is well known, it is possible to extract the PMT gain and its variation by reconstructing the signal obtained.

Once again, the laser measurements depend on the response of the downstream readout system. By sending calibrated pulses into the electronic readout chain, the Charge Injection System (CIS) leads to a precise estimation of the electronic noise and linearity and thus solves this uncertainty.

As a summary, by using the three calibration systems together, one can calibrate all parts of the detector. A more detailed explanation about how this process is done step by step can be found in [14].

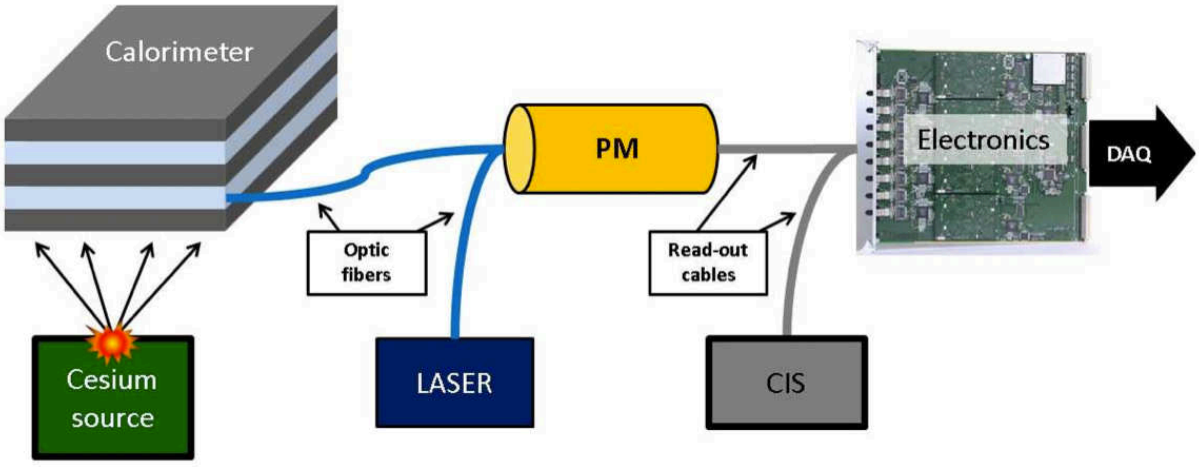

Figure 4.1: Hardware calibration chain of ATLAS TileCal.

4.3 The LASER system

The LASER monitoring system was proposed for ATLAS TileCal initially in 1994 [122], its concept had already been used by some HEP experiments [123]. As said before its main role is to monitor the linearity and stability of the 9852 PMTs and associated electronics used in the detector. Laser light is sent via clear optical fibers to the PMTs. Assuming that the laser light intensity is well known and calibrated, one can extract the PMT gain and its variation by reconstructing the measured signal.

The LASER system is divided into two main parts: the LASER box and the light distribution system. The description given in this section will be focused on the first one. All the technical aspects involved in this system are described in detail in [14].

4.3.1 Description

The LASER box is depicted in Fig. 4.2(a). It contains the light source and the internal calibration system. The light source is a frequency-doubled infrared laser emitting a 532 nm green light beam, which is close to the one of the light produced by the physics signals (480 nm). The energy of the pulses is a few μJ, which is sufficient to simultaneously saturate all TileCal PMTs.

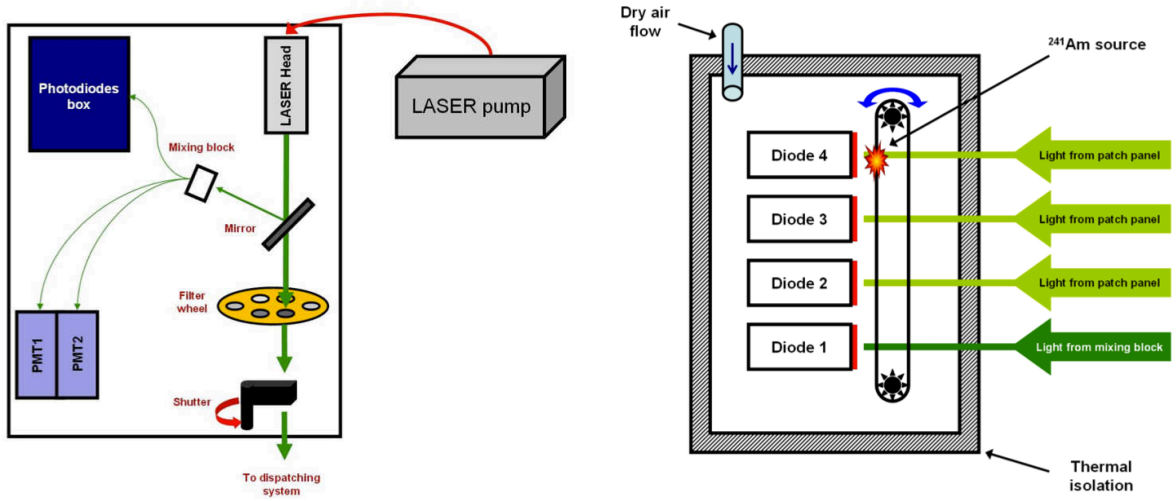

Figure 4.2: The LASER box (a) contains the light source and the internal calibration system. The photodiodes used to measure the intensity of the laser light are located inside the photodiodes box (b).

The light emitted by the laser first encounters a semi-reflecting mirror. A part of this light (currently $8.8\% \pm 0.2\%$) is then transmitted through a light-mixing block. This block contains two light diffusers (thin unpolished glass lenses) and two metallic neutral-density filters providing an attenuation factor light of $\sim 10^5$. This light is evenly distributed among fibers, each of which transmits light to one of the 4 photodiodes used for calibration, and two PMTs used for timing purposes. The other 3 photodiodes are getting information at another level of the system.

Laser light not reflected by the mirror passes through a filter wheel which contains 8 holes.

One hole is empty, whereas the others contain seven neutral-density filters, each one applying a specific attenuation factor from 3 to 1000 to the crossing beam.

A last component in the LASER box is a custom-built electromechanical shutter, which is closed when light is not sent to TileCal. If a laser pulse is emitted when the shutter is opened, the light exits the LASER box and enters into an optical fiber, which links the LASER box output to the first component of the light distribution system, known as the *Coimbra box*. It distributes the light towards all the TileCal modules via 384 optic fibers connected to a patch-panel. When the light reaches the modules, it is split a last time in order to reach all the PMTs.

Not all of the fibers coming out of the Coimbra box go to the TileCal. The remaining fibers are either kept as spares, or used to feed the three remaining diodes in the LASER box, so that the diodes 2, 3 and 4 receive light collected after the patch-panel.

As stated before, the LASER calibration assumes that the intensity of the light of each laser pulse is well known. The four photodiodes are therefore used for the absolute measurement of this intensity, event by event. The main point in this calibration is the comparison of the signal obtained in the Tile PMTs with the signal collected by the photodiodes in the LASER box. These photodiodes are located in a specific box (the photodiodes box), inside the LASER box. The photodiodes box is depicted in Fig. 4.2(b).

Before any use of the LASER system for calibration purposes, one first has to calibrate the system itself. This is the main reason for which the photodiodes response stability has to be clearly monitored. Naturally, this monitoring has to be independent from the laser light. Therefore, an alpha radioactive source is used for the absolute calibration of the photodiodes system. This intrinsic calibration is described in the following section.

4.3.2 LASER system calibration tool

The photodiodes box constitutes the LASER system calibration tool. As said previously, the box contains the 4 photodiodes used to measure the intensity of the laser pulse, and the ^{241}Am source used for their calibration. This radioactive source is emitting alpha particles to a rate of 1.77×10^3 s^{-1} per 2π stereoradian.

The source has a circular shape with a diameter of 16 mm, while the photodiodes are rectangular with a size of 10×20 mm^2. The minimal separation between the photodiodes and the source is not well known. It is estimated to be greater than 0.5 mm.

During calibration periods, the source moves along a straight line formed by the photodiodes in a periodic motion, and it stops in front of each photodiode for a predetermined amount of time. Otherwise, the source is stored in one of the two shielded garages located on the top and bottom of the diodes box. Humidity and temperature in the box are constantly monitored and controlled via dry air flow and Peltier elements, respectively.

The signals coming out of each of the four photodiodes (after a shaper and an amplifier) are fed into an electronic card which generates an internal trigger if at least one of them is above a given threshold. This internal trigger generates the gate needed by the ADC to digitize the delayed photodiodes signals: for each event, only one photodiode contains energy from the alpha radiation, the three other signals are only pedestals. A typical alpha spectrum acquired for one of the photodiodes is shown on the left side in the Fig. 4.3, the response of the photodiode in presence of the alpha source is shown in the right side. The left tail in the alpha spectrum is the consequence of a well-understood geometrical effect. Alpha particles emitted in the air to different angles cover different distances in order to arrive to the photodiode surface. Even if

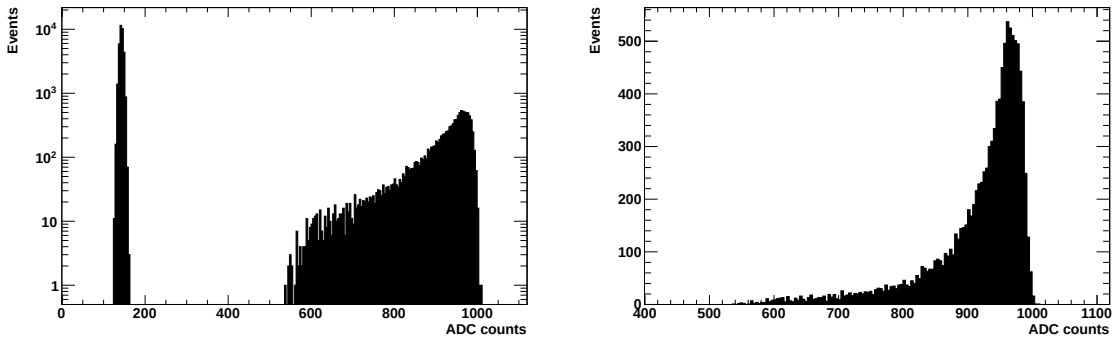

Figure 4.3: Left: A typical spectrum acquired for one of the photodiodes. Right: Response of one photodiode in presence of the alpha source.

the paths are the same, large fluctuations can occur in the energy loss (straggling) of a particle traveling in the air due to the ionization. As a consequence, the energy loss is not the same for all alpha particles, thus causing the low energy tail.

The photodiodes calibration was made twice in a week via **Tile Laser Alpha Scan** by the TileCal shifter until March 9^{th}, 2012. However, from January 2012, it was also made automatically during the stop of ATLAS run, taking just 2'15". Long runs were also taken by the shifter during Cesium scans, taking around 6 hours via **Long Laser Alpha Scan**. The calibration process includes:

- **Pedestal run:** It is taken automatically before the source scan, and it measures the response of the electronics without signal. The averages over all recorded events of the outputs of the photodiodes are the pedestals of these signals, the RMS of each distribution is the noise.
- **Alpha scan:** It is taken while the source is scanning. It measures the response of the photodiodes in the presence of the americium source (alpha spectrum), and the pedestal when the source is in front of the other photodiodes.

These types of runs (pedestal and alpha) will be used to study the stability of the photodiodes response in the following section. The data were taken from February 2^{nd}, 2011 to February 19^{th}, 2013.

4.4 Periods of data taking

The photodiodes stability was studied by periods[1]. These periods are separated by a hardware intervention. They are described below:

- **Period A**: from February 2^{nd} until March 31^{st}, 2011. There is no data before February 2^{nd}, 2011, for that reason this date is considered as the beginning of the period before the first intervention.

[1]The periods and their notation in this chapter do not have to be confused with the periods of ATLAS data taking.

- **Period B**: from March 31^{st} until July 6^{th}, 2011. During the period A, when a photodiode had too high a signal, hence saturating the ADC, it would have an effect on the pedestal of the other photodiodes (electronic cross-talk). As a consequence, the intervention at the end of March consisted in switching off the photodiodes which saturate the ADC. This modification has no effect on the pedestal runs nor the alpha scans because, in these runs, the ADC is never saturated. But, in order to implement this modification, the amplifiers were changed, which may have an effect on the response of the electronics.

- **Period C**: from July 6^{th} until December 5^{th}, 2011. During the first two periods, the pedestal of the photodiodes readout electronics was not very stable: in order to solve this problem, the motherboard inside the photodiodes box was changed at the beginning of July, implementing a new grounding scheme.

- **Period D:** from December 5^{th}, 2011, until February 19^{th}, 2013. During the period C, the noise measured in the alpha scan was slightly bigger than the one in the pedestal run, which could have been related to the alpha source motor. For that reason, a new version of the CmdMotor[2] firmware was implemented on December 5^{th}, 2011. Since then the alpha source motor is powered off when it is in front of the photodiodes. As a consequence, the noise extracted from the pedestal in the alpha scan is slightly smaller than for the previous periods.

The total number of calibrations taken in each period is shown in the second column of Table 4.1. For each period, a reference run was used for comparison (in Section 4.5.1.2 and 4.6). The reference runs correspond to high statistics runs taken in standalone mode for the periods A, B, and C. For the period D, the reference run corresponds to the first Long Laser Alpha Scan taken in this period. The date when the reference runs were taken together with the data taking mode are shown in the third and fourth columns of Table 4.1.

Period	Number of runs	Reference date	Reference data taking mode
A	15	March 3^{rd}, 2011	Standalone
B	48	April 4^{th}, 2011	Standalone
C	23	July 6^{th}, 2011	Standalone
D	314	February 4^{th}, 2012	Long Laser Alpha Scan

Table 4.1: The second column shows to the total number of calibrations taken during each period. The third and fourth columns indicate the date when the reference data were taken and their data taking mode, respectively.

4.5 Stability of the photodiodes electronics

In order to monitor the stability of the photodiodes, it is essential to understand the behavior of their readout electronics. In particular, it is important to check that the pedestal and the noise in the alpha scans are well understood, i.e. are the same as in the pedestal runs. This is

[2]CmdMotor is a VME board controlling the positions and movements of all the moving components of the LASER system: the filter wheel, the radioactive source, and the shutter.

presented in Section 4.5.1. The linearity of the photodiodes electronics is also a crucial point to understand the system. This is studied in Section 4.5.2.

4.5.1 Pedestal and noise

The first step is to study the behavior of the readout electronics response when no energy is deposited in the photodiodes. For this, one can use the *pedestal run* and the pedestal events recorded in the *alpha scan.* The data used for the analysis of each photodiode have the following characteristics:

- Pedestal runs: 5000 recorded events each after August 2011, 2000 recorded events before.
- Pedestal extracted from the alpha scans: $\approx$ 35000 recorded events each after August 2011, $\approx$ 21000 before[3].

4.5.1.1 Mean pedestal

The starting point to determine the stability of the readout electronics response is to study the behavior of its average pedestal. The goal is to compare the mean value extracted from the pedestal run ($\mathsf{P}_{\mathsf{Ped}}$) with the one extracted from the alpha scan (P_{α}) for all the data taken from February, 2011 to February, 2013. The results obtained are shown on the upper plot of the Figs. 4.4, 4.5, 4.6 and 4.7, for the photodiodes 1, 2, 3 and 4, respectively. The variable $\mathsf{R}^{\mathsf{Ped}}_{\alpha/\mathsf{Ped}}$ represents the ratio $\mathsf{P}_{\alpha}/\mathsf{P}_{\mathsf{Ped}}$ and is shown in the lower plots. The statistical uncertainty is also shown in these plots.

As can be seen, for all photodiodes, the hardware intervention with which the period A finished had a big impact on both averages by decreasing them. However, the interventions at the end of the periods B and C had a less significant effect. It is evident that the variations of the mean pedestal –and as a consequence of the ratio– from one period to another one are due to the hardware interventions, but the reason for which the mean pedestal has such a behavior is unknown. However, the big variation at the beginning of 2013 is attributed to temperature and humidity changes, since everything was powered off during the winter shutdown. On the other hand, though the absolute value of the response of the electronics is independent for each photodiode (i.e. it can change enormously from one photodiode to another one due to intrinsic variations of the electronic components), it is possible to observe a big correlation between the photodiodes 2 and 3 (see Figs. 4.5 and 4.6), and between the photodiodes 1 and 4 (see Figs. 4.4 and 4.7). At the same time, an anticorrelation of the average pedestal behavior is also seen between the photodiodes 2 and 3, with respect to the photodiodes 1 and 4. These correlations and anticorrelations have been observed since the motherboard inside the photodiodes box was changed on July 6^{th}, 2011 [15].

However, the main variable under scrutiny here is the ratio $\mathsf{R}^{\mathsf{Ped}}_{\alpha/\mathsf{Ped}}$. If everything is consistent, it should remain around 1, which means that the mean value extracted from the pedestal in the alpha scan is equal to the one extracted from the pedestal run. For the periods A and B, the ratio $\mathsf{R}^{\mathsf{Ped}}_{\alpha/\mathsf{Ped}}$ is smaller than 1 for the photodiodes 1, 2 and 3, with a maximum deviation of 0.9%, 1.7% and 1.2%, respectively (see Figs. 4.4, 4.5 and 4.6). It is not the case for the

[3]New data taking conditions have been used since August, 2011 for the Tile Laser Alpha Scan. The change consisted in increasing the exposure time of the photodiodes to the alpha source and reducing its number of cycles of motion. As a consequence, there are more events recorded in almost the same amount of time.

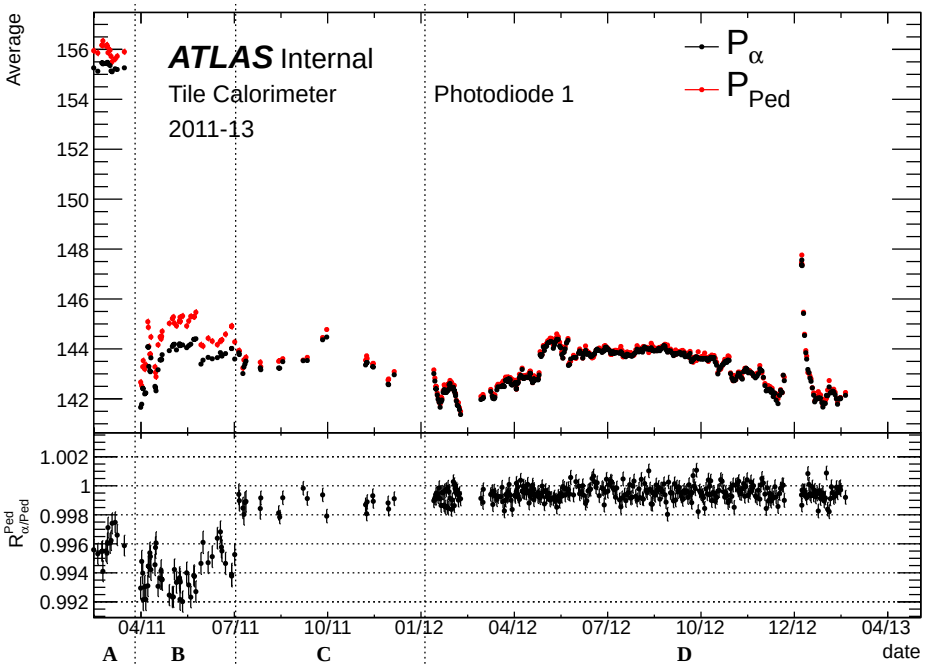

Figure 4.4: Evolution of the mean pedestal value in the pedestal run and the one extracted from the alpha scan (top), and their ratio (bottom) for the photodiode 1 from February 2011 to February 2013. The error bars represent the statistical uncertainties on the averages and the ratios.

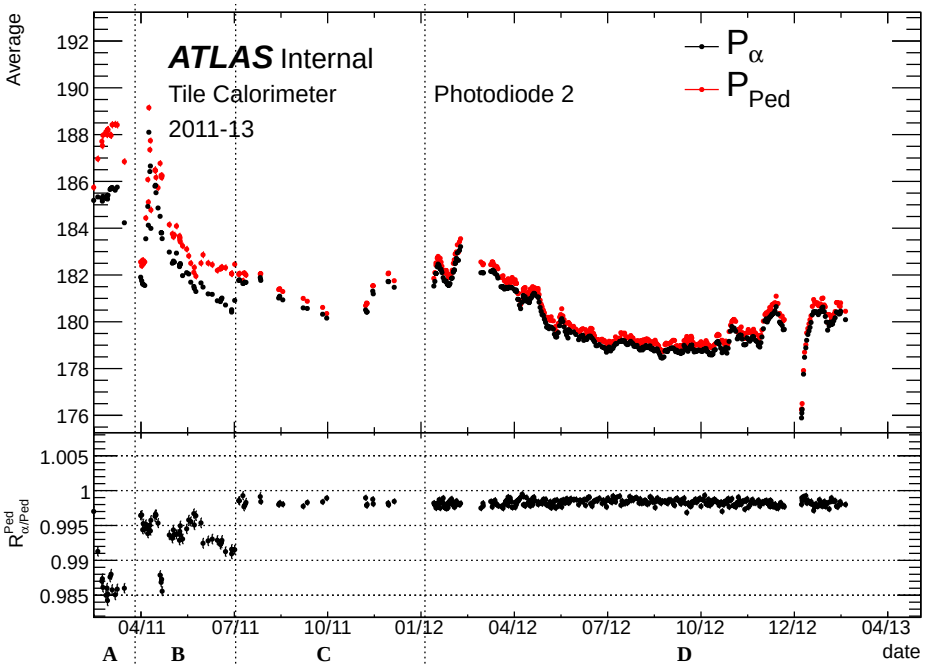

Figure 4.5: Evolution of the mean pedestal value in the pedestal run and the one extracted from the alpha scan (top), and their ratio (bottom) for the photodiode 2 from February 2011 to February 2013. The error bars represent the statistical uncertainties on the averages and the ratios.

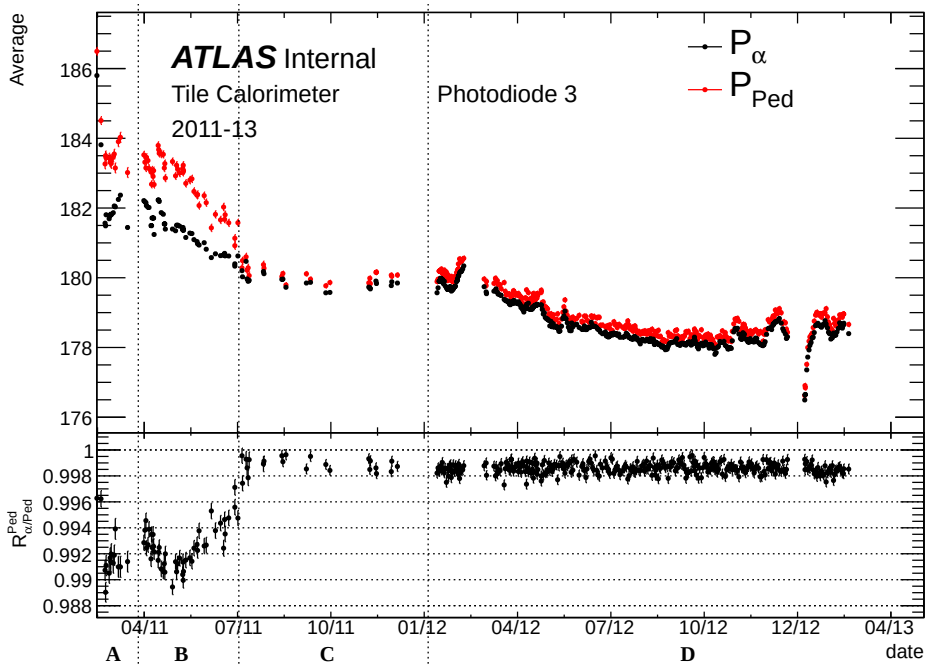

Figure 4.6: Evolution of the mean pedestal value in the pedestal run and the one extracted from the alpha scan (top), and their ratio (bottom) for the photodiode 3 from February 2011 to February 2013. The error bars represent the statistical uncertainties on the averages and the ratios.

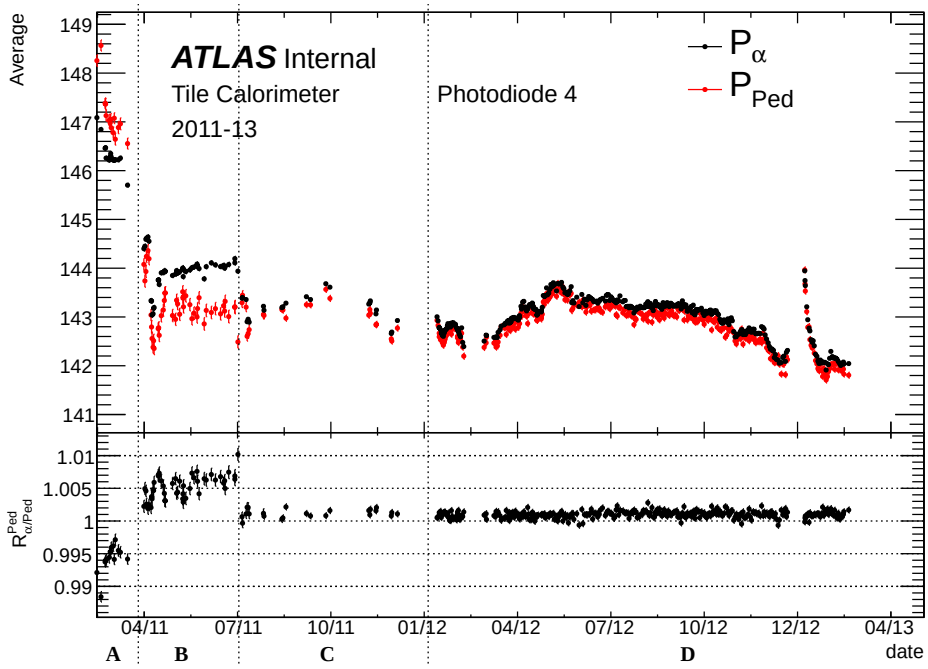

Figure 4.7: Evolution of the mean pedestal value in the pedestal run and the one extracted from the alpha scan (top), and their ratio (bottom) for the photodiode 4 from February 2011 to February 2013. The error bars represent the statistical uncertainties on the averages and the ratios.

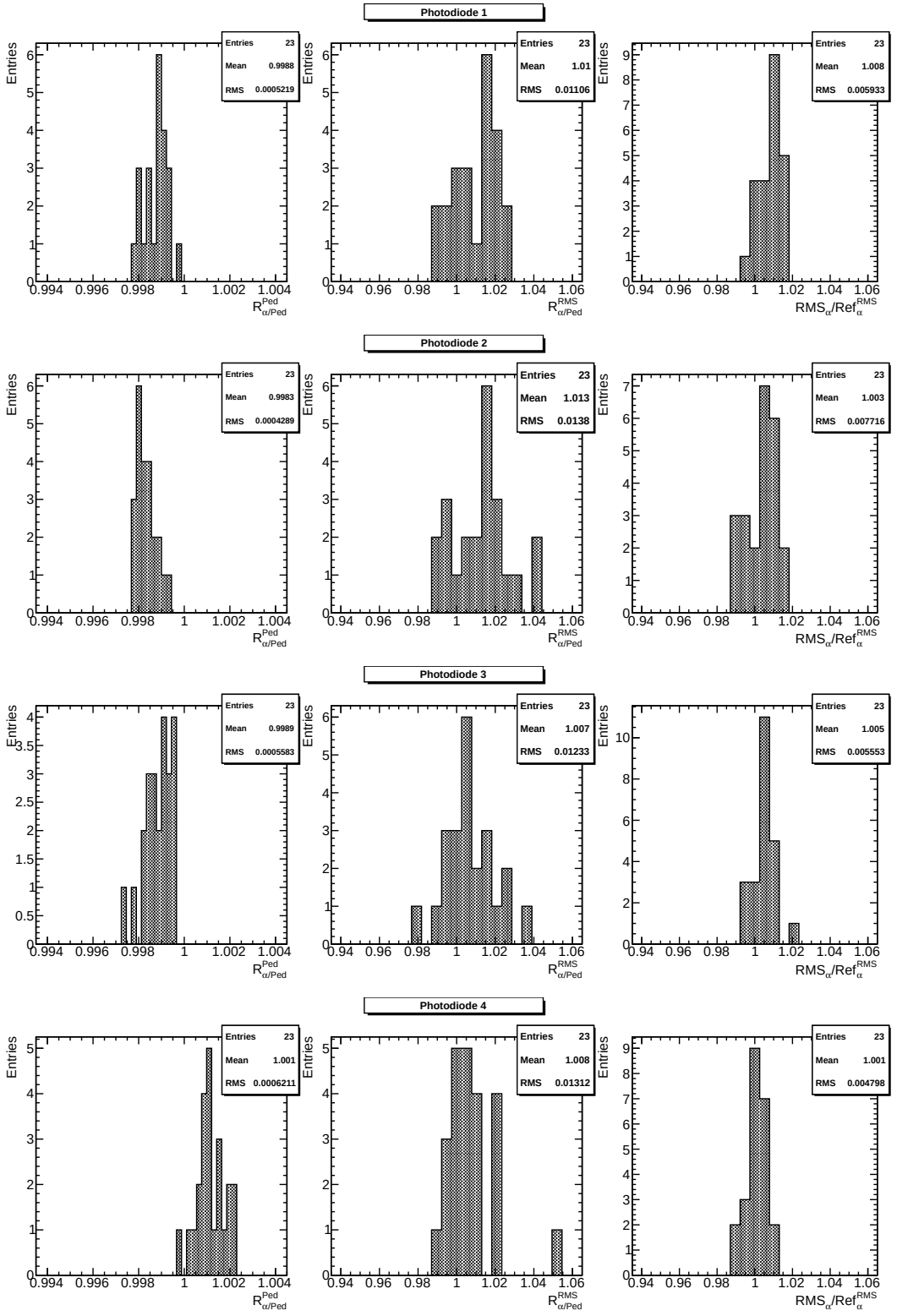

Figure 4.8: Distributions of the ratios $\mathsf{R}^{\mathsf{Ped}}_{\alpha/\mathsf{Ped}}$ (left), $\mathsf{R}^{\mathsf{RMS}}_{\alpha/\mathsf{Ped}}$ (center) and $\mathsf{RMS}_\alpha/\mathsf{Ref}^{\mathsf{RMS}}_\alpha$ (right) for the period C for the photodiodes 1, 2, 3 and 4, from top to bottom, respectively.

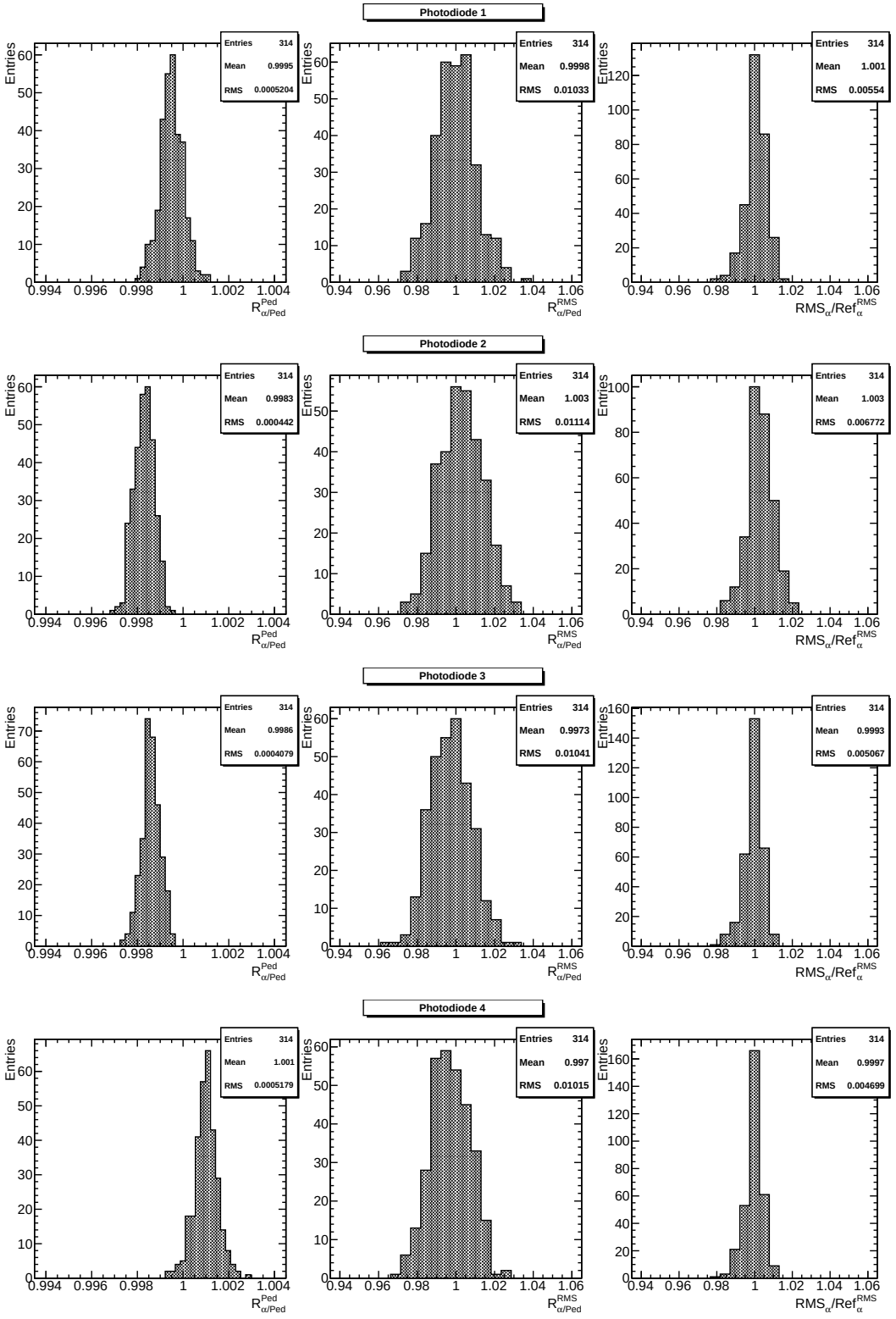

Figure 4.9: Distributions of the ratios $\mathsf{R}^{\mathsf{Ped}}_{\alpha/\mathsf{Ped}}$ (left), $\mathsf{R}^{\mathsf{RMS}}_{\alpha/\mathsf{Ped}}$ (center) and $\mathsf{RMS}_\alpha/\mathsf{Ref}^{\mathsf{RMS}}_\alpha$ (right) for the period D for the photodiodes 1, 2, 3 and 4, from top to bottom, respectively.

photodiode 4, where it is seen that $\mathsf{R}^{\mathsf{Ped}}_{\alpha/\mathsf{Ped}}$ is bigger than 1 for the period B, and which has a maximum deviation of 1.2% during this period (see Fig. 4.7). This is interpreted as a cross-talk effect between readout channels: the intervention at the end of the period B was intended to remove this effect.

For the period C, it is clear that the ratio $\mathsf{R}^{\mathsf{Ped}}_{\alpha/\mathsf{Ped}}$ is closer to 1 than for the previous periods. This ratio is stable within a range of 0.3% for all photodiodes, which means that the pedestal is almost no longer affected by the signal on the other photodiodes. This way, the system became much more stable after the intervention made at the end of the period B. The left plots of Fig. 4.8 show the distribution of $\mathsf{R}^{\mathsf{Ped}}_{\alpha/\mathsf{Ped}}$ for each photodiode over the period C.

For the period D, the ratio $\mathsf{R}^{\mathsf{Ped}}_{\alpha/\mathsf{Ped}}$ is closer to one for the photodiode 1 than for the other photodiodes, with a maximum deviation of 0.25% (see Fig. 4.4). For the photodiodes 2 and 3, it is evident that $\mathsf{R}^{\mathsf{Ped}}_{\alpha/\mathsf{Ped}}$ was below 1 during all this period, presenting a maximum deviation of 0.35% and 0.3%, respectively (see Figs. 4.5 and 4.6). It is not the case for the photodiode 4, where it is seen that $\mathsf{R}^{\mathsf{Ped}}_{\alpha/\mathsf{Ped}}$ is in general bigger than 1, and which has a maximum deviation of around 0.35% (see Fig. 4.7). The left plots of Fig. 4.9 show the distribution of $\mathsf{R}^{\mathsf{Ped}}_{\alpha/\mathsf{Ped}}$ for each photodiode for this period. This ratio is stable within a range of 0.35% for all photodiodes[4]. Looking at the mean value of the distributions of $\mathsf{R}^{\mathsf{Ped}}_{\alpha/\mathsf{Ped}}$, it is possible to see that the system was slightly more stable during this period than for the period C.

To summarize, the mean pedestal is much more stable since the motherboard inside the photodiodes box was changed at the end of the period B. Moreover the cross-talk among the photodiodes was dramatically reduced by this intervention. Now, it is possible to safely perform the pedestal subtraction to study the alpha spectra.

4.5.1.2 Noise

The second important parameter in the study of the readout electronics is the noise. Similarly to the mean pedestal, the goal is to compare the noise extracted from the pedestal run ($\mathsf{RMS}_{\mathsf{Ped}}$) with the one extracted from the alpha scan (RMS_{α}). The results obtained are shown on the upper plot of the Figs. 4.10, 4.11, 4.12 and 4.13, for the photodiodes 1, 2, 3 and 4, respectively. In each plot, the reference noise $\mathsf{Ref}^{\mathsf{RMS}}_{\alpha}$ is also represented. This noise is extracted from the reference alpha scan taken in each period, and which will be also used as a reference in the Section 4.6.3. The number of pedestal events extracted from the reference alpha scan are shown in Table 4.2. As in the previous section, the variable $\mathsf{R}^{\mathsf{RMS}}_{\alpha/\mathsf{Ped}}$ represents the ratio $\mathsf{RMS}_{\alpha}/\mathsf{RMS}_{\mathsf{Ped}}$ and is shown in the lower plot together with its uncertainty.

Period	Photodiode 1	Photodiode 2	Photodiode 3	Photodiode 4
A	201888	200658	204382	200666
B	373426	373490	371800	371819
C	1140680	1138120	1135510	1136760
D	3228063	3219662	3210836	3225242

Table 4.2: Number of pedestal events extracted from the reference alpha scan for each period.

As for the average pedestal, the hardware interventions had an important effect on both RMS by decreasing the noise. Again, the important variable to study here is $\mathsf{R}^{\mathsf{RMS}}_{\alpha/\mathsf{Ped}}$, which should

[4]This range of stability is for the photodiode with the biggest variation obtained from the left plots in Fig. 4.9.

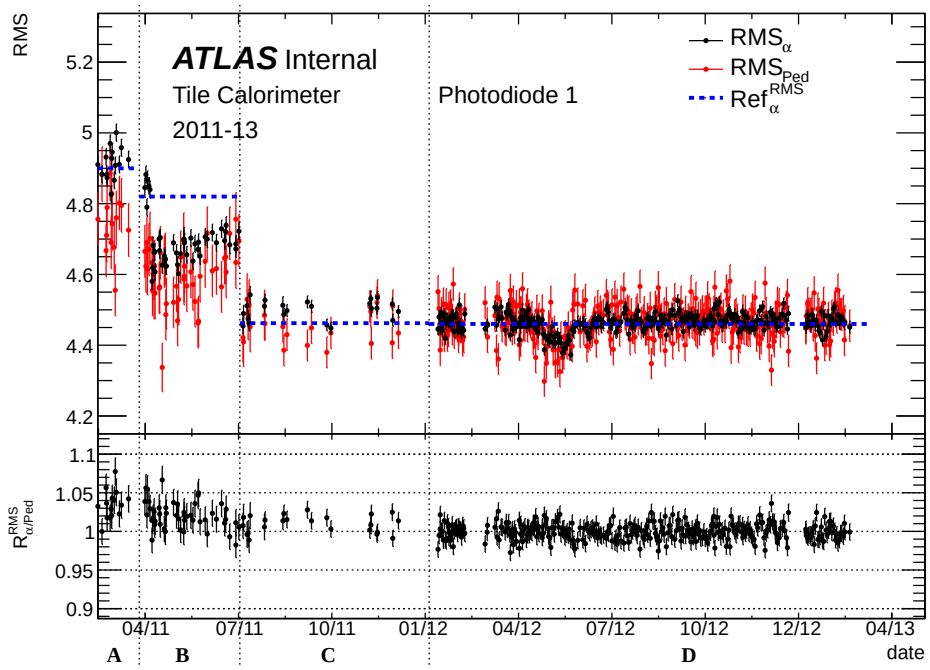

Figure 4.10: Evolution of the noise measured in the pedestal run and the one extracted from the alpha scan (top), and their ratio (bottom) for the photodiode 1 from February 2011 to February 2013. The error bars represent the statistical uncertainties on the averages and the ratios.

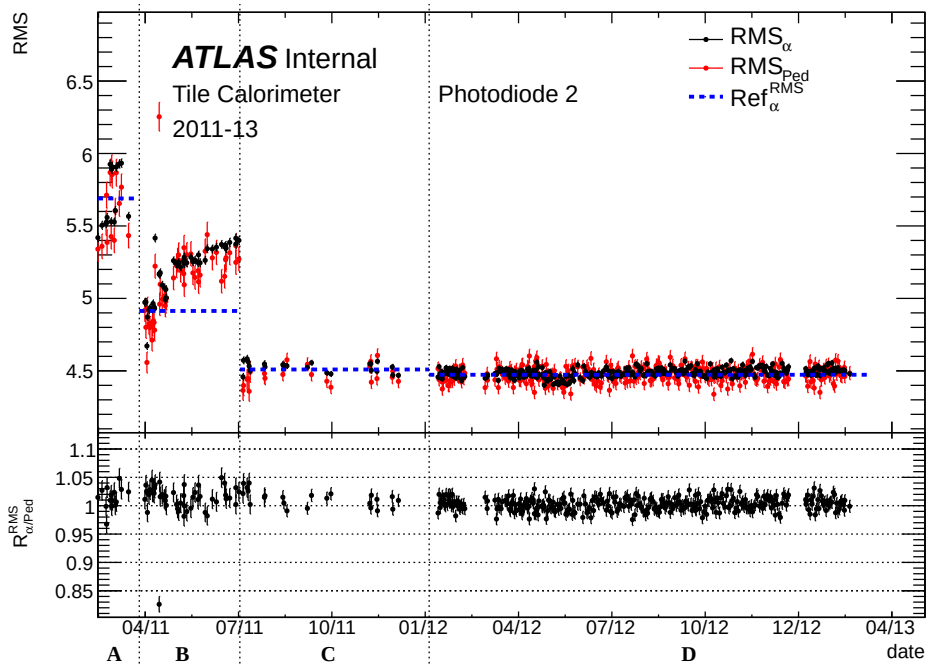

Figure 4.11: Evolution of the noise measured in the pedestal run and the one extracted from the alpha scan (top), and their ratio (bottom) for the photodiode 2 from February 2011 to February 2013. The error bars represent the statistical uncertainties on the averages and the ratios.

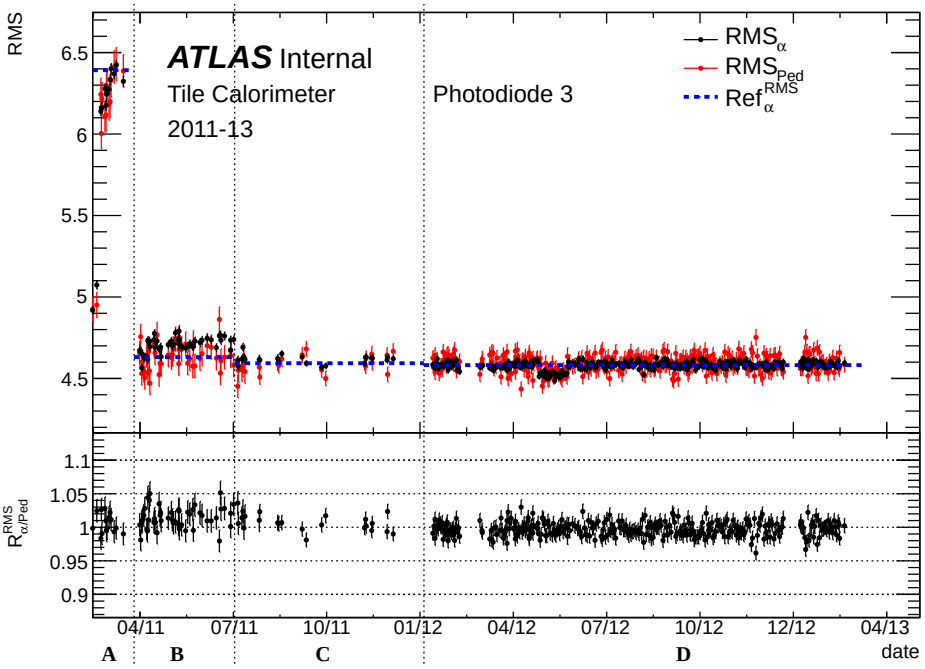

Figure 4.12: Evolution of the noise measured in the pedestal run and the one extracted from the alpha scan (top), and their ratio (bottom) for the photodiode 3 from February 2011 to February 2013. The error bars represent the statistical uncertainties on the averages and the ratios.

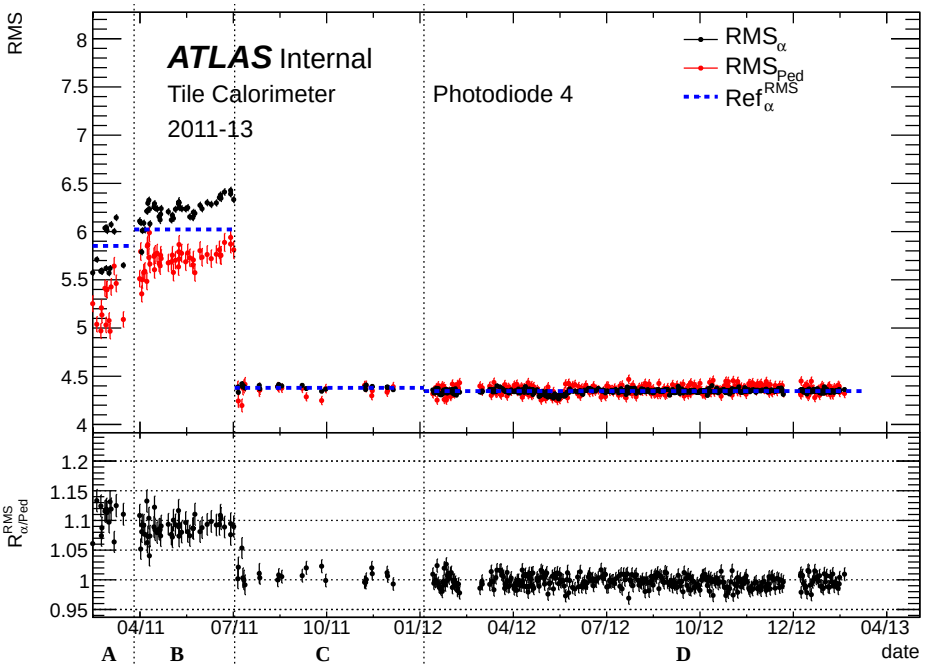

Figure 4.13: Evolution of the noise measured in the pedestal run and the one extracted from the alpha scan (top), and their ratio (bottom) for the photodiode 4 from February 2011 to February 2013. The error bars represent the statistical uncertainties on the averages and the ratios.

remain around 1: it would imply that the noise in the alpha scan is the same as the one in the pedestal run.

For the four periods, there are no significant changes in the ratio $\mathsf{R}^{\mathsf{RMS}}_{\alpha/\mathsf{Ped}}$ for the photodiodes 2 and 3, which were rather stable with a maximum deviation of 7% for the periods A and B, and 6% for the period C (see Figs. 4.11 and 4.12). However, for the photodiodes 1 and 4, $\mathsf{R}^{\mathsf{RMS}}_{\alpha/\mathsf{Ped}}$ has a range of 10% and 16% for the first two periods, and 4% and 5% for the period C, respectively (see Figs. 4.10 and 4.13): the noise in these photodiodes has been well reduced in the July, 2011 intervention and there is no longer a big discrepancy between the noise in the alpha scan and in the pedestal run. The plots on the center of Fig. 4.8 show the distribution of $\mathsf{R}^{\mathsf{RMS}}_{\alpha/\mathsf{Ped}}$ for each photodiode over the period C.

In general, for the periods A, B and C, the noise is a few percent higher in the alpha scan than in the pedestal run, which may be related to the alpha source motor: during these three periods, it was powered on while the source was in front of the photodiodes. As a consequence, it could have introduced additional noise to the response of the electronics. As it was already explained, an intervention on December 5^{th}, 2011 was done in order to solve this problem. Since then, the alpha source motor is powered off when it is in front of the photodiodes.

For the period D, no significant varioations are seen in the ratio $\mathsf{R}^{\mathsf{RMS}}_{\alpha/\mathsf{Ped}}$ for all photodiodes, which were rather stables with a maximum deviation of 4% for the photodiodes 2 and 4 (see Figs. 4.11 and 4.13), and 5% for the photodiodes 1 and 3 (see Figs. 4.10 and 4.12). The plots on the center of Fig. 4.9 show the distribution of $\mathsf{R}^{\mathsf{RMS}}_{\alpha/\mathsf{Ped}}$ for each photodiode over this period. This ratio is stable within a range of 4% for all photodiodes[5]. Looking at their mean values, it is possible to see that these ratios are closer to 1 for this period than for the period C. It means that the noise is under control for all photodiodes since the intervention done on December, 2011.

In particular, it is important to remark the good agreement between the noise extracted from both types of runs: the one extracted from the pedestal in the alpha scan and from the pedestal in the reference alpha scan for the periods C and D (see plots on the right side of Figs. 4.8 and 4.9, respectively). A slightly better agreement between these runs is seen for the period D.

4.5.2 Linearity of the photodiodes electronics

Another crucial point for the understanding of the system is testing that the readout electronics of the photodiodes used to measure the intensity of the laser light is linear.

The linearity of the photodiodes electronics is studied by injecting calibrated charges in it. During the linearity runs, a Digital to Analog Converter (DAC) is used to set an electric level from which a charge proportional to the DAC level will be generated. Once this charge is injected the response of the electronics is digitized by the ADC. Then, the response of the photodiodes electronics and the value of the DAC level are recorded.

There are two ways of injecting charges in the photodiodes electronics: single and multi-charge injection modes. Both are explained below.

[5] As for the mean pedestal, this range of stability is for the photodiode with the biggest variation obtained from the center plots in Fig. 4.9.

4.5.2.1 Single charge injection mode

This mode is used to make sure that the system that injects charges is stable. In this mode the injected charge is constant. However, the measured value varies due to the noise introduced by the electronics of the system. Thus, the response of the photodiodes electronics versus the charge injected to the four photodiodes looks like the plots shown in Fig. 4.14. The distribution of the injected charge as well as the distribution of the response of the electronics of each photodiode are shown in Fig. 4.15, together with a Gaussian fit. All the plots shown in both figures are made after pedestal subtraction.

As can be seen from Fig. 4.15, the measured values of the injected charges are distributed following a Gaussian distribution. The mean value of this distribution corresponds to the real injected charge. As expected, the distribution of the response of the electronics of the photodiodes follows the same distribution. This way we can conclude that the single charge injection system is stable.

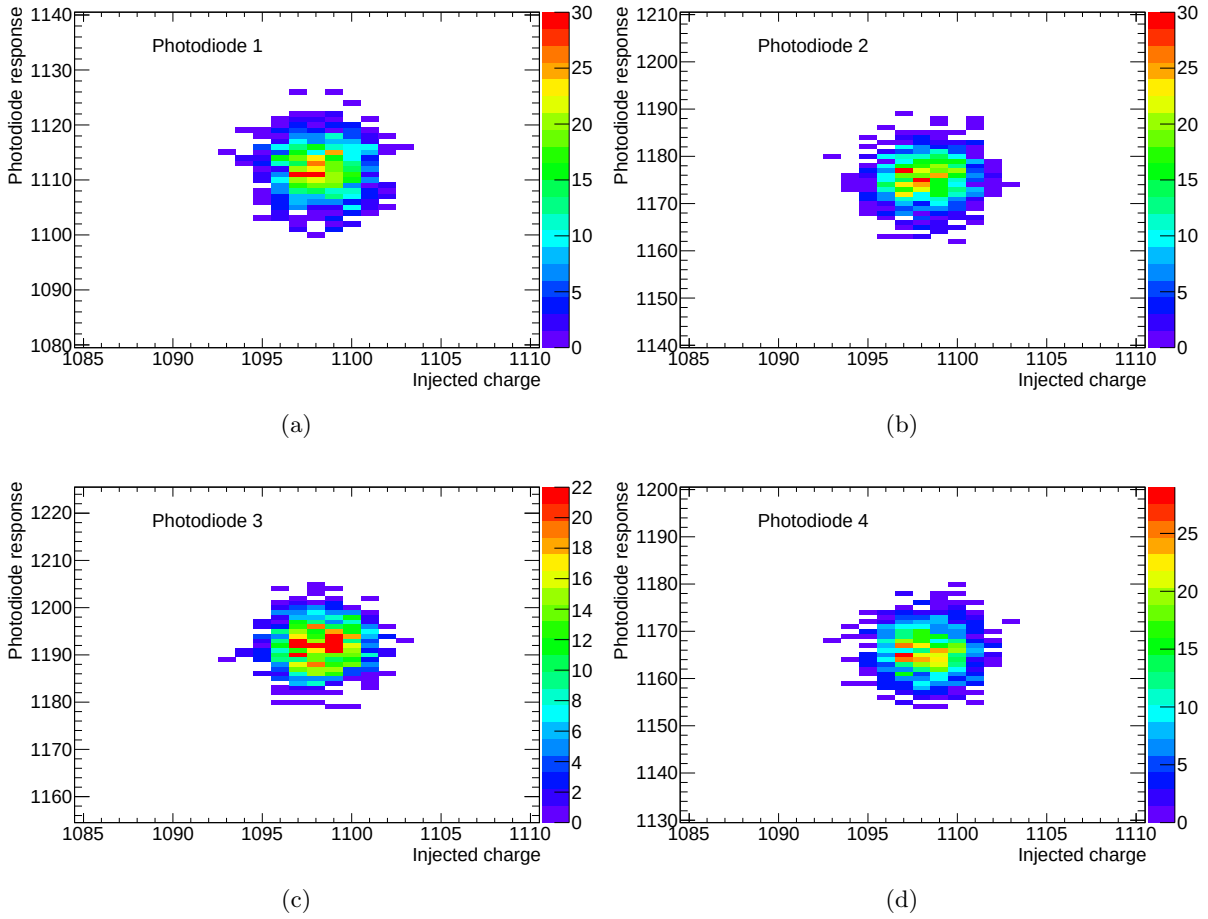

Figure 4.14: Response of the photodiodes electronics versus the injected charge for the photodiodes 1 (a), 2 (b), 3 (c) and 4 (d), in the single charge injection mode after pedestal subtraction.

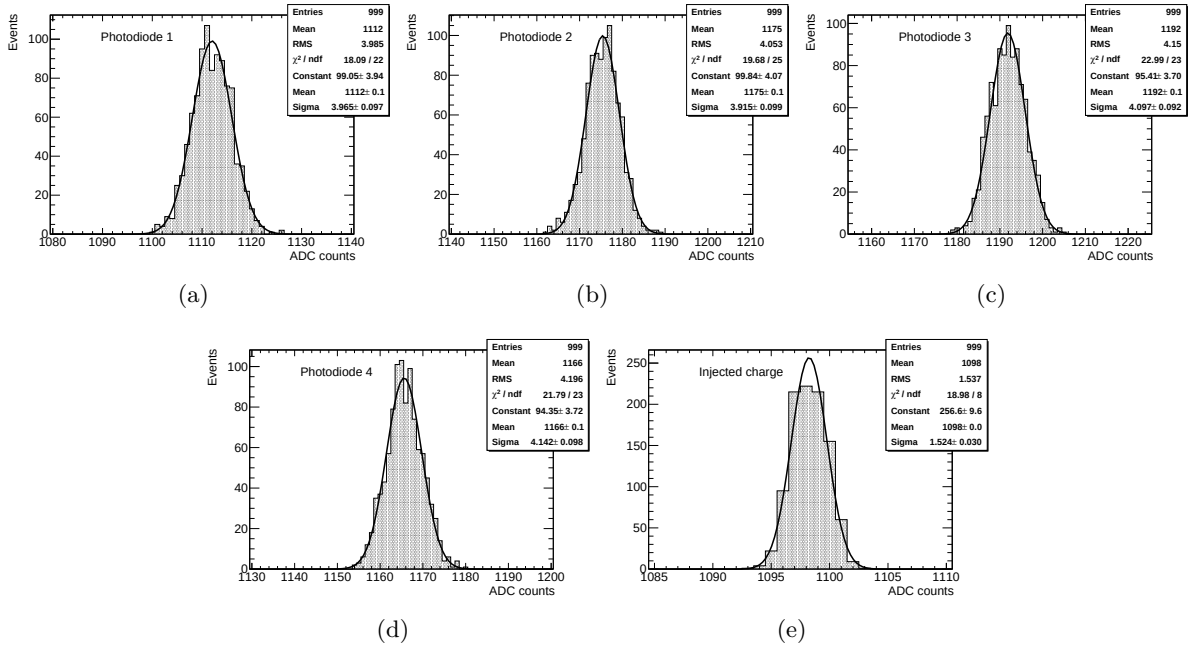

Figure 4.15: Distributions of the response of the electronics of the photodiodes 1 (a), 2 (b), 3 (c) and 4 (d). The distribution of the injected charge to the electronics of all photodiodes is shown in (e). All the distributions correspond to the single charge injection mode.

4.5.2.2 Multicharge injection mode

The multicharge injection mode is the one used to test the linearity of the photodiodes electronics. It is basically the single charge injection mode, but with the value of the charge increasing each certain interval of time. The charge is increased up to the saturation point of the photodiodes electronics. The data used for this linearity study were taken in standalone mode on July 1^{st}, 2012, and correspond to a high statistics linearity run. Around 100 000 events were recorded for each photodiode, in 100 single charge injection modes.

The response of the electronics of each photodiode versus the injected charge is shown on the upper plots of Fig. 4.16. Each point in these plots corresponds to a single charge injection mode. That means that the values shown as for the injected charge as for the response of the photodiodes electronics correspond to the mean values extracted from their corresponding Gaussian fits as done in Section 4.5.2.1 once the pedestal has been subtracted. The uncertainties on these values are extracted from the quadratic medium deviation of their fits.

The linearity of the electronics of each photodiode is tested by fitting its response to the injected charge with a polynomial of order 1, and computing the relative distance of the experimental point with respect to the predicted value of the fit (relative residuals). The linear fit on the response of the electronics is also shown on the upper plots of Fig. 4.16, while the relative residuals are shown in the bottom plots of the same figure. As can be seen for all photodiodes, the values of chi-squared per degree of freedom obtained from the linear fit give very good results. However, the values of the intercepting points (p_0) are not at zero. In principle, it affects the linearity of the electronics, since for zero injected charge the response of the photodiodes should be null. This effect has been found also in all older linearity runs since June 2008. A cross-check

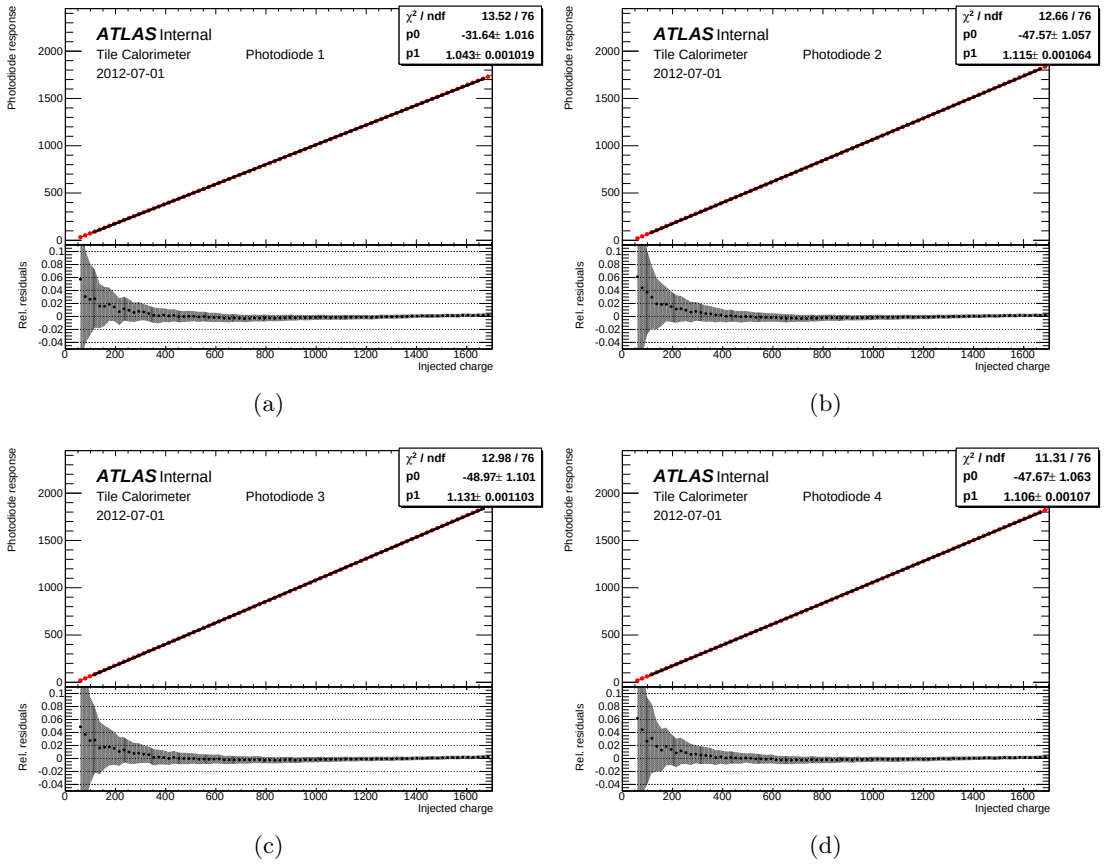

Figure 4.16: Response of the photodiodes electronics versus the injected charge with the corresponding fitted line (top) for the photodiodes 1 (a), 2 (b), 3 (c) and 4 (d). The relative distance to the linear fit as a function of the injected charge is shown in the bottom plots.

was done by studying the linearity of the photodiodes electronics on a replica of the system, and this effect is not present. The shift of the interception point can be attributed to variations in the pedestal of the photodiodes or the injected charge. As the mean pedestal of the photodiodes electronics measured in the linearity run coincide with the one measured in the pedestal run and in the alpha scan, that means that this difference can be assumed to come from a variation in the pedestal of the injected charge. This variation was estimated to be around 25%. Nevertheless, the effect of this kind of variations in the LASER calibration is considered to be negligible. As a consequence, the linearity of the photodiodes here will be determined following only the goodness of the linear fit, and the results of the relative residuals.

From the bottom plots in Fig. 4.16, it is possible to see that the relative residuals are within 8% for all photodiodes, with statistical uncertainties that can raise to 20% when the injected charge is small, and which decrease as long as the injected charge increases. This behavior is expected since the statistical uncertainty on the response of the photodiodes electronics is more or less constant, independently of the numerical value of the response itself. Therefore, small values of the response of photodiodes electronics will be affected in a greater proportion. The distributions of the relative residuals for each photodiode are shown in Fig. 4.17. As can be

seen, most of the points are within 1% of the estimated fit.

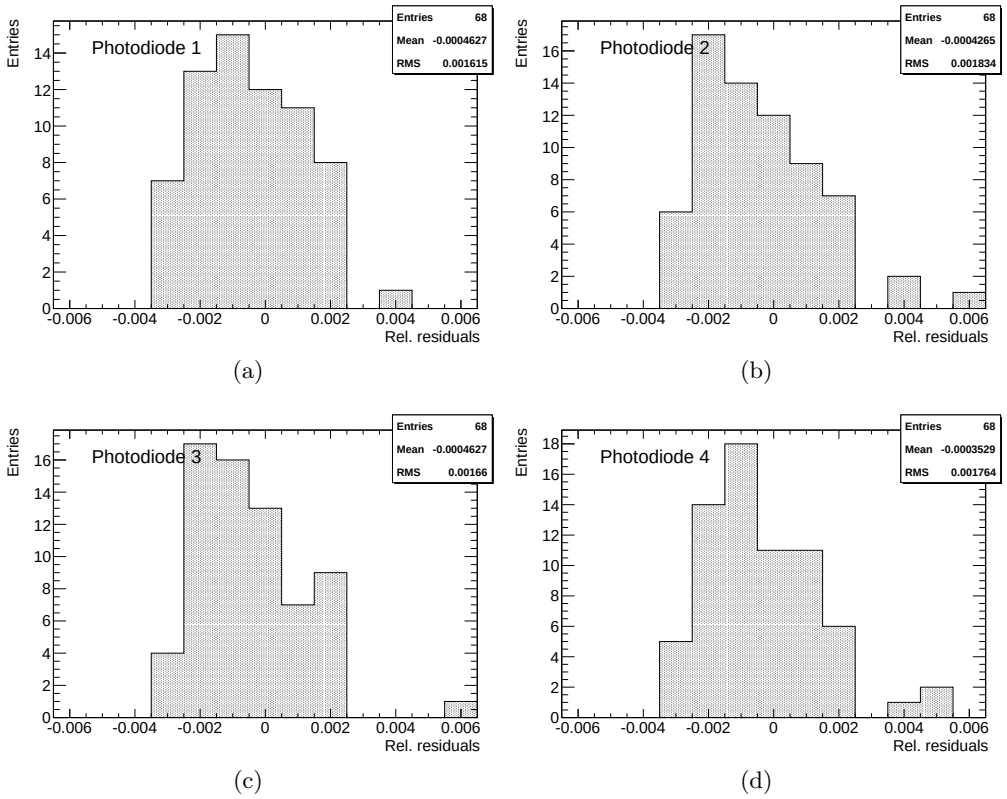

Figure 4.17: Distributions of the relative residuals for the photodiodes 1 (a), 2 (b), 3 (c) and 4 (d). Values at low injected charge have been excluded in these distributions.

A cross-check of these results can be done by using other linearity runs taken also in standalone mode on July, 2012. This is done by looking at the evolution of the slope (m) and the interception point (p) given by the linear fit with respect to the reference values. These last ones correspond to the slope (p_1) and the interception point (p_0) obtained from the linear fit of the first linearity run taken on July, 2012 (this run also corresponds to the one analyzed in this section, therefore the values of p_0 and p_1 are the ones shown in Fig. 4.16). The evolutions of m/p_1 and p/p_0 are shown in Figs. 4.18(a) and 4.18(b), respectively. As can be seen, for the four photodiodes the slope is stable within 0.2% with respect to the reference value, while the interception point does within 4%.

4.5.3 Summary: stability of the photodiodes electronics

For all photodiodes the mean pedestal is much more stable after the intervention made at the end of the period B. Since then, the value measured in the alpha scans has had a maximum deviation of 0.35% of the one measured in the pedestal runs. That means that the cross-talk was dramatically reduced by this intervention. Now, the pedestal in the alpha scans is well understood, i.e. it is possible to safely perform the pedestal subtraction to study the alpha spectra.

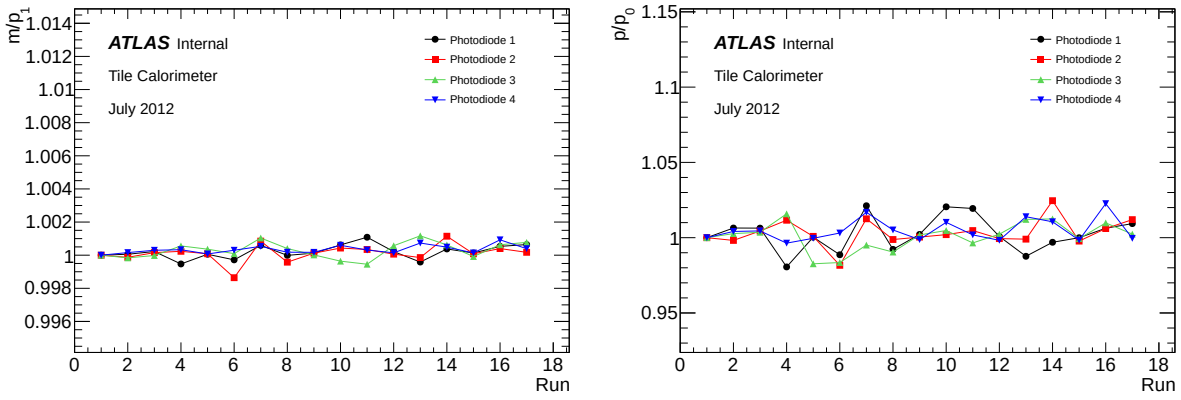

(a) (b)

Figure 4.18: Evolution of the relative slope m/p_1 (a) and p/p_0 (b) as function of the run number for all the runs taken on July, 2012.

The noise was significantly reduced by the various interventions. On the other hand, the value measured in the alpha scans was a few percent higher than in the pedestal runs during the periods A-C. It could be related to the alpha source motor, since it could introduce additional noise to the response of the electronics. In order to solve this problem, an intervention on December 5^{th}, 2011 was done. Since then, the alpha source motor is powered off when the source is in front of the photodiodes. The ratio $R^{RMS}_{\alpha/Ped}$ is closer to 1 for the period D than for previous periods, meaning that the noise is well under control for all photodiodes after this intervention, i.e. the noise in the alpha scans does not have big variations and is close enough to the noise in the pedestal runs.

The response of the photodiodes electronics was found to be linear. However, there is a shift in the pedestal of the measurement of the injected charge that is not understood. This shift is estimated to be around 25% and it has been observed since June 2008. Nevertheless it does not affect the photodiodes themselves, and its effect in the LASER calibration is considered to be negligible.

4.6 Stability of the alpha response

Once the photodiodes electronics has been studied, the next step is to study the stability of the photodiodes response in presence of the alpha source. In this section, this response is always the value after subtracting the pedestal, ensuring that when the deposited energy is zero, the photodiodes response is null.

Before this study, the stability of the alpha response was studied by simply looking at the mean of the alpha spectra. An alternative method has been proposed: the *scale factor*. This method is based on the assumption that the variation in the measured alpha spectra is due to a variation of the gain of the photodiodes and/or their readout electronics, thus only implying a rescaling of the spectra and not a distortion. Therefore, in this method, the spectrum under study is compared to a reference spectrum, taken during a high statistics run. A test spectrum is first built by rescaling the reference one, i.e. by multiplying the photodiode response for each

recorded event by a constant number, called the scale factor. Then, this scale factor is varied until the resulting distribution fits as well as possible the one under study. The resulting scale factor is then a measurement of the gain variation, being equal to one if no rescaling is needed to fit the reference distribution to the studied one.

In Section 4.6.1, the two methods, scale factor and normalized mean value, are compared using simulated data. It will be demonstrated that the scale factor is more sensitive than the mean value. Then, in Section 4.6.2, it will be studied, still on simulated data, the bias introduced on the scale factor determination by uncontrolled variations of the pedestal and the noise. These effects will also be studied on the mean value method. Finally, in Section 4.6.3, the scale factor method will be applied on all alpha scans taken between 2011 and 2013 in order to study the stabillty of the photodiodes over this period.

4.6.1 Comparison of the scale factor and mean value methods

In this section, the two criteria to study the stability of the alpha response will be compared: mean value and scale factor. In order to evaluate the relative precision and stability of the two approaches, pseudoexperiments are generated, and are explained in the following paragraph.

A *simulated alpha scan* is generated in order to simulate the impact of a constant scale shift. The first step consists in generating a distribution with the same shape as the reference data (Fig. 4.19(a)), but with a lower statistics (the same statistics as the data taken during the stop of the ATLAS run, i.e. 10000 events). The reference data corresponds to the first Long Laser Alpha Scan taken in 2012 (1074848 events) for the photodiode 2. The lower statistics reference (see Fig. 4.19(b)) is then multiplied by a scale factor SF_0 , the resulting distribution is the simulated alpha scan (Fig. 4.19(c)).

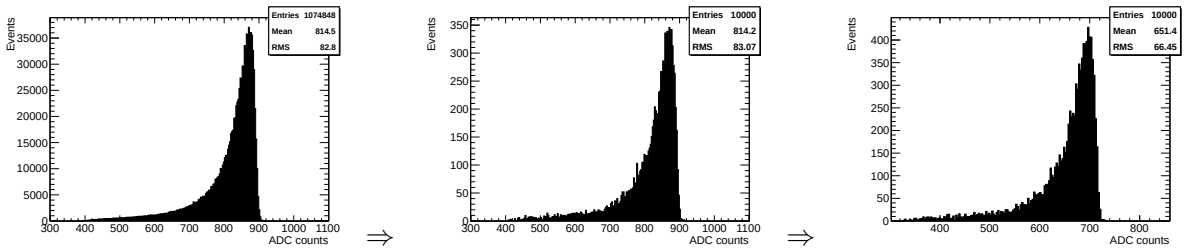

(a) Reference data

(b) Reference data with a low statistics

(c) Simulated alpha scan

Figure 4.19: From the reference data is generated a distribution with a low statistics, which is then multiplied by the scale factor SF_0 in order to obtain the simulated alpha scan. In this example $\mathsf{SF}_0 = 0.8$.

The procedure in order to compare the methods can be described as:

Scale factor:

1. The reference spectrum is multiplied by a scale factor SF_1. Then the values of χ^2/ndf and the p-value between this distribution and the simulated alpha scan are computed using the χ^2 and Kolmogorov tests, respectively.

2. The previous step is repeated for different values of SF_1. The goal is to construct a plot of χ^2/ndf as a function of SF_1, and the p-value also as a function of SF_1: the scale factor

with the minimum (maximum) value of χ^2 (p-value), i.e. the simulated alpha scan that better fits the reference data, is the best scale factor found for this simulated alpha scan (see plots in Fig. 4.20).

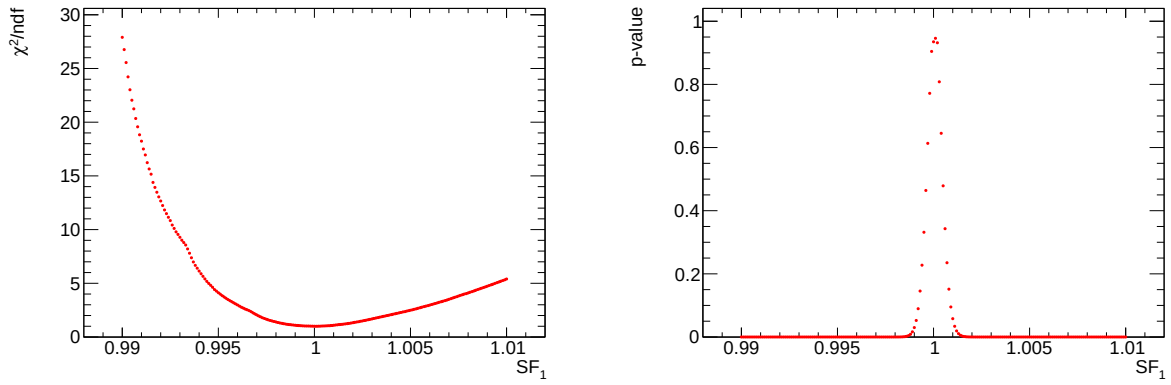

Figure 4.20: Example of a plot of χ^2/ndf (left) and p-value (right) as a function of the scale factor $\mathsf{SF_1}$ for a simulated alpha scan. Both plots correspond to a scale factor $\mathsf{SF_0} = 1$. The best scale factor found in both cases corresponds to $\mathsf{SF_1} = 1.0001$.

3. A new simulated alpha scan is generated and the two previous steps are repeated (using the same value for $\mathsf{SF_0}$) to obtain a distribution $\mathsf{SF_1}/\mathsf{SF_0}$. This distribution is shown in Fig. 4.21(a) for the χ^2 test, and Fig. 4.21(b) for the Kolmogorov test. The width of these distributions gives the precision of the method. The value of χ^2/ndf (p-value) as a function of the best scale factor found $\mathsf{SF_1}$ for each simulated alpha scan generated is shown in the right (left) plot of Fig. 4.22.

Mean value:

1. The mean value of the reference data, μ_0, is computed.
2. The mean value of the simulated alpha scan, μ_1, is computed.
3. A new simulated alpha scan is generated and the previous step is repeated to obtain a distribution $\mu_1/(\mu_0 \times \mathsf{SF_0})$ (see Fig. 4.21(c)) for the same value of $\mathsf{SF_0}$. Again, the width of the distribution gives the precision of the method.

From the results in Figs. 4.21(a)-4.21(c), it is possible to see that the three distributions are well centered on 1. As can be seen from Figs. 4.21(a) and 4.21(b), the standard deviations of the distributions $\mathsf{SF_1}/\mathsf{SF_0}$ are $\sigma_{SF} = 0.00028$ and $\sigma_{SF} = 0.00052$, respectively. They are smaller than the one extracted from the distribution $\mu_1/(\mu_0 \times \mathsf{SF_0})$, $\sigma_\mu = 0.0010$ (see Fig. 4.21(c)). This situation is more visible in Fig. 4.21(d). It means that the scale factor is a more precise method than the mean value.

All plots presented in this section correspond to a scale factor $\mathsf{SF_0} = 1$, and for an alpha spectrum with 500 bins. In principle, in the scale factor method, χ^2 gives better results than the Kolomogorov test, since the standard deviation of its distribution $\mathsf{SF_1}/\mathsf{SF_0}$ is smaller. Nevertheless, it is necessary to check if these results are stable when different values of $\mathsf{SF_0}$ are used.

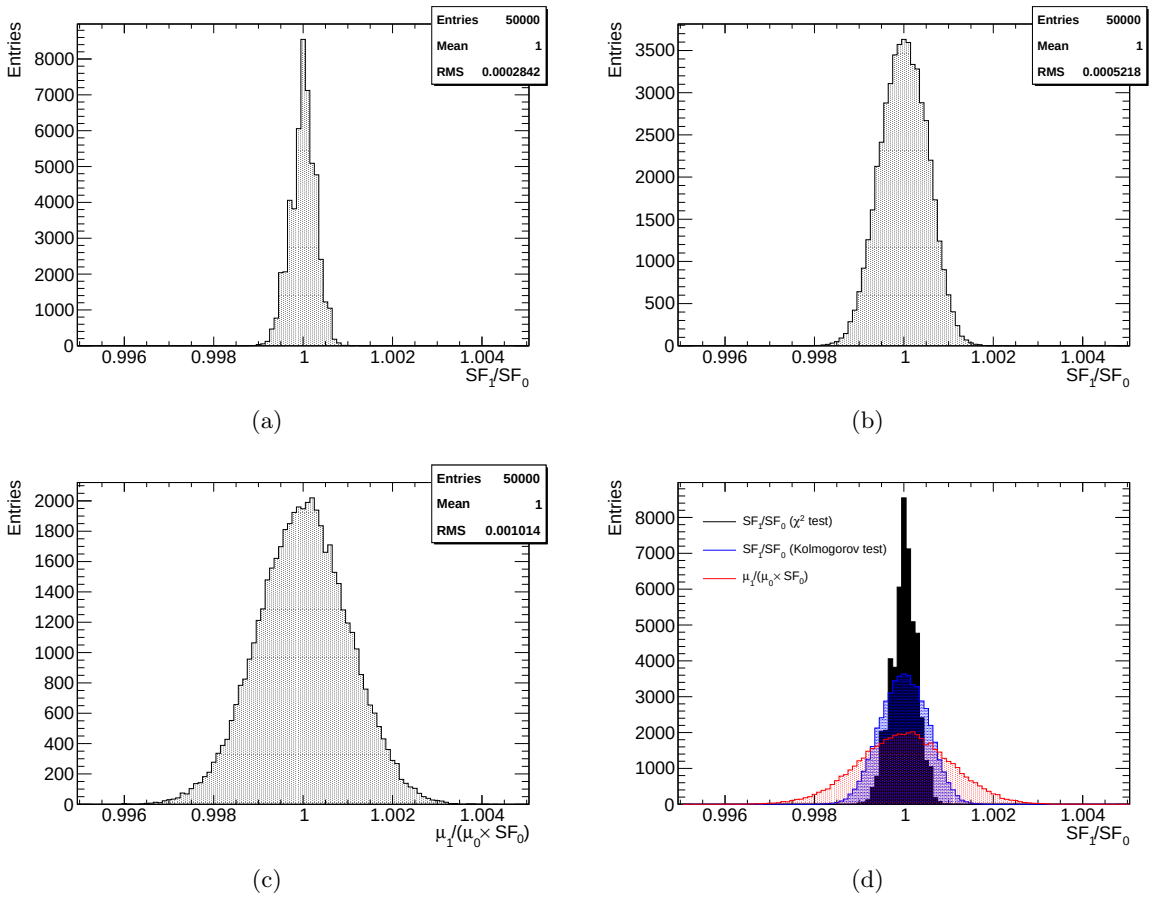

Figure 4.21: Distributions of $\mathsf{SF}_1/\mathsf{SF}_0$ obtained using the χ^2 test (a) and the Kolmogorov test (b). The distribution of $\mu_1/(\mu_0 \times \mathsf{SF}_0)$ is shown in (c). The comparison of these three distributions is shown in (d). In this example 50 000 pseudoexperiments were generated and $\mathsf{SF}_0 = 1$.

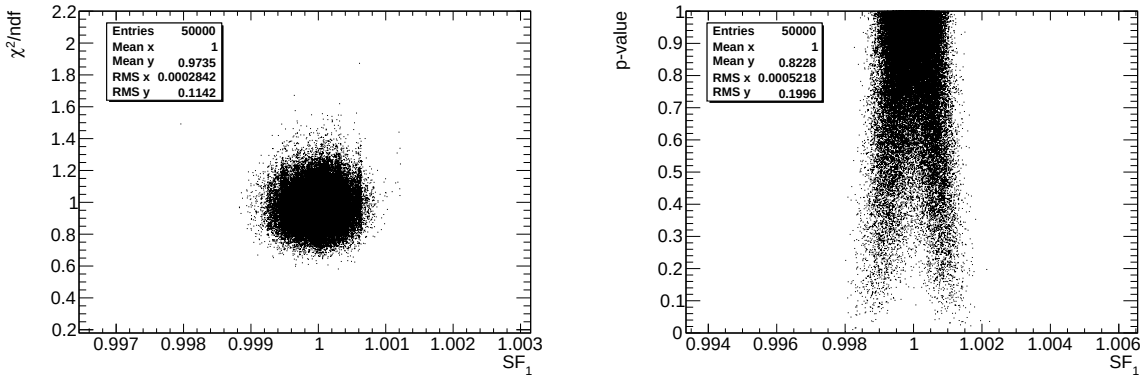

Figure 4.22: χ^2/ndf (left) and p-value (right) as a function of the best scale factor found SF_1 for each simulated alpha scan. These values have been computed using the χ^2 test and the Kolmogorov test, respectively. In this example $\mathsf{SF}_0 = 1$.

The values tested here go from $\mathsf{SF_0} = 0.8$ to $\mathsf{SF_0} = 1.2$ per steps of 0.002. The distributions of $\langle \mathsf{SF_1/SF_0} \rangle$ obtained using both methods, χ^2 and the Kolmogorov tests are shown in Fig. 4.23(a). The distribution of $\langle \mu_1/(\mu_0 \times \mathsf{SF_0}) \rangle$ is also shown in this plot. As can be seen, the results obtained from the Kolmogorov test are well centered in 1, while the scale factors computed using the χ^2 test are biased to values bigger than $\mathsf{SF_0}$. This bias becomes more important when the binning of the alpha spectra decreases (see Figs. 4.23(b) and 4.23(c)), with a maximum deviation of 0.51%. Scale factors computed via the Kolmogorov test are stable within 0.005%. For that reason, the Kolmogorov test will be used to determine the stability of the alpha spectra with the scale factor method.

The standard deviations extracted from the distributions $\mathsf{SF_1/SF_0}$ and $\mu_1/(\mu_0 \times \mathsf{SF_0})$ for a range between $\mathsf{SF_0} = 0.8$ and $\mathsf{SF_0} = 1.2$ per steps of 0.002 are shown in Fig. 4.24. As can be seen the standard deviation for the scale factor is always smaller than the one for the normalized mean value. It corroborates that the scale factor is a more precise method than the mean value. Therefore, it will be the main method used to monitor the stability of the alpha spectra via the Kolmogorov test.

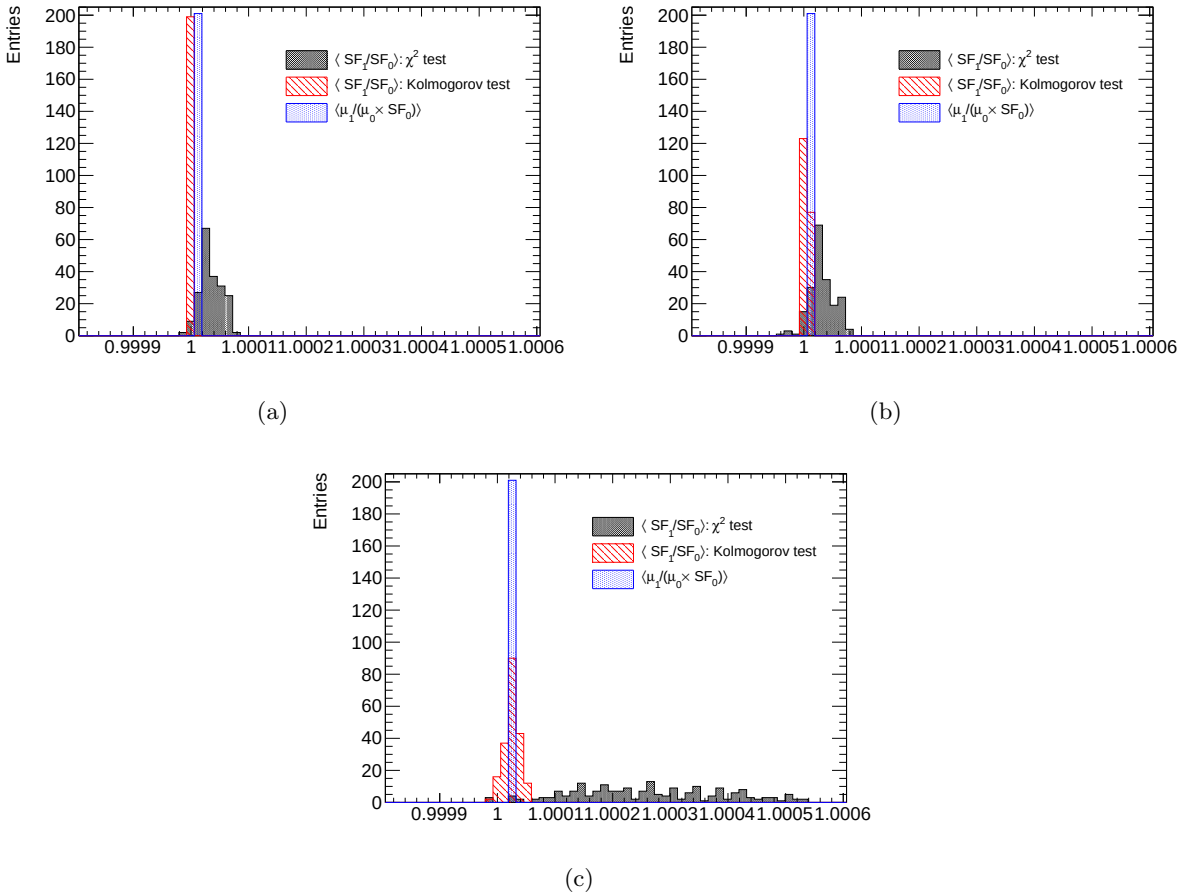

(a) (b)

(c)

Figure 4.23: Distributions of $\langle \mathsf{SF_1/SF_0} \rangle$ obtained using both methods, χ^2 and the Kolmogorov test for alpha spectra with 750 (a), 500 (b) and 250 (c) bins. The distribution of $\langle \mu_1/(\mu_0 \times \mathsf{SF_0}) \rangle$ is also shown in each plot. The values of $\mathsf{SF_0}$ used go from 0.8 to 1.2 per steps of 0.002.

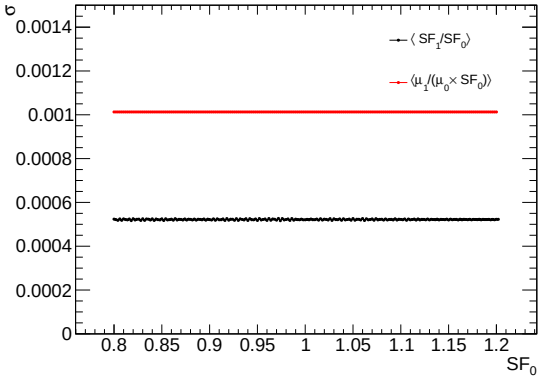

Figure 4.24: Standard deviation of $\mu_1/(\mu_0 \times \mathsf{SF_0})$ (black) and $\mathsf{SF_1}/\mathsf{SF_0}$ (red) for $\mathsf{SF_0} = 0.8$ to $\mathsf{SF_0} = 1.2$ per steps of 0.002.

4.6.2 Effects on the scale factor and mean value of variations in the readout electronics

As stated previously, the scale factor method assumes that there is no distortion of the alpha spectra, only rescaling. Distortion could arise from variations of the characteristics of the readout electronics, pedestal and noise. Therefore, in this section, it will study, still using pseudoexperiments, the effect of adding variations of the readout electronics characteristics on the alpha response, using the Kolmogorov test to determine the scale factor. The procedure in order to produce these simulated data is equivalent to the one presented in the previous section: from a reference data is generated a distribution with a low statistics, but here a constant variation of the readout electronics is added, the resulting distribution is the simulated alpha scan.

In order to determine the scale factor and mean value, the same procedure presented in the Section 4.6.1 is used. This time, the interest resides in obtaining the distributions $\Delta\mu(\%) = [\mu_1/(\mu_0 \times \mathsf{SF_0}) - 1] \times 100$ and $\Delta\mathsf{SF}(\%) = (\mathsf{SF_1}/\mathsf{SF_0} - 1) \times 100$ for the mean value and the scale factor, respectively. The mean value of these distributions gives the variation in the scale factor or mean value for the specific variation of the readout electronics. The goal is to construct a plot of $\Delta\mathsf{SF}(\%)$ and $\Delta\mu(\%)$ as a function of this variation.

The studied variations of the readout electronics are the pedestal and noise variations. The effect of each one of them is studied separately.

An example of the distributions $\Delta\mathsf{SF}(\%)$ and $\Delta\mu(\%)$ for a scale factor $\mathsf{SF_0} = 1$ and a pedestal variation $\Delta p = 1\%$ is shown in the Fig. 4.25. From there, it is possible to see that the scale factor is shifted by 0.21% if a pedestal variation of 1% is added. A similar result is obtained for the mean value: 0.22%.

The plots of the $\Delta\mathsf{SF}(\%)$ and $\Delta\mu(\%)$ for different values of $\mathsf{SF_0}$ as a function of the pedestal variation can be found in the left and right sides of the Fig. 4.26, respectively. The error bars represent the standard deviation of the distributions $\Delta\mathsf{SF}(\%)$ or $\Delta\mu(\%)$ for the given pedestal variation. The range of the pedestal variation studied goes from -10% to +10%. As can be seen, in both cases the relation is linear, the slope of each line gives the sensitivity of its respective method with respect to the parameter studied. For $\mathsf{SF_0} = 1$, the scale factor has a sensitivity of $\approx 0.21\%$, while for the mean value it is $\approx 0.22\%$, but its uncertainty is bigger than for the scale factor. Basically, the two methods have almost the same sensitivity, which means the same

bias. In a few words, if the knowledge of the pedestal in the real data is bad, it will result in the same bias for the scale factor as for the mean value. It is important to remark that for a given variation of the pedestal, the bias depends very weakly on SF_0.

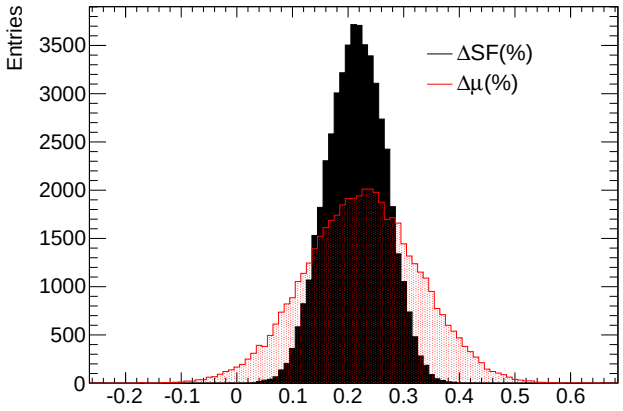

Figure 4.25: An example of the distributions $\Delta\mathsf{SF}(\%)$ and $\Delta\mu(\%)$ for a pedestal variation $\Delta p = 1\%$.

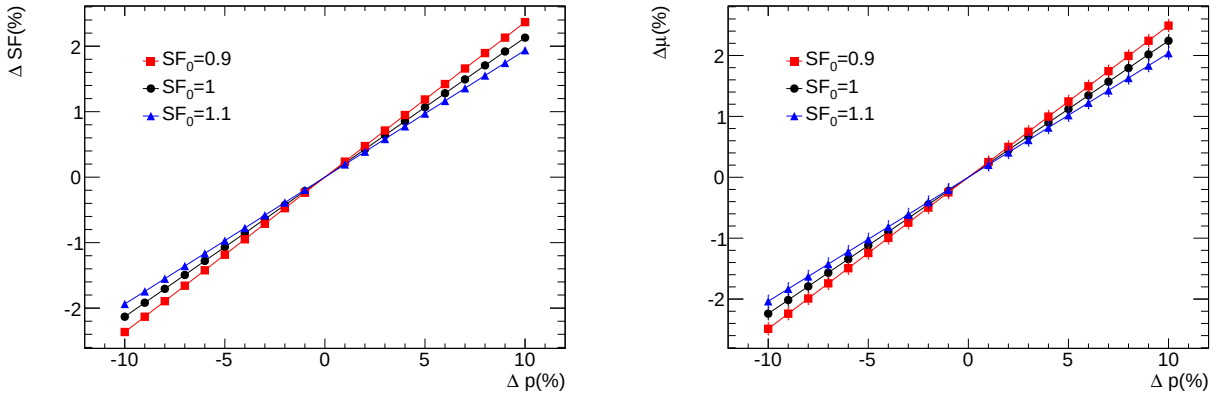

Figure 4.26: Variation of the scale factor (left side) and of the mean value (right side) as a function of the pedestal variation Δp.

From the real data, the estimation of the pedestal in the alpha scan may be wrong by at most 0.35% for the period D (see left plots of Fig. 4.9), such error would imply a shift in the scale factor (or mean value) of $\approx 0.07\%$, a small value but detectable.

About the noise, an example of the distributions $\Delta\mathsf{SF}(\%)$ and $\Delta\mu(\%)$ for a scale factor $\mathsf{SF}_0 = 1$ and a noise variation $\Delta\sigma = 50\%$ is shown in the left side of the Fig. 4.27. The range studied goes from -100% to +100%. Again, the error bars represent the standard deviation of the distributions $\Delta\mathsf{SF}(\%)$ or $\Delta\mu(\%)$ for the given noise variation. As can be seen, the variation in the scale factor is very small: it just changes in only $\approx$0.0006% when 50% of noise is added. The plot of the $\Delta\mathsf{SF}(\%)$ for different values of SF_0 as a function of the noise variation is shown in the right plot of the same figure. In contrast to the pedestal variation, the relation here is not linear. Again, a variation of 10% in SF_0 for noise variations between -50% and +50% would

leave the shift in the scale factor practically unchanged. The effect on the mean value within the range is less than 0.001%, which is undetectable at this level.

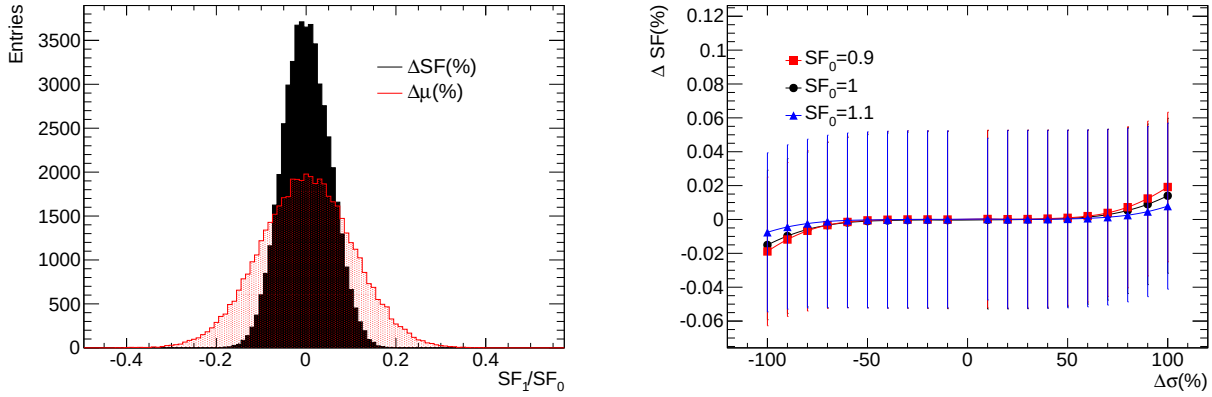

Figure 4.27: Left: an example of the distributions $\Delta\mathsf{SF}(\%)$ and $\Delta\mu(\%)$ for a noise variation $\Delta\sigma = 50\%$. Right: variation of the scale factor as a function of the noise variation.

In the real data, noise variations are smaller than 5% for the period D (see middle plots in Fig. 4.9), which corresponds to a shift in the scale factor of ≈0.0003%, which is completely negligible.

From this study, it is possible to conclude that an approximative knowledge of the pedestal within the range established in Section 4.5.1.1 would have a small but detectable effect on both the scale factor and the mean value. The variations of the noise observed in Section 4.5.1.2 are completely negligible.

4.6.3 Stability of the alpha response from 2011 to 2013

As determined in Section 4.6.1 the scale factor will be the main method to monitor the stability of the alpha spectra. The procedure applied for each alpha scan is described as follows:

1. The reference data is multiplied by a scale factor SF_1. Then, the probability of equality between this distribution and the alpha spectrum extracted from the alpha scan is computed using the Kolmogorov test. The number of recorded events of the reference data is given in the Table 4.3.

Period	Photodiode 1	Photodiode 2	Photodiode 3	Photodiode 4
A	67305	68537	64811	68523
B	123409	123348	125025	125018
C	376322	378869	381486	380250
D	1066460	1074850	1083680	1069270

Table 4.3: Number of recorded events of the reference data used for each period for each photodiode.

2. The previous step is repeated for different values of SF_1 in order to construct a plot of the probability as a function of SF_1. The scan is done with a granularity of 1/10000 from $\mathsf{SF}_1 = 0.99$ to $\mathsf{SF}_1 = 1.01$. One example of this plot is shown in the left side of Fig. 4.28 for an alpha scan taken on March 15^{th}, 2012 for the photodiode 2.

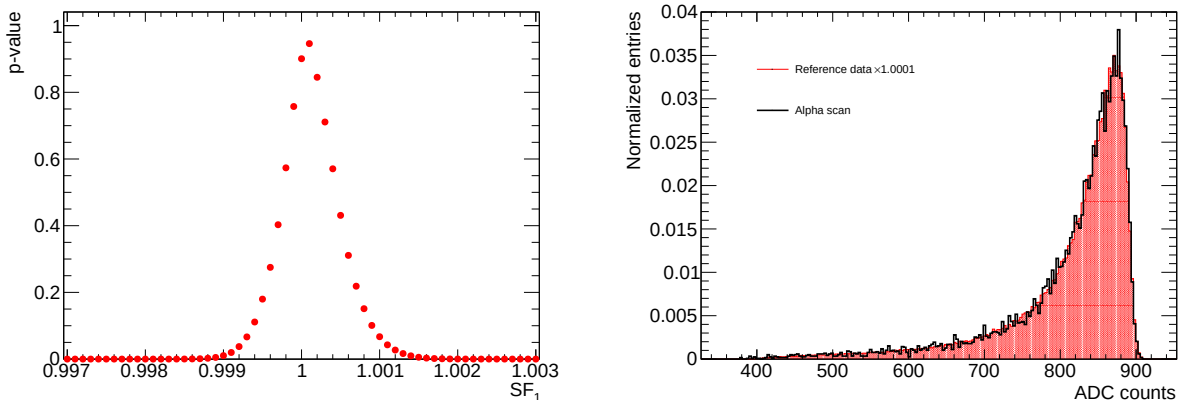

Figure 4.28: Left: One example of the probability as a function of the scale factor SF_1. Right: Comparison between the reference data and the alpha response of the alpha scan for the scale factor with the highest probability extracted from the plot in the left, $\mathsf{SF}_1 = 1.0001$. The alpha scan corresponds to a run taken on March 15^{th}, 2012. The photodiode under study here is the photodiode 2.

3. The scale factor with the highest probability is the best scale factor found for this alpha spectrum. This last value is used to study the stability of the system. For the example shown in the left plot of the Fig. 4.28, this value corresponds to $\mathsf{SF}_1 = 1.0001$. A comparison between the distribution obtained by multiplying the reference data with this scale factor and the alpha scan is shown in the right plot of the Fig. 4.28.

The results obtained for the best scale factor found for each alpha scan taken between 2011 and the first months of 2013, as a function of time, are shown in the Figs. 4.29-4.32 for the photodiodes 1, 2, 3 and 4, respectively. The uncertainty is taken to be the mean value of the distribution of Fig. 4.21(b). Although the scale factor was determined as a better method than the mean value, in order to study its correlation with this last one, the normalized mean value with its statistical uncertainty is also plotted. This normalized mean value is given by the ratio μ_1/μ_0, where μ_1 is the mean value computed from the alpha response in the alpha scan, and μ_0 is the one computed from the reference data. As for the response of the electronics, the changes shown by the scale factor and normalized mean value from one period to another one are due to the hardware interventions, but the exact shapes are not understood. As can be seen from Fig. 4.33, the scale factor and the normalized mean value are well correlated: as long as the scale factor increases, the normalized mean value also increases. The distributions of the probabilities of the scale factors of each photodiode can be seen in Fig. 4.34 and Fig. 4.35, for the periods C and D, respectively. These distributions show that the probability of equality between the alpha scan and the reference data times the best scale factor found is bigger than 0.8 for around the 50% of the runs.

In general, for the periods A-C the scale factor is bigger than one for all photodiodes. For the first two periods, the alpha response has a maximum deviation in the scale factor of 0.6%,

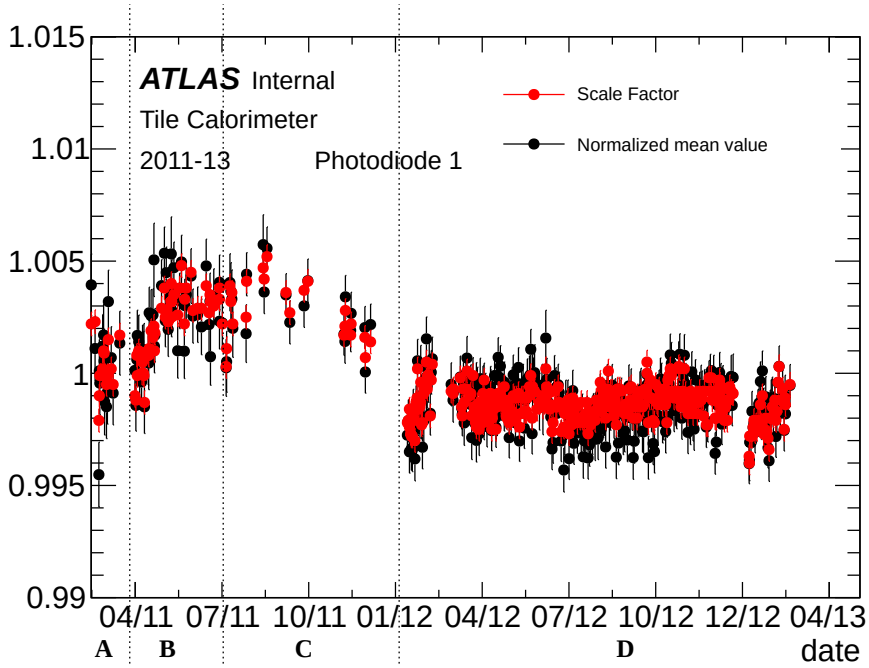

Figure 4.29: Evolution of the scale factor and the normalized mean value for the photodiodes 1 between 2011 and the first months of 2013.

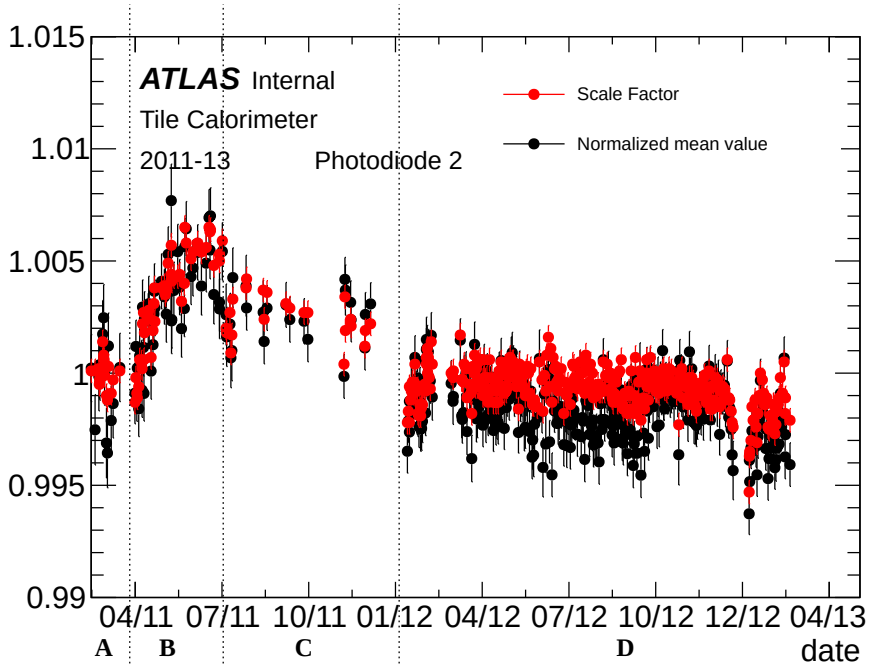

Figure 4.30: Evolution of the scale factor and the normalized mean value for the photodiodes 2 between 2011 and the first months of 2013.

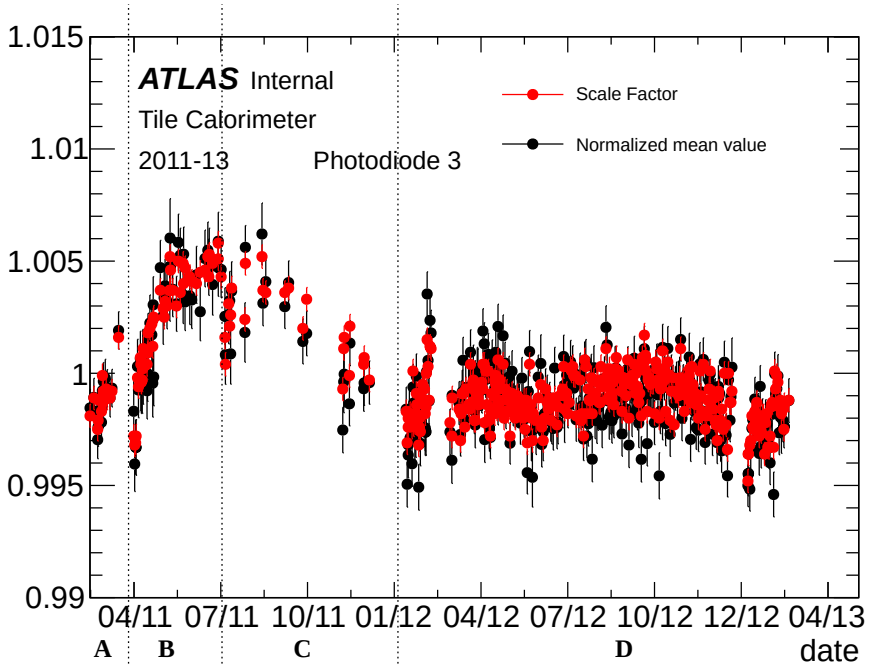

Figure 4.31: Evolution of the scale factor and the normalized mean value for the photodiodes 3 between 2011 and the first months of 2013.

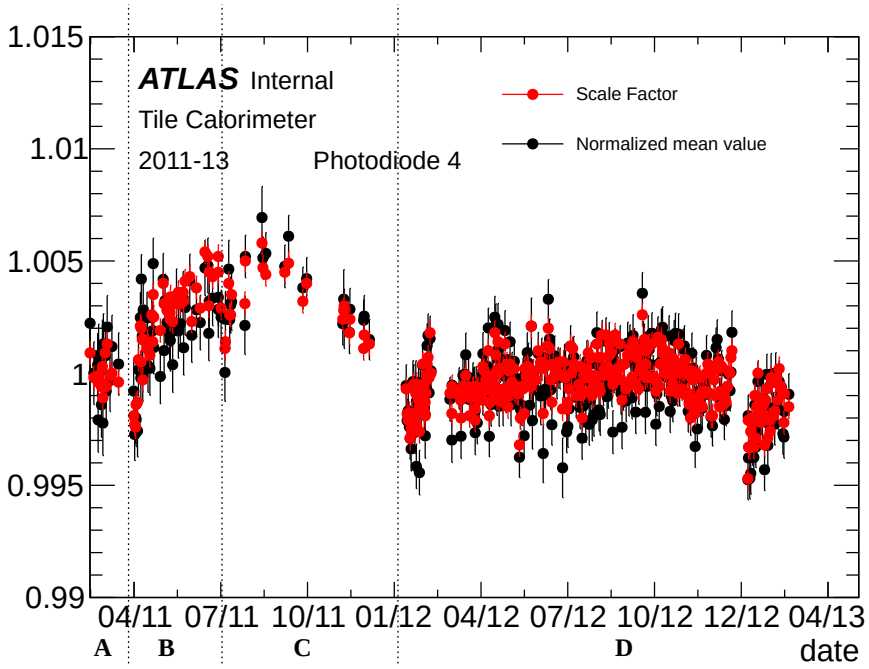

Figure 4.32: Evolution of the scale factor and the normalized mean value for the photodiodes 3 between 2011 and the first months of 2013.

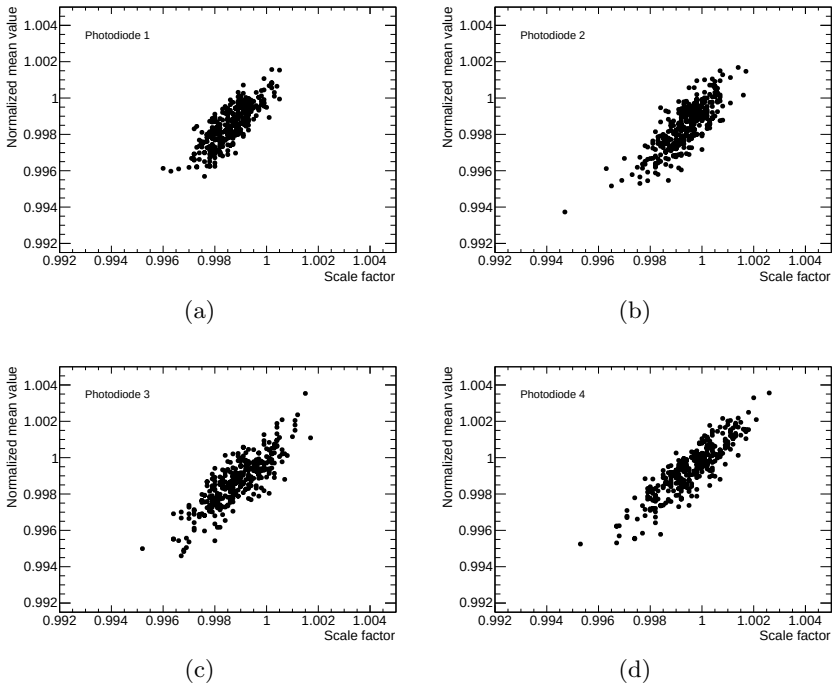

Figure 4.33: Normalized mean value as a function of the scale factor found of the photodiodes 1 (a), 2 (b), 3 (c) and 4 (d) for all the alpha scans taken in the period D.

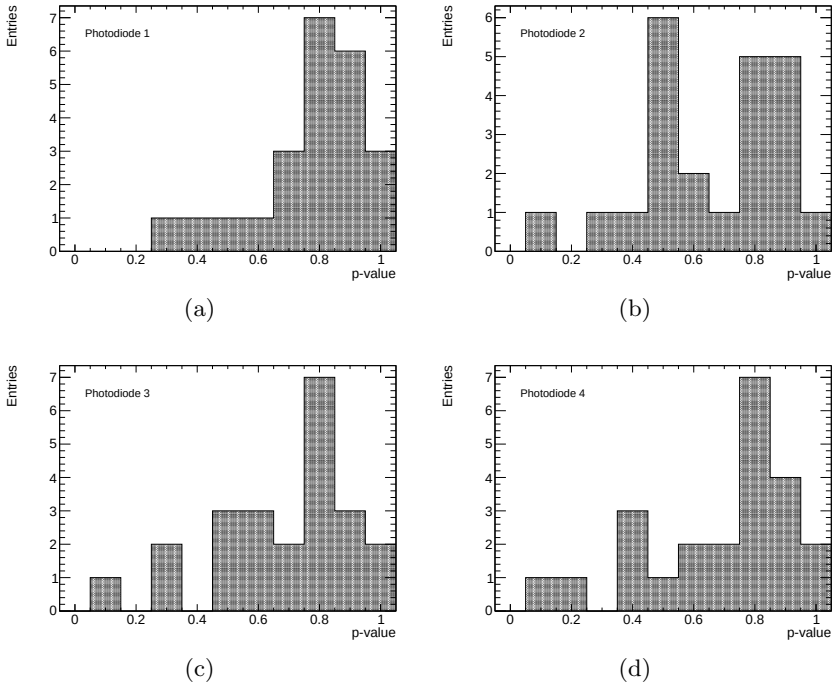

Figure 4.34: Distributions of the probabilities of the scale factors found of the photodiodes 1 (a), 2 (b), 3 (c) and 4 (d) for all the alpha scans taken in the period C.

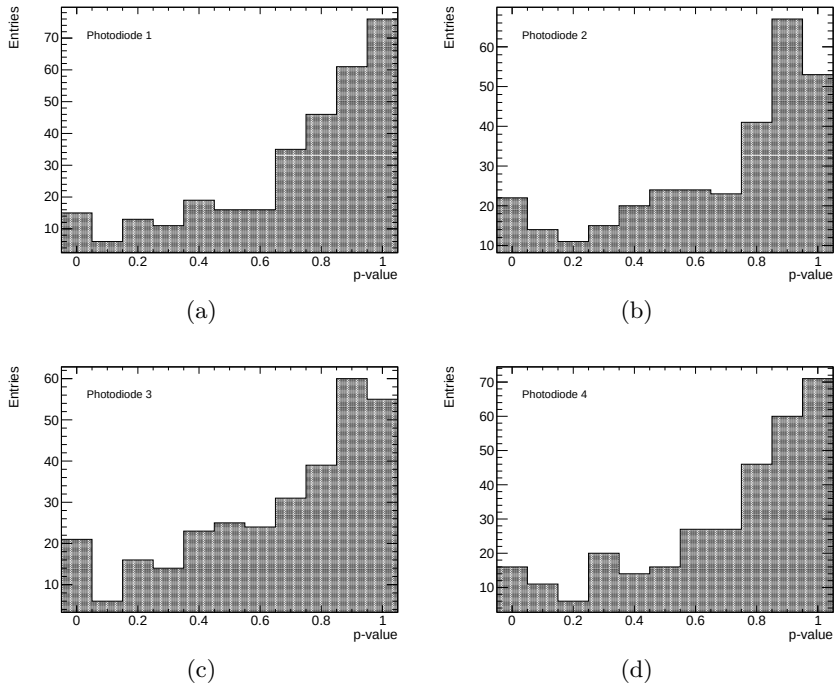

Figure 4.35: Distributions of the probabilities of the scale factors found of the photodiodes 1 (a), 2 (b), 3 (c) and 4 (d) for all the alpha scans taken in the period D.

0.7%, 0.6% and 0.6%, for the photodiodes 1, 2, 3 and 4, respectively (see Figs. 4.29-4.32). A little improvement is seen in the period C for the photodiode 2, where the scale factor is closer to 1 than for the previous periods, with a maximum deviation of 0.5%. However, for the photodiodes 1, 3 and 4, although their stability was within a range of 0.6%, the hardware interventions do not seem to have improved them. The distributions of the scale factors for each photodiode can be seen in Fig. 4.36 for the period C.

In contrast with the periods A-C, the scale factor is slightly smaller than one for all photodiodes (see Fig. 4.37) for the period D. No significant variations were observed in the alpha response during this period, where the scale factor was rather stable with a maximum deviation of 0.4% for the photodiode 1, and 0.5% for the remaining photodiodes (see Figs. 4.29-4.32). It represents a slight improvement with respect to the period C.

As stated in Section 4.6.2, pedestal variations can introduce small variations in both the scale factor and the mean normalized value, with the same bias for both methods. From the real data, the estimation of the pedestal in the alpha scan may be wrong by at most 0.35%. Such error would imply a shift in the scale factor or normalized mean value of $\approx 0.07\%$, a small value but detectable, and which can explain around 14% of the variation in the scale factor for the data taken in the period D. Uncontrolled noise variations of around 5% were found in the data, and as it was shown in Section 4.6.2, variations of this order do not affect the scale factor.

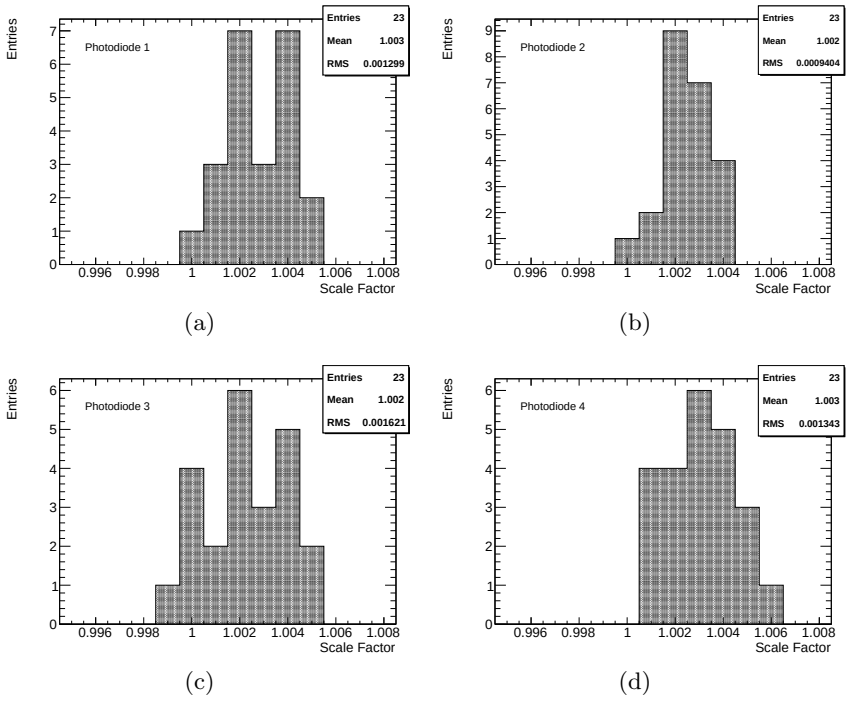

Figure 4.36: Distributions of the scale factors of the photodiodes 1 (a), 2 (b), 3 (c) and 4 (d) for all the alpha scans in the period C.

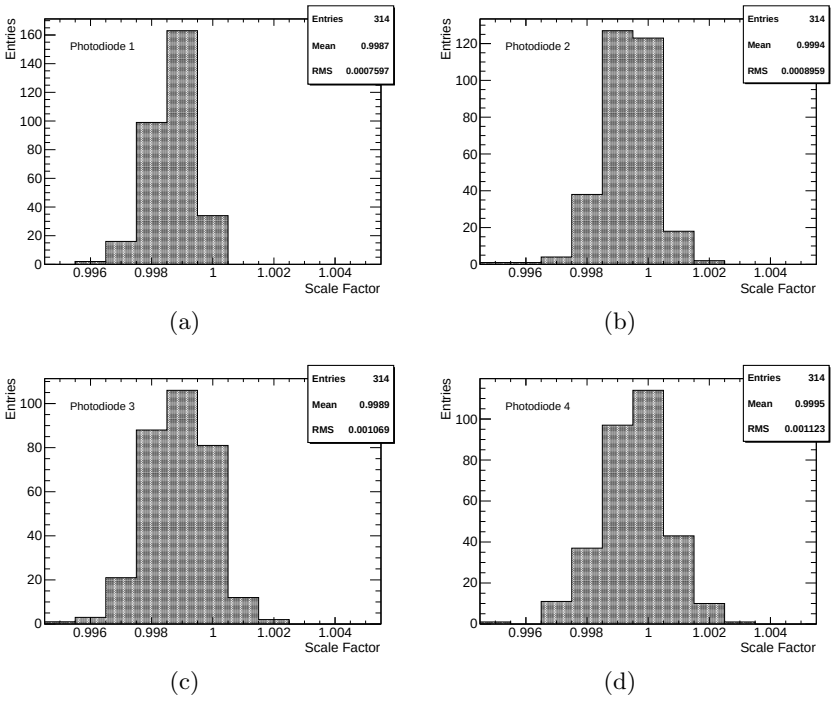

Figure 4.37: Distributions of the scale factors of the photodiodes 1 (a), 2 (b), 3 (c) and 4 (d) for all the alpha scans in the period D.

4.6.4 Summary: stability of the alpha response

It was demonstrated that the scale factor –via the Kolmogorov test– is a more sensitive method than the mean value in order to study the stability of the alpha response, which was stable with a maximum deviation of 0.5% for all the data taken in 2012 and the first months of 2013. It represents a slight improvement with respect to the year 2011.

It was also found that an uncontrolled pedestal variation for this period explains only a very small part of the variation in the scale factor. The noise variation is completely negligible.

Finally, it was observed that the scale factor and the normalized mean value are well correlated for all photodiodes.

4.7 Summary and conclusions

A precise knowledge of the photodiodes response is the first step towards the understanding of the LASER system. In order to monitor the stability of the photodiodes it is essential to understand their readout electronics, as well as the stability of the alpha response.

The stability of the photodiodes was monitored using data taken between 2011 and the first months of 2013. This monitoring activity has been split in four different periods, where two periods are separated by a hardware intervention. For all photodiodes, the mean pedestal is much more stable after the intervention made at the end of the period B. That means that the pedestal of each photodiode is no longer affected by the signal on the other ones: the cross-talk among the photodiodes has been dramatically reduced by the July, 2011 hardware intervention. Now, the pedestal in the alpha scan is well understood, i.e. it is possible to safely perform the pedestal subtraction to study the alpha spectra.

The noise was significantly reduced by the various interventions. On the other hand, the value measured in the alpha scans was a few percent higher than in the pedestal runs during the periods A-C. It could be related to the alpha source motor, since it could introduce additional noise to the response of the electronics. In order to solve this problem, an intervention on December 5th, 2011 was done. Since then, the alpha source motor is powered off when the source is in front of the photodiodes. Now the noise extracted from the pedestal in the alpha scans is closer to the one extracted from the pedestal runs, meaning that the noise is under control for all photodiodes after this intervention.

The response of the photodiodes electronics was also found to be linear. However, there is a shift in the injected charge pedestal that is not understood. This shift is estimated to be around 25% and it has been observed since June 2008. Nevertheless it does not affect the photodiodes themselves, and its effect in the LASER calibration is negligible.

It was demonstrated that the scale factor is a more precise method than the mean value. From the beginning of 2012, the worst observed variation in the photodiode gain was 0.5% which is within the acceptable variations for the photodiodes system. Following the studies done about the effects on the scale factor and mean value of variations in the readout electronics characteristics, it was found that pedestal or noise variations are not sufficient to explain the variations found in the scale factor.

As a general conclusion, the change of the motherboard inside the photodiodes box had a big effect in the system by making it much more stable. Moreover, the photodiodes absolute response is stable within a range of 0.5%. This value could be added as a systematic uncertainty on the computation of the LASER constants, which would be propagated on the TileCal energy

and then to the jet energy. However, the LASER constants include a correction factor term to compensate light instabilities that occur at the level of the light mixing. A variation in the response of the photodiode in time is seen as a light instability and is compensated with a precision of 0.3%. Thus, 0.5% of variation in the alpha response should not affect the LASER constants and therefore the impact in the jet energy should be negligible. However, if there is no compensation for the light instabilities, a systematic uncertainty of 0.5% on the LASER constants would bias the energy measurement in TileCal by the same magnitude. In 2012 only 10% of the TileCal channels were corrected. As it contributes by a mean factor of 0.3 to the energy of the jets, a bias of 0.5% of the alpha response would represent a bias in the jet energy of 0.015%.

For the next LHC run, the LASER calibration system will be replaced by the LASER II. The laser light will be measured by ten photodiodes, which will be calibrated with a light-emitting-diode (LED). An additional photodiode will be used as a reference to measure the light of the LED, which will be monitored by an alpha source. In that sense, the studies presented in this thesis will be useful for the LASER II calibration system.

Chapter 5

Analysis overview

This thesis describes the search for New Physics in events with 4 top quarks using the data collected during 2011 and a part of 2012 by the ATLAS experiment at the LHC in pp collisions at $\sqrt{s} = 7$ TeV and 8 TeV.

This analysis follows the approach presented in Ref. [13] and described in Section 1.5.1.3. It consists of searching for the experimental signature of a four right-handed top quark contact interaction, where only the contact interaction operator with right-handed top quarks is considered, as left-handed top operators are already strongly constrained by electroweak precision data [77]. The contact interaction is an effective (non-renormalizable) operator which is not specific to a particular BSM theory. For that reason, this analysis does not test a particular theory but rather a class of theories where new physics manifests itself at low energy as a four right-handed top contact interaction. This is the case of theories predicting new heavy vector particles strongly coupled to the right handed top such as top compositeness [73, 72, 11] or Randall-Sundrum theories [67]. Many of these new physics theories predict an enhanced rate for events containing four top quarks with respect to the Standard Model production, which is very small at 7 or 8 TeV (~ 1 fb at 8 TeV [51]). Therefore, searching for events containing four top quarks could open a window on new physics phenomena which do not affect the $t\bar{t}$ production for which no deviation from the SM expectations has been observed so far. Moreover, there is no published result on the experimental search for the production of events containing four top quarks.

The four tops decay topology considered in this analysis corresponds to events with two isolated leptons (electrons or muons[1]) with the same electric charge, including contributions from $\tau \to e$ and $\tau \to \mu$. The signature will then be two leptons of the same electric charge in addition to missing transverse momentum from the neutrinos and several jets. Moreover, among the jets of these events, it is expected to have at least one jet arising from a b quark (see Section 1.3.2). The branching fraction of this topology is smaller than the one for the most hadronic (see Section 1.3.2). However, it is experimentally favored since the presence of two same-sign leptons in the final state allows to reduce the background coming from Standard Model processes, since this kind of event is rarely produced in the Standard Model. On the other

[1]The τ particles are not directly considered, since taus are more difficult to identify.

hand, it has potentially large contributions from new phenomena. Once the decay topology has been chosen, the events are grouped depending on the flavor of each charged lepton in the event. This way they are classified as $e^{\pm}e^{\pm}$, $e^{\pm}\mu^{\pm}$ or $\mu^{\pm}\mu^{\pm}$ channel.

Backgrounds to this search arise from two principal sources: SM production of same-sign lepton pairs, and instrumental backgrounds where objects are mis-identified or mis-reconstructed such that they appear to have the same-sign final state. The former is estimated from simulated samples and includes WZ and ZZ production in association with jets, $W^{\pm}W^{\pm}jj$ production and $t\bar{t}+W/Z/W^{+}W^{-}$ production. The latter is estimated using data-driven techniques and includes the events that contain two leptons of opposite charge –where one of the charges has been mis-measured–, and events with mis-reconstructed leptons. Both sources of background have been estimated and validated in control regions which are orthogonal to the signal selection.

Different systematic uncertainties are taken into account in this analysis. They are classified depending on the samples that they are affecting. This way, there are uncertainties affecting the Monte Carlo samples and the data-driven background.

The final selection has been optimized by aiming at minimizing the expected upper limit on the four tops production cross-section in the case no signal is discovered. After the final selection, the signal region has been analyzed by looking for an excess of events with respect to the predicted background. No excess of events has been observed, and the observed and predicted yields have been used to derive upper limits on the four tops production cross-section for the signal studied. This limit is then translated to an upper limit on the coupling strength C/Λ^2 of the contact interaction operator with right-handed top quarks. The upper limit on the four tops production cross-section in the Standard Model is also placed using the same final selection.

The data and Monte Carlo samples used in the analysis, together with the description of the physics objects identification, the event preselection and the identification of the discriminant variables are given in Chapter 6. The estimation of the background is described in Chapter 7. Finally, the final selection, the different systematic uncertainties and the results are presented in Chapter 8.

Chapter 6

Data and event preselection

Contents

6.1 Introduction

This chapter has been dedicated to the presentation of the data and Monte Carlo samples used in the analysis, including the signal simulated samples. A preselection of events is carried out based on the standard/quality selection applied to the top physics. This preselection also takes into account the corresponding final state of the signal studied. After the event preselection the discriminant variables of the analysis are identified.

The data and Monte Carlo samples are presented in Section 6.2. This is followed by the description of the physics objects identification in Section 6.3. The requirements of the event preselection are presented in Section 6.4. Finally, the discriminant variables of the analysis are defined in Section 6.5.

6.2 Data and Monte Carlo samples

The analysis presented in this thesis makes use of the data collected by the ATLAS experiment in 2011 and a part of 2012, as well as simulated data samples for both the signal and background processes. The data used and the Monte Carlo samples are detailed in this section.

6.2.1 Data sample

The measurements presented here are based on proton-proton collision data collected with the ATLAS detector at the CERN LHC between March and December 2011 at a center-of-mass energy of $\sqrt{s} = 7$ TeV, and between March and September 2012 at $\sqrt{s} = 8$ TeV. The data were collected by using an unprescaled single electron or muon trigger. The trigger signatures varied among the different data taking periods as shown in Table 6.1.

Data period	$\mathcal{L}$ [pb^{-1}]	Electron	Muon
B-I (2011)	1465	EF_e20_medium	EF_mu18
J (2011)	226	EF_e20_medium	EF_mu18_medium
K (2011)	590	EF_e22_medium	EF_mu18_medium
L-M (2011)	2432	EF_e22vh_medium1 or EF_e45_medium1	EF_mu18_medium
A-G (2012)	14300	EF_e24vhi_medium1 or EF_e60_medium1	EF_mu24i_tight or EF_mu36_tight

Table 6.1: Electron and muon triggers used in the different data periods in 2011 and 2012.

The "i" in the name of the trigger indicates the requirement of lepton isolation. For the muon, it means a cut at event filter level on $p_{\mathrm{T}}^{\mathrm{cone20}} < 0.12 p_{\mathrm{T}}^{\mu}$, where $p_{\mathrm{T}}^{\mathrm{cone20}}$ is the p_{T} sum, in a cone $\Delta R = 0.2$ around the muon track, of inner detector tracks having $p_{\mathrm{T}} > 1$ GeV and $|z_0^{\mu} - z_0^{\mathrm{track}}| < 6$ mm, excluding the muon track itself, and p_{T}^{μ} is the muon p_{T}. For the electron, it means a requirement on track isolation at event filter level of $p_{\mathrm{T}}^{\mathrm{cone20}} < 0.10 E_{\mathrm{T}}^{e}$, where E_{T}^{e} is the electron E_{T}. The "v" stands for varied threshold and it is a coarse dead material correction applied on a single L1 EM trigger threshold. The "h" is a cut on the hadronic core isolation at L1 trigger of less than 1 GeV.

The dataset corresponds to a total integrated luminosity of approximately 4.7 ± 0.2 fb^{-1} at $\sqrt{s} = 7$ TeV, and 14.3 ± 0.5 fb^{-1} at $\sqrt{s} = 8$ TeV after the trigger selection and applying the standard Top Good Run list[1] [115, 125].

6.2.2 Monte Carlo samples

In order to develop and validate the analysis, Monte Carlo simulation samples have been used. The simulated samples were generated either with CTEQ6L1 [126], MSTW2008LO [127] or CT10 [128] parton distribution functions (PDF) at $\sqrt{s} = 7$ TeV and 8 TeV. The generation of the simulated samples includes the effect of multiple *pp* interactions per bunch crossing, and also the effect of the detector response to collisions from bunch crossings before or after the one containing the hard interaction. Events are reweighted so that the distribution of the number of *pp* collisions occurring in addition to the hard scatter process matches that in data. The detector response was modeled using either a GEANT4 [129] simulation or a faster simulation (ATLFASTII [130]) that combined GEANT4 simulation of the inner tracker and of muons with a fast simulation of

[1]Good Run Lists (GRLs) are used to define a set of data taking runs and luminosity blocks, for which the data are found to be of good enough quality for further analysis. They are formed by applying the appropriate Data Quality (DQ) criteria to the whole list of all physics runs and luminosity blocks and test which parts of data pass them. The criteria are characterized by the Data Quality status flags [124]. These flags identify faults in the detector operation. They vary from detector conditions and are filled for each sub-detector and for each luminosity block. Each analysis uses a GRL to reject those events affected by issues in the relevant subdetectors. The GRLs ensures that all the elements of the detector needed for object reconstruction were operating properly.

shower development in the calorimeter. These samples are then reconstructed with the same algorithms used as for data. The simulated response is corrected for the small differences in efficiencies, momentum scales, and momentum resolutions between data and simulation, using scale factors and smearing techniques.

6.2.2.1 Signal process

The four tops signal ($t\bar{t}t\bar{t}$) has been generated at $\sqrt{s} = 7$ (resp. 8) TeV using a MADGRAPH v5.1.3.2 (resp. v5.1.3.33) [131] model provided by the authors of Ref. [13], and showered and hadronized with PYTHIA v6.425 (resp. v8.165) [132, 133]. In this model, the contact interaction is not directly implemented. Instead, a new heavy colorless vector particle (ρ) coupling to the right-handed component of the top quark is introduced. This model has therefore two additional parameters to those in the SM: the mass of ρ (M_ρ), and the coupling constant between the top quark and ρ (g_ρ). The values of these new parameters are arbitrary, but in order to be in the contact interaction regime, M_ρ has to be set to a high value. In this regime, the four top production depends only on the ratio of these two parameters, which are related to the coupling strength by $C/\Lambda^2 = -g_\rho^2/(2M_\rho^2)$. There is thus a unique free parameter: C/Λ^2. The values used in this analysis are the same as the ones used in [13]: $g_\rho = 100\sqrt{8\pi}$ and $M_\rho = 100$ TeV. It corresponds to a value of $C/\Lambda^2 = -4\pi$ TeV^{-2}. For this choice, the production cross-section computed by MADGRAPH at LO is 12.6 fb at 7 TeV and 42.2 fb at 8 TeV. At this point, it is important to remark that only the cross section depends on these parameters, while the event kinematics does not, as long as the parameters leave the model in the contact interaction regime (see Appendix A.1 for a demonstration). This way, the acceptance computed using these values does not need to be calculated for other values of the parameters M_ρ and g_ρ, and can be used to set a limit on the four tops production cross-section, or equivalently on C/Λ^2. However, when M_ρ is not large enough to be in the contact interaction regime the signal acceptance does not change dramatically (see Appendix A.2). It means that this analysis is thus also sensitive to such low M_ρ scenarios.

The interference between the SM and the new physics process described above has been found to be negligible [13]. Only new physics events have therefore been generated and included in the signal sample. The renormalization and factorization scales have been set to $4m_t$, where m_t is the top quark mass. All W decays are included. The number of generated signal events is 100 000 at 7 TeV and 165 000 at 8 TeV.

Since the four top quarks process has never been observed, even in Standard Model production, it is also interesting to set a limit on this process. Therefore, a sample of Standard Model four tops has been generated at 8 TeV using the same setup as for the contact interaction, and removing, of course, the non-Standard Model operators. All the information related to the signal samples is summarized in Table 6.2.

6.2.2.2 Same-sign dilepton background processes

As mentioned in Chapter 5, several background processes can contribute to the final state of same-sign dilepton events. They are estimated either from data or from simulated samples. The one estimated from data corresponds to the false same-sign dilepton pairs, and includes the $t\bar{t}$ production, $W + jets$, single top quark, and other processes which are not included in the Monte Carlo samples, because they are already included here. It comes from the lepton charge

$\sqrt{s}$ [TeV]	Process	Generator	PDF	σ [fb]	$\mathcal{L}$ [fb^{-1}]	Det. Sim.
7	Contact inter.	MadGraph5	CTEQ6L1	12.6	7 936	Geant4
8	Standard Model	MadGraph5	MSTW2008LO	0.685	291 780	Geant4
8	Contact inter.	MadGraph5	MSTW2008LO	42.2	3 906	Geant4

Table 6.2: Monte Carlo samples for the various four top quarks signals together with their generators, PDFs, cross-sections, integrated luminosities and detector simulation. All decays of the W bosons (leptonic and hadronic) are included.

mis-identification (called here *Q mis-id*), and mis-reconstructed leptons (called here *fakes*). This section only lists the samples and the corresponding generation of these background processes which are estimated from simulations. A full description of the whole background, sources and estimation, is given in Chapter 7.

Background coming from diboson and $t\bar{t} + W/Z/W^+W^-$ processes is estimated from simulations. The Monte Carlo samples are generated as explained below:

- Diboson production:
  - WZ and ZZ were generated at 7 TeV at LO using Alpgen v2.13 [134], accounting for hard emission of up to three patrons (Np), and Herwig v6.53 [135] with Jimmy v4.31 [136] to describe the soft emission, showering and hadronization. At 8 TeV, these samples were generated at LO using Sherpa v1.4.0 [137], where the accepted vector boson decays were restricted to $WW \to \ell\ell\ell\nu$ and $ZZ \to \ell\ell\ell\ell$ with all three generations of leptons allowed. In both cases, the cross-sections are normalized to NLO theoretical calculations computed with MC@NLO v3.41 [138];
  - $W^{\pm}W^{\pm}jj$ was generated at LO with Madgraph v4.4 [139] at 7 TeV and v5.1 at 8 TeV. It was showered and hadronized with Pythia [132]. The cross-section calculated by Madgraph is not rescaled.
- $t\bar{t}W(+jets)$, $t\bar{t}Z(+jets)$ and $t\bar{t}W^+W^-$ were generated at 7 and 8 TeV with Madgraph v5.1. They were showered and hadronized with Pythia. Cross-sections for the $t\bar{t}W/Z(+jets)$ are rescaled to NLO calculations [140, 141].

The Monte Carlo background samples with their corresponding generators, PDFs, cross-sections, K-factors, integrated luminosities and detector simulation are shown in Tables 6.3 and 6.4 for the analysis done at 7 and 8 TeV, respectively.

6.3 Object reconstruction

The information recorded by the detector needs to be processed in order to reconstruct the physical objects that will be used in the different analyses. This information comes mainly from hits and energy depositions that particles generated in the collision leave in the detector. After the pp collision, the primary vertex is identified as the vertex with the highest summed track p_{T}^2, each having $p_{\mathrm{T}} > 0.4$ GeV, and the physics objects are reconstructed as candidates for jets, electrons and muons. These physics objects are required to satisfy the following criteria:

Process	Generator	PDF	σ [pb]	K-factor	$\mathcal{L}$ [fb^{-1}]	Det. Sim.
WZ Np0	Alpgen+Jimmy	CTEQ6L1	0.67	1.28	70	Geant4
WZ Np1	Alpgen+Jimmy	CTEQ6L1	0.41	1.28	76	Geant4
WZ Np2	Alpgen+Jimmy	CTEQ6L1	0.22	1.28	69	Geant4
WZ Np3	Alpgen+Jimmy	CTEQ6L1	0.10	1.28	164	Geant4
ZZ Np0	Alpgen+Jimmy	CTEQ6L1	0.51	1.30	60	Geant4
ZZ Np1	Alpgen+Jimmy	CTEQ6L1	0.23	1.30	66	Geant4
ZZ Np2	Alpgen+Jimmy	CTEQ6L1	0.09	1.30	174	Geant4
ZZ Np3	Alpgen+Jimmy	CTEQ6L1	0.03	1.30	245	Geant4
$W^{\pm}W^{\pm}jj$	Madgraph+Pythia	CTEQ6L1	0.22	1	433	Geant4
$t\bar{t}W$	Madgraph+Pythia	CTEQ6L1	0.082	1.2	2041	Geant4
$t\bar{t}Wj$	Madgraph+Pythia	CTEQ6L1	0.063	1.2	2628	Geant4
$t\bar{t}Z$	Madgraph+Pythia	CTEQ6L1	0.050	1.3	3089	Geant4
$t\bar{t}Zj$	Madgraph+Pythia	CTEQ6L1	0.055	1.3	2802	Geant4
$t\bar{t}W^{+}W^{-}$	Madgraph+Pythia	CTEQ6L1	0.001	1	80064	Geant4

Table 6.3: Monte Carlo samples used for the background estimation at $\sqrt{s} = 7$ TeV together with their generators, PDFs, cross-sections, K-factors (the rescaling factor between LO and NLO cross sections), integrated luminosities and detector simulation.

Process	Generator	PDF	σ [pb]	K-factor	$\mathcal{L}$ [fb^{-1}]	Det. Sim.
$WZ \to \ell\ell\ell\nu$	Sherpa	CT10	9.75	1.06	261	Geant4
$ZZ \to \ell\ell\ell\ell$	Sherpa	CT10	8.73	1.11	186	Geant4
$W^{\pm}W^{\pm}jj$	Madgraph+Pythia	MSTW2008LO	0.369	1	528	AtlFastII
$t\bar{t}W$	Madgraph+Pythia	CTEQ6L1	0.104	1.18	3270	Geant4
$t\bar{t}Wj$	Madgraph+Pythia	CTEQ6L1	0.053	1.18	7493	Geant4
$t\bar{t}Wjj$	Madgraph+Pythia	CTEQ6L1	0.041	1.18	9638	Geant4
$t\bar{t}Z$	Madgraph+Pythia	CTEQ6L1	0.068	1.34	4409	Geant4
$t\bar{t}Zj$	Madgraph+Pythia	CTEQ6L1	0.045	1.34	8819	Geant4
$t\bar{t}Zjj$	Madgraph+Pythia	CTEQ6L1	0.040	1.34	10050	Geant4
$t\bar{t}W^{+}W^{-}$	Madgraph+Pythia	MSTW2008LO	0.002	1	91730	AtlFastII

Table 6.4: Monte Carlo samples used for the background estimation at $\sqrt{s} = 8$ TeV together with their generators, PDFs, cross-sections, K-factors (the rescaling factor between LO and NLO cross sections), integrated luminosities and detector simulation.

- **Jets:** They are reconstructed in the calorimeter from topological clusters[2] using the anti-k_t algorithm [142] with a radius $R = 0.4$, and calibrated to the hadronic energy scale using p_{T}- and η-dependent corrections[3]. They are required to have $p_{\mathrm{T}} > 25$ GeV and $|\eta| < 2.5$. In order to avoid reconstructing electrons as jets, the closest jet within a cone of radius $\Delta R(\mathrm{jet}, e) = 0.2$ from an electron passing the electron selection quality cuts is removed (both probably correspond to the same object). Jets without any associated track are also accepted. To reject events from pileup, a quantity called jet-vertex-fraction (JVF) has been used. It corresponds to the ratio of the sum of the p_{T} of all tracks, with $p_{\mathrm{T}} > 0.4$ GeV, within the jet that originate from the primary vertex associated with the hard-scattering collision, over the sum of the p_{T} of all tracks matched to the jet. Jets selected have to satisfy a $|\mathrm{JVF}| > 0.75$ (resp. 0.5) at 7 (resp. 8) TeV.

- **b-jets:** There are different b-tagging algorithms in ATLAS. They exploit the fact that B mesons have a long lifetime and can travel a few mm in the detector before decaying. This way, a certain number of tracks point to a secondary vertex instead of pointing to the reconstructed primary vertex. The impact parameters of these tracks are large. Thus, there are algorithms based on the impact parameter (`IP3D`), on the secondary vertex (`SV1`) and on the decay chain reconstruction (`JetFitter`). A multivariate b-tagging algorithm [144] at an operating point of 70% efficiency for b-jets in $t\bar{t}$ events is used in this analysis to select jets from the decay of heavy flavor hadrons. This is a neural network-based algorithm that uses the output weights of `IP3D`, `SV1` and `JetFitter` as inputs. The operating point corresponds to a mis-tag rate of less than 1%, as determined in simulated $t\bar{t}$ events.

- **Electrons:** Candidate electrons are identified by means of a shower in the EM calorimeter consistent with expectation, as well as a good quality track pointing to the cluster in the calorimeter. They are required to have a transverse energy $E_{\mathrm{T}} > 25$ GeV and satisfy the Tight ATLAS electron criteria [145]. They have to fall in a well instrumented region of the detector, i.e. $|\eta_{\mathrm{cluster}}| < 2.47$, excluding the calorimeter transition region $1.37 < |\eta_{\mathrm{cluster}}| < 1.52$. Isolation cuts are also imposed such that the efficiency of each isolation requirement is 90%. These cuts depend on the transverse energy in a cone $\Delta R = 0.2$ around the electron ($E_{\mathrm{T}}^{\Delta R=0.2}$), and on the total transverse momentum of all tracks within $\Delta R = 0.3$ of the electron ($p_{\mathrm{T}}^{\Delta R=0.3}$). At 7 (resp. 8) TeV, the values used in the cuts range from 1.4 (resp. 1.08) GeV to 3.7 (resp. 2.7) GeV for $E_{\mathrm{T}}^{\Delta R=0.2}$, and from 1 (resp. 0.9) GeV to 1.05 (resp. 1.15) GeV for $p_{\mathrm{T}}^{\Delta R=0.3}$. Electrons within a cone $\Delta R(e, \mathrm{jet}) = 0.4$ of a reconstructed jet are removed. At 8 TeV, the track is required to be consistent within 2 mm in z with the reconstructed primary vertex of the event, and a hit in the innermost layer of the inner detector is also required, for active modules, to reject electrons from conversions.

- **Muons:** Candidate muon tracks are required to be well measured in both the inner detector and the muon spectrometer. They have to pass the ATLAS muon quality cuts [146]. Muons are required to fall within $|\eta| < 2.5$ and to satisfy a $p_{\mathrm{T}} > 20$ (resp. 25) GeV at 7 (resp. 8) TeV. As for the electrons, isolation cuts are also applied. At 7 TeV, they require a transverse energy within a cone $\Delta R = 0.2$ along the direction of the muon candidate to

[2]Topological clusters algorithm or topoclusters is one of the two different cells clustering algorithms used by ATLAS. They are a dynamically formed combination of cells around seed cells that exceed a given signal-to-noise ratio threshold, and which are used as inputs for the jet reconstruction algorithm.

[3]The corrections are derived from collision and test-beam data as well as simulation [143].

be less than 4 GeV, and a total transverse momentum of all tracks within $\Delta R = 0.3$ to be less than 2.5 GeV. At 8 TeV, muon candidates are required to be isolated from other central track activity within a cone with radius that decreases with increasing muon p_{T}: $\Delta R = 0.4/(p_{\mathrm{T}}/10\ \mathrm{GeV})$. The summed p_{T} of all tracks (other than the muon track) in that cone is required to be less than 5% of the muon p_{T}. Muons are also required to have $\Delta R(\mu, \mathrm{jet}) > 0.4$ from any jet. Events with an electron candidate that shares a track with a muon candidate are rejected. Cosmic rejection of muons is also applied when the angle between two muons in the transverse plane satisfies $\Delta\phi(\mu_1, \mu_2) > 3.1$ rad.

- **Missing transverse momentum ($E_{\mathrm{T}}^{\mathrm{miss}}$):** The $E_{\mathrm{T}}^{\mathrm{miss}}$ reconstruction includes contributions from energy deposits in the calorimeters and muons reconstructed in the muon spectrometer as [147]:

$$E_{x(y)}^{\mathrm{miss}} = E_{x(y)}^{\mathrm{miss,calo}} + E_{x(y)}^{\mathrm{miss},\mu}. \tag{6.1}$$

It uses calorimeter cells calibrated according to the reconstructed physics object to which they are associated in a chosen order: electrons, photons, hadronically decaying τ-leptons, jets and muons. Cells not associated with any such objects are also taken into account ($E_{\mathrm{T}}^{\mathrm{miss,CellOut}}$). Thus, the calorimeter term is computed as:

$$E_{x(y)}^{\mathrm{miss,calo}} = E_{x(y)}^{\mathrm{miss,e}} + E_{x(y)}^{\mathrm{miss},\gamma} + E_{x(y)}^{\mathrm{miss},\tau} + E_{x(y)}^{\mathrm{miss,jets}} + E_{x(y)}^{\mathrm{miss,softjets}} + (E_{x(y)}^{\mathrm{miss,calo},\mu}) + E_{x(y)}^{\mathrm{miss,CellOut}}, \tag{6.2}$$

where each term is calculated from the negative sum of calibrated cell energies inside the corresponding objects.

The $E_{\mathrm{T}}^{\mathrm{miss}}$ muon term is computed from the momenta of the muon tracks reconstructed with $|\eta| < 2.7$:

$$E_{x(y)}^{\mathrm{miss},\mu} = -\sum_{\mathrm{muons}} p_{x(y)}^{\mu}. \tag{6.3}$$

6.4 Preselection of events

The preselection of events is based on the standard/quality selection applied for studies of top quark physics in ATLAS. It is applied basically to clean-up the samples and to select the events corresponding to the final state of the signal studied. In this analysis, the final state of four top quarks has to contain at least one lepton pair with the same electric charge, missing transverse momentum ($E_{\mathrm{T}}^{\mathrm{miss}}$) due to the presence of neutrinos, and large jet multiplicity, including b-jets. All the selected events have to satisfy the following requirements:

1. Events in data are required to pass the 2011 (resp. 2012) Good Run List selection defined by the ATLAS Top Group for the data collected at $\sqrt{s} = 7$ (resp. 8) TeV.

2. One primary vertex determined from at least five tracks, each with $p_{\mathrm{T}} > 0.4$ GeV, is required. If there are multiple vertices reconstructed, the vertex with the largest sum of the squared transverse momenta of its associated tracks is taken as the primary vertex.

3. Events with noise bursts and data integrity errors in the LAr and TileCal calorimeter are rejected.

4. For the analysis performed with the setup of $\sqrt{s} = 7$ TeV, events must contain at least two isolated leptons of the same electric charge. In events with more than one same-sign pair, the pairs are sorted according to the leading lepton p_{T}, then by the subleading lepton p_{T}. The first pair is chosen. At $\sqrt{s} = 8$ TeV, events with exactly two leptons of the same electric charge are required. The leading lepton of the pair is required to have $p_{\mathrm{T}} > 25$ GeV. In this step of the analysis, the events are classified in three channels: ee, $e\mu$ and $\mu\mu$, depending on the selected lepton flavors.

5. At least one of the selected leptons must match the one that triggered the readout of the event as shown in Table 6.1.

6. In the ee and $\mu\mu$ channels, the invariant mass of the selected leptons must exceed 15 GeV and be out of the Z-boson mass region, i.e. $|m_{\ell\ell} - m_Z| > 10$ GeV.

7. At least two jets are required, including at least one b-tagged jet.

8. The missing transverse momentum must satisfy $E_{\mathrm{T}}^{\mathrm{miss}} > 40$ GeV.

9. The scalar sum of the p_{T} of all leptons and jets, defined as H_{T} is required to exceed 350 GeV.

6.5 Discriminant variables

After the preselection, the discriminant variables were identified to be the number of jets ($\mathrm{N_{jets}}$), the number of b-jets ($\mathrm{N_{b-jets}}$), the scalar sum of p_{T} of all leptons and jets (H_{T}), and the missing transverse momentum ($E_{\mathrm{T}}^{\mathrm{miss}}$). Their distributions are shown in Figs. 6.1, 6.2 and 6.3, for the ee, $e\mu$ and $\mu\mu$ channels at $\sqrt{s} = 7$ TeV, respectively. The distributions of these variables at $\sqrt{s} = 8$ TeV can be seen in Figs. 6.4, 6.5 and 6.6. The distributions of the leading lepton p_{T} and sub-leading lepton p_{T} are also shown, together with the four tops signal for the contact interaction. The cuts on $E_{\mathrm{T}}^{\mathrm{miss}}$ and H_{T} have been removed. These discriminant variables will be used to optimize the signal selection in Chapter 8.

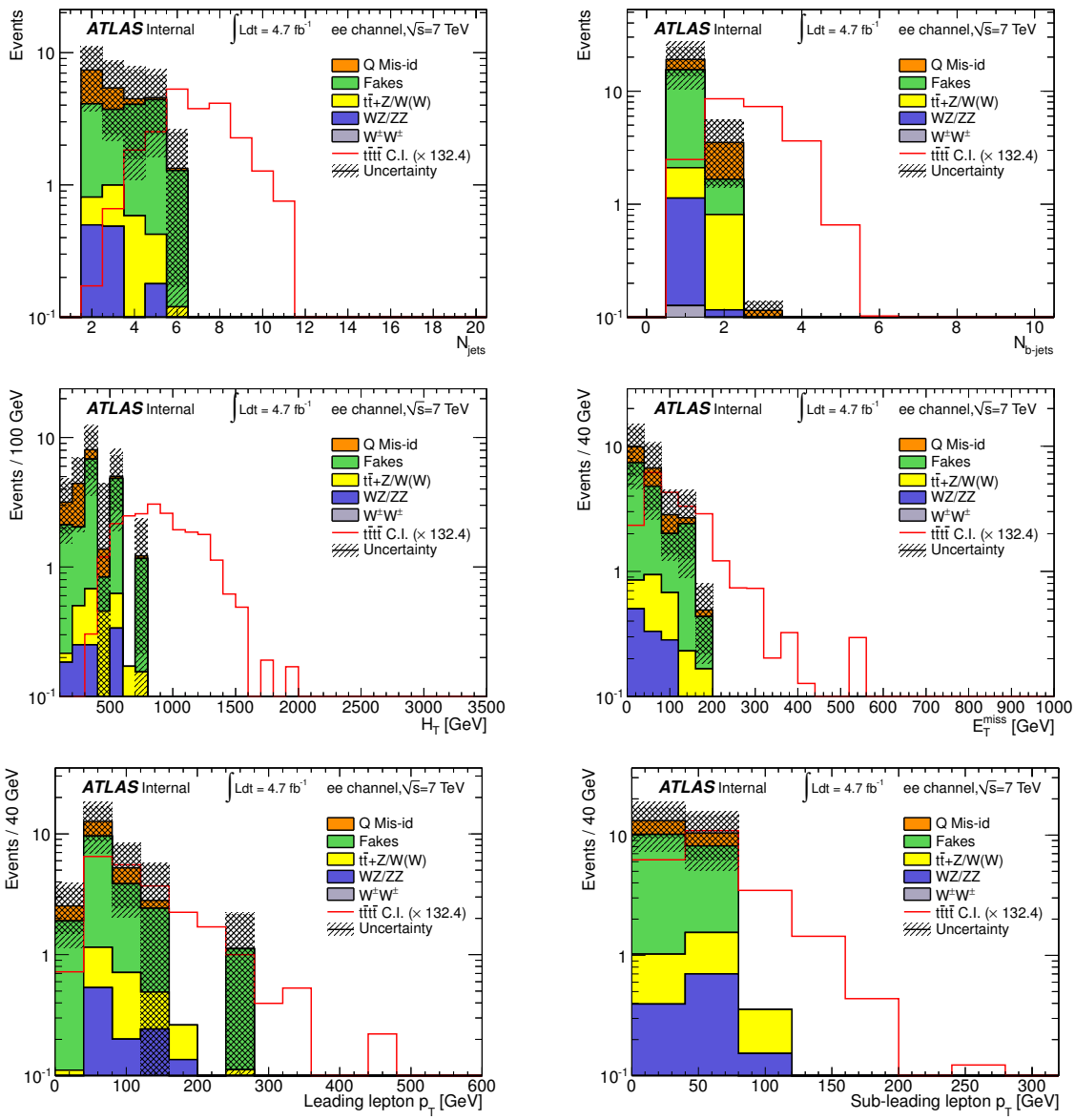

Figure 6.1: Distribution of the kinematical variables in the *ee* channel at $\sqrt{s} = 7$ TeV after preselection removing the cut on $E_{\mathrm{T}}^{\mathrm{miss}}$ and H_{T}. The cross section of the signal is scaled up so that the signal integral is equal to the background integral. The background histograms are stacked to show the total expected background.

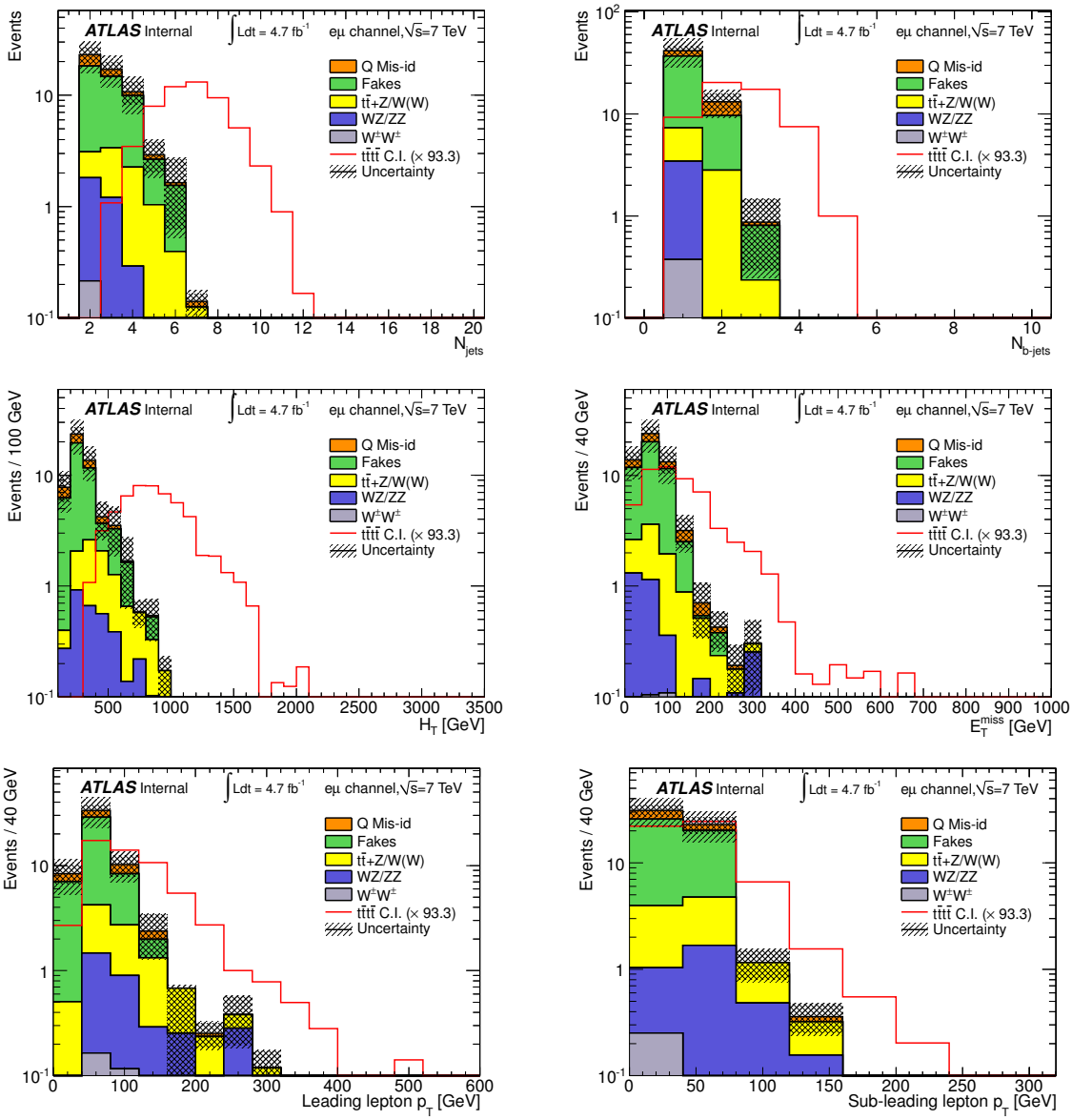

Figure 6.2: Distribution of the kinematical variables in the $e\mu$ channel at $\sqrt{s} = 7$ TeV after preselection removing the cut on $E_{\mathrm{T}}^{\mathrm{miss}}$ and H_{T}. The cross section of the signal is scaled up so that the signal integral is equal to the background integral. The background histograms are stacked to show the total expected background.

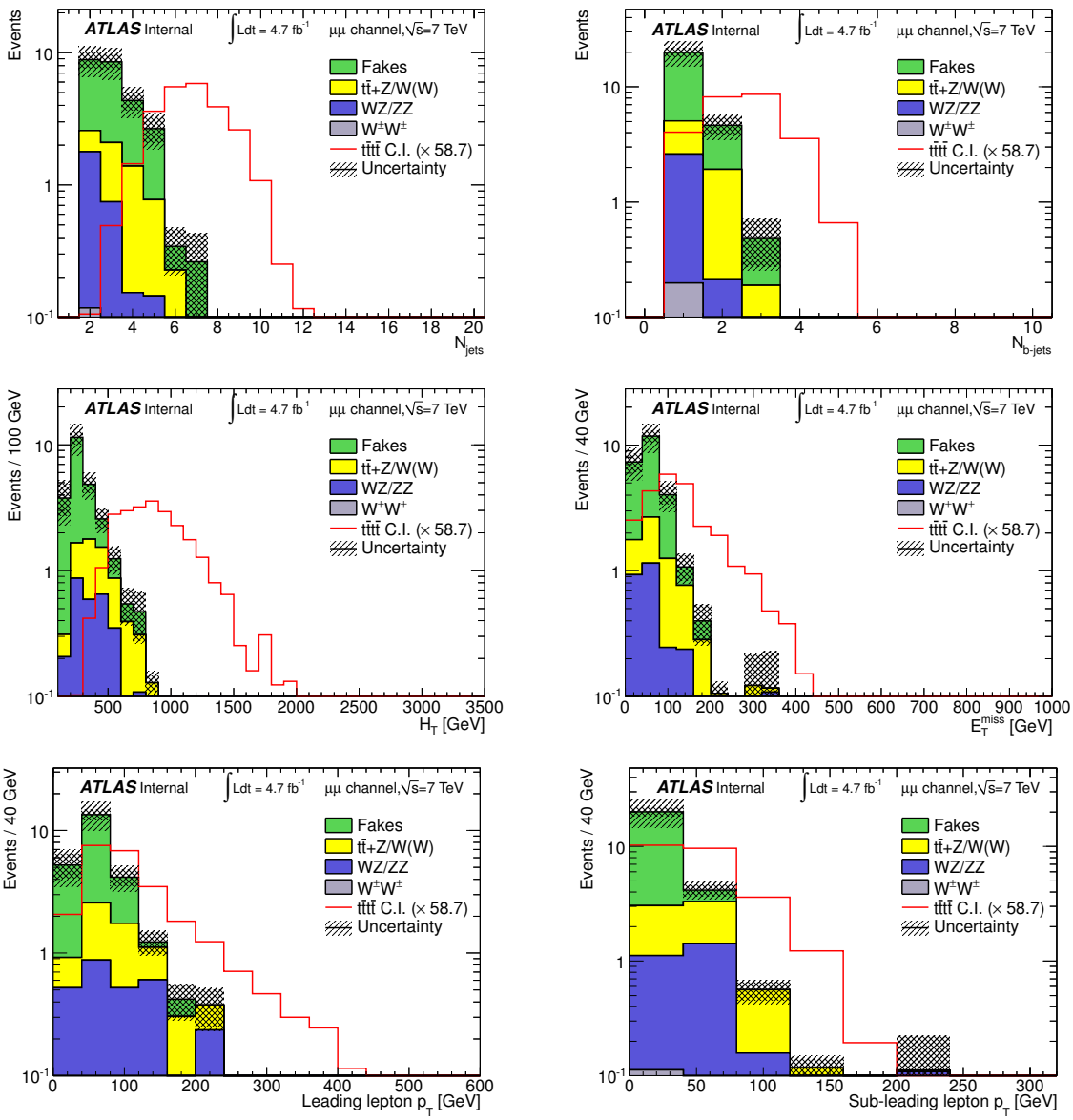

Figure 6.3: Distribution of the kinematical variables in the $\mu\mu$ channel at $\sqrt{s} = 7$ TeV after preselection removing the cut on $E_{\mathrm{T}}^{\mathrm{miss}}$ and H_{T}. The cross section of the signal is scaled up so that the signal integral is equal to the background integral. The background histograms are stacked to show the total expected background.

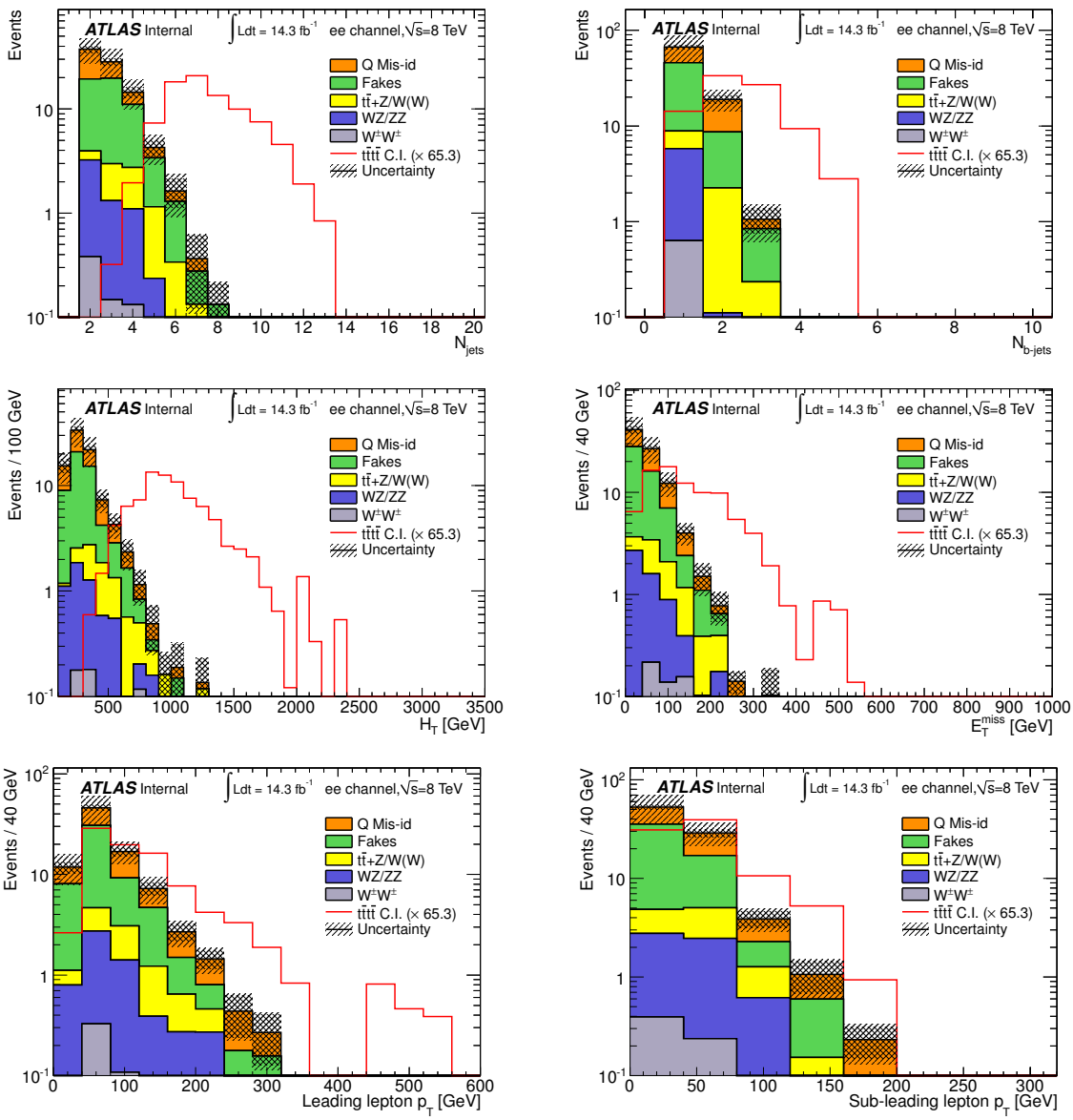

Figure 6.4: Distribution of the kinematical variables in the *ee* channel at $\sqrt{s} = 8$ TeV after preselection removing the cut on $E_{\mathrm{T}}^{\mathrm{miss}}$ and H_T. The cross section of the signal is scaled up so that the signal integral is equal to the background integral. The background histograms are stacked to show the total expected background.

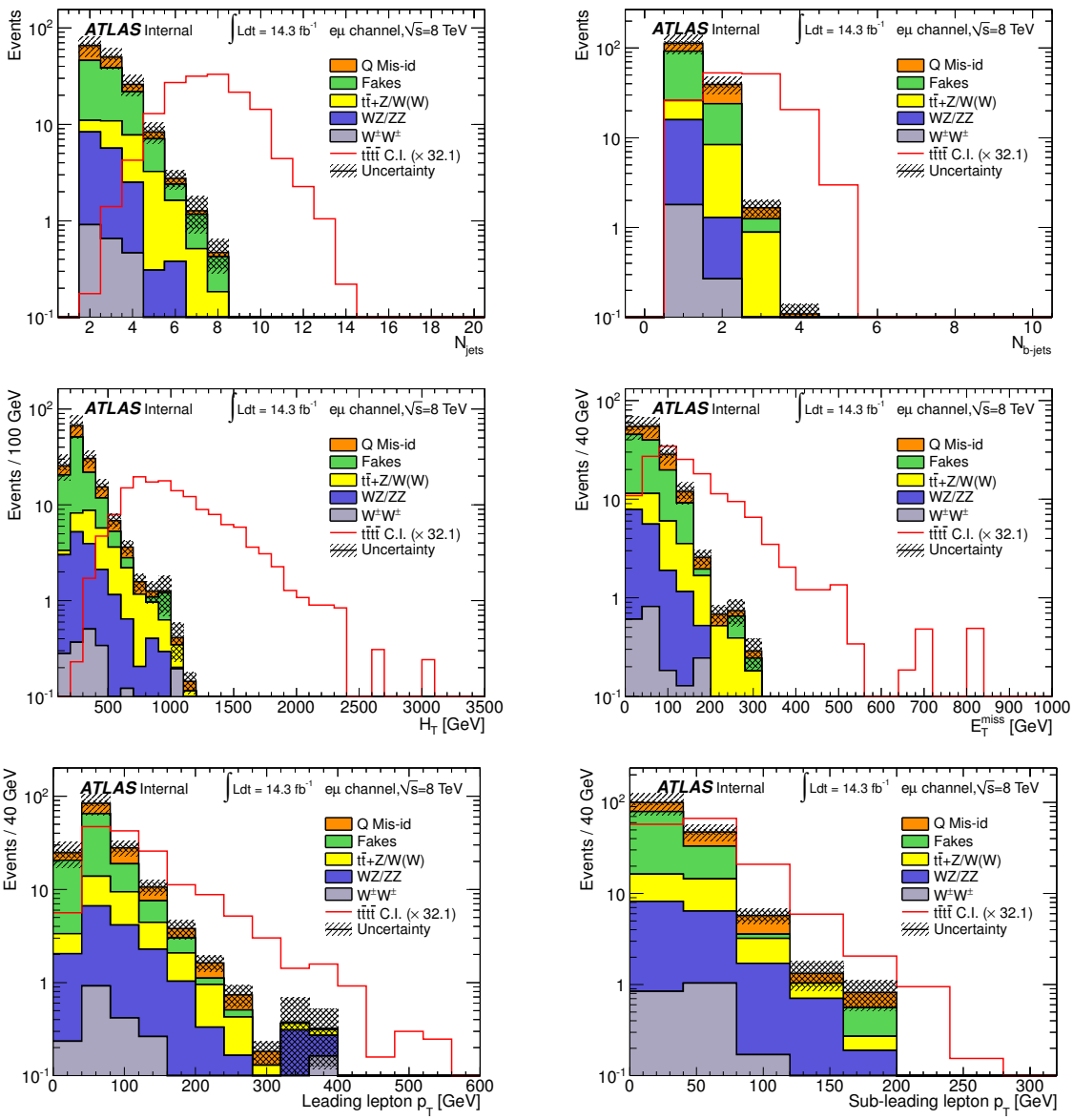

Figure 6.5: Distribution of the kinematical variables in the $e\mu$ channel at $\sqrt{s} = 8$ TeV after preselection removing the cut on $E_{\mathrm{T}}^{\mathrm{miss}}$ and H_T. The cross section of the signal is scaled up so that the signal integral is equal to the background integral. The background histograms are stacked to show the total expected background.

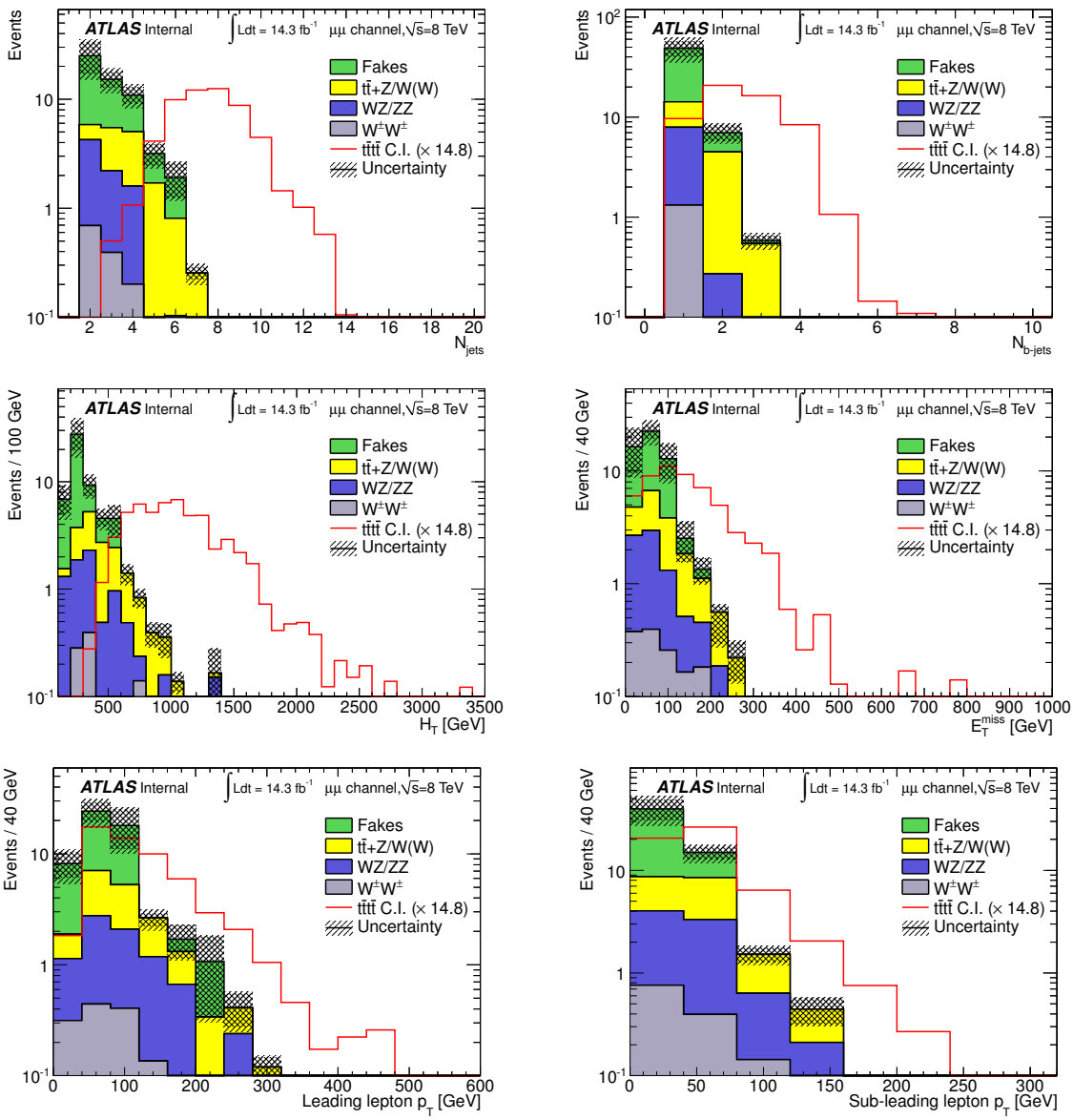

Figure 6.6: Distribution of the kinematical variables in the $\mu\mu$ channel at $\sqrt{s} = 8$ TeV after preselection removing the cut on $E_{\mathrm{T}}^{\mathrm{miss}}$ and H_T. The cross section of the signal is scaled up so that the signal integral is equal to the background integral. The background histograms are stacked to show the total expected background.

Chapter 7

Background estimation

Contents

7.1 Introduction

Several SM processes can mimic the final state of four top quarks. In particular, for a final state with two leptons of the same electric charge, the contribution of the SM processes with two promptly produced same-sign leptons is very small, since this kind of events is rarely produced in the SM. The main contribution is coming from the instrumental backgrounds, where the objects are mis-identified or mis-reconstructed. This way, the background can be divided into two main categories:

- Irreducible background.
- False same-sign dilepton pairs.

The irreducible background is estimated from simulated samples, while the background coming from false same-sign dilepton pairs is estimated from data. Both sources of background are validated in control regions which are orthogonal to the signal selection.

This chapter is dedicated to give a full description of the background estimation. The sources of irreducible background are discussed in Section 7.2. The sources and estimation of the background coming from false same-sign dilepton pairs are presented in Section 7.3. Finally, the validation of the background is given in Section 7.4.

7.2 Irreducible background

This kind of background corresponds to Standard Model processes with real same-sign dilepton pairs. The dominant process contributing (see cross-section production in Table 6.3 and 6.4) is the diboson production, WZ and ZZ, where both gauge bosons decay leptonically as

$$W^{\pm}Z \rightarrow \ell^{\pm}\nu\ell^{+}\ell^{-}, \tag{7.1}$$

$$ZZ \rightarrow \ell^{+}\ell^{-}\ell^{+}\ell^{-}. \tag{7.2}$$

Less significant contributions are coming from production of like-sign W bosons in association with two jets, and from associated production of $t\bar{t}$ pairs with a W or Z boson as

$$W^{\pm}W^{\pm}jj \rightarrow \ell^{\pm}\nu\ell^{\pm}\nu jj, \tag{7.3}$$

$$\begin{aligned} t\bar{t}W^{\pm} &\rightarrow W^{+}bW^{-}\bar{b}W^{\pm} \\ &\rightarrow \ell^{+}\nu bjj\bar{b}\ell^{\pm}\nu, \quad jjb\ell^{-}\nu\bar{b}\ell^{\pm}\nu \quad \text{or} \quad \ell^{+}\nu b\ell^{-}\nu\bar{b}\ell^{\pm}\nu, \end{aligned} \tag{7.4}$$

$$\begin{aligned} t\bar{t}Z &\rightarrow W^{+}bW^{-}\bar{b}Z \\ &\rightarrow \ell^{+}\nu bjj\bar{b}\ell^{+}\ell^{-}, \quad jjb\ell^{-}\nu\bar{b}\ell^{+}\ell^{-} \quad \text{or} \quad \ell^{+}\nu b\ell^{-}\nu\bar{b}\ell^{+}\ell^{-}. \end{aligned} \tag{7.5}$$

A last and almost negligible contribution comes from the production of $t\bar{t}W^{+}W^{-}$ events as

$$t\bar{t}W^{+}W^{-} \rightarrow W^{+}bW^{-}\bar{b}W^{+}W^{-} \tag{7.6}$$

$$\begin{aligned} &\rightarrow \ell^{+}\nu bjj\bar{b}\ell^{+}\nu jj, \quad \ell^{+}\nu b\ell^{-}\nu\bar{b}\ell^{+}\nu jj, \quad \ell^{+}\nu bjj\bar{b}\ell^{+}\nu\ell^{-}\nu, \quad \ell^{+}\nu b\ell^{-}\nu\bar{b}\ell^{+}\nu\ell^{-}\nu, \\ &\quad jjb\ell^{-}\nu\bar{b}jj\ell^{-}\nu \quad \text{or} \quad jjb\ell^{-}\nu\bar{b}\ell^{+}\nu\ell^{-}\nu. \end{aligned} \tag{7.7}$$

Each one of these processes is illustrated in Fig. 7.1. As stated before, this background is estimated from simulated samples. The Monte Carlo samples together with their generators were already detailed in Section 6.2.2.2. Background coming from $tbZ + jets$ and multi parton interactions giving same-sign dibosons and jets have been neglected.

7.3 False same-sign dilepton pairs

This background corresponds to physics processes which do not give same-sign dilepton events, but are reconstructed as such. It comes from:

- **Mis-reconstructed leptons:** At least one of the two leptons in the selected same-sign pair is not a real isolated lepton but has been reconstructed as such.
- **Mis-identification of the electron charge:** The sign of the electric charge of one of the two leptons in the selected same-sign pair has been mis-reconstructed, leading to a true opposite-sign lepton pair being reconstructed as a same-sign pair. The charge mis-identification of muons is much smaller (around 10^7 smaller [148]) and has therefore been neglected in this analysis.

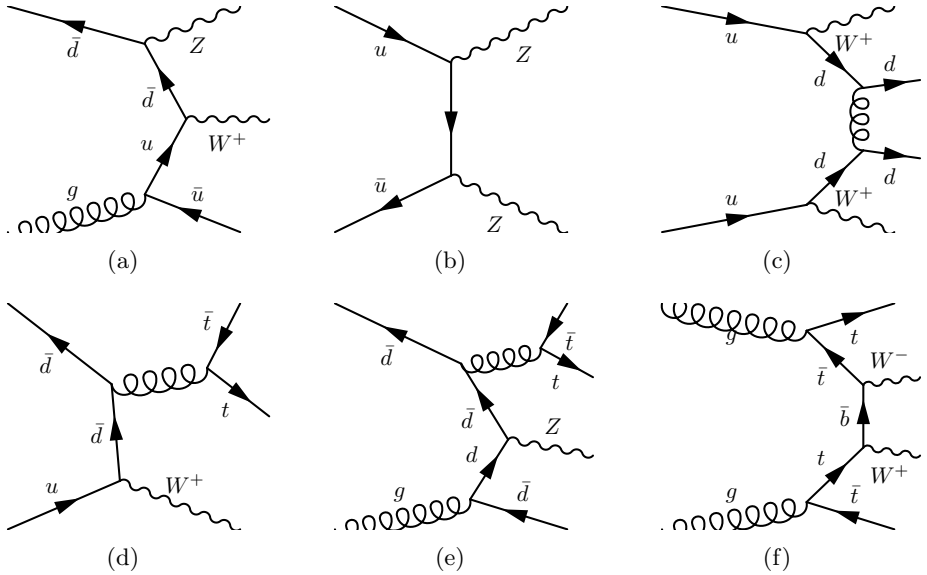

Figure 7.1: Examples of Feynman diagrams illustrating the WZ (a), ZZ (b), $W^{\pm}W^{\pm}jj$ (c), $t\bar{t}W$ (d), $t\bar{t}Z$ (e) and $t\bar{t}W^{+}W^{-}$ (f) productions.

These two sources of background are estimated using data-driven techniques and not using Monte Carlo samples. These techniques are explained below.

7.3.1 Mis-reconstructed leptons

The fake leptons[1] constitute the largest SM background source. It includes all the processes where at least one of the leptons in the pair is non-prompt. The dominant contribution comes from $W + jets$ and QCD multijet (including $b\bar{b}$ and $c\bar{c}$), with smaller contributions from $Z + jets$ and $t\bar{t}$ production.

There are several sources for this background depending on the lepton type. For electrons, a fake lepton may arise from a photon conversion, from a heavy flavor decay, or a light flavor jet with a leading π^0 overlapping with a charged particle. For muons, the dominant mechanism for the creation of fake leptons is the semi-leptonic decay of a heavy flavor hadron, where a muon survives the isolation requirement.

To estimate this background, two sets of lepton selection criteria are defined, named *loose* and *tight*. The *tight* lepton definition is the same as in the analysis as detailed in Section 6.3, and it has to be a subset of the *loose* definition. The *anti-tight* lepton is defined to be an exclusively *loose* lepton, i.e. required not to be *tight*. The probabilities r and f that a real or fake *loose* lepton passes the *tight* criteria are measured using purified control regions and they depend on the characteristics of the event. The *matrix method* [149, 150] is then used to estimate the number of events in the signal region with at least one fake lepton.

The matrix method is discussed in Section 7.3.1.1. The evaluation of the probabilities r and f for the analysis performed with the data taken at $\sqrt{s} = 7$ TeV and 8 TeV is given in

[1] "Fake leptons" include real leptons that are non-prompt.

Sections 7.3.1.2, and 7.3.1.3, respectively. The values of r and f for both, electrons and muons, were estimated by the Top Fakes Group[2]. At 7 (resp. 8) TeV, the events were weighted by LPNHE (resp. Arizona) group[3].

7.3.1.1 Matrix method

In the matrix method, the number of events that contain two *tight* leptons is denoted N_{TT}. The number of events with one *tight* and one *anti-tight* is denoted N_{TA} or N_{AT}, distinguished by p_T-ordering. Similarly, the two *anti-tight* lepton count is referred to as N_{AA}. The total number of events with two *loose* leptons is therefore $N^{ll} = N_{TT} + N_{TA} + N_{AT} + N_{AA}$.

N^{ll}_{RR} is the number of events that contain two real leptons, the number of events with one real and one fake leptons is denoted N^{ll}_{RF} or N^{ll}_{FR} depending on the p_{T} of the leptons, and the number for two fake leptons is N^{ll}_{FF}. The total number of events with two *loose* leptons is therefore $N^{ll} = N^{ll}_{RR} + N^{ll}_{RF} + N^{ll}_{FR} + N^{ll}_{FF}$. These numbers are unknown.

The number of events with two *tight* leptons, in the signal region sample, can be written as $N_{TT} = N^{tt}_{RR} + N^{tt}_{RF} + N^{tt}_{FR} + N^{tt}_{FF}$ and the final fake estimation is $N^{\mathrm{fakes}}_{TT} = r_1 f_2 N^{ll}_{RF} + f_1 r_2 N^{ll}_{FR} + f_1 f_2 N^{ll}_{FF}$, where r_1 and f_1 are the probabilities for the first lepton, and r_2 and f_2 for the second lepton.

Linear expressions are obtained for the observed yields $N_{TT,TA,AT,AA}$ as a function of the unknown numbers $N^{ll}_{RR,RF,FR,FF}$ and the measured rates r and f. These linear expressions form a matrix that is inverted to extract the real and fake content of the selected dilepton event sample:

$$\begin{bmatrix} N_{TT} \\ N_{TA} \\ N_{AT} \\ N_{AA} \end{bmatrix} = \begin{bmatrix} r_1 r_2 & r_1 f_2 & f_1 r_2 & f_1 f_2 \\ r_1(1-r_2) & r_1(1-f_2) & f_1(1-r_2) & f_1(1-f_2) \\ (1-r_1) r_2 & (1-r_1) f_2 & (1-f_1) r_2 & (1-f_1) f_2 \\ (1-r_1)(1-r_2) & (1-r_1)(1-f_2) & (1-f_1)(1-r_2) & (1-f_1)(1-f_2) \end{bmatrix} \begin{bmatrix} N^{ll}_{RR} \\ N^{ll}_{RF} \\ N^{ll}_{FR} \\ N^{ll}_{FF} \end{bmatrix} \tag{7.8}$$

In terms of real and fake leptons within the *loose* selection, the sum of the fake contribution to the *tight* event selection is

$$\begin{aligned} N^{\mathrm{fakes}}_{TT} &= r_1 f_2 N^{LL}_{RF} + f_1 r_2 N^{LL}_{FR} + f_1 f_2 N^{LL}_{FF}, \\ &= \alpha r_1 f_2 [(f_1 - 1)(1 - r_2) N^{TT} + (1 - f_1) r_2 N^{TA} + f_1 (1 - r_2) N^{AT} - f_1 r_2 N^{AA}] + \\ &\quad \alpha f_1 r_2 [(r_1 - 1)(1 - f_2) N^{TT} + (1 - r_1) f_2 N^{TA} + r_1 (1 - f_2) N^{AT} - r_1 f_2 N^{AA}] + \\ &\quad \alpha f_1 f_2 [(1 - r_1)(1 - r_2) N^{TT} + (r_1 - 1) r_2 N^{TA} + r_1 (r_2 - 1) N^{AT} - r_1 r_2 N^{AA}], \end{aligned} \tag{7.9}$$

where

$$\alpha = \frac{1}{(r_1 - f_1)(r_2 - f_2)}. \tag{7.10}$$

7.3.1.2 Estimation of the rates r and f at $\sqrt{s} = 7$ TeV

As said earlier, the *tight* lepton definitions are the same as in the analysis. The *loose* electron selection is equivalent to the *tight* electron selection with the isolation requirement replaced by

[2]The Top Fakes Group is an ATLAS internal group specialized in the computation of the background coming from fake leptons.

[3]The author of this thesis does not have any contribution to the computation of this background.

a looser cut, and looser quality requirements. The *loose* muon selection is equivalent to the *tight* muon selection with the isolation requirement removed. *Loose* muons close to a jet with a $\Delta R(\mu, \text{jet}) < 0.4$ are removed.

The way in which the values of r and f have been computed for the analysis at $\sqrt{s} = 7$ TeV for both, electrons and muons, based on the previous definitions of *loose* and *tight*, is described as follows:

- **Electrons:** for computing the value of r, a highly purified sample of Z bosons was chosen in order to create a control region rich in real electrons. Thus the value of r was estimated with a tag-and-probe method on a sample $Z \to e^+e^-$ events. The Z sample was created by asking for one *tight* electron (*tag* electron) and one *loose* electron (*probe* electron). Different background subtraction methods based on the Z-peak were applied: removal of same-sign events from opposite sign events in the signal region, side-band method on same-sign events, fit using a model for the signal and for the background components. The main systematic uncertainties are coming from the contamination of the sample of *probe* electrons by background: variations based in different signal regions and different fit ranges were used to extract the background with the three different methods. A procedure using the different variations has been developed in order to define the baseline selection. It consists of considering the central value and the statistical uncertainty of an efficiency measurement as the averages of these quantities among all the variations of this measurement. The systematic uncertainty is then given by the spread of all variations.

  For fake electrons, f was estimated in a sample with at least one jet, and exactly one *loose* electron. A cut on the distance between the leading jet and the lepton is also applied $\Delta R(\text{leading jet}, e) \geq 0.7$. Overlap removal is performed between electrons and jets using the *loose* leptons. The efficiency was measured in a control region with $E_{\text{T}}^{\text{miss}} \leq 20$ GeV in order to enrich the sample in multijets. Contamination from signal leptons from W and Z decays is still present in the low $E_{\text{T}}^{\text{miss}}$ region, for that reason a higher purity of the sample is required. This is managed by correcting the number of observed *loose* and *tight* events in data based on Monte Carlo. A first systematic uncertainty is obtained by varying the $E_{\text{T}}^{\text{miss}}$ region from 15 GeV to 25 GeV. The fake efficiency is measured for the different components of the background of signal leptons, which is made mostly from fake leptons from light flavor jets, leptons from heavy flavor jets and photon conversion. These efficiencies are combined to get the central efficiency in the signal region and the systematic uncertainty.

  Both real and fake efficiencies are parametrized as a function of $|\eta|$ and electron p_{T}.

- **Muons:** the efficiencies for muons were determined for two different data taking periods: The first period (BK) goes from March 2011 to August 2011 and gives stable results, while the second period (LM) goes from September 2011 to the end of the same year and gives results slightly different due to the pile-up effect.

  As for real electrons, the value of r for real muons was estimated using the tag-and-probe method on the sample $Z \to \mu^+\mu^-$, requiring events with one *tight* muon (*tag* muon) and one *loose* muon (*probe* muon).

  The efficiencies for fake muons were optimized for $t\bar{t} \to \mu + \text{jets}$ events. The fakes control region was chosen to be orthogonal to $t\bar{t} \to \mu + \text{jets}$, and created by requiring one *loose*

muon. The fake efficiencies have been determined in a low transverse W mass region $m_{\mathrm{T}}(W) < 20$ GeV[4] with an additional inverted triangular cut $E_{\mathrm{T}}^{\mathrm{miss}} + m_{\mathrm{T}}(W) < 60$ GeV. The contribution from $W+$jets and $Z+$jets in the control region was subtracted in order to obtain a more pure QCD estimate.

The fake and real efficiencies are a function of the muon $|\eta|$ and p_{T} of the leading jet in order to take into account for dependencies on muon detector acceptance and hadronic activity from hard jets affecting the muon isolation.

7.3.1.3 Estimation of the rates r and f at $\sqrt{s} = 8$ TeV

As in the previous case, the *tight* leptons are required to satisfy all of the selection criteria as for the analysis. The *loose* electron selection is similar to the *tight* selection with the identification criteria relaxed and the isolation requirement removed. The *loose* muon selection is defined by removing the isolation requirement if the muon p_{T} is greater than 37 GeV, and requiring the sum of all track p_{T}'s in a cone of $R = 0.2$ around the muon to be less than 0.12 times the muons p_{T} otherwise. In both cases, the real and fake efficiencies are measured in samples with at least one jet and exactly one *loose* lepton.

- **Electrons:** the real efficiencies r are measured in a dedicated control region, enriched with real electrons. This way, they are determined in events with $E_{\mathrm{T}}^{\mathrm{miss}} > 120$ GeV.

  The efficiencies for fake electrons are measured in a region with a low amount of $E_{\mathrm{T}}^{\mathrm{miss}}$. The contamination of events with real electrons is removed using simulated events passing the fake control region cuts. Thus, the fake efficiencies are evaluated in events with $E_{\mathrm{T}}^{\mathrm{miss}} <$ 20 GeV or $E_{\mathrm{T}}^{\mathrm{miss}} + m_{\mathrm{T}}(W) < 60$ GeV.

  The fake and real efficiencies for electrons are parametrized as a function of different variables: $|\eta|$ and lepton p_{T}, $\Delta\phi$ between the electron and the $E_{\mathrm{T}}^{\mathrm{miss}}$ vector, ΔR between the electron and the jets, $\sum E_{\mathrm{T}}$ and $E_{\mathrm{T}}^{\mathrm{miss}}$.

- **Muons:** the efficiencies for a real muon passing the *tight* requirements are measured in events with $m_{\mathrm{T}}(W) > 100$ GeV.

  Fake efficiencies for muons are determined from events where the impact parameter d_0 of the muon with respect to the primary vertex was more than five standard deviations from zero, i.e. $|d_0^{\mathrm{sig}}| > 5$. As for electrons, the contribution of events with real muons in this region is extracted using Monte Carlo samples.

  The efficiencies are a function of muon η and p_{T}, ΔR between the muon and the closest jet and the number of b-tagged jets in the event.

7.3.1.4 Yield measurement

In order to measure the yield of events with at least one fake lepton, the same selection of events that will be estimated for the signal region has to be applied, but requiring *loose* leptons instead of *tight* leptons. Then the efficiencies r and f are applied to these events as expressed by Eq. 7.9.

[4]The transverse mass is defined as $m_{\mathrm{T}} = \sqrt{2 p_{\mathrm{T}} E_{\mathrm{T}}^{\mathrm{miss}} (1 - \cos\Delta\phi)}$, where p_{T} is the transverse momentum of the charged lepton and $\Delta\phi$ is the azimuthal angle between the charged lepton and the missing transverse momentum.

At 7 TeV, uncertainties on the estimate of background coming from fake leptons are 50% for the ee channel, 40% for the $e\mu$ channel, and 30% for the $\mu\mu$ channel. At 8 TeV, the uncertainties were determined to be 30% in all channels (see Chapter 8).

7.3.2 Mis-identification of the electron charge

Opposite-sign leptons from SM processes as Drell-Yan, W^+W^-, and mainly $t\bar{t}$, could contribute to the same-sign dilepton background if the charge of one of the leptons coming from the dileptonic decay of these processes is mis-measured.

There are two main sources of electron charge mis-identification:

- Hard Bremsstrahlung producing trident electrons ($e^{\pm} \to e^{\pm}\gamma^* \to e^{\pm}e^+e^-$) whose EM cluster is identified with the wrong electron's track, leading to a mis-identification of the charge. This source represents the main contribution to the background. The fraction of trident electrons depends on the amount of material that the electrons traverse. In the detector, the distribution of the material depends on $|\eta|$. Therefore, a strong dependence on $|\eta|$ is expected in the mis-identification rates.

- A slightly curved track that induces a measurement error. This effect is important at high transverse momentum. Thus, a small dependence on electron p_{T} is also expected in the mis-identification rates.

As said before, for muons this background is negligible compared to other background processes, and therefore is not considered in the analysis[5].

The main strategy to estimate this background together with some preliminary concepts to compute the mis-identification rates of the electron charge are presented in Section 7.3.2.1. The estimation of the rates in simulated samples is presented in Section 7.3.2.2. The different methods used to measure these rates in data are given in Section 7.3.2.3. Finally, the estimation of the rates for the different analyses at $\sqrt{s} = 7$ TeV and 8 TeV are presented in Sections 7.3.2.4 and 7.3.2.5, respectively.

7.3.2.1 Main strategy and preliminary concepts

When a true opposite-sign event (for example $t\bar{t} \to bW^+\bar{b}W^- \to b\bar{b}e^+e^-\nu\bar{\nu}$) is produced, and assuming that ϵ is the rate of charge mis-identification for a single electron, there are three possibilities for this event to be reconstructed:

1. $e^+e^- + X$ without any charge mis-identification, with a probability of $(1-\epsilon)^2$,
2. $e^+e^- + X$ with the two electrons having a charge flip, with a probability of ϵ^2,
3. $e^{\pm}e^{\pm} + X$ when only one of the two electrons is mis-identified, with a probability of $2\epsilon(1-\epsilon)$.

Therefore, if there are N true opposite-sign events, the reconstructed events will be:

- $N^{os} = (1 - 2\epsilon + 2\epsilon^2)N$ opposite-sign events,

[5]The rate of charge mis-identification for muons is only affected by the track curvature. Because of the long lever arm to the muon system and the fact that the charge is measured in both the inner detector and muon spectrometer the mis-identification rates of the muon charge are very low, making this background negligible compared to the other sources of background.

- $N^{ss} = 2\epsilon(1-\epsilon)N \simeq 2\epsilon N$ same-sign events,

where the last approximation for N^{ss} corresponds to the assumption that ϵ is very small.

Knowing this charge mis-identification rate ϵ, it is therefore possible to compute the estimated number of same-sign events N^{ss} from the measured number of opposite-sign events N^{os}, using the following expressions:

- $N^{ss} = \frac{\epsilon_i+\epsilon_j-2\epsilon_i\epsilon_j}{1-\epsilon_i-\epsilon_j+2\epsilon_i\epsilon_j} N^{os}$ for the ee channel,
- $N^{ss} = \frac{\epsilon}{1-\epsilon} N^{os}$ for the $e\mu$ channel,

where ϵ_i and ϵ_j are the charge mis-identification rates for the two different electrons.

Finally, the method to estimate the number of same-sign events produced by the Standard Model true opposite-sign processes has two steps:

1. the measurement of the charge mis-identification rate ϵ,
2. the application of the measured rate to measured opposite-sign events N^{os}. The last one gives the estimation of N^{ss}.

The mis-identification rates have been measured in a very clean sample of $Z \to e^+e^-$, where the electrons fill the same requirements as the ones used in the analysis. They have been computed as a function of electron $|\eta|$ (to be more precise, the full $|\eta|$ range of the electron acceptance has been divided in regions, named *bins*, so that the rates are determined as a function of $|\eta|$ bins). In the analysis at $\sqrt{s} = 8$ TeV, they have been corrected using a p_{T}-dependent factor.

7.3.2.2 Estimation of the mis-identification rates of the electron charge in simulated samples: truth-matching

In simulated samples, the reconstructed electrons can be matched to the generated ones from the Z decay. A matching cone $\Delta R \leq 0.2$ is used to find reconstructed electrons that correspond to true electrons produced from the Z decay[6]. The matching is done only to the electrons produced directly from the Z decay (primary electrons). It does not match reconstructed electrons to electrons produced in the conversion of radiated photons from primary electrons, to electron-positron pairs, or to electrons produced in other secondary processes. If trident electrons, the reconstructed electrons are matched to the primary electron if the electrons produced in the conversion are almost collinear to the primary electron.

7.3.2.3 Estimation of the mis-identification rates of the electron charge in data

Different methods can be used to measure the mis-identification rates in data. These methods can be also applied to compute the rates in simulated samples. Each one of these methods uses electrons coming from the leptonic decay of the Z boson. This way, the sample has been created asking for exactly two electrons and no muons, where at least one of the selected leptons matches the corresponding trigger.

All the three methods studied here use Z *signal* events. Therefore, background coming from other processes where the dilepton invariant mass corresponds to the one of the Z boson

[6] It has been shown that for $\Delta R > 0.05$, the size of the cone has no incidence on the matching performance [151].

needs to be subtracted. The background subtraction is done using a simple side-band method. This method consists in dividing the Z invariant mass in three regions, i.e. A, B and C, where B is the central region corresponding to the Z peak. The number of events is counted in the regions on the sides of the peak, i.e. n_A and n_C, and removed from the total number of events in the peak region B, n_B. This way, the number of signal events N_Z is given by

$$N_Z = n_B - \frac{n_A + n_C}{2}. \tag{7.11}$$

Once the background has been subtracted, the different methods can be applied to extract the rates. They are explained below:

- **Tag-and-probe:** In the tag-and-probe method, the electrons are divided in two classes: *tag* and *probe*. In each pair, the tag electron is required to have a very low charge mis-identification rate. The sign of the other electron (probe electron) is the one under study.

  As it will be shown later, the mis-identification rate of the electron charge in the central region of the detector is around two orders of magnitude lower than for electrons in the endcap regions. Therefore, the tag electrons are signal electrons with pseudorapidity within the interval established for the first $|\eta|$ bin (the bin corresponding to the lowest value of $|\eta|$). At least one of the electrons in the pair must satisfy the tag condition. Otherwise, the event is rejected.

  The number of same-sign N_{ss} and opposite-sign N_{os} events in the Z peak is evaluated based on the $|\eta|$ properties of the probe electron after background rejection. Thus, the charge mis-identification rates are obtained as follows:

  $$\delta_e^i = \frac{N_{ss}^i}{N_{ss}^i + N_{os}^i}, \tag{7.12}$$

  where i corresponds to each bin in $|\eta|$. These values contain the mis-id rates of one tag and one probe electron. In order to obtain the charge flip for each lepton, the tag efficiency needs to be extracted. This way, for the first $|\eta|$ bin 2 tag electrons are accepted. Therefore, the final charge mis-identification rate, ϵ, in this bin is computed as:

  $$\epsilon^0 = \frac{\delta_e^0}{2}. \tag{7.13}$$

  For the remaining bins, the tag efficiency has to be computed as:

  $$\epsilon^i = \delta_e^i - \epsilon^0, \quad i \neq 0. \tag{7.14}$$

- **Direct extraction:** in this method both electrons in the pair are required to be in the same $|\eta|$ bin. Otherwise the event is rejected. The charge flip is given by:

  $$\epsilon^i = \frac{N_{ss}^i}{2(N_{ss}^i + N_{os}^i)}, \tag{7.15}$$

  where N_{ss}^i (N_{os}^i) is the number of events in the Z peak with both same-sign (opposite-sign) electrons in the same $|\eta|$ bin i after background subtraction. The factor of 2 comes from the fact that the two electrons in the pair are in the same $|\eta|$ bin.

- **Likelihood:** the tag-and-probe and direct extraction methods force the electrons to be in a determined kinematical region. This biases the kinematical properties of the electrons and it reduces the statistics of the sample. However, the likelihood method takes into account electron pairs with all $|\eta|$ combinations. It does not bias the kinematical properties of the electrons, and it does not reject events.

  The likelihood method assumes that the mis-identification rates of the electron charge are independent for different pseudorapidity regions. Therefore, the probability to have a number of same-sign events (N_{ss}^{ij}) with electrons in $|\eta|$ region i and j can be written as a function of the number of events N^{ij} as follows:

$$N_{ss}^{ij} = N^{ij}(\epsilon_i + \epsilon_j). \tag{7.16}$$

  If all the same-sign events in the Z peak are produced by charge flip, then N_{ss}^{ij} is described by a Poisson distribution:

$$f(k, \lambda) = \frac{\lambda^k e^{-\lambda}}{k!}, \tag{7.17}$$

  where k is the observed number of occurrences of the event, i.e. $k = N_{ss}^{ij}$, and λ is the expected number, i.e. $\lambda = N^{ij}(\epsilon_i + \epsilon_j)$. Thus, the probability for both electrons to produce a charge flip is expressed by:

$$P(\epsilon_i, \epsilon_j | N_{ss}^{ij}, N^{ij}) = \frac{[N^{ij}(\epsilon_i + \epsilon_j)]^{N^{ij}} e^{-N^{ij}(\epsilon_i+\epsilon_j)}}{N_{ss}^{ij}!}. \tag{7.18}$$

  The likelihood L for all the events is obtained by evaluating all the $|\eta|$ combinations:

$$L(\epsilon | N_{ss}, N) = \prod_{i,j} \frac{[N^{ij}(\epsilon_i + \epsilon_j)]^{N^{ij}} e^{-N^{ij}(\epsilon_i+\epsilon_j)}}{N_{ss}^{ij}!}, \tag{7.19}$$

  where the rates ϵ_i and ϵ_j can be obtained by minimizing the likelihood function. In this process, the $-\ln L$ is used in order to simplify and make easier the minimization. Terms which do not depend on the rates ϵ_i and ϵ_j are removed in this step. This way, the final function to minimize is given by the following expression:

$$-\ln L(\epsilon | N_{ss}, N) \approx \sum_{i,j} \ln(N^{ij}(\epsilon_i + \epsilon_j)) N_{ss}^{ij} - N^{ij}(\epsilon_i + \epsilon_j). \tag{7.20}$$

  The events are selected within the Z peak and stored –with the electron order by $|\eta|$– in two triangular matrices: one for the same-sign events N_{ss}^{ij}, and the other one for all events N^{ij}. The likelihood method contains the information provided by the two previous methods: the first raw of each matrix contains the same information as the one needed for the tag-and-probe method, while the diagonal terms contain the ones used by the direct extraction method. It also adds the correlations from all possible electron $|\eta|$ combinations, allowing to use all the electron pairs, and therefore to get lower statistical uncertainties.

7.3.2.4 Estimation of the mis-identification rates at $\sqrt{s} = 7$ TeV

The rates of charge mis-identification for electrons were estimated as a function of the electron $|\eta|$ for the three different methods as shown in Fig. 7.2(a), where they are denoted as $\epsilon_{\text{mis-id}}$. The p_{T} dependence of the rates was not considered in the analysis at $\sqrt{s} = 7$ TeV. Differences on the rates extracted from these methods come from the kinematic selection. The regions used to subtract the background were defined as $A \in [61, 81]$, $B \in [81, 101]$ and $C \in [101, 121]$.

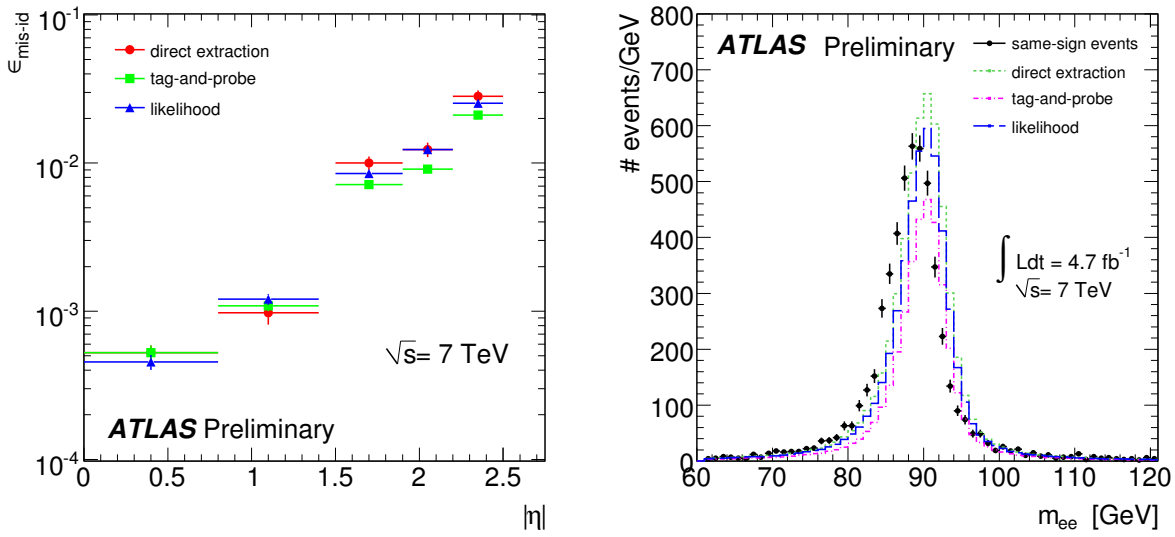

(a) (b)

Figure 7.2: a) Charge mis-identification rate as a function of the electron $|\eta|$ b) Invariant mass distribution for same-sign and reweighed opposite-sign events around the Z-peak [18].

A closure test was performed by comparing the numbers of events selected in the Z-peak region using same-sign electron pairs, and opposite-sign electron pairs reweighted by the mis-id weight depending on each method. These distributions are shown in Fig. 7.2(b). In this figure, the Z-peak for same-sign electrons is shifted to lower values with respect to opposite-sign electrons because a larger momentum fraction has been radiated for the same-sign case, due to trident electrons. Around 5143 same-sign events are estimated in the Z-peak region. The tag-and-probe method gives an under-estimation of the events with 3700 predicted events, while direct extraction predicts around 5500 events with an over-estimation. The likelihood method gives the best agreement with 5000 events estimated. The differences on the rates estimation are well-understood and come from the different kinematic requirements in the three methods. As a consequence, the likelihood method was used to extract the nominal yield, while the other two methods were used to estimate the systematic uncertainty. This background has been estimated at 7 TeV by Saclay group[7].

[7]Thanks to Léa Gauthier for producing these rates [148].

7.3.2.5 Estimation of the mis-identification rates at $\sqrt{s} = 8$ TeV

The estimation of the mis-identification rates in the analysis performed at $\sqrt{s} = 8$ TeV presents some differences with respect to the one at $\sqrt{s} = 7$ TeV. These differences are enumerated below:

1. As shown in Fig. 7.2(b), the Z-peak for same-sign electrons is shifted to lower values with respect to opposite-sign electrons. It could introduce in some way a mis-measurement of the rates. Therefore, the three different regions used by the side-band method to extract the background have been redefined differently in the opposite-sign and same-sign distributions. The definitions of these regions are shown in Fig. 7.3. Their specific values are shown in Table 7.1. These values have been obtained by means of a Gaussian fit in a reduced region around the Z-peak for both the distributions of same-sign and opposite-sign invariant mass. They have been determined using the mean value κ and the standard deviation σ given by the fit. Thus, the region B was defined as $\kappa \pm 4\sigma$. The specific value 4σ is chosen since with this peak width, the closure test gives the best results. The regions A and C are defined so that they have the same width as the central region, i.e. 8σ.

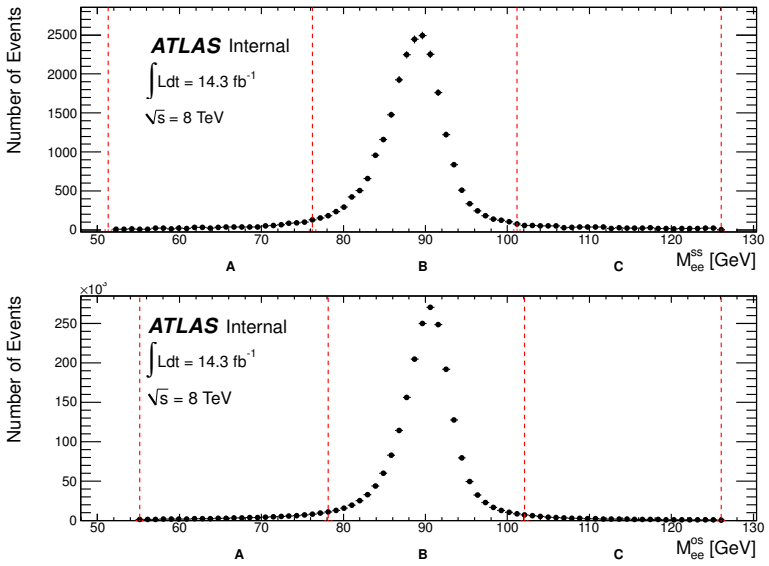

Figure 7.3: Dilepton mass spectra for the same-sign (top) and opposite-sign (bottom) electron pairs in data. The vertical lines represent the boundaries of the regions used for the background rejection.

Sample	A	B	C
Same-sign	[51.7,76.5]	[76.5,101.3]	[101.3,126.0]
Opposite-sign	[54.7,78.5]	[78.5,102.3]	[102.3,126.0]

Table 7.1: Ranges of the A, B and C regions for the background and signal definitions in data.

2. The $|\eta|$ binning has been redefined. The new binning has been obtained by computing the mis-identification rates in simulated Z samples using the truth-matching method with a

bin width in $|\eta| = 0.1$ as shown in Fig. 7.4(a). As can be seen, the rates are more or less constant in some regions. In the plot they are separated by the vertical lines. Therefore, seven different regions have been identified, which have been used to define the new $|\eta|$ binning, shown in Table 7.2.

Bin	0	1	2	3	4	5	6
$\|\eta\|$ region	[0,0.6]	[0.6,1.1]	[1.1,1.37]	[1.37,1.52]	[1.52,1.8]	[1.8,2.2]	[2.2,2.47]

Table 7.2: New $|\eta|$ binning defined using the mis-identification rates computed with the truth-matching method in simulated Z events for a very fine binning.

In addition, the rates are smaller in the central region of the detector where the material budget is also smaller and the track resolution has the best performance (see Fig. 7.4(b)). Once moving to the outer part of the inner detector, the amount of material the electrons go through increases, raising the number of trident electrons, and therefore the mismeasurement of the charge. The mis-identification rates as a function of $|\eta|$ are related to the material distribution of the inner detector at least up to one bin after the crack region ($|\eta| \in [1.37, 1.52]$). The reason for which they increase after this region is unknown.

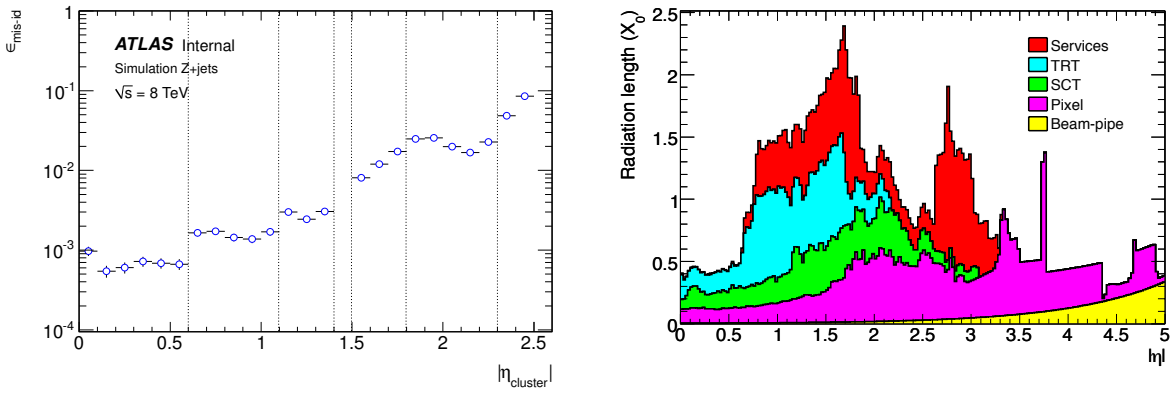

(a) (b)

Figure 7.4: a) Charge mis-identification rate as a function of the electron $|\eta|$ measured in Monte Carlo $Z + jets$ using the truth-matching method for a very fine binning. The vertical lines separate the regions where the rates are more or less constant. b) Material distribution at the exit of the inner detector as a function of $|\eta|$ [4].

3. The dependence on electron p_{T} of the rates has been taken into account. The likelihood method is kept as the baseline to compute the rates from the data, which are then corrected using a p_{T} dependent factor extracted from $t\bar{t}$ simulated events.

4. The systematic uncertainty is not computed anymore using the tag-and-probe and direct extraction methods. Different methods have been used to compute them, and different sources have been considered.

The last two points are developed in the next two sections. But before going to the p_{T} correction it is necessary to validate the likelihood method. This is done by comparing the mis-identification rates computed with both likelihood and truth-matching methods on simulated Z events. This comparison is shown in Fig. 7.5. As can be seen, the rates are compatible within uncertainties.

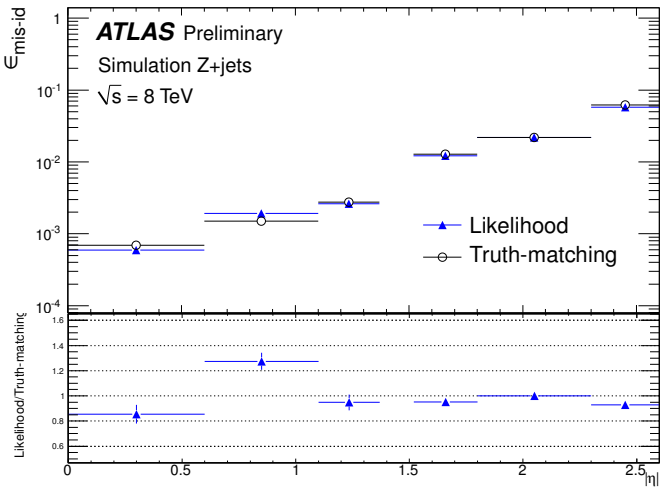

Figure 7.5: Comparison between the true and measured mis-identification rates as a function of $|\eta|$ in simulated Z events.

All the simulated samples used in this section are detailed in Table 7.3.

Process	Generator	PDF	Detector Simulation
$Z \to e^+e^-$ Np0	ALPGEN+PYTHIA	CTEQ6L1	GEANT4
$Z \to e^+e^-$ Np1	ALPGEN+PYTHIA	CTEQ6L1	GEANT4
$Z \to e^+e^-$ Np2	ALPGEN+PYTHIA	CTEQ6L1	GEANT4
$Z \to e^+e^-$ Np3	ALPGEN+PYTHIA	CTEQ6L1	GEANT4
$Z \to e^+e^-$ Np4	ALPGEN+PYTHIA	CTEQ6L1	GEANT4
$Z \to e^+e^-$ Np5	ALPGEN+PYTHIA	CTEQ6L1	GEANT4
$t\bar{t}$	MC@NLO+HERWIG	AUET2 CT10	GEANT4
$t\bar{t}$	POWHEG+HERWIG	AUET2 CT10	ATLFASTII
$t\bar{t}$	POWHEG+PYTHIA	AUET2B CT10	ATLFASTII

Table 7.3: Monte-Carlo samples used for the charge mis-identification studies, together with their generators, PDF and detector simulation. The $t\bar{t}$ sample used as a baseline for the p_{T} correction is the one generated with MC@NLO+HERWIG. The other $t\bar{t}$ samples have been used to compute the systematic uncertainties.

7.3.2.5.1 Likelihood method and p_{T} correction

As previously stated, the charge mis-identification rates are measured on $Z \to e^+e^-$ events. The advantage of this method is that a clean peak can be seen in the dilepton mass spectrum, at the Z mass. The drawback is that these rates depend also on the p_{T} of the electrons and that the p_{T} spectrum of the electrons coming from a Z decay is not the same as the one in the $t\bar{t}$ decay. Therefore, the rates measured in the Z decays must be corrected in order to take into account the dependence on p_{T}.

This information is corroborated when computing the rates is simulated Z events with the truth-matching method as a function of $|\eta|$ and parametrized on p_{T}. The full p_{T} range has been divided in three different regions: [15,100], [100,200] and [200,1000] GeV. As can be seen from Fig. 7.6, the rates measured with the Z events are clearly dominated by the low p_{T} region, while the rates for $t\bar{t}$ events should be larger for larger p_{T}.

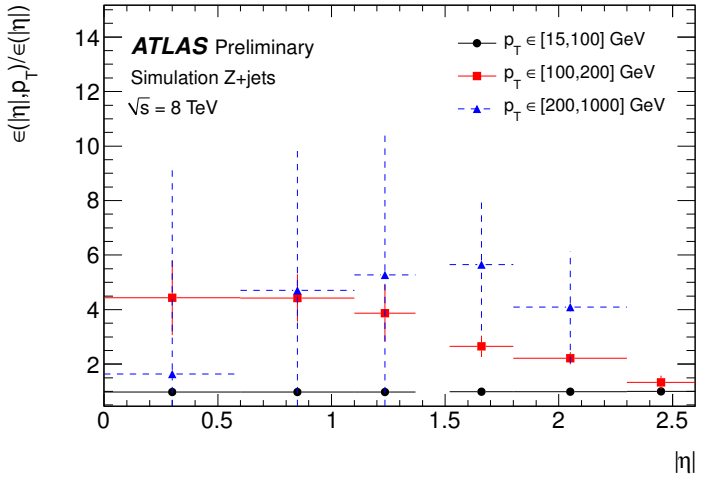

Figure 7.6: Distribution of the ratio $\epsilon(|\eta|, p_{\mathrm{T}})/\epsilon(|\eta|)$ for Z events computed by truth-matching, as a function of $|\eta|$ and for different p_{T} bins. It shows that the average rate $\epsilon(|\eta|)$ is largely dominated by the first bin in p_{T}.

In Z events with high p_{T}, the statistics is too low to give an accurate measurement of the charge mis-identification rates in this region. Therefore, the low-p_{T} measured rate in Z events will be corrected by a p_{T} dependent factor. This factor is extracted from $t\bar{t}$ events and it is defined as:

$$\alpha(|\eta|, p_{\mathrm{T}}) = \frac{\epsilon(|\eta|, p_{\mathrm{T}})}{\epsilon(|\eta|, p_{\mathrm{T}} < 100 \text{ GeV})}. \tag{7.21}$$

Fig. 7.7 shows the correction factor α as a function of $|\eta|$ and parametrized in p_{T}. By definition, it is set to 1 in the low-p_{T} region. Finally, the mis-identification rates after correction will be given by

$$\epsilon(|\eta|, p_{\mathrm{T}}) = \epsilon(|\eta|)_Z \times \alpha(|\eta|, p_{\mathrm{T}}), \tag{7.22}$$

where the first term $\epsilon(|\eta|)_Z$ is determined in data with the likelihood method from Z events where both electrons satisfy $p_{\mathrm{T}} < 100$ GeV. The rates after correction for data are shown in Fig. 7.8.

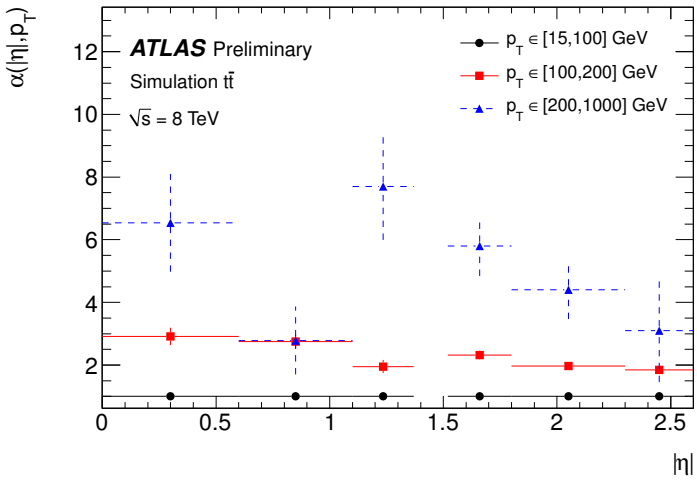

Figure 7.7: Correction factor $\alpha(|\eta|, p_{\mathrm{T}}) = \epsilon(|\eta|, p_{\mathrm{T}})/\epsilon(|\eta|, p_{\mathrm{T}} < 100\ \mathrm{GeV})$ for $t\bar{t}$ events computed by truth-matching, as a function of $|\eta|$ and for different p_{T} bins. By definition, the correction factor is 1 in the first p_{T} bin.

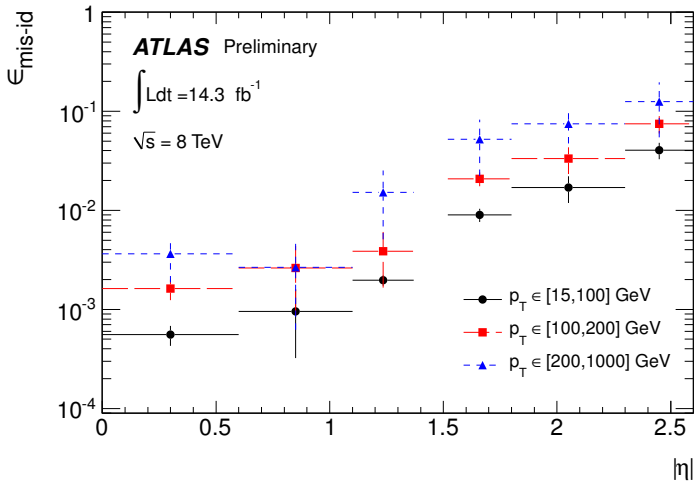

Figure 7.8: Charge mis-identification rates, $\epsilon_{\mathrm{mis-id}}$, measured in data using the likelihood method on Z events, as a function of $|\eta|$ (black points). Applying the p_{T} dependent correction factor $\alpha(|\eta|, p_{\mathrm{T}})$, determined with simulated $t\bar{t}$ events gives the final charge mis-identification rates $\epsilon(|\eta|, p_{\mathrm{T}})$ (black points, red squares and blue triangles).

The rates after correction are finally validated by comparing the number of measured same-sign events with the estimated number of same-sign events, where these last ones have been computed by reweighting the measured number of opposite-sign events. This comparison was done in both, data and simulated $Z \to e^+e^-$ samples. The invariant mass of the Z can be seen on Figure 7.9. In the simulated Z samples, the number of same-sign Z events is $32\,995 \pm 790$ while the estimation is $32\,493^{+6364}_{-6306}$. In data, the number of same-sign Z events is 22 067 for an estimate of $21\,824^{+5678}_{-5706}$. The uncertainties combine the statistical and systematic uncertainties, and their computation is explained in the next section. In both cases, the closure test gives compatible results within uncertainties.

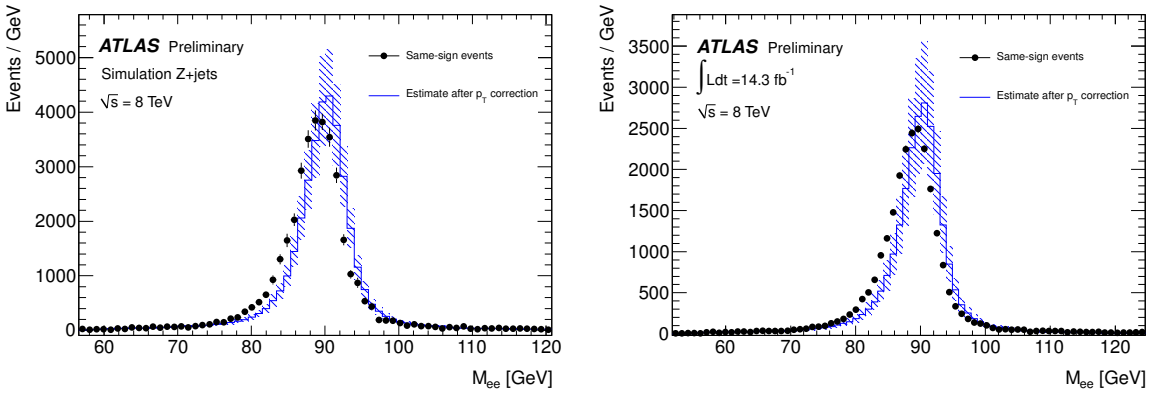

Figure 7.9: Closure test on simulated $Z \to e^+e^-$ (left) and data (right) events. The black circles show the distribution of same-sign events while the blue histograms show the distribution of the reweighted opposite-sign events. The distributions are not expected to overlay exactly, due to the loss of energy of the trident electrons for the same-sign peak.

A final validation of the rates can be done on simulated samples. In this case, the mis-identification rates are computed using the likelihood method as a function of $|\eta|$ in Z Monte Carlo, and they are after corrected using the p_{T} correction factor extracted from simulated $t\bar{t}$ events. The cross-check is done by comparing the number of same-sign events with the number of reweighted opposite-sign events, obtained from the Monte Carlo $t\bar{t}$ sample. The p_{T} distribution of these events can be seen in Fig. 7.10 and shows a very good agreement within uncertainties: above 100 GeV, the total number of same-sign events is 121 ± 19, for an estimate of 146 ± 36.

The nominal correction factor $\alpha(|\eta|, p_{\mathrm{T}})$ has been extracted from a $t\bar{t}$ sample simulated using a specific framework, here MC@NLO+Herwig, with the detector response modelled by Geant4. The dependence of this factor on other frameworks need to be verified. Two other simulated $t\bar{t}$ samples, one generated with Powheg+Herwig, and the other one generated with Powheg+Pythia, both with a detector response modelled by AtlFastII, have been used to check this dependence (see Table 7.3). A comparison of the different correction factors is shown in Fig. 7.11. There is a reasonable agreement between the three samples. The differences between the three samples in the same $(|\eta|, p_{\mathrm{T}})$ configuration will be taken into account as a systematic uncertainty.

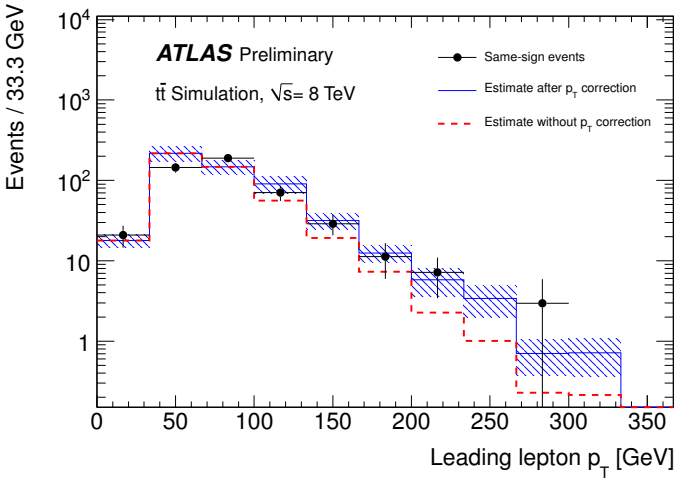

Figure 7.10: Distribution of the leading lepton p_{T} for the same-sign events (points) and reweighted opposite-sign events (histogram), in simulated $t\bar{t}$ events. The weights have been determined using the likelihood method on simulated Z events and have been corrected using the factor $\alpha(|\eta|, p_{\mathrm{T}})$ extracted from $t\bar{t}$ events. The uncertainty band includes all uncertainties. The dashed line shows the estimate while using the weights without applying the p_{T} correction factor.

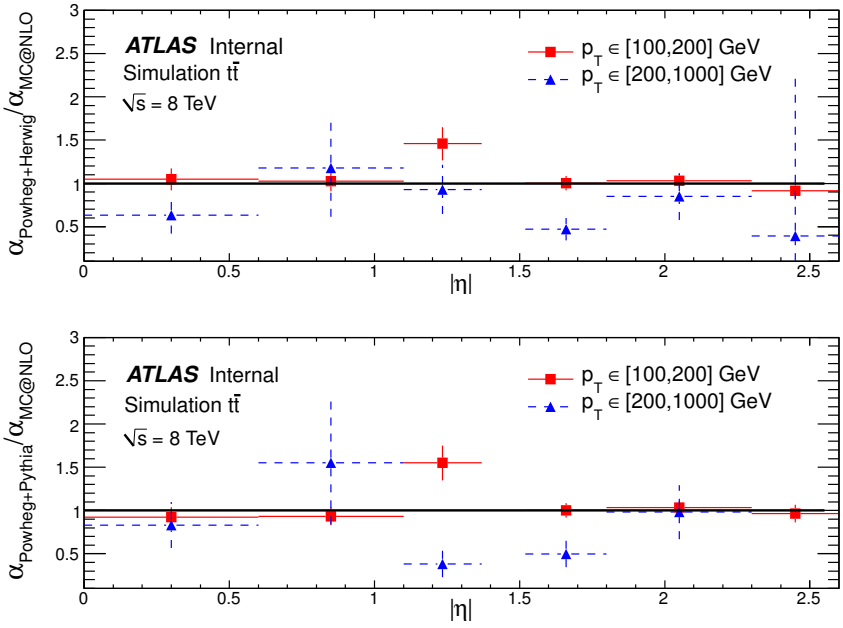

Figure 7.11: Comparison of the p_{T} correction factors obtained with the POWHEG+HERWIG sample (top), $\alpha_{\mathsf{Powheg+Herwig}}$, or the POWHEG+PYTHIA sample (bottom), $\alpha_{\mathsf{Powheg+Pythia}}$, with the one obtained with the MC@NLO sample, $\alpha_{\mathsf{MC@NLO}}$, as a function of $|\eta|$ and for different p_{T} bins.

7.3.2.5.2 Estimation of the systematic uncertainty

Different sources of systematic uncertainties have been taken into account in the charge mis-identification rates. The final uncertainty σ_ϵ on the rates is the quadratic sum of five different contributions. They are enumerated below:

- The statistical uncertainty from the likelihood method $\sigma_\epsilon^{\text{likelihood}}(|\eta|) \times \alpha(|\eta|, p_{\text{T}})$.
- The statistical uncertainty on the correction factor $\epsilon(|\eta|)_Z^{\text{likelihood}} \times \sigma_\alpha(|\eta|, p_{\text{T}})$.
- The difference between the rates measured with the likelihood method after correction and truth-matching on simulated $Z \to e^+e^-$ events.
- The difference between the rates measured after correction with the correction factor extracted from the different $t\bar{t}$ simulated samples. In this case, the uncertainty is taken into account only in the $(|\eta|, p_{\text{T}})$ configurations where the ratio on the different correction factors is not around 1 within uncertainties.
- The variation of the rates due to the variation of the Z-peak region definition when the background is extracted. In this case, the different regions have been variated by 1 σ.

The contribution of each one of these factors to the final uncertainty for the different $(|\eta|, p_{\text{T}})$ configurations is shown in Fig. 7.12. The main contribution comes from the difference between the rates measured with the likelihood method after correction and truth-matching on simulated Z events. The systematic uncertainty coming from the variation of the rates due to the variation of the Z-peak region definition is completely negligible.

7.3.3 Overlap between the electron charge mis-identification and fake electrons

As stated before, trident electrons are the main source of the background coming from the mis-identification of electron charge. Trident electrons have also a smaller probability of passing the *tight* electron selection criteria in the fakes estimate, thus a fraction of them are partially captured by the matrix method, and they are therefore included in the fakes background. This means that there is an overlap between the fakes and mis-id background, which must be removed.

At 7 TeV, this overlap/double-counting between trident electrons and fake electrons is estimated and removed by applying the matrix method to the same-sign events with a dilepton mass inside the Z-peak, which is dominated by trident electrons. The result of this estimation indicates that around 22% of mis-id events are captured as fake background. Since trident electron background is estimated independently from the jet background, the estimated mis-identification of the electron charge is scaled down to 78% to remove the overlap between the two estimates.

At 8 TeV, the overlap is determined by recalculating the charge mis-identification rates with the estimated fake electron contribution removed from the *tight* selection[8]. The correction factor is determined by taking the ratio between the rates computed with all *tight* electrons and the recalculated rates. This factor is a function of $|\eta|$ and p_{T} as shown in Fig. 7.13.

[8] Just to remember, the mis-identification rates obtained in Section 7.3.2.5 have been computed using *tight* electrons which fill all the requirements as in the analysis.

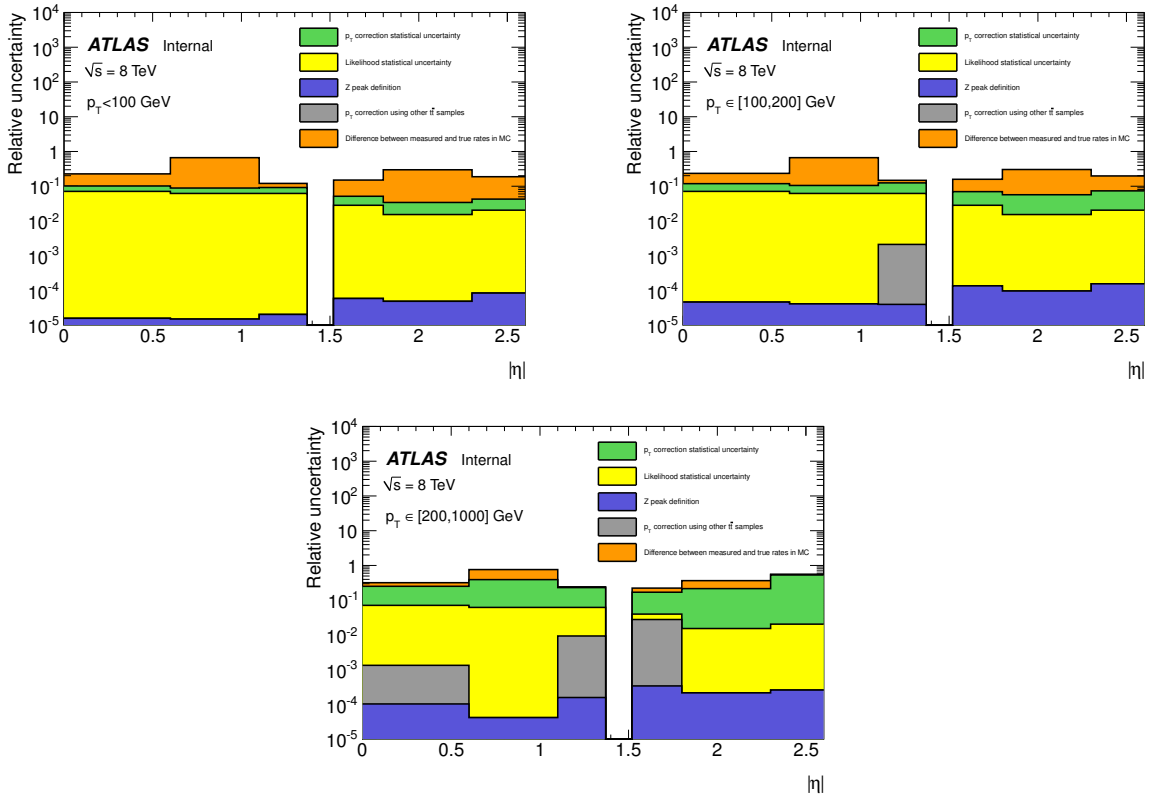

Figure 7.12: Relative systematic uncertainty contributions on the charge mis-identification rate, for different bins in p_{T} and $|\eta|$.

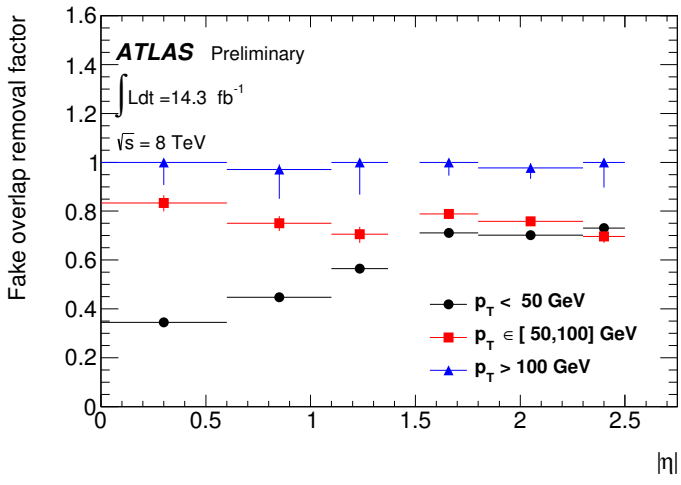

Figure 7.13: Factor to be binwise applied to charge mis-id rates to compensate for the double-counting with background from fakes estimate [17].

7.4 Background validation

In order to validate the estimation of the SM background processes, several control regions are examined. Control regions are orthogonal to the signal selection and defined by selections that suppress as much as possible signal contributions. As this analysis aims to look for objects with high H_{T}, some $E_{\mathrm{T}}^{\mathrm{miss}}$, and b-tagged jets, each control region has been defined basically by looking for a low H_{T}, by inverting the cut on $E_{\mathrm{T}}^{\mathrm{miss}}$ with respect to the event preselection, or asking for no b-tagged jets. Then, the background estimation in this region is compared with the recorded data. The control regions defined for the analysis at 7 TeV and 8 TeV are defined in the following sections.

7.4.1 Control regions at $\sqrt{s} = 7$ TeV

Four different control regions have been defined in the analysis at 7 TeV. Three of them are related to the low H_{T} region, the other one aims for a comparison of data and expected background in the high H_{T} region. These control regions are defined below.

7.4.1.1 Control region 1

This is the main control region (named here $E_{\mathrm{T}}^{\mathrm{miss}}$ control region). It aims to compare the recorded data with the estimated background in a low H_{T} region. The cut on $E_{\mathrm{T}}^{\mathrm{miss}}$ has been removed in order to increase the statistics and to validate the $E_{\mathrm{T}}^{\mathrm{miss}}$ distribution. It requires the following event selection:

- Events must contain at least one same-sign pair of leptons.
- Events must contain at least one b-tagged jet.
- Z veto in the ee and $\mu\mu$ channels.
- $H_{\mathrm{T}} \in [100, 500]$ GeV.

The distributions of some kinematical variables for the background estimation and the data after applying this selection are shown in Figures 7.14, 7.15 and 7.16, for the ee, $e\mu$ and $\mu\mu$ channels, respectively. The inner shaded areas correspond to the statistical uncertainties. For the outer shaded areas, the systematic uncertainties on the production cross-sections for the Monte Carlo samples, and global systematic uncertainties for the data-driven backgrounds are included. This is also valid for all the distributions of the kinematical variables shown in this chapter. The estimation of these uncertainties is explained in Chapter 8. The agreement between the measured number of events and the predicted ones from the background estimation is reasonable. The significance does not exceed 3σ. The total number of events observed in data and predicted by the background estimation for this first control region are shown in Table 7.4: they are compatible within the uncertainties. In order to investigate the small discrepancy in the $e\mu$ channel, the low H_{T} region has been restricted to $H_{\mathrm{T}} \in [400, 500]$ GeV since this analysis focuses on high H_{T}. The results are in Table 7.5, where the agreement is better, although the statistics is very small.

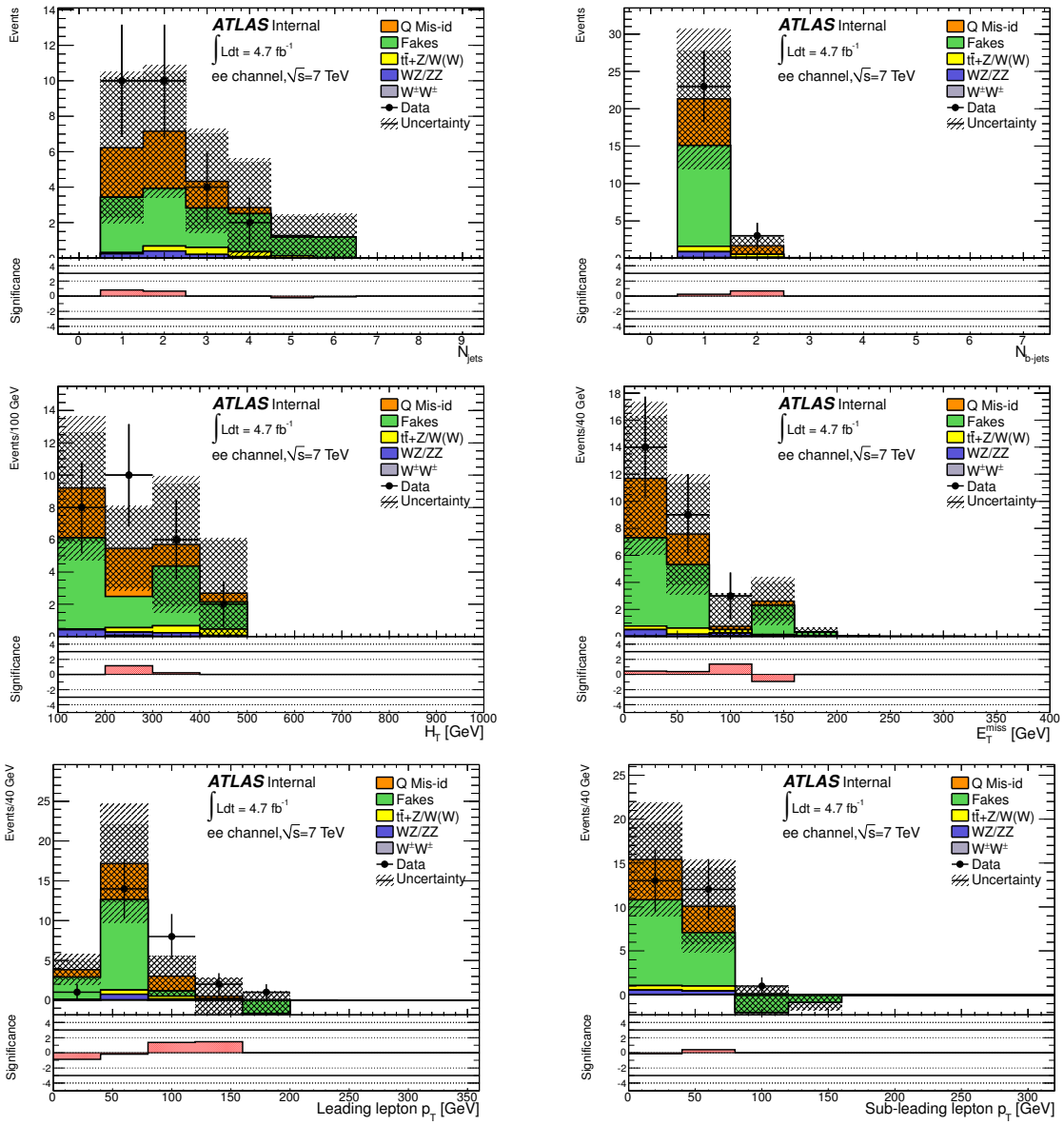

Figure 7.14: Distributions of some kinematical variables in the *ee* channel after the $E_{\mathrm{T}}^{\mathrm{miss}}$ control region selection at $\sqrt{s} = 7$ TeV for both the background estimation and the data. The bottom plots show the significance of the measured number of events in the data compared to the estimated number of events from the backgrounds.

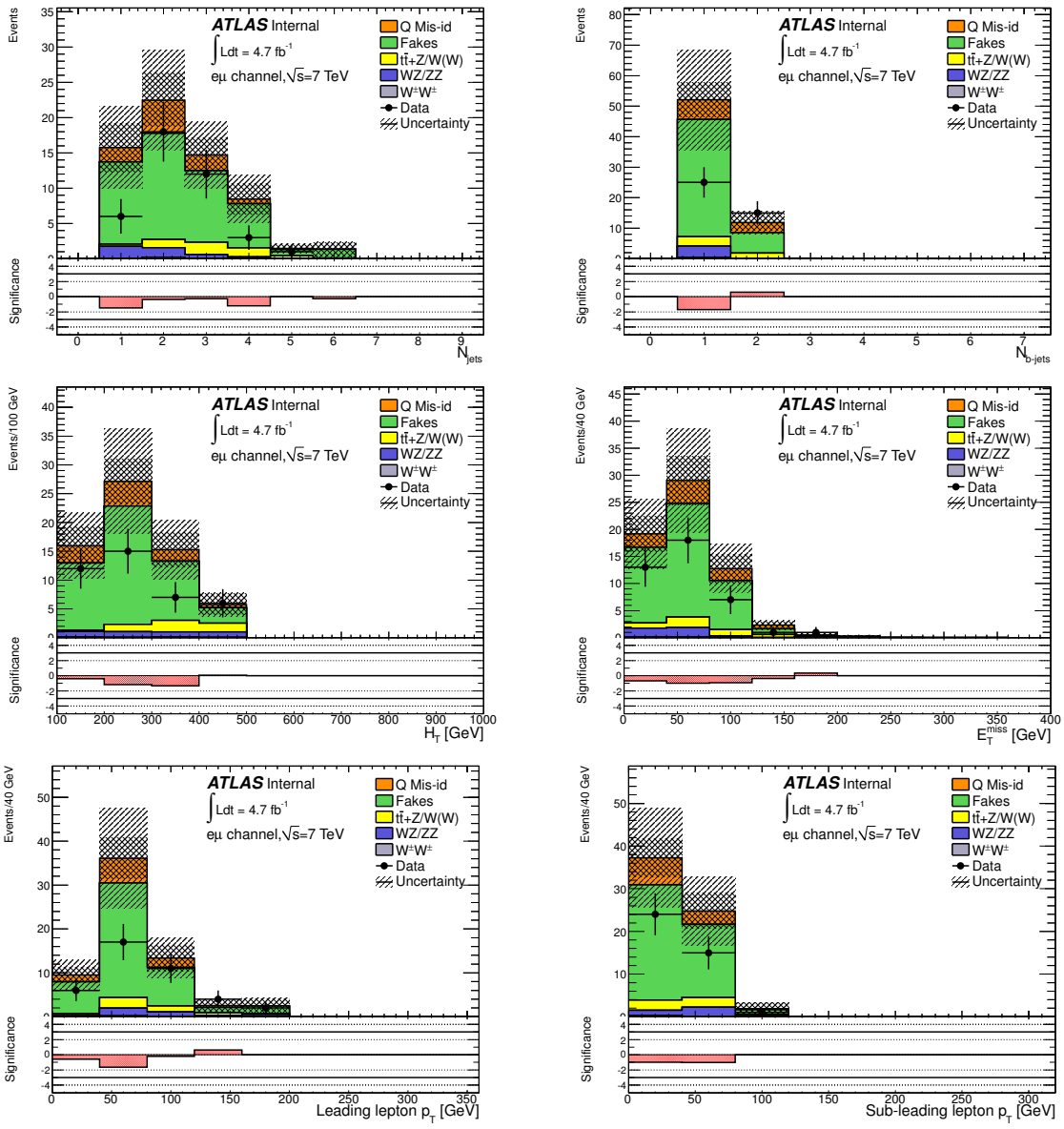

Figure 7.15: Distributions of some kinematical variables in the $e\mu$ channel after the $E_{\mathrm{T}}^{\mathrm{miss}}$ control region selection at $\sqrt{s} = 7$ TeV for both the background estimation and the data. The bottom plots show the significance of the measured number of events in the data compared to the estimated number of events from the backgrounds.

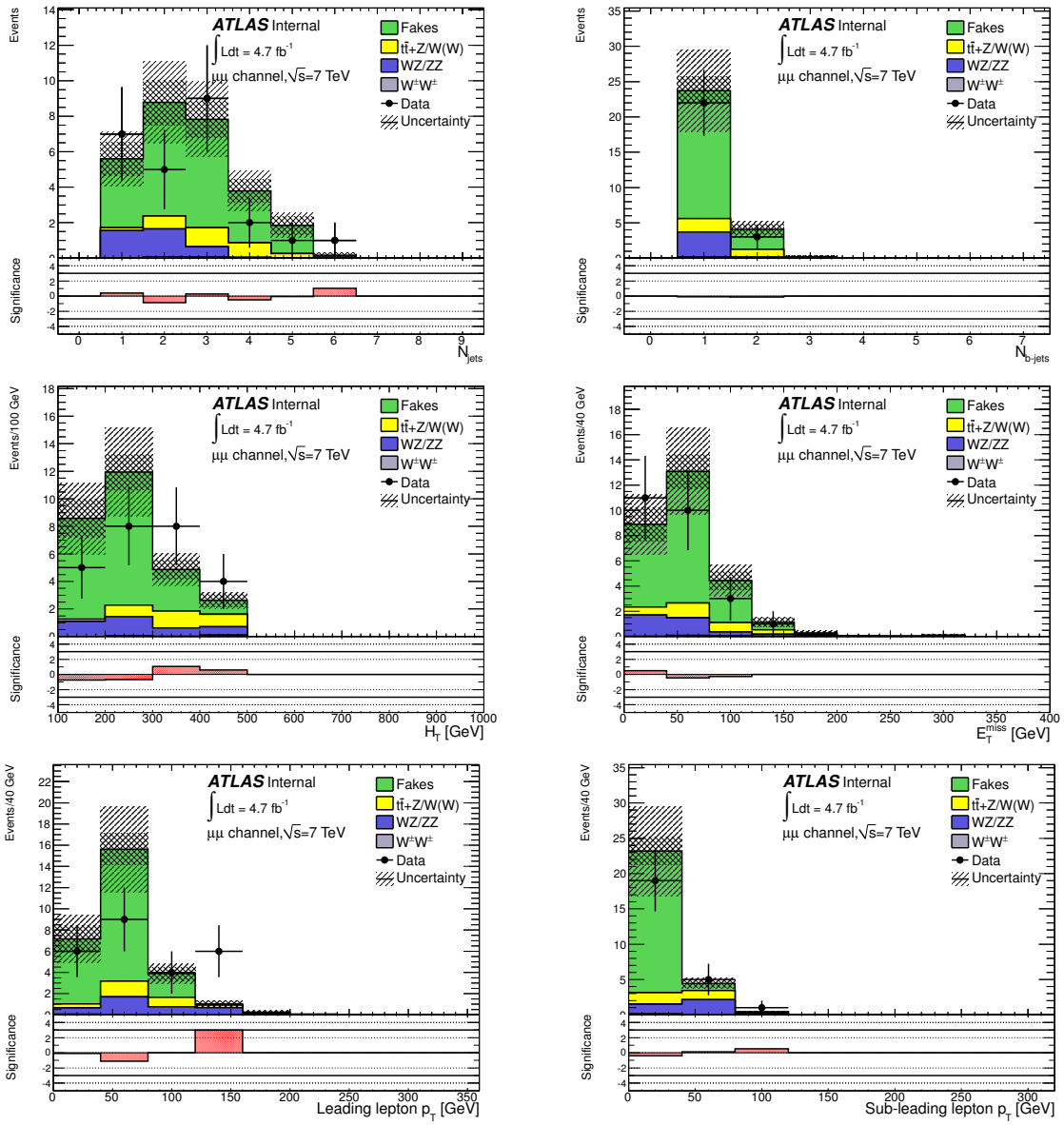

Figure 7.16: Distributions of some kinematical variables in the $\mu\mu$ channel after the $E_{\mathrm{T}}^{\mathrm{miss}}$ control region selection at $\sqrt{s} = 7$ TeV for both the background estimation and the data. The bottom plots show the significance of the measured number of events in the data compared to the estimated number of events from the backgrounds.

Samples	Channel		
	ee	$e\mu$	$\mu\mu$
Q Mis-id	$8.1 \pm 0.3 \pm 1.0$	$10.0 \pm 0.3 \pm 1.2$	—
Fakes	$13.1 \pm 6.6 \pm 6.6$	$45.8 \pm 6.2 \pm 18.3$	$21.3 \pm 2.0 \pm 6.4$
Diboson			
• $WZ/ZZ(+jets)$	$0.92 \pm 0.26 \pm 0.17$	$3.89 \pm 0.55 \pm 0.62$	$3.74 \pm 0.51 \pm 0.60$
• $W^{\pm}W^{\pm}jj$	$0.08 \pm 0.03 \pm 0.04$	$0.32 \pm 0.07 \pm 0.16$	$0.15 \pm 0.04 \pm 0.07$
$t\bar{t} + W/Z$			
• $t\bar{t}W(j)$	$0.82 \pm 0.04 \pm 0.18$	$3.6 \pm 0.1 \pm 0.8$	$2.18 \pm 0.07 \pm 0.48$
• $t\bar{t}Z(j)$	$0.33 \pm 0.02 \pm 0.12$	$1.40 \pm 0.05 \pm 0.51$	$0.92 \pm 0.04 \pm 0.34$
• $t\bar{t}W^{+}W^{-}$	$0.008 \pm 0.001 \pm 0.002$	$0.033 \pm 0.001 \pm 0.010$	$0.025 \pm 0.001 \pm 0.007$
Total	$23.4 \pm 6.6 \pm 6.7$	$65.1 \pm 6.2 \pm 18.4$	$28.3 \pm 2.1 \pm 6.5$
Observed	26	40	25
Signal contamination			
• $t\bar{t}t\bar{t}$ C.I.	0.012 ± 0.003	0.046 ± 0.005	0.027 ± 0.004
($C/\Lambda^2 = -4\pi$ TeV^{-2})			

Table 7.4: Observed number of events and expected number of background events with statistical (first) and systematic (second) uncertainties for the first control region selection at 7 TeV. The signal contamination in this region is also shown. For the Monte Carlo samples, the systematic uncertainties include only the production cross section uncertainty.

Samples	Channel		
	ee	$e\mu$	$\mu\mu$
Q Mis-id	$0.56 \pm 0.08 \pm 0.07$	$0.54 \pm 0.05 \pm 0.06$	—
Fakes	$1.70 \pm 3.33 \pm 0.85$	$2.73 \pm 1.81 \pm 1.09$	$1.04 \pm 0.40 \pm 0.31$
Diboson			
• $WZ/ZZ(+jets)$	$0.07 \pm 0.19 \pm 0.02$	$0.94 \pm 0.33 \pm 0.15$	$0.62 \pm 0.24 \pm 0.14$
• $W^{\pm}W^{\pm}jj$	0 ± 0.01	$0.08 \pm 0.03 \pm 0.04$	$0.09 \pm 0.03 \pm 0.05$
$t\bar{t} + W/Z$			
• $t\bar{t}W(+jet)$	$0.23 \pm 0.02 \pm 0.05$	$0.95 \pm 0.05 \pm 0.20$	$0.54 \pm 0.03 \pm 0.12$
• $t\bar{t}Z(+jet)$	$0.15 \pm 0.02 \pm 0.06$	$0.56 \pm 0.03 \pm 0.20$	$0.34 \pm 0.03 \pm 0.12$
• $t\bar{t}W^{+}W^{-}$	$0.004 \pm 0.001 \pm 0.001$	$0.015 \pm 0.001 \pm 0.005$	$0.012 \pm 0.001 \pm 0.003$
Total	$2.72 \pm 3.34 \pm 0.86$	$5.82 \pm 1.84 \pm 1.14$	$2.64 \pm 0.47 \pm 0.38$
Observed	2	6	4
Signal contamination			
• $t\bar{t}t\bar{t}$ C.I.	0.009 ± 0.002	0.034 ± 0.005	0.018 ± 0.003
($C/\Lambda^2 = -4\pi$ TeV^{-2})			

Table 7.5: Observed number of events and expected number of background events with statistical (first) and systematic (second) uncertainties for the first control region selection at 7 TeV, restricting to the region $H_{\mathrm{T}} \in [400, 500]$ GeV. The signal contamination in this region is also shown. For the Monte Carlo samples, the systematic uncertainties include only the production cross section uncertainty.

7.4.1.2 Control region 2

This control region is defined as the first one, but requesting at least two jets in the event. The distributions of some kinematical variables for the background estimation and the data after applying this selection are shown in Figures 7.17, 7.18 and 7.19, for the ee, $e\mu$ and $\mu\mu$ channels, respectively. Despite the low statistics the agreement between the expected background and data is even better than in the first control region. Again, the significance does not exceed 3σ. The total number of events observed in data and predicted by the background estimation for this second control region are shown in Table 7.6. There is a good agreement within the uncertainties.

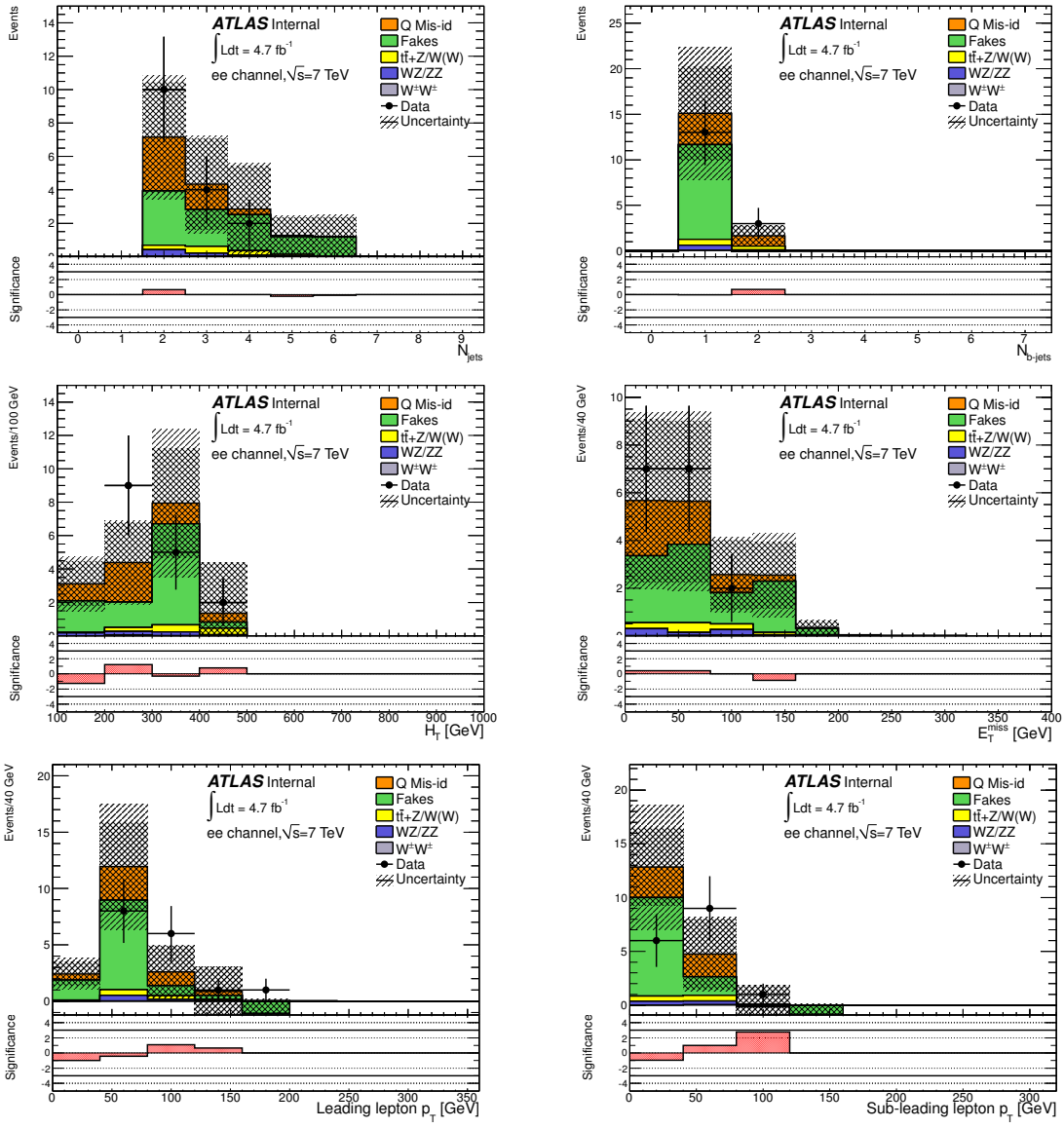

Figure 7.17: Distributions of some kinematical variables in the ee channel after the second control region selection at $\sqrt{s} = 7$ TeV for both the background estimation and the data. The bottom plots show the significance of the measured number of events in the data compared to the estimated number of events from the backgrounds.

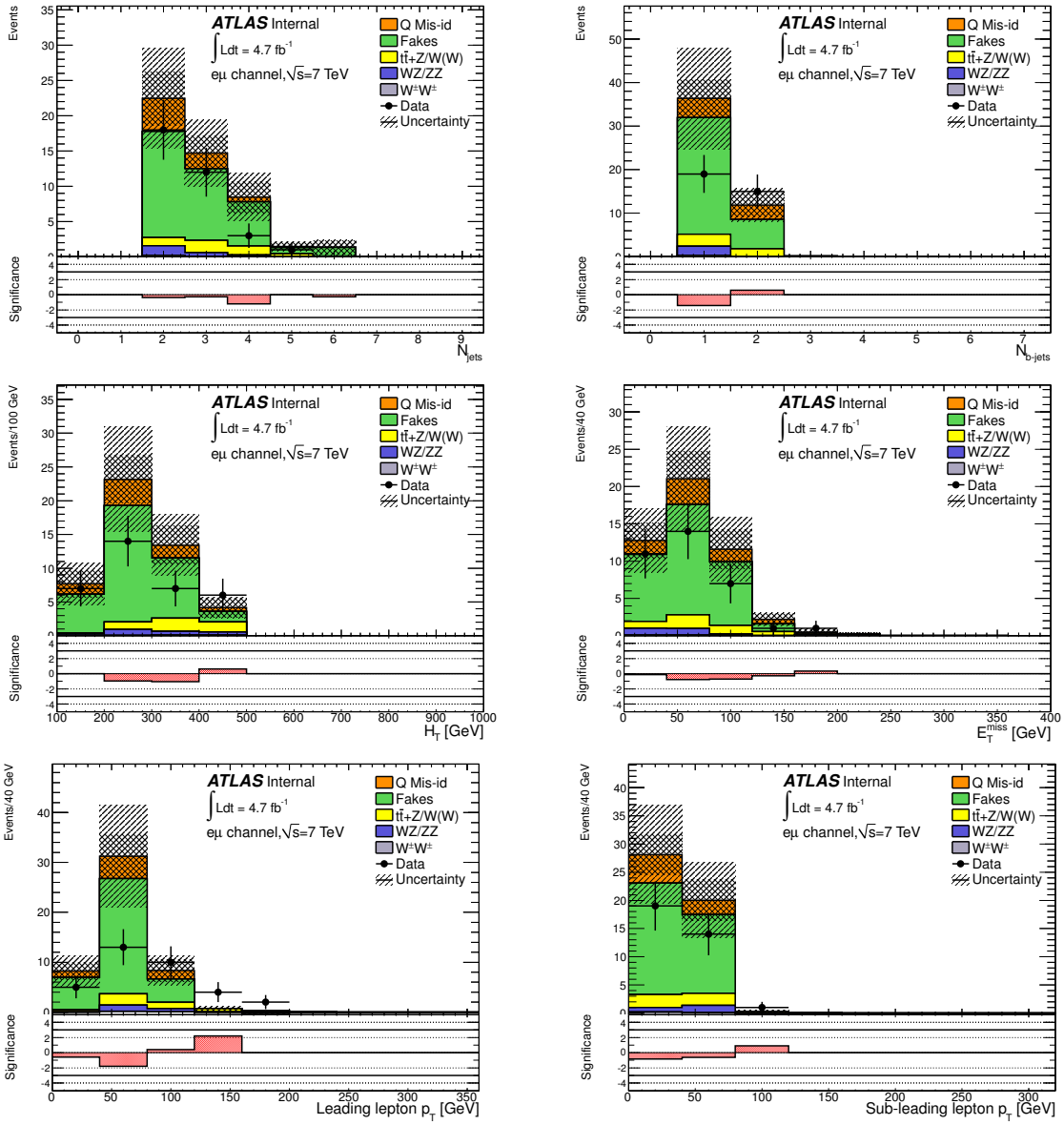

Figure 7.18: Distributions of some kinematical variables in the $e\mu$ channel after the second control region selection at $\sqrt{s} = 7$ TeV for both the background estimation and the data. The bottom plots show the significance of the measured number of events in the data compared to the estimated number of events from the backgrounds.

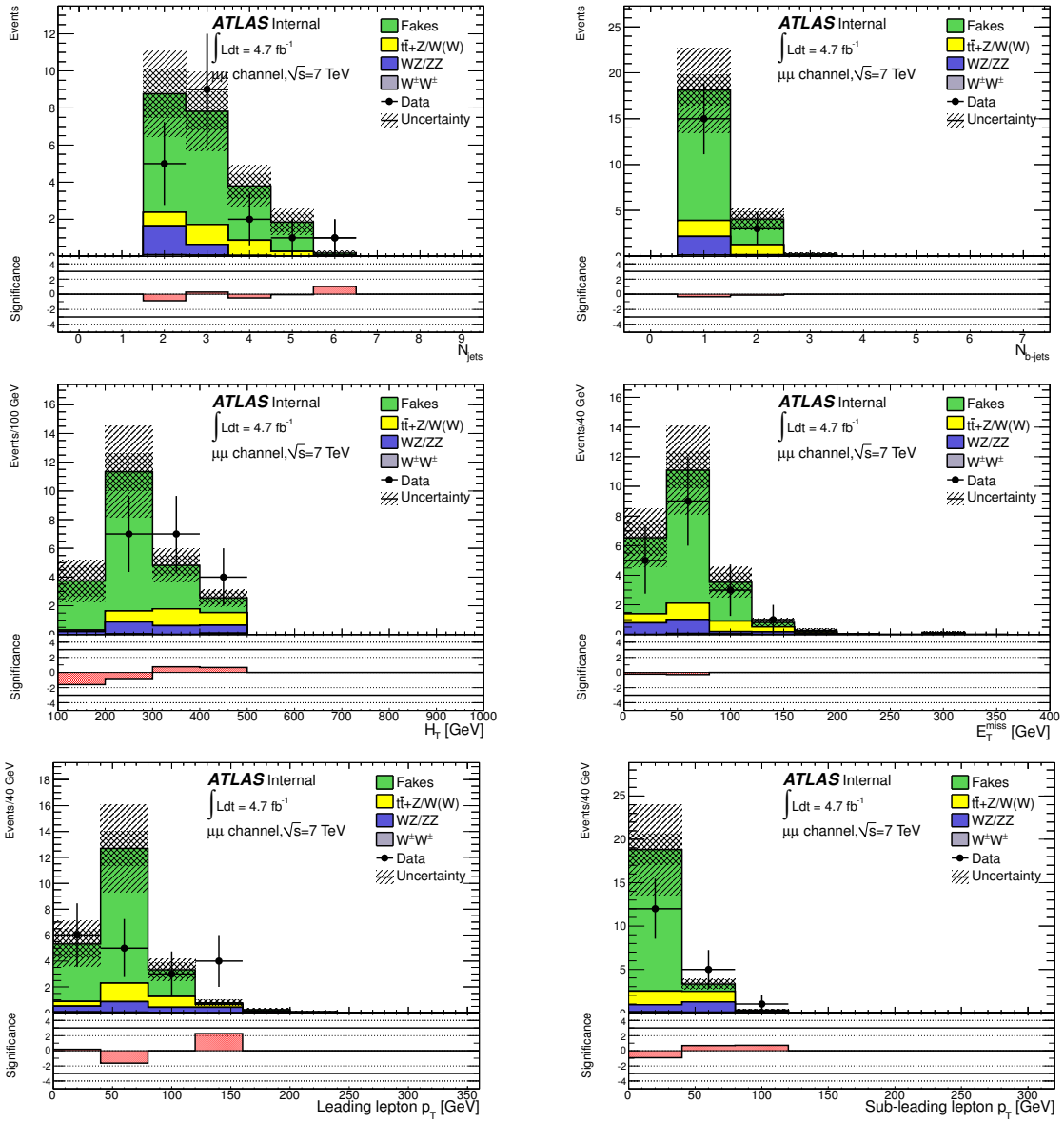

Figure 7.19: Distributions of some kinematical variables in the $\mu\mu$ channel after the second control region selection at $\sqrt{s} = 7$ TeV for both the background estimation and the data. The bottom plots show the significance of the measured number of events in the data compared to the estimated number of events from the backgrounds.

Samples	Channel		
	ee	eμ	$\mu\mu$
Q Mis-id	$5.2 \pm 0.3 \pm 0.6$	$7.9 \pm 0.3 \pm 1.0$	—
Fakes	$10.0 \pm 5.3 \pm 5.0$	$34.0 \pm 5.2 \pm 13.6$	$17.4 \pm 1.8 \pm 5.2$
Diboson			
• $WZ/ZZ(+jets)$	$0.69 \pm 0.23 \pm 0.12$	$2.15 \pm 0.36 \pm 0.37$	$2.17 \pm 0.40 \pm 0.44$
• $W^{\pm}W^{\pm}jj$	$0.06 \pm 0.03 \pm 0.03$	$0.27 \pm 0.06 \pm 0.14$	$0.15 \pm 0.04 \pm 0.07$
$t\bar{t} + W/Z$			
• $t\bar{t}W(+jet)$	$0.77 \pm 0.04 \pm 0.17$	$3.34 \pm 0.09 \pm 0.73$	$2.06 \pm 0.07 \pm 0.45$
• $t\bar{t}Z(+jet)$	$0.32 \pm 0.02 \pm 0.12$	$1.33 \pm 0.05 \pm 0.48$	$0.88 \pm 0.04 \pm 0.32$
• $t\bar{t}W^{+}W^{-}$	$0.008 \pm 0.001 \pm 0.002$	$0.033 \pm 0.001 \pm 0.010$	$0.024 \pm 0.001 \pm 0.007$
Total	$17.0 \pm 5.3 \pm 5.0$	$49.0 \pm 5.2 \pm 13.7$	$22.7 \pm 1.8 \pm 5.2$
Observed	16	34	18
Signal contamination			
• $t\bar{t}t\bar{t}$ C.I.	0.012 ± 0.003	0.046 ± 0.005	0.027 ± 0.004
($C/\Lambda^2 = -4\pi$ TeV^{-2})			

Table 7.6: Observed number of events and expected number of background events with statistical (first) and systematic (second) uncertainties for the second control region selection at 7 TeV. The signal contamination in this region is also shown. For the Monte Carlo samples, the systematic uncertainties include only the production cross section uncertainty.

7.4.1.3 Control region 3

The third control region is defined as the second one, but with the additional requirement of $E_{\mathrm{T}}^{\mathrm{miss}} > 40$ GeV. The distributions of some kinematical variables for the background estimation and the data after applying this selection are shown in Figures 7.20, 7.21 and 7.22, for the ee, $e\mu$ and $\mu\mu$ channels, respectively. In terms of significance there is a better agreement than in the previous control regions since it does not exceed 2σ. The total number of events observed in data and predicted by the background estimation for this third control region are shown in Table 7.7. They are compatible within the uncertainties.

7.4.1.4 Control region 4

A last control region is defined, but this time in the high H_{T} region. It requires the following selection:

- Events must contain at least one same-sign pair of leptons.
- Events must contain at least one b-tagged jet. There is no other requirement on the number of jets.
- Z veto in ee and $\mu\mu$ channels.
- $H_{\mathrm{T}} > 400$ GeV and $E_{\mathrm{T}}^{\mathrm{miss}} < 40$ GeV.

In this control region, the statistics here is very low as to show distributions. The total number of events observed in data and predicted by the background estimation for this fourth control region are shown in Table 7.8. They are compatible within the uncertainties.

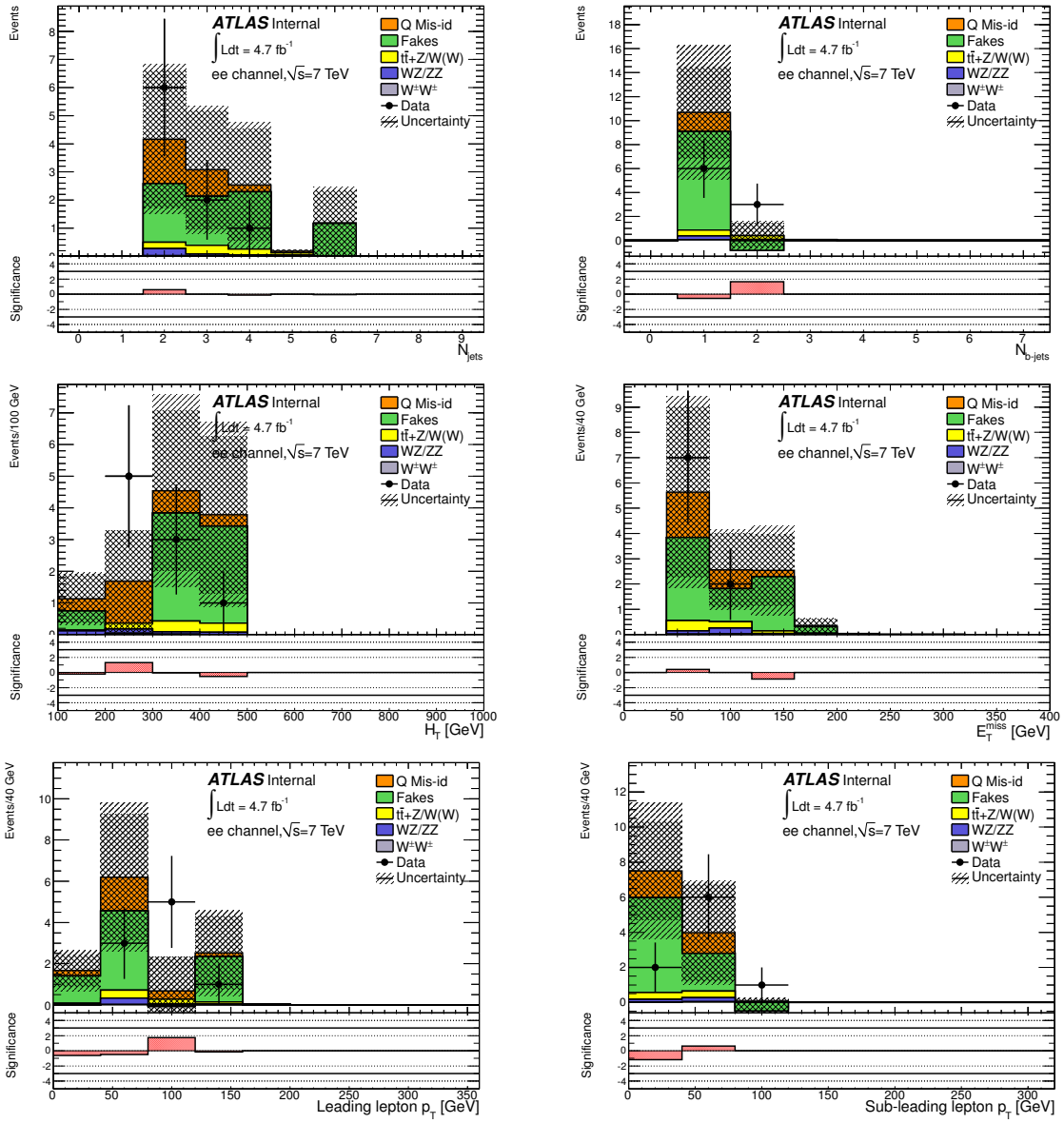

Figure 7.20: Distributions of some kinematical variables in the *ee* channel after the third control region selection at $\sqrt{s} = 7$ TeV for both the background estimation and the data. The bottom plots show the significance of the measured number of events in the data compared to the estimated number of events from the backgrounds

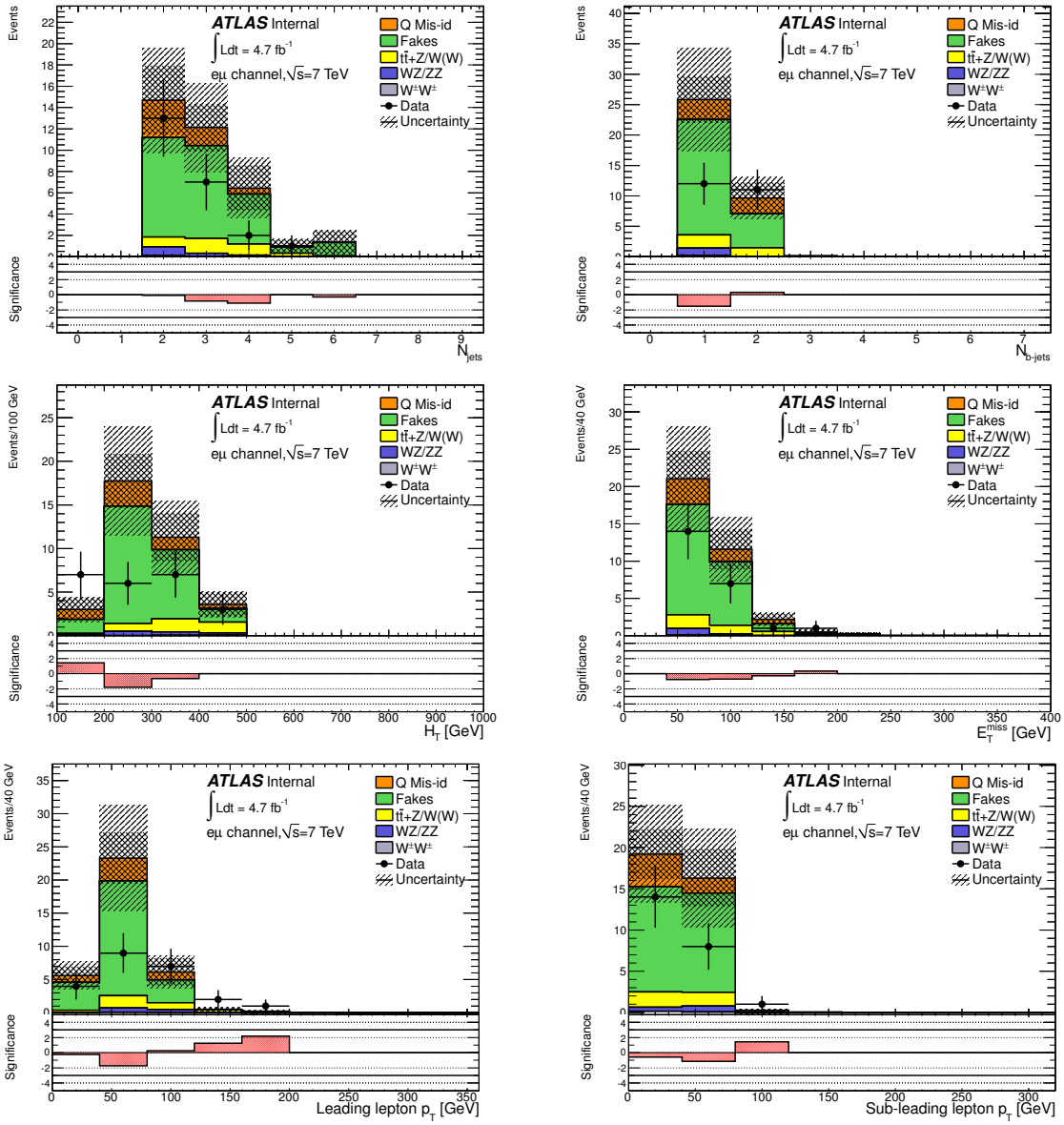

Figure 7.21: Distributions of some kinematical variables in the $e\mu$ channel after the third control region selection at $\sqrt{s} = 7$ TeV for both the background estimation and the data. The bottom plots show the significance of the measured number of events in the data compared to the estimated number of events from the backgrounds.

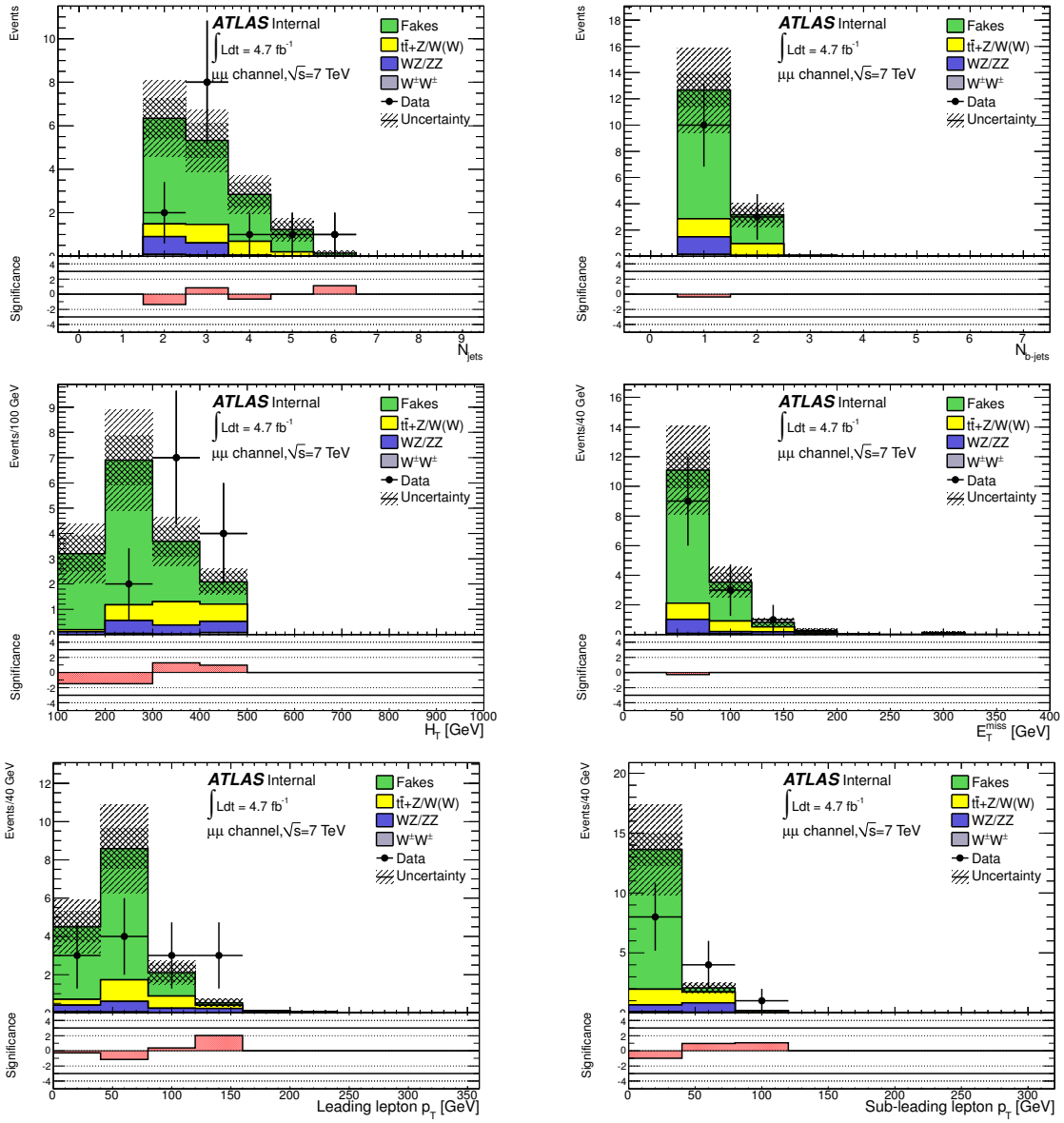

Figure 7.22: Distributions of some kinematical variables in the $\mu\mu$ channel after the third control region selection at $\sqrt{s} = 7$ TeV for both the background estimation and the data. The bottom plots show the significance of the measured number of events in the data compared to the estimated number of events from the backgrounds.

Samples	Channel		
	ee	$e\mu$	$\mu\mu$
Q Mis-id	$2.88 \pm 0.17 \pm 0.35$	$6.01 \pm 0.24 \pm 0.72$	—
Fakes	$7.10 \pm 3.99 \pm 3.55$	$24.9 \pm 4.6 \pm 9.9$	$12.2 \pm 1.4 \pm 3.6$
Diboson			
• $WZ/ZZ(+jets)$	$0.40 \pm 0.21 \pm 0.08$	$1.21 \pm 0.29 \pm 0.23$	$1.40 \pm 0.33 \pm 0.28$
• $W^{\pm}W^{\pm}jj$	$0.05 \pm 0.03 \pm 0.03$	$0.19 \pm 0.05 \pm 0.09$	$0.13 \pm 0.04 \pm 0.07$
$t\bar{t} + W/Z$			
• $t\bar{t}W(+jet)$	$0.61 \pm 0.04 \pm 0.14$	$2.72 \pm 0.08 \pm 0.59$	$1.66 \pm 0.06 \pm 0.36$
• $t\bar{t}Z(+jet)$	$0.23 \pm 0.02 \pm 0.09$	$1.03 \pm 0.04 \pm 0.37$	$0.66 \pm 0.03 \pm 0.24$
• $t\bar{t}W^{+}W^{-}$	$0.006 \pm 0.001 \pm 0.002$	$0.028 \pm 0.001 \pm 0.008$	$0.021 \pm 0.001 \pm 0.006$
Total	$11.3 \pm 4.0 \pm 3.6$	$36.1 \pm 4.6 \pm 10.0$	$16.1 \pm 1.4 \pm 3.6$
Observed	9	23	13
Signal contamination			
• $t\bar{t}t\bar{t}$ C.I.	0.010 ± 0.002	0.039 ± 0.005	0.022 ± 0.004
($C/\Lambda^2 = -4\pi$ TeV^{-2})			

Table 7.7: Observed number of events and expected number of background events with statistical (first) and systematic (second) uncertainties for the third control region selection at 7 TeV. The signal contamination in this region is also shown. For the Monte Carlo samples, the systematic uncertainties include only the production cross section uncertainty.

Samples	Channel		
	ee	eμ	$\mu\mu$
Q Mis-id	$0.33 \pm 0.08 \pm 0.04$	$0.17 \pm 0.04 \pm 0.02$	—
Fakes	$2.28 \pm 3.21 \pm 1.14$	$1.19 \pm 1.19 \pm 0.48$	$0.71 \pm 0.32 \pm 0.21$
Diboson			
• $WZ/ZZ(+jets)$	$0.20 \pm 0.21 \pm 0.05$	$0.92 \pm 0.33 \pm 0.15$	$0.25 \pm 0.19 \pm 0.06$
• $W^{\pm}W^{\pm}jj$	0 ± 0.01	$0.014 \pm 0.014 \pm 0.007$	$0.03 \pm 0.02 \pm 0.01$
$t\bar{t} + W/Z$			
• $t\bar{t}W(+jet)$	$0.10 \pm 0.02 \pm 0.02$	$0.31 \pm 0.03 \pm 0.07$	$0.18 \pm 0.02 \pm 0.04$
• $t\bar{t}Z(+jet)$	$0.10 \pm 0.01 \pm 0.03$	$0.33 \pm 0.02 \pm 0.12$	$0.22 \pm 0.02 \pm 0.08$
• $t\bar{t}W^{+}W^{-}$	$0.0022 \pm 0.0004 \pm 0.0007$	$0.0064 \pm 0.0007 \pm 0.0019$	$0.0046 \pm 0.0005 \pm 0.0014$
Total	$3.01 \pm 3.22 \pm 1.14$	$2.94 \pm 1.24 \pm 0.52$	$1.39 \pm 0.37 \pm 0.24$
Observed	1	4	0
Signal contamination			
• $t\bar{t}t\bar{t}$ C.I.	0.018 ± 0.004	0.058 ± 0.006	0.041 ± 0.005
($C/\Lambda^2 = -4\pi$ TeV^{-2})			

Table 7.8: Observed number of events and expected number of background events with statistical (first) and systematic (second) uncertainties for the fourth control region selection at 7 TeV. The signal contamination in this region is also shown. For the Monte Carlo samples, the systematic uncertainties include only the production cross section uncertainty.

7.4.2 Control regions at $\sqrt{s} = 8$ TeV

Three different control regions have been defined in the analysis at 8 TeV. They allow to control the $E_{\mathrm{T}}^{\mathrm{miss}}$, H_{T}, and both distributions at the same time. They are defined as explained below.

7.4.2.1 Control region 1

This control region has been defined similarly as the $E_{\mathrm{T}}^{\mathrm{miss}}$ control region as for the analysis at 7 TeV, but it restricts a little more the low H_{T} region. It requires the following event selection:

- Events must contain exactly one same-sign pair of leptons.
- Events must contain at least two jets with one b-tagged jet
- Z veto in the ee and $\mu\mu$ channels.
- $H_{\mathrm{T}} \in [100, 400]$ GeV.

The distributions of some kinematical variables for the background estimation and the data after applying this selection are shown in Figures 7.23, 7.24 and 7.25, for the ee, $e\mu$ and $\mu\mu$ channels, respectively. The total number of events observed in data and predicted by the background estimation for this first control region are shown in Table 7.9. A good agreement within uncertainties is observed.

	Channel		
Samples	ee	$e\mu$	$\mu\mu$
Q Mis-id	$25.66 \pm 0.68 \pm 6.64$	$30.24 \pm 0.64 \pm 7.92$	—
Fakes	$38.7 \pm 3.67 \pm 11.6$	$73.1 \pm 5.3 \pm 21.9$	$33.4 \pm 8.5 \pm 10.0$
Diboson			
• $WZ/ZZ(+jets)$	$3.85 \pm 0.68 \pm 1.31$	$10.92 \pm 1.22 \pm 3.71$	$5.10 \pm 0.82 \pm 1.73$
• $W^{\pm}W^{\pm}jj$	$0.43 \pm 0.16 \pm 0.22$	$1.18 \pm 0.26 \pm 0.59$	$0.75 \pm 0.20 \pm 0.38$
$t\bar{t} + W/Z$			
• $t\bar{t}W(+jet(s))$	$1.65 \pm 0.10 \pm 0.50$	$6.6 \pm 0.2 \pm 2.0$	$4.31 \pm 0.17 \pm 1.29$
• $t\bar{t}Z(+jet(s))$	$0.48 \pm 0.05 \pm 0.14$	$1.50 \pm 0.09 \pm 0.45$	$0.79 \pm 0.06 \pm 0.24$
• $t\bar{t}W^{+}W^{-}$	0.014 ± 0.002	0.050 ± 0.004	0.029 ± 0.003
Total	$71 \pm 5 \pm 13$	$124 \pm 8 \pm 24$	$44 \pm 11 \pm 10$
Observed	64	97	38
Signal contamination			
• $t\bar{t}t\bar{t}$ C.I.	0.009 ± 0.005	0.06 ± 0.02	0.02 ± 0.01
($C/\Lambda^2 = -4\pi$ TeV^{-2})			

Table 7.9: Observed number of events and expected number of background events with statistical (first) and systematic (second) uncertainties for the $E_{\mathrm{T}}^{\mathrm{miss}}$ control region selection at 8 TeV. The signal contamination in this region is also shown. For the Monte Carlo samples, the systematic uncertainties include only the production cross section uncertainty

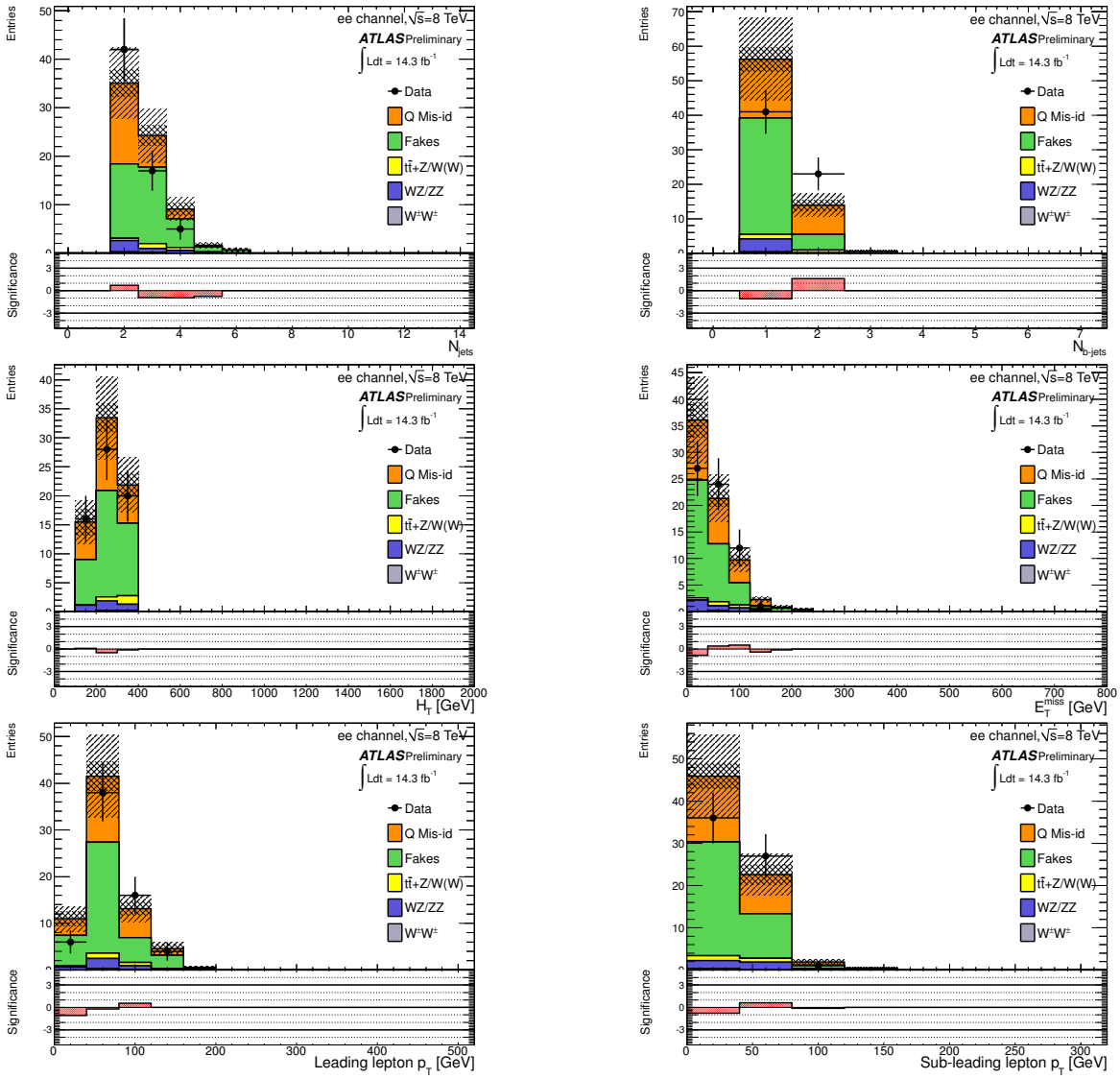

Figure 7.23: Distributions of some kinematical variables in the *ee* channel, after the $E_{\mathrm{T}}^{\mathrm{miss}}$ control region selection at 8 TeV, for both the background estimation and the data. The bottom plots show the significance of the measured number of events in the data compared to the estimated number of events from the backgrounds.

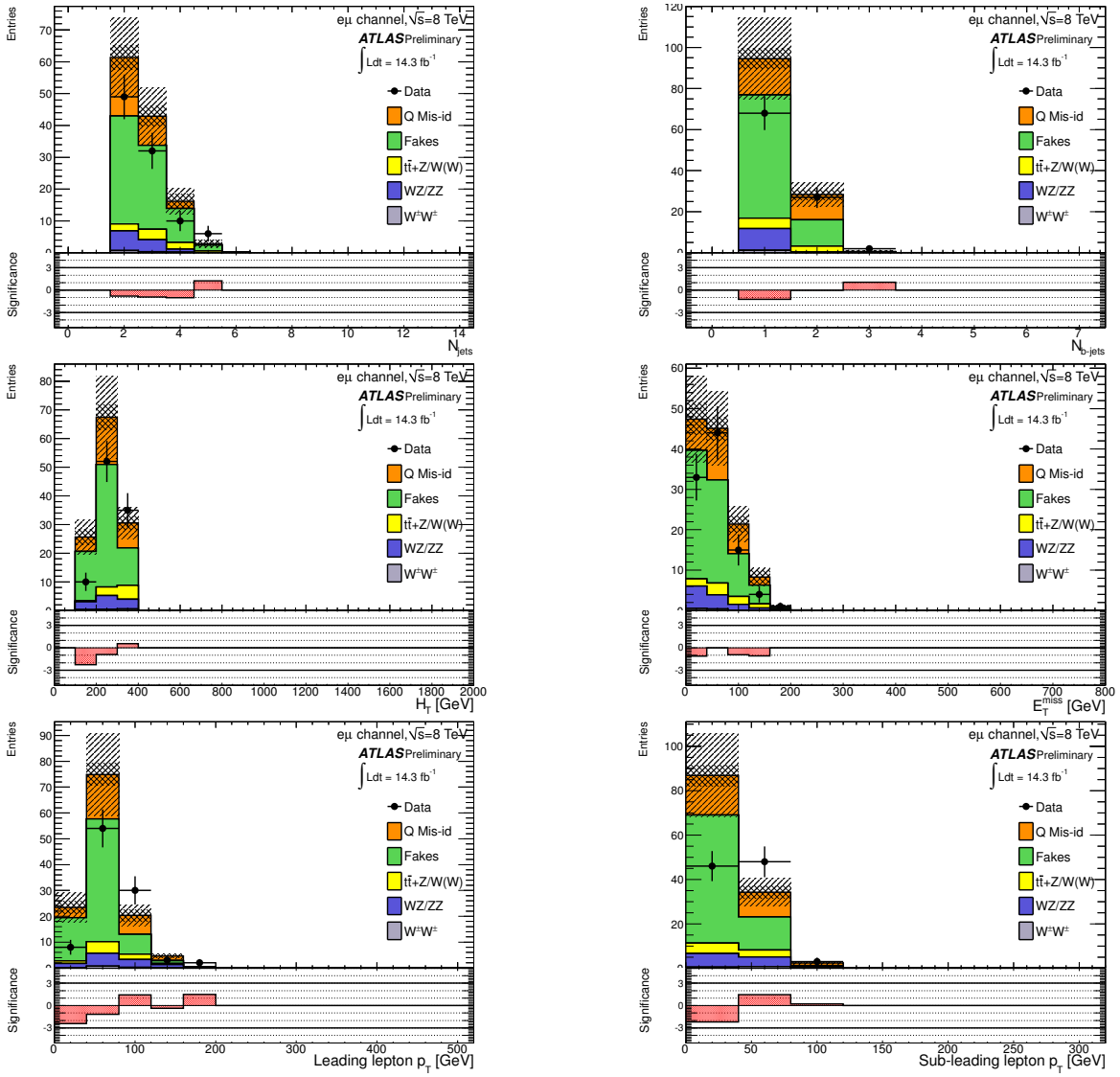

Figure 7.24: Distributions of some kinematical variables in the $e\mu$ channel, after the $E_{\mathrm{T}}^{\mathrm{miss}}$ control region selection at 8 TeV, for both the background estimation and the data. The bottom plots show the significance of the measured number of events in the data compared to the estimated number of events from the backgrounds.

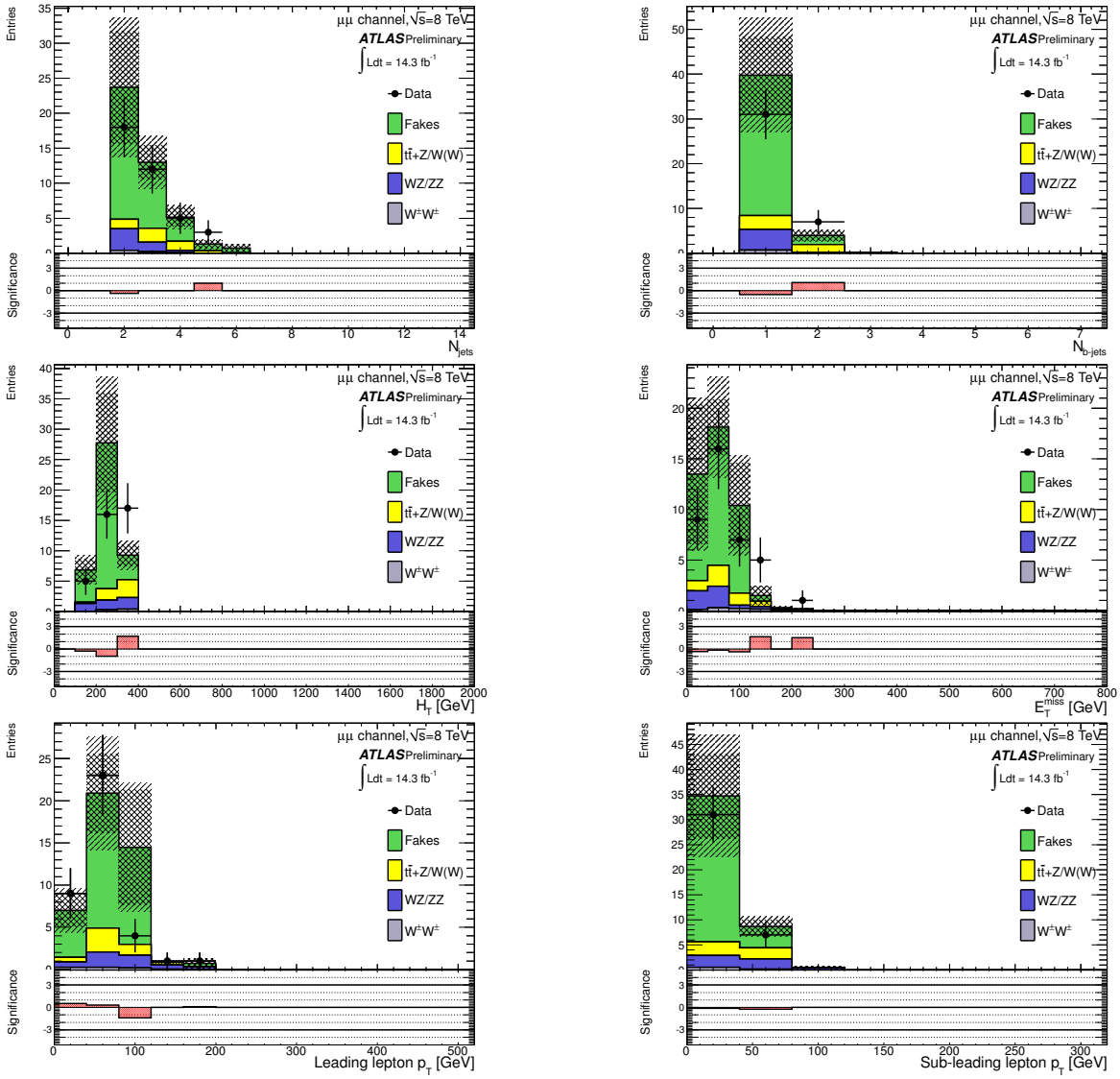

Figure 7.25: Distributions of some kinematical variables in the $\mu\mu$ channel, after the $E_{\mathrm{T}}^{\mathrm{miss}}$ control region selection at 8 TeV, for both the background estimation and the data. The bottom plots show the significance of the measured number of events in the data compared to the estimated number of events from the backgrounds.

7.4.2.2 Control region 2

The second control region is called "H_{T} control region". The event selection is the following:

- Events must contain exactly one same-sign pair of leptons.
- Events must contain at least two jets with one b-tagged jet.
- Z veto in the ee or $\mu\mu$ channel.
- $E_{\mathrm{T}}^{\mathrm{miss}} < 40$ GeV.
- $H_{\mathrm{T}} > 100$ GeV.

Comparing to the event preselection, the cut on H_{T} has been removed, and the one on $E_{\mathrm{T}}^{\mathrm{miss}}$ has been reverted. Therefore, this region allows to control the H_{T} distribution, but in a low $E_{\mathrm{T}}^{\mathrm{miss}}$ region. The distributions of some kinematic variables for the background estimation and the data after applying this H_{T} control region selection are shown in Figures 7.26, 7.27 and 7.28 for the ee, $e\mu$ and $\mu\mu$ channels, respectively. The total number of events observed in data and predicted by the background estimation for this second control region are shown in Table 7.10. Again, the agreement between the measured number of events and the predicted one from the background estimation is good.

	Channel		
Samples	ee	$e\mu$	$\mu\mu$
Q Mis-id	$13.29 \pm 0.52 \pm 3.54$	$9.27 \pm 0.37 \pm 2.47$	—
Fakes	$24.27 \pm 3.33 \pm 7.28$	$34.0 \pm 3.9 \pm 10.2$	$11.69 \pm 6.86 \pm 3.51$
Diboson			
• $WZ/ZZ(+jets)$	$2.60 \pm 0.56 \pm 0.88$	$7.09 \pm 0.97 \pm 2.41$	$2.40 \pm 0.59 \pm 0.82$
• $W^{\pm}W^{\pm}jj$	$0.09 \pm 0.06 \pm 0.05$	$0.70 \pm 0.20 \pm 0.35$	$0.38 \pm 0.14 \pm 0.19$
$t\bar{t} + W/Z$			
• $t\bar{t}W(+jet(s))$	$0.60 \pm 0.06 \pm 0.18$	$2.52 \pm 0.12 \pm 0.76$	$1.61 \pm 0.10 \pm 0.48$
• $t\bar{t}Z(+jet(s))$	$0.38 \pm 0.04 \pm 0.11$	$0.96 \pm 0.06 \pm 0.29$	$0.54 \pm 0.05 \pm 0.16$
• $t\bar{t}W^{+}W^{-}$	0.007 ± 0.001	0.034 ± 0.003	0.021 ± 0.003
Total	$41 \pm 5 \pm 8$	$55 \pm 6 \pm 11$	$17 \pm 9 \pm 4$
Observed	35	39	10
Signal contamination			
• $t\bar{t}t\bar{t}$ C.I.	0.10 ± 0.03	0.34 ± 0.05	0.41 ± 0.05
$(C/\Lambda^2 = -4\pi$ TeV$^{-2})$			

Table 7.10: Observed number of events and expected number of background events with statistical (first) and systematic (second) uncertainties for the H_{T} control region selection at 8 TeV. The signal contamination in this region is also shown. For the Monte Carlo samples, the systematic uncertainties include only the production cross section uncertainty.

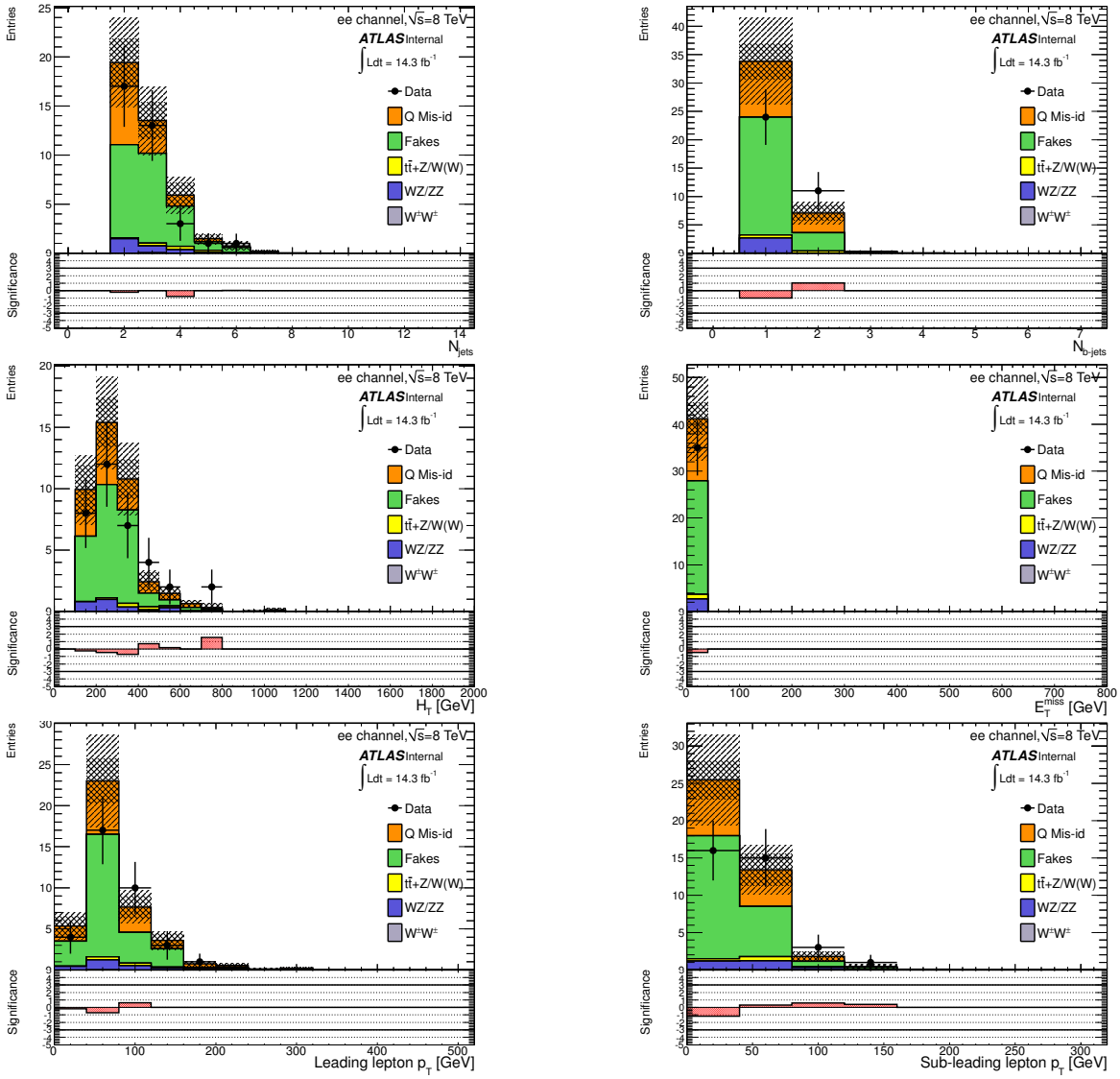

Figure 7.26: Distributions of some kinematic variables in the *ee* channel, after the H_{T} control region selection at 8 TeV, for both the background estimation and the data. The bottom plots show the significance of the measured number of events in the data compared to the estimated number of events from the backgrounds.

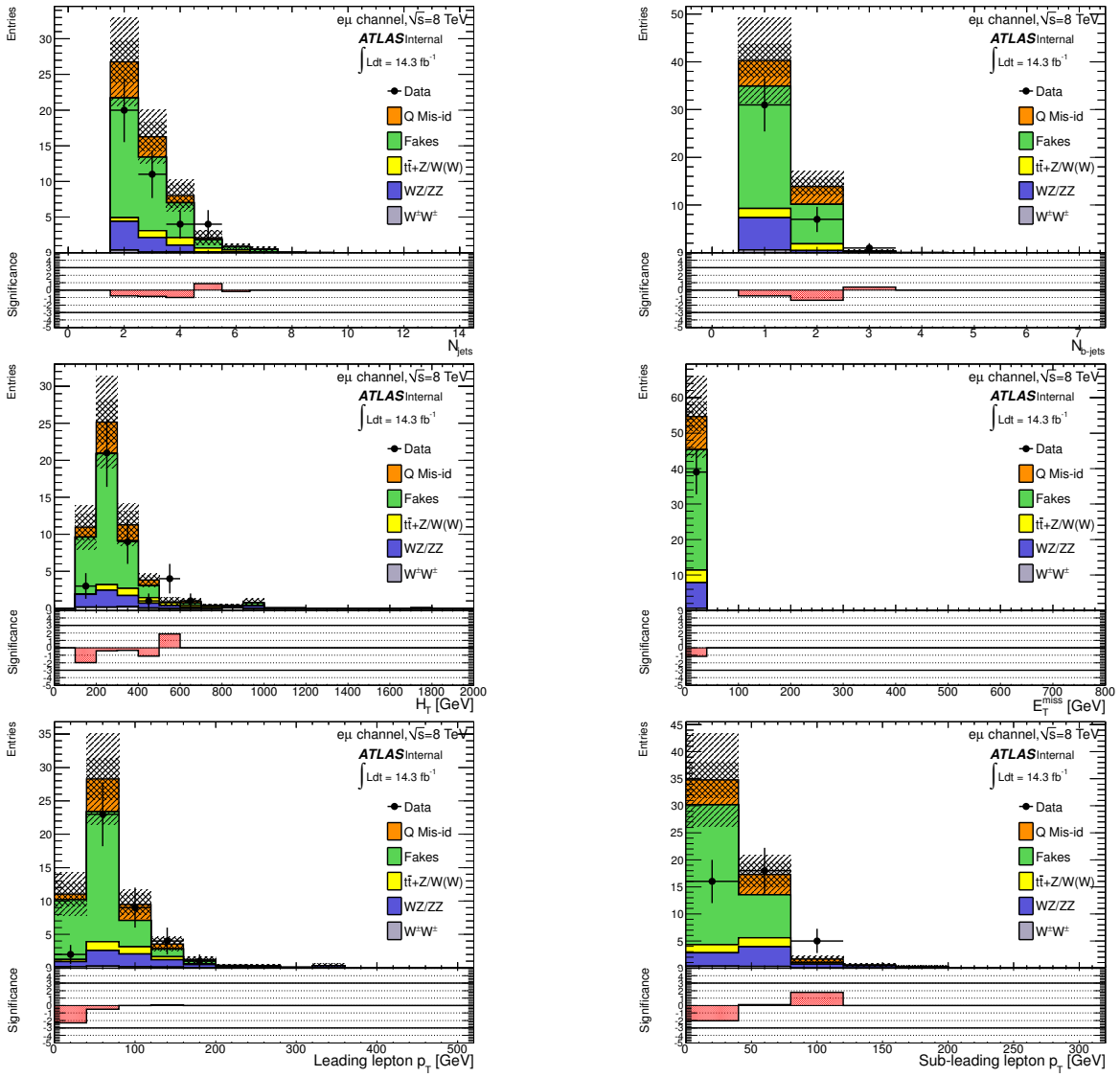

Figure 7.27: Distributions of some kinematic variables in the $e\mu$ channel, after the H_{T} control region selection at 8 TeV, for both the background estimation and the data. The bottom plots show the significance of the measured number of events in the data compared to the estimated number of events from the backgrounds.

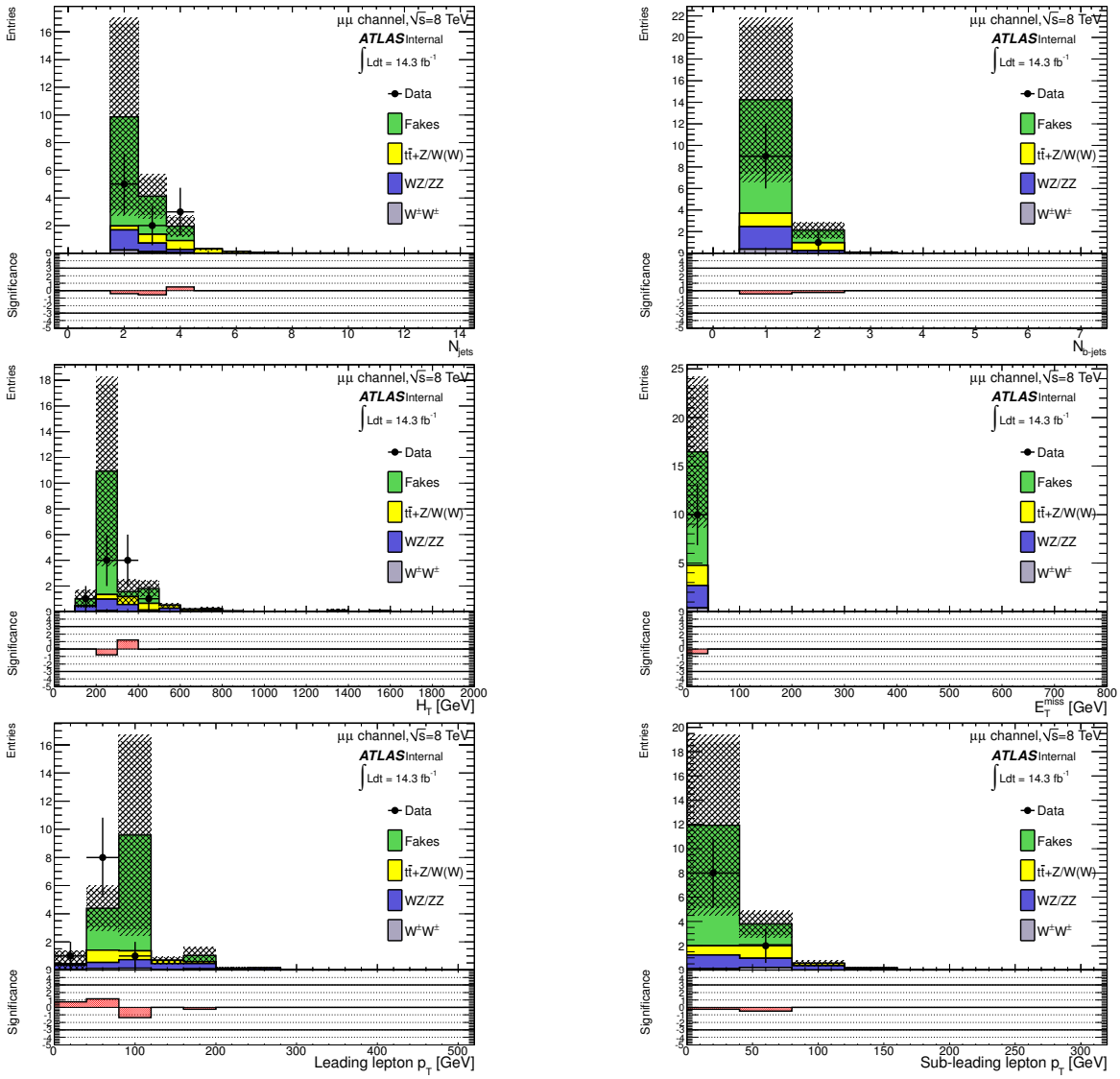

Figure 7.28: Distributions of some kinematic variables in the $\mu\mu$ channel, after the H_{T} control region selection at 8 TeV, for both the background estimation and the data. The bottom plots show the significance of the measured number of events in the data compared to the estimated number of events from the backgrounds.

7.4.2.3 Control region 3

The third control region is called "zero-b-tag control region". The event selection is the following:

- Events must contain exactly one same-sign pair of leptons.
- Events must contain at least two jets but zero b-tagged jet.
- Z veto in the ee or $\mu\mu$ channel.
- $H_{\mathrm{T}} > 100$ GeV.

Comparing to the event preselection, the cuts on H_{T} and $E_{\mathrm{T}}^{\mathrm{miss}}$ have been removed, and no b-jets are requested. Therefore, this region allows to control the H_{T} and $E_{\mathrm{T}}^{\mathrm{miss}}$ distributions, but in a region without b-jets. The distributions of some kinematic variables for the background estimation and the data after applying this zero-b-tag control region selection are shown in Figures 7.29, 7.30 and 7.31 for the ee, $e\mu$ and $\mu\mu$ channels, respectively. The total number of events observed in data and predicted by the background estimation for this third control region are shown in Table 7.11. Despite the differences in the ee channel, the significance is less than 3σ.

	Channel		
Samples	ee	$e\mu$	$\mu\mu$
Q Mis-id	$99.07 \pm 1.55 \pm 26.29$	$11.95 \pm 0.44 \pm 3.23$	—
Fakes	$80.22 \pm 8.01 \pm 24.1$	$80.72 \pm 6.07 \pm 24.2$	$21.34 \pm 3.97 \pm 6.40$
Diboson			
• $WZ/ZZ + jets$	$40.46 \pm 2.05 \pm 13.76$	$89.93 \pm 3.03 \pm 30.47$	$36.70 \pm 1.97 \pm 12.48$
• $W^{\pm}W^{\pm}jj$	$6.03 \pm 0.54 \pm 3.02$	$21.95 \pm 1.04 \pm 10.98$	$12.03 \pm 0.76 \pm 6.02$
$t\bar{t} + W/Z$			
• $t\bar{t}W(+jet(s))$	$0.89 \pm 0.08 \pm 0.27$	$2.85 \pm 0.14 \pm 0.86$	$2.01 \pm 0.12 \pm 0.60$
• $t\bar{t}Z(+jet(s))$	$0.29 \pm 0.04 \pm 0.09$	$0.99 \pm 0.07 \pm 0.30$	$0.50 \pm 0.06 \pm 0.15$
• $t\bar{t}W^{+}W^{-}$	0.021 ± 0.003	0.053 ± 0.004	0.039 ± 0.004
Total	$227 \pm 12 \pm 38$	$208 \pm 11 \pm 41$	$73 \pm 8 \pm 15$
Observed	281	205	80
Signal contamination			
• $t\bar{t}t\bar{t}$ C.I. ($C/\Lambda^2 = -4\pi$ TeV^{-2})	0.06 ± 0.02	0.17 ± 0.04	0.12 ± 0.03

Table 7.11: Observed number of events and expected number of background events with statistical (first) and systematic (second) uncertainties for the zero-b-tag control region selection at 8 TeV. The signal contamination in this region is also shown. For the Monte Carlo samples, the systematic uncertainties include only the production cross section uncertainty.

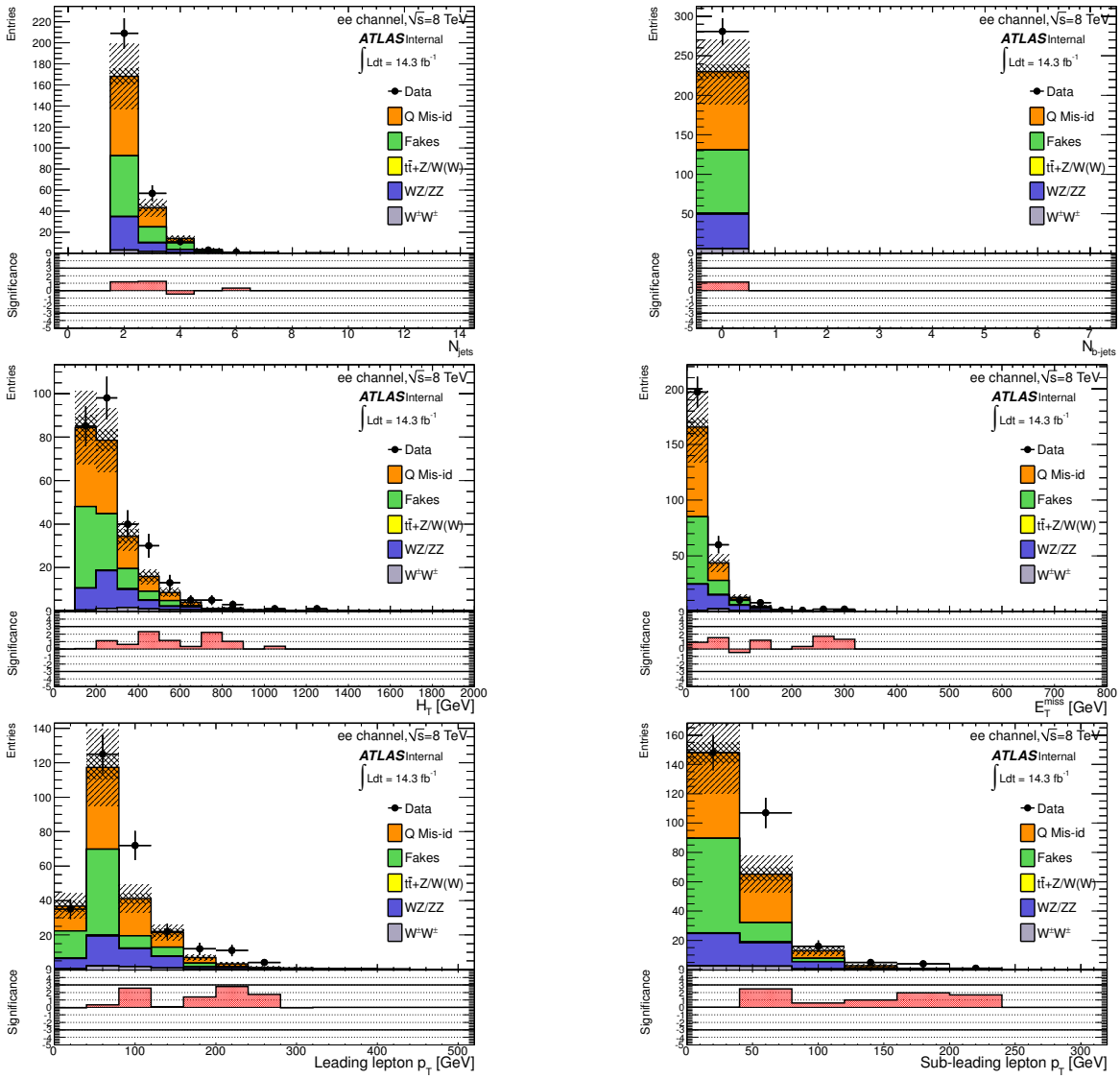

Figure 7.29: Distributions of some kinematic variables in the *ee* channel, after the zero-*b*-tag control region selection at 8 TeV, for both the background estimation and the data. The bottom plots show the significance of the measured number of events in the data compared to the estimated number of events from the backgrounds.

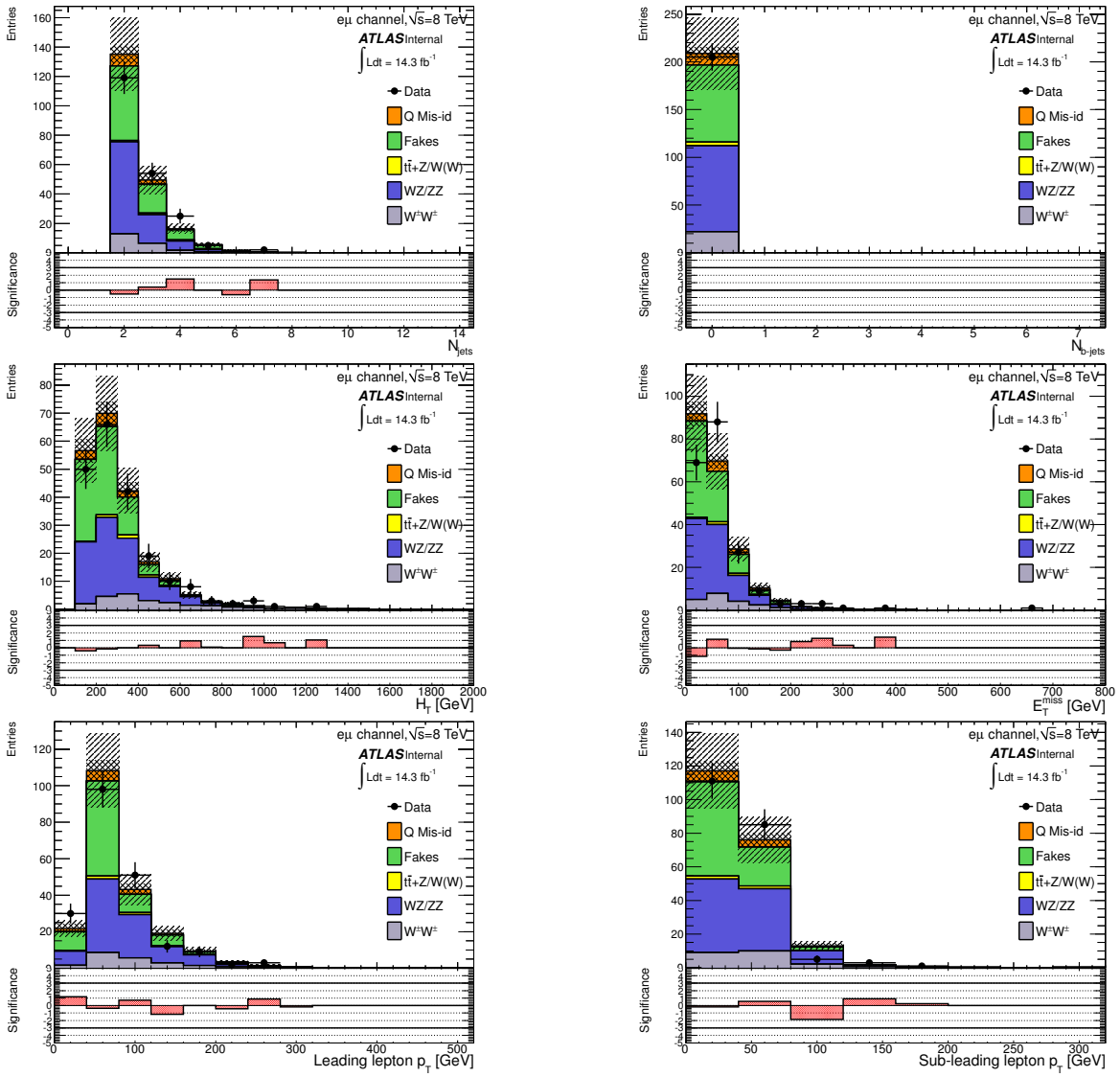

Figure 7.30: Distributions of some kinematic variables in the $e\mu$ channel, after the zero-b-tag control region selection at 8 TeV, for both the background estimation and the data. The bottom plots show the significance of the measured number of events in the data compared to the estimated number of events from the backgrounds.

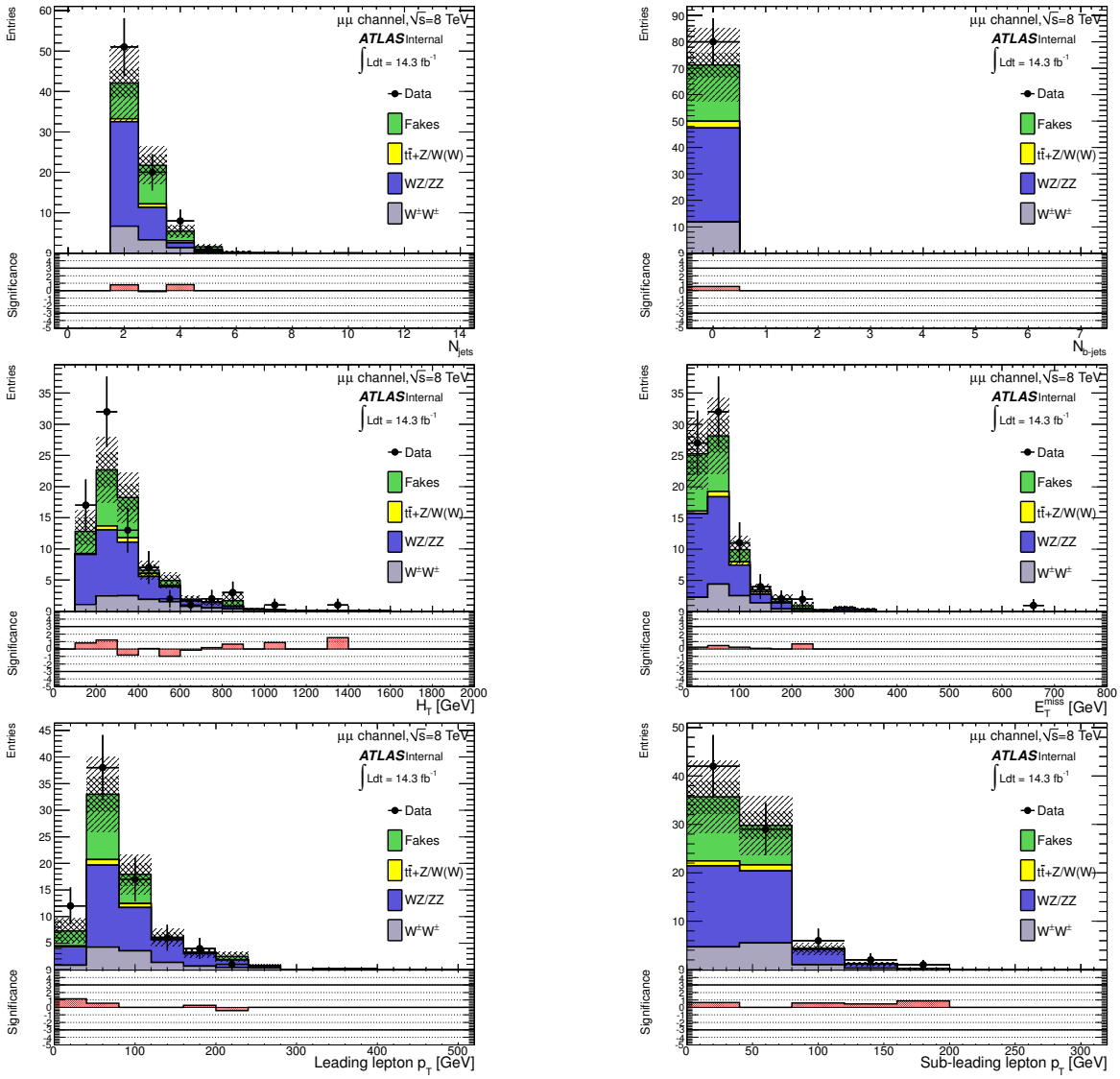

Figure 7.31: Distributions of some kinematic variables in the $\mu\mu$ channel, after the zero-b-tag control region selection at 8 TeV, for both the background estimation and the data. The bottom plots show the significance of the measured number of events in the data compared to the estimated number of events from the backgrounds.

Chapter 8

Final selection and results

Contents

This chapter presents the last step of the analysis. Once the methods to estimate the background have been established, the final event selection has to be done. The procedure to determine the final event selection is presented in Section 8.1. The different systematic uncertainties taken into account in the analysis are listed in Section 8.2. Finally, the results of the search of New Physics in events with four top quarks are presented in Section 8.3.

8.1 Event selection optimization

This stage of the analysis aims to minimize the expected upper limit on the four tops contact interaction production cross-section in the case of no signal event found. The optimization was done on the discriminant variables variating the cuts in the following way:

- $H_{\mathrm{T}} > 350$ GeV to $H_{\mathrm{T}} > 650$ (resp. 750) GeV per step of 50 GeV for the analysis done at $\sqrt{s} = 7$ (resp. 8) TeV.
- $\mathrm{N_{jets}} \geq 2$ to $\mathrm{N_{jets}} \geq 4$.
- $\mathrm{N_{b-jets}} \geq 1$ to $\mathrm{N_{b-jets}} \geq 3$.

- $E_{\mathrm{T}}^{\mathrm{miss}} > 40$ GeV and $E_{\mathrm{T}}^{\mathrm{miss}} > 60$ GeV.

For each set of cuts, a new expected limit has been computed at 95% C.L. using the CL_s method [152, 153], including the full systematic uncertainties detailed in Section 8.2. Each limit is calculated using a cut&count experiment with 50 000 pseudo-experiments. The procedure to compute the expected limit is explained in Section 8.3.2.

The expected limits as a function of the cut on H_{T} for the various sets of cuts on the number of jets and b-jets are shown in Figs. 8.1 and 8.2 for the analysis done at $\sqrt{s} = 7$ TeV and 8 TeV, respectively, and for the two different cuts on the $E_{\mathrm{T}}^{\mathrm{miss}}$. From these figures, it is clear that the best limits are obtained for $N_{\mathrm{b-jets}} \geq 1$, $H_{\mathrm{T}} > 550$ GeV and $E_{\mathrm{T}}^{\mathrm{miss}} > 40$ GeV at $\sqrt{s} = 7$ TeV, and $N_{\mathrm{b-jets}} \geq 2$, $H_{\mathrm{T}} > 650$ GeV and $E_{\mathrm{T}}^{\mathrm{miss}} > 40$ GeV at $\sqrt{s} = 8$ TeV. In both cases, a harder cut than the one of the preselection on the number of jets just improves slightly the limit, as a consequence, the less hard cut on $\mathrm{N_{jets}}$ was chosen, i.e. $\mathrm{N_{jets}} \geq 2$. The final event selection is detailed in Table 8.1.

	Final selection			
$\sqrt{s}$ [TeV]	H_{T} [GeV]	$\mathrm{N_{jets}}$	$\mathrm{N_{b-jets}}$	$E_{\mathrm{T}}^{\mathrm{miss}}$ [GeV]
7	> 550	≥ 2	≥ 1	> 40
8	> 650	≥ 2	≥ 2	> 40

Table 8.1: Final event selection for the signal region. The final selection has been obtained by minimizing the expected limit on the four tops contact interaction production cross section. The optimization was done based on the discriminant variables.

		Channel		
$\sqrt{s}$ [TeV]	Process	ee	$e\mu$	$\mu\mu$
7	Contact Interaction	0.14 ± 0.01	0.48 ± 0.02	0.34 ± 0.02
8	Standard Model	0.011 ± 0.001	0.038 ± 0.002	0.028 ± 0.002
	Contact Interaction	0.93 ± 0.08	3.23 ± 0.16	2.49 ± 0.13

Table 8.2: Expected number of events after the final selection with Monte Carlo statistical uncertainties. The assumed strength of the $t\bar{t}t\bar{t}$ contact interaction is $C/\Lambda^2 = -4\pi$ TeV^{-2}. The number of events has been scaled using the total cross-section to be tested.

		Channel		
$\sqrt{s}$ [TeV]	Process	ee	$e\mu$	$\mu\mu$
7	Contact Interaction	0.23 ± 0.05 %	0.81 ± 0.10 %	0.58 ± 0.09 %
8	Standard Model	0.11 ± 0.01 %	0.39 ± 0.01 %	0.28 ± 0.01 %
	Contact Interaction	0.15 ± 0.01 %	0.53 ± 0.02 %	0.41 ± 0.02 %

Table 8.3: Signal acceptance for the final selection computed with respect to the full signal production including all decays of the W bosons.

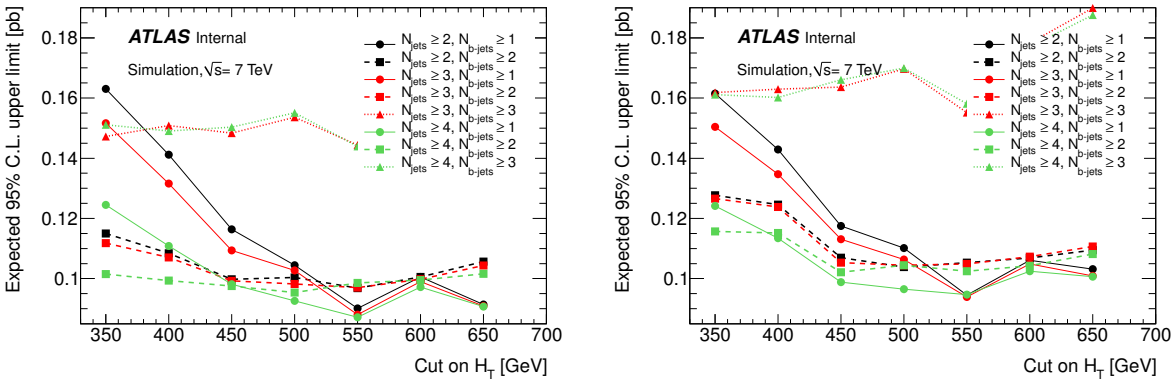

(a) (b)

Figure 8.1: Expected 95% C.L. upper limit on the four tops contact interaction production cross-section as a function of the cut on H_{T} for various sets of cuts on the number of jets (different colors) and b-jets (different markers), using a cut on the $E_{\mathrm{T}}^{\mathrm{miss}} > 40$ GeV (a) and $E_{\mathrm{T}}^{\mathrm{miss}} > 60$ GeV (b) for the analysis done at $\sqrt{s} = 7$ TeV. The final selection is chosen so that it can provide the minimum value on the cross-section.

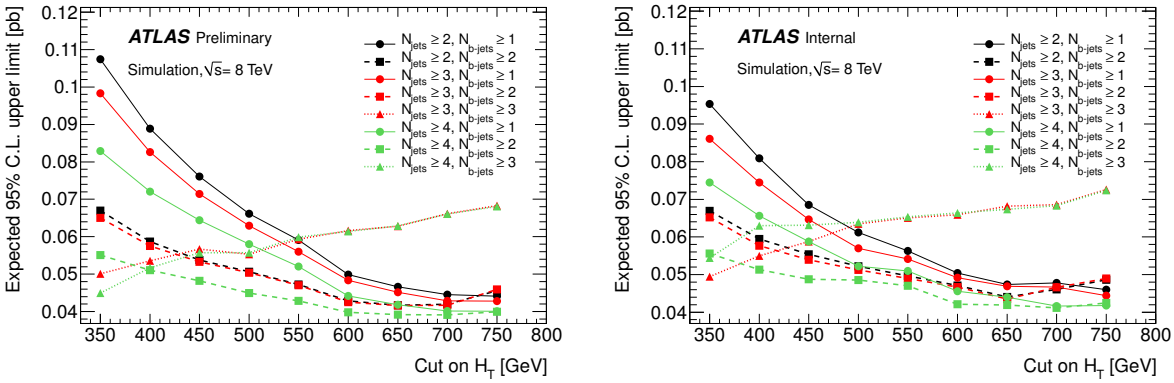

(a) (b)

Figure 8.2: Expected 95% C.L. upper limit on the four tops contact interaction production cross-section as a function of the cut on H_{T} for various sets of cuts on the number of jets (different colors) and b-jets (different markers), using a cut on the $E_{\mathrm{T}}^{\mathrm{miss}} > 40$ GeV (a) and $E_{\mathrm{T}}^{\mathrm{miss}} > 60$ GeV (b) for the analysis done at $\sqrt{s} = 8$ TeV. The final selection is chosen so that it can provide the minimum value on the cross-section.

The expected number of signal events for each channel after the final selection is shown in Table 8.2. Since the production cross-section for four top quarks is not predicted, the number of events have been rescaled to the cross-section to be tested. For the contact interaction, it corresponds to $C/\Lambda^2 = -4\pi$ TeV^{-2}. The number of background events after the final selection is presented in Section 8.3.1, where a comparison between data and expectation after the event

selection is done. The signal acceptance after the respective final selection is shown in Table 8.3. The acceptance was computed with respect to the full signal production including all decays of the W bosons.

8.2 Systematic uncertainties

The imperfect knowledge of the parameters affecting the measurements either from simulated samples or from data-driven estimates leads to systematic uncertainties which have to be evaluated in dedicated studies.

Several systematic uncertainties have been considered in this analysis. They are classified here depending on the samples that they are affecting. Thus, there are uncertainties affecting the Monte Carlo samples and the data-driven backgrounds. They are described in this section together with their estimation. Their specific values are detailed in Appendix B.

8.2.1 Uncertainties on Monte Carlo samples

Trigger, identification and reconstruction for leptons: In the Monte Carlo samples, the modeling of lepton triggers as well as reconstruction and identification efficiencies are corrected by scale factors. These scale factors are a function of the lepton kinematics. Together with their uncertainties, they are obtained from studies based on the decays of $Z \to \mu\mu$ and $Z \to ee$. The uncertainties on the overall yield are determined by varying each parameter by one standard deviation in each direction and recomputing the yield of each sample. The uncertainties were computed independently for trigger, reconstruction and identification efficiencies, and estimated to be smaller than 5%.

Energy scale and energy resolution of leptons: Correction factors on the energy or momentum calibration and resolution of leptons have been used in order to take into account discrepancies between simulation and data. For electrons, the electron energy for simulated events is smeared. For muons, the energy resolution is computed separately from the energy measured in the inner detector and the muon spectrometer. Uncertainties on these correction factors lead to systematic uncertainties on the signal and background acceptance. These uncertainties are evaluated by shifting the energy or momenta of leptons up and down by one standard deviation. As for the trigger, identification and lepton reconstruction, the uncertainties are computed independently for the energy scale and energy resolution of the leptons, by recomputing the yield for each sample after variations. For muons, the uncertainties on the energy resolution are added in quadrature.

Energy scale, energy resolution and reconstruction efficiency of jets: As for the leptons, correction factors have to be applied to the jets in order to take into account discrepancies between data and simulation. The uncertainties on jets considered in this analysis are related to the jet energy scale, the jet energy resolution, and the jet reconstruction efficiency. Uncertainties on these factors result from uncertainties on calorimeter response, dead material description, calorimeter cell noise thresholds description, fragmentation, underlying event modeling and flavor composition. These uncertainties are computed by variating each parameter independently within uncertainties and recomputing the yield for each sample. In order to take into account the pile-up, uncertainties on JVF were also considered.

b-tagging: Uncertainties on the b-tagging, c-tagging and light-jets tagging scale factors have been considered. These uncertainties were computed by variating the scale factors independently within uncertainties. They were evaluated separately for each scale factor, and added in quadrature.

Luminosity: The uncertainty on the integrated luminosity of the real data leads to an uncertainty on the overall scale of all samples that are derived using Monte Carlo. This uncertainty was determined using van der Meer scans and estimated to be 3.9% at 7 TeV and 3.6% at 8 TeV [115, 125].

Production cross sections: Uncertainties on the production cross-sections are included separately for each Monte Carlo background considered. At 7 TeV, they are taken to be 30% for the $t\bar{t}W(+jet)$ [154] sample, 34% for the WZ and ZZ samples, +35% and −24% for the $t\bar{t}W^+W^-$ sample, and 50% for the $W^\pm W^\pm jj$ and $t\bar{t}Z(+jets)$ [155] samples. At 8 TeV, the same values as for 7 TeV were used for the samples $t\bar{t}W(jet(s))$, WW and ZZ, while uncertainties of +38/-26% were set for the $t\bar{t}W^+W^-$ sample, 30% for the $t\bar{t}Z(+jets(s))$ and 25% for the $W^\pm W^\pm jj$ sample. For the samples $t\bar{t}W^+W^-$ and $W^\pm W^\pm jj$, the uncertainties have been evaluated by setting the renormalization and factorization scales to the values of 0.5 and 2, and rerunning the MadGraph event generator in these two configurations. Uncertainties on the cross-section production constitute the largest systematic uncertainties for the backgrounds estimated from simulation. For the four tops signal, the systematic uncertainty on the production cross-section was not considered, since as stated before, the cross-section in this model is a free parameter which depends on C/Λ^2.

Parton Distribution Function (PDF): The PDFs are determined experimentally with uncertainties coming from experimental measurements and theoretical models used to extract PDFs. The usage of any PDF in the calculations introduces an additional systematic uncertainty to the calculated cross-section. This effect also affects the signal event selection efficiency from a Monte Carlo simulation. The uncertainty has been estimated using the Reweighting method [156] applied to the analysis searching for fourth generation down-type quark b', for a mass point of 500 GeV, in the process $pp \to b'\bar{b}' \to tW^-\bar{t}W^+ \to bW^+W^-\bar{b}W^-W^+$ with two same-sign leptons (electrons or muons) in the final state, which is similar to the four tops topology. For this particular case, the uncertainty coming from the PDF choice was determined to be +1% and −0.9%. The same values were applied to the four tops signal.

ISR/FSR: This uncertainty has been computed for a four tops sample (produced via pair production of sgluon) and it is around 5%. However, at the time when the analyses were done, it was not available for the four tops signal through contact interaction due to a technical problem with Pythia 8, so it was not included in the analysis.

8.2.2 Uncertainties on data-driven backgrounds

Mis-identification of the electron charge: At 7 TeV, the uncertainty for this background was determined by means of a comparison on the charge-flip rate extracted by the tag-and-probe, direct extraction and likelihood methods. Based on this comparison, the systematic uncertainty attributed to the mis-identification of the electron charge was estimated to be

between −13% and +10% for the final selection of events. At 8 TeV, the sources of these uncertainty are coming from the uncertainty on the charge mis-identification rates (presented in Section 7.3.2.5.2) and the fake overlap removal correction factor. Both uncertainties are added quadratically in order to give the final estimate, which is around 30%.

Mis-reconstructed leptons: At 7 TeV, the systematic uncertainties associated to the estimation of background coming from fake leptons are determined independently for electrons and muons. For electrons, the uncertainty was estimated by using different *loose* electron definitions. For muons, it was estimated by changing the definition of the multijet enriched region, and using the number of jets, instead of the leading jet p_{T}, for the weight parametrization. Thus, these uncertainties were set to 50% for the ee channel, 40% for the $e\mu$ channel, and 30% for the $\mu\mu$ channel. At 8 TeV, the systematic uncertainty on the fake yield was estimated using the three control regions discussed in Section 7.4.2. The level of agreement between the observed and predicted yields in these control regions is taken as an estimate of the systematic uncertainty. The observed and expected yields with the fake yield scaled by a factor s_F are compared after performing a Poisson likelihood fit, where s_F is the only parameter of the fit. The value of s_F that maximizes the likelihood across all three control regions is noted, and the fractional uncertainty on the fake yield is set by summing in quadrature $|s_F - 1|$ and the uncertainty on s_F from the fit. Since the values obtained in the three different channels are very similar, the biggest one, 30%, has been set in all channels.

8.2.3 Summary

The systematic uncertainties with the most relevant impact on the analysis are detailed in Tables 8.4 and 8.5 for the analysis done at 7 TeV and 8 TeV, respectively. Only the uncertainties where the impact on at least one of the background samples is greater than 5% have been included in these tables.

	Uncertainty in [%]					
	$t\bar{t}t\bar{t}$ C.I.			Background		
Source	ee	$e\mu$	$\mu\mu$	ee	$e\mu$	$\mu\mu$
Cross section	–	–	–	+19.6/-19.5	+24.5/-24.4	+33.4/-33.3
Fakes	–	–	–	+19.4/-19.4	+11.2/-11.2	+2.9/-2.9
Charge misidentification	–	–	–	+1.0/-1.2	+0.5/-1.0	–
Jet energy scale	+4.2/-1.4	+0.8/-2.4	+0.0/-1.1	+5.1/-5.3	+6.4/-6.0	+6.0/-6.7
b-tagging efficiency	+5.0/-5.9	+0.1/-0.9	+2.8/-3.3	+5.7/-5.9	+4.2/-4.8	+8.6/-9.6
Jet energy resolution	+2.9/-2.9	+1.3/-1.3	+0.5/-0.5	+1.2/-1.2	+4.3/-4.3	+3.4/-3.4
JVF selection efficiency	+8.8/-7.4	+8.7/-7.4	+9.2/-9.7	+0.6/-0.8	+0.9/-1.1	+1.3/-1.5

Table 8.4: Leading sources of systematic uncertainty on the signal and total background estimates for the analysis at $\sqrt{s} = 7$ TeV.

	Uncertainty in [%]					
	$t\bar{t}t\bar{t}$ C.I.			Background		
Source	ee	$e\mu$	$\mu\mu$	ee	$e\mu$	$\mu\mu$
Cross section	–	–	–	+16.6/-16.4	+22.4/-22.2	+30.2/-29.9
Fakes	–	–	–	+7.2/-7.2	+1.1/-1.1	–
Charge misidentification	–	–	–	+6.8/-6.8	+6.3/-6.3	–
Jet energy scale	+1.5/-2.8	+3.1/-3.3	+0.0/-2.4	+6.6/-9.6	+6.4/-6.2	+9.0/-8.0
b-tagging efficiency	+2.0/-2.9	+5.3/-8.2	+7.0/-8.2	+10.1/-9.2	+16.2/-15.2	+21.6/-19.8
Jet energy resolution	+1.1/-1.1	+1.2/-1.2	+1.6/-1.6	+1.7/-1.7	+1.5/-1.5	+0.9/-0.9
JVF selection efficiency	+8.8/-7.4	+2.4/-2.8	+2.2/-2.9	+1.0/-1.2	+1.6/-1.7	+2.0/-2.2

Table 8.5: Leading sources of systematic uncertainty on the signal and total background estimates for the analysis at $\sqrt{s} = 8$ TeV.

8.3 Results

In this section the results of the search of New Physics in events with four top quarks are presented. First, a comparison between the expected background and data is done in Section 8.3.1. Then, the results of this comparison are interpreted in Section 8.3.2, where an upper limit on the four tops production cross-section is set.

8.3.1 Data versus background expectation comparison

In the analysis performed with the data taken at $\sqrt{s} = 7$ TeV, and after applying the final selection, 5.6 ± 1.7 events are expected from SM background, while 4 events have been observed in data. The details of the observed number of events are shown in Table 8.6, as well as the total expected number of background events for the three different channels. The total number of expected and observed events agree within uncertainties, which means that no significant excess is observed in data.

In the analysis performed with the data taken at $\sqrt{s} = 8$ TeV, 8 events are observed with 3.6 ± 1.3 expected from background. The details of the observed number of events are shown in Table 8.7, as well as the total expected number of background events for the three different channels. As can be seen, there is a small excess of observed events with respect to the total background, which is coming from the $e\mu$ channel, since the yields in the ee and $\mu\mu$ channels are consistent with the background expectations. For the $e\mu$ channel, the probability of observing six or more events, given the expected background and the statistical and systematic uncertainties on that expectation, is 3.9%. Since this probability is not small enough as to claim observation of new physics, the data is interpreted as constraining the four tops contact interaction production cross-section.

The distributions of some kinematical variables after the final selection are shown in Appendix C.

	Channel		
Backgrounds	ee	$e\mu$	$\mu\mu$
Q Mis-id	$0.13 \pm 0.04 \pm 0.02$	$0.23 \pm 0.04 \pm 0.03$	—
Fakes	$0.5 \pm 1.1 \pm 0.3$	$0.8 \pm 1.1 \pm 0.3$	$0.13 \pm 0.13 \pm 0.04$
Diboson			
• $WZ/ZZ(+jets)$	$0.19 \pm 0.20 \pm 0.07$	$0.34 \pm 0.21 \pm 0.13$	$0.28 \pm 0.22 \pm 0.10$
• $W^{\pm}W^{\pm}jj$	$0.06 \pm 0.03 \pm 0.03$	$0.07 \pm 0.03 \pm 0.03$	$0.03 \pm 0.02 \pm 0.03$
$t\bar{t} + W/Z$			
• $t\bar{t}W(+jet)$	$0.23 \pm 0.02 \pm 0.07$	$0.79 \pm 0.04 \pm 0.24$	$0.57 \pm 0.04 \pm 0.18$
• $t\bar{t}Z(+jet)$	$0.17 \pm 0.02 \pm 0.09$	$0.61 \pm 0.03 \pm 0.31$	$0.33 \pm 0.02 \pm 0.17$
• $t\bar{t}W^{+}W^{-}$	$0.008 \pm 0.001 \pm 0.002$	$0.023 \pm 0.001 \pm 0.007$	$0.016 \pm 0.001 \pm 0.005$
Total expected	$1.3 \pm 1.1 \pm 0.3$	$2.9 \pm 1.1 \pm 0.5$	$1.36 \pm 0.26 \pm 0.27$
Observed	2	2	0

Table 8.6: Expected number of background events with statistical (first) uncertainties and the dominant systematic (second) uncertainties for the final signal selection at $\sqrt{s} = 7$ TeV, compared to the number of events observed in data.

	Channel		
Samples	ee	$e\mu$	$\mu\mu$
Q Mis-id	$0.16 \pm 0.04 \pm 0.05$	$0.41 \pm 0.07 \pm 0.12$	—
Fakes	$0.18 \pm 0.17 \pm 0.05$	$0.07 \pm 0.28 \pm 0.02$	< 1.14
Diboson			
• $WZ/ZZ(+jets)$	< 0.11	$0.01 \pm 0.09 \pm 0.01$	< 0.11
• $W^{\pm}W^{\pm}jj$	< 0.03	$0.18 \pm 0.16 \pm 0.07$	< 0.03
$t\bar{t} + W/Z$			
• $t\bar{t}W(+jet(s))$	$0.31 \pm 0.04 \pm 0.12$	$0.93 \pm 0.06 \pm 0.35$	$0.65 \pm 0.06 \pm 0.25$
• $t\bar{t}Z(+jet(s))$	$0.09 \pm 0.02 \pm 0.04$	$0.34 \pm 0.04 \pm 0.14$	$0.14 \pm 0.02 \pm 0.06$
• $t\bar{t}W^{+}W^{-}$	$0.012 \pm 0.002 \pm 0.005$	$0.039 \pm 0.003 \pm 0.016$	$0.024 \pm 0.003 \pm 0.01$
Total	$0.75 \pm 0.21 \pm 0.14$	$1.98 \pm 0.35 \pm 0.40$	$0.82 \pm 1.15 \pm 0.26$
Observed	1	6	1

Table 8.7: Expected number of background events with statistical (first) uncertainties and the dominant systematic (second) uncertainties for the final signal selection at $\sqrt{s} = 8$ TeV, compared to the number of events observed in data.

8.3.2 Interpretation of results: setting limit

Because no significant excess of events has been found in data, an upper limit at 95% C.L. on the four tops production cross-section has been computed using CL_s method with the LLR (Log-Likelihood Ratio) as a test statistic. This is defined as

$$LLR = -2 \log \frac{L_{s+b}}{L_b}, \tag{8.1}$$

where L_{s+b} (L_b) is the Poisson likelihood to observe the data under the signal-plus-background (background-only) hypothesis. Pseudo-experiments are generated under each of both hypothesis, taking into account statistical fluctuations of the total predictions according to Poisson statistics, as well as Gaussian fluctuations in the signal and background expectations describing the effect of systematic uncertainties. Correlations of the systematic uncertainties across the samples and channels are taken into account. Each sample is statistically varied independently, using a Gaussian function truncated at zero, in order to avoid negative contributions, in particular for the samples which have a very low yield and a large statistical uncertainty. When no event is selected for a given sample, its yield is set to 0 with a statistical uncertainty given by the 68% C.L. upper limit using Poisson statistics, which is then rescaled to the data integrated luminosity. The fraction of $s + b$ and b pseudo-experiments with LLR larger than the expected median or observed LLR defines CL_{s+b} and CL_b for the expected and observed limits, respectively. Signal cross-sections for which $CL_s = CL_{s+b}/CL_b < 0.05$ are considered excluded at the 95% C.L.

Single-bin counting experiments have been used to compute the limits. The combined limits have been calculated by considering each channel separately and summing their LLR. The corresponding upper limits on the four tops contact interaction production cross-section, channel by channel, and for the combination, obtained for the analyses performed at $\sqrt{s} = 7$ TeV and 8 TeV, and considering all the systematic uncertainties are shown in Tables 8.8 and 8.9, respectively.

	95% C.L. upper limit [fb]			
Channel	Observed	Expected	1σ range	2σ range
ee alone	473	474	280-706	280-954
$e\mu$ alone	122	148	101-208	82-307
$\mu\mu$ alone	113	150	112-241	112-244
Combination	61	90	63-133	39-194

Table 8.8: Upper limits at 95% C.L. obtained for each channel and their combination on $\sigma(pp \to t\bar{t}t\bar{t})$ for the contact interaction model at 7 TeV.

	95% C.L. upper limit [fb]			
Channel	Observed	Expected	1σ range	2σ range
ee alone	196	197	141-260	142-326
$e\mu$ alone	133	66	53-97	42-133
$\mu\mu$ alone	70	90	54-112	53-182
Combination	59	42	29-61	23-90

Table 8.9: Upper limits at 95% C.L. obtained for each channel and their combination on $\sigma(pp \to t\bar{t}t\bar{t})$ for the contact interaction model at 8 TeV.

In the analysis at $\sqrt{s} = 8$ TeV, and in the $\mu\mu$ channel, the estimate of the fakes contribution is vanishing after the final selection. However, a statistical uncertainty on this yield is computed as the 68% C.L. upper limit. Since this background is extracted from data, this yield, and therefore its uncertainty, are not rescaled to the luminosity. Thus, an upper limit of 1.14 events

is used as can be seen in Table 8.7. This uncertainty is clearly over-estimated, and its effect is seen in the upper limit on the four tops production cross-section in the $\mu\mu$ channel (see Table 8.9): because the number of observed events in this channel is very similar to the one of the estimated background, it should be expected to have an observed limit similar to the expected one, however the observed limit is 70 fb for an expected limit of 90 fb.

An alternative method has been developed in order to give a more realistic estimation of this uncertainty in the $\mu\mu$ channel in the analysis at 8 TeV. The H_{T} cut has been relaxed until some events pass the selection cuts in the fakes estimation. For a cut of $H_{\mathrm{T}} > 400$ GeV (instead 650 GeV), the fakes contribution is 0.14 ± 0.25. From this number, it has been evaluated that the contribution at $H_{\mathrm{T}} > 650$ GeV should be smaller than $0.14 + 0.25 = 0.39$ events. Therefore, alternative results have been computed using this uncertainty. A comparison of the two different results is presented in Table 8.10. As can be seen, although the expected and observed limits using the alternative uncertainty for the fakes background are the same, the observed limits in both cases, the default and the alternative estimate of the fakes uncertainty, are very similar. This is also true for the combination. Thus, the default uncertainty was used to give the final result.

	95% C.L. upper limit [fb]			
Channel	Observed	Expected	1σ range	2σ range
Using fakes $= 0 \pm 0.39$				
$\mu\mu$ alone	72	72	54-94	54-142
Combination	61	39	28-57	22-80
Using fakes $= 0 \pm 1.14$				
$\mu\mu$ alone	70	90	54-112	53-182
Combination	59	42	29-61	23-90

Table 8.10: Comparison of the 95% C.L. upper limits on $\sigma(pp \to t\bar{t}t\bar{t})$ from the contact interaction model, for the two different configurations of the fakes estimation in the $\mu\mu$ channel. The effect in the channel combination is also shown.

In the analysis performed with the data taken at $\sqrt{s} = 7$ TeV, an upper limit of 61 fb is calculated for the production cross-section of the four top quarks events through a contact interaction, with an expected limit of 90 fb. At 8 TeV, the observed upper limit on the production cross-section was found to be 59 fb, with an expectaction of 42 fb. In both cases, the observed limit is within 2σ and 1σ range, respectively. These results are summarized in Table 8.11, which also shows the upper limit on the production cross-section of $t\bar{t}t\bar{t}$ in the SM. The expected upper limit without taking into account the systematic uncertainties for the four tops contact interaction at 8 (resp. 7) TeV is 38^{+17}_{-10} (resp. 85^{+36}_{-24}) fb, and for the SM 53^{+25}_{-15} fb. It shows that this analysis is largely dominated by the statistical uncertainties rather than the systematic ones.

In the case of the contact interaction, the limits can be translated to a limit on the model parameter $|C|/\Lambda^2$ as shown in Fig. 8.3. The maximum theoretical value that the parameter $|C|$ can take is $(4\pi)^2$. As can be seen, the limit set at $\sqrt{s} = 7$ TeV does not restrict so much the plane $|C| - \Lambda^2$. A better exclusion is obtained with the results at $\sqrt{s} = 8$ TeV. However, combining the 7 and 8 TeV results allows to slightly improve the constraints from the 8 TeV analysis.

This result can be extrapolated to other models, as long as the kinematical properties of

the produced events are similar to the ones generated by the four top quark contact interaction.

		95% C.L. upper limit				
		$\sigma(pp \to t\bar{t}t\bar{t})$ [fb]				$\lvert C\rvert/\Lambda^2$ [TeV^{-2}]
		Expected				
$\sqrt{s}$ [TeV]	Model	Median	1σ	2σ	Observed	Observed
7	Contact Interaction	90	63-133	39-194	61	28
8	Standard Model	61	43-89	35-129	85	—
	Contact Interaction	42	29-61	23-90	59	15
7+8	Contact Interaction	–	–	–	–	14

Table 8.11: Observed limits at 95% C.L. on the four top quarks signals together with their expected 1σ and 2σ ranges. The upper limit on the parameter $|C|/\Lambda^2$ is also shown.

8.4 Conclusion

The search for New Physics in events containing four top quarks through a four-top quark contact interaction has been presented. This search made use of the data collected by the ATLAS detector at the LHC in pp collisions at $\sqrt{s} = 7$ TeV and 8 TeV, using the full 2011 and a part of the 2012 ATLAS dataset corresponding to 4.7 fb^{-1} and 14.3 fb^{-1}, respectively.

The search was focused in the same-sign dilepton plus jets signature. At 7 TeV, the events were selected by requiring at least two jets, including at least one b-tagged jet, $E_{\mathrm{T}}^{\mathrm{miss}} > 40$ GeV and $H_{\mathrm{T}} > 550$ GeV. Four events have been observed with an expected background of 5.6 ± 1.7 events. At 8 TeV, the events were selected by requiring at least two jets, including at least two b-tagged jets, $E_{\mathrm{T}}^{\mathrm{miss}} > 40$ GeV and $H_{\mathrm{T}} > 650$ GeV. Eight events were observed with 3.6 ± 1.3 expected from background. In both cases, no significant excess of events has been observed. Therefore an upper limit on the four tops production cross-section has been computed at 95% C.L. At 7 (resp. 8) TeV, a limit of 61 (resp. 59) fb has been obtained with an expected limit of 90 (resp. 42) fb. These limits were translated to limits on the model parameters $|C|$ and Λ, and combining the 7 and 8 TeV analysis gives an upper limit of $|C|/\Lambda^2 < 14$ TeV^{-2}. In the SM and at 8 TeV, the upper limit on the production cross-section was set to 85 fb.

These limits constitute the first published results on the experimental search for the production of events containing four top quarks. These results were made public on September 2012 and May 2013 and can be found in [18, 17].

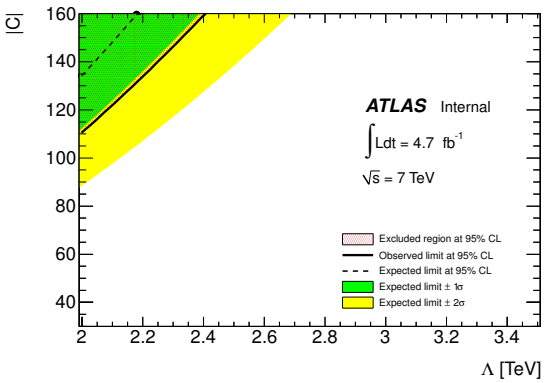

(a)

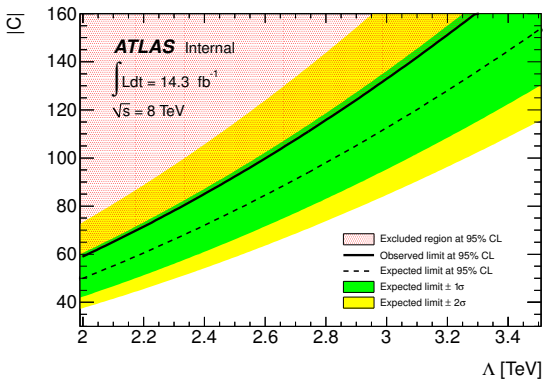

(b)

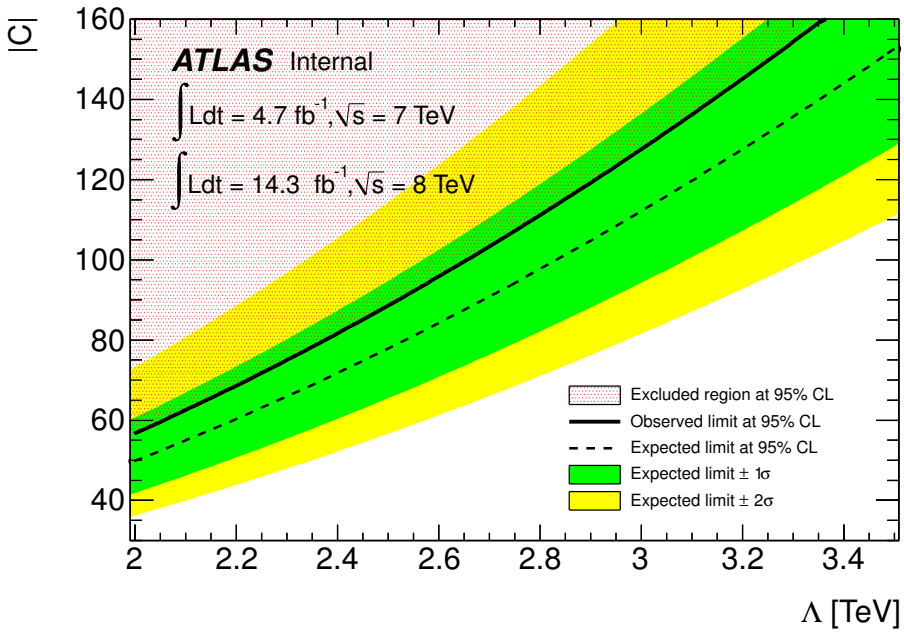

(c)

Figure 8.3: Observed and expected limits obtained in the analysis performed with the data taken at $\sqrt{s} = 7$ TeV (a), 8 TeV (b), and combination of both (c), on the contact interaction model parameters $|C|$ and Λ. The region above the observed line is excluded at 95% C.L. The signal sample has been generated with a value of $C/\Lambda^2 = -4\pi$ TeV^{-2}. Below $\Lambda = 2$ TeV the low energy effective field theory with the four tops contact interaction is not expected to be valid anymore.

Conclusion

Currently, the LHC is capable of colliding particles up to energies never reached by the human being, providing access to a yet unexplored energy regime. It is hoped that it clarifies at least some of the questions not answered by the Standard Model and helps to construct that so wished Theory of Everything. Many beyond-the-SM theories could be tested at the LHC. Some of these theories predict final states involving four top quarks ($t\bar{t}t\bar{t}$). Therefore, this kind of events provides an open window in order to look for new physics phenomena.

In this thesis, two topics have been treated. The main one has been focused in the search for New Physics in events with four top quarks in a model-independent approach, using the data collected by the ATLAS detector at LHC in pp collisions at $\sqrt{s} = 7$ TeV and 8 TeV during 2011 and a part of 2012, corresponding to 4.7 fb^{-1} and 14.3 fb^{-1}, respectively. The other topic is related to the LASER calibration system of the ATLAS Tile calorimeter.

For this last topic, the stability and linearity of the electronics of the photodiodes, used to measure the intensity of the laser light, was monitored using the data collected between 2011 and the first months of 2013. The monitoring activity was split in four different periods, where two periods are separated by a hardware intervention. One of these interventions in particular made the system much more stable: the change of the motherboard inside the photodiodes box. After this intervention (made on July 6^{th}, 2011) the photodiodes absolute response was stable within a range of 0.5%. This measurement was done with a new method used to determine the stability of the alpha spectra: the scale factor. It was demonstrated that this method is more stable than the normalized mean value (default method used in studies previous to this one). To finalize this part, the study of the photodiodes response is the first step towards the understanding of the LASER system. This calibration system is crucial to monitor correctly the Tile calorimeter readout electronics, which is essential for measuring the energy and direction of the hadrons produced in the collisions, as well as the missing transverse momentum.

Concerning the search for New Physics in events with four top quarks, the analysis was focused in a final state with two leptons (electrons or muons) with the same electric charge. This channel was chosen since this kind of events is rarely produced in Standard Model processes. Different event selections were used in each one of the two analyses performed at 7 TeV and 8 TeV. In both cases, no significant excess of events has been observed. Therefore an upper limit on the four tops contact interaction production cross-section has been computed at 95% C.L. At 7 (resp. 8) TeV, a limit of 61 (resp. 59) fb has been obtained with an expected limit of 90 (resp. 42) fb. In the SM and at 8 TeV, the upper limit on the production cross-section was set to

85 fb with an expected limit of 61 fb. In the case of the contact interaction, the upper limit on the production cross-section can be translated to a limit on the model parameter $|C|/\Lambda^2$. Combining the 7 and 8 TeV analyses the upper limit on this parameter is $|C|/\Lambda^2 < 14$ TeV^{-2}. The limits presented in this thesis constitute the first published results on the experimental search for the production of events containing four top quarks. They can be found in [18, 17].

Although no new physics phenomena were observed in this analysis, the model-independent nature of the framework used to set the upper limits on the four tops contact interaction production cross-sections allows to extrapolate to other models, as long as the kinematical properties of the produced events are similar to the ones generated by the four top quark contact interaction.

About the estimation of the background coming from the mis-identification of the electron charge, a new method was developed in order to take into account the dependence on the electron p_{T} of the mis-identification rates. Basically, the likelihood method is kept as the baseline in order to compute the rates as a function of $|\eta|$, which are then corrected using a p_{T} dependent factor extracted from $t\bar{t}$ simulated events. The regions used by the side-band method to extract the background from the Z-peak have been also redefined. It now takes into account the shift of the same-sign invariant mass distribution to lower values with respect to the opposite-sign distribution. The computation of the systematic uncertainty has also been improved. Different sources of systematics are now considered, which are related to the change of the Z peak definition, the use of different $t\bar{t}$ samples to extract the p_{T} correction factor, the differences between the measured and true rates extracted from simulated samples, and the statistical uncertainties coming from the likelihood method and the p_{T} correction.

Future improvements of the present analysis can include an event selection optimization performed channel by channel (i.e. ee, $e\mu$ and $\mu\mu$). As it was shown, the analysis is largely dominated by the statistical uncertainties. Thus, the inclusion of more data, providing much more statistics could help to reduce the impact of these uncertainties, and therefore to set stronger limits on the production cross-sections. The analysis will be redone with the full 2012 dataset, corresponding to 20.3 fb^{-1}, which does not increase so much the statistics, but which will allow, in principle, to provide better measurements. The analysis could also be extended to other channels (i.e. not only same-sign dilepton), with a final result coming from the combination of all these channels.

Finally, after the long shutdown, it is expected that the LHC delivers around $\sim 75{-}100$ fb^{-1} over a period of three years at a center-of-mass energy of $13-14$ TeV. In these conditions, the SM production of four top quarks ($\sigma_{t\bar{t}t\bar{t}} \sim 7-11$ fb) will not be negligible anymore, and hundreds of four tops events are expected to be produced at the LHC. It will therefore be possible to measure the four tops events production cross-section and compare it to the SM prediction in order to constrain a possible enhancement from New Physics.

Appendices

Appendix A

Study of the four top events kinematic

This appendix is dedicated to the study of the four top events kinematic at the parton level. These studies were done by E. Busato.

A.1 Four top events kinematic for large M_ρ

In order to demonstrate that the event kinematics do not depend on M_ρ and g_ρ when M_ρ is large (i.e. when the four top interaction can be approximated by a contact interaction), three different configurations were compared:

- $g_\rho = 10\sqrt{8\pi}$, $M_\rho = 10$ TeV,
- $g_\rho = 100\sqrt{8\pi}$, $M_\rho = 100$ TeV (values used to generate the signal in this analysis),
- $g_\rho = 1000\sqrt{8\pi}$, $M_\rho = 1000$ TeV.

The Fig. A.1 shows the inclusive distributions of η and energy at parton level for top quarks, W bosons, electrons and muons, neutrinos and b quarks for the configurations studied. It demonstrates that the event kinematics is the same for the three configurations, and that it does not depend on the values of M_ρ and g_ρ when M_ρ is large. That means that the signal acceptance is the same for all M_ρ in the contact interaction regime, and that only the cross-section depends on the parameters M_ρ and g_ρ.

A.2 Four top events kinematic for low M_ρ and comparison to the large M_ρ case

This section is dedicated to give an estimation of the signal acceptance for low M_ρ and comparing the result to the acceptance for large M_ρ. In order to do that, the following configurations were compared:

- $g_\rho = \sqrt{2\pi}$, $M_\rho = 500$ GeV,
- $g_\rho = \sqrt{8\pi}$, $M_\rho = 1$ TeV,
- $g_\rho = 10\sqrt{8\pi}$, $M_\rho = 10$ TeV,
- $g_\rho = 100\sqrt{8\pi}$, $M_\rho = 100$ TeV (values used to generate the signal in this analysis),
- Standard Model.

A comparison of the first three configurations is shown in Fig. A.2. As can be seen, as M_ρ decreases, the objets get softer, meaning that the event kinematic starts to change. These changes are quantified at parton level by computing the acceptances. These values are shown in Table A.1 for the $\mu\mu$ channel. Similar results are obtained in ee and $e\mu$ channel. Due to the absence of trigger, reconstruction and identification efficiencies, all analysis cuts cannot be applied. Only these relevant at the parton level were therefore applied. For that reason, the acceptances calculated at the parton level are very different from the ones used in the analysis, which are computed after full detector simulation. Thus, the information of interest resides in their relative differences rather than in their absolute values. This way, the acceptance for $M_\rho = 500$ GeV is about 30% lower than the one in the contact interaction regime. It means that upper limits on the production cross-section for low M_ρ are approximately 30% worse than in the large M_ρ case. However, it should be noted that cross sections generally increase as M_ρ decreases, so the analysis sensitivity decreases by less than 30%. Table A.1 also shows that the acceptance for the Standard Model production of 4 top events is close to the one for $g_\rho = 100\sqrt{8\pi}$, $M_\rho = 100$ TeV. Summarizing, even if the analysis described is based on a large value of M_ρ, it is also sensitive to configurations where the contact interaction approximation is not valid.

Cut	$g_\rho = \sqrt{2\pi}$ $M_\rho = 500$ GeV	$g_\rho = \sqrt{8\pi}$ $M_\rho = 1$ TeV	$g_\rho = 10\sqrt{8\pi}$ $M_\rho = 10$ TeV	$g_\rho = 100\sqrt{8\pi}$ $M_\rho = 100$ TeV	SM
≥ 2 muons	4.6	4.7	4.9	5.1	4.8
Same sign	1.6	1.8	1.9	2	1.9
Z veto	1.4	1.6	1.7	1.9	1.6
$N_{\text{jets}} \geq 2$	1.4	1.6	1.7	1.9	1.6
$E_{\text{T}}^{\text{miss}} > 40$ GeV	1.1	1.4	1.5	1.7	1.5
$H_{\text{T}} > 500$ GeV	1	1.3	1.4	1.5	1.3

Table A.1: Parton level acceptance (in %) for all the configurations described in the text after analysis cuts in the $\mu\mu$ channel.

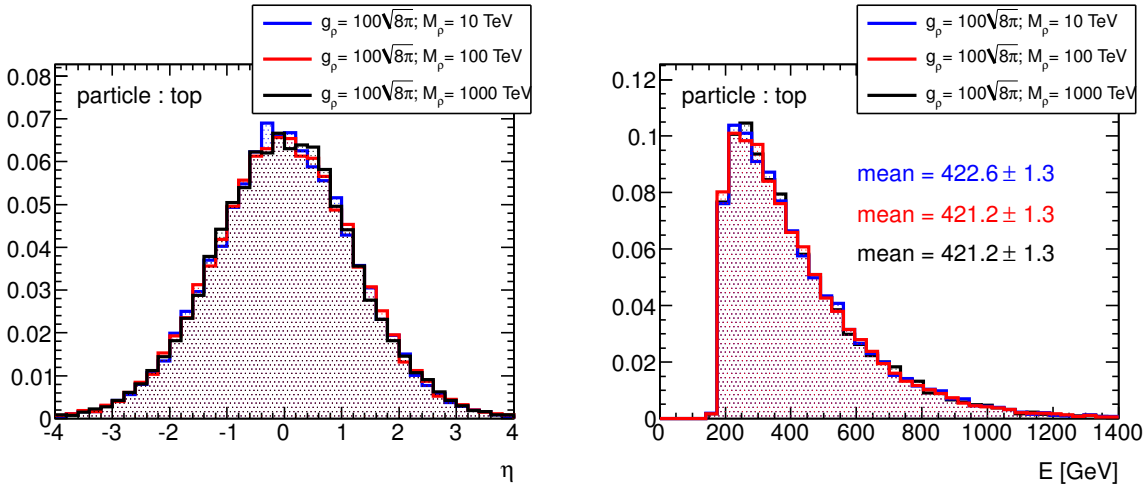
g_ρ= 100√8π; M_ρ= 10 TeV
g_ρ= 100√8π; M_ρ= 100 TeV
g_ρ= 100√8π; M_ρ= 1000 TeV
particle : top
η
E [GeV]
mean = 422.6 ± 1.3
mean = 421.2 ± 1.3
mean = 421.2 ± 1.3

(a)

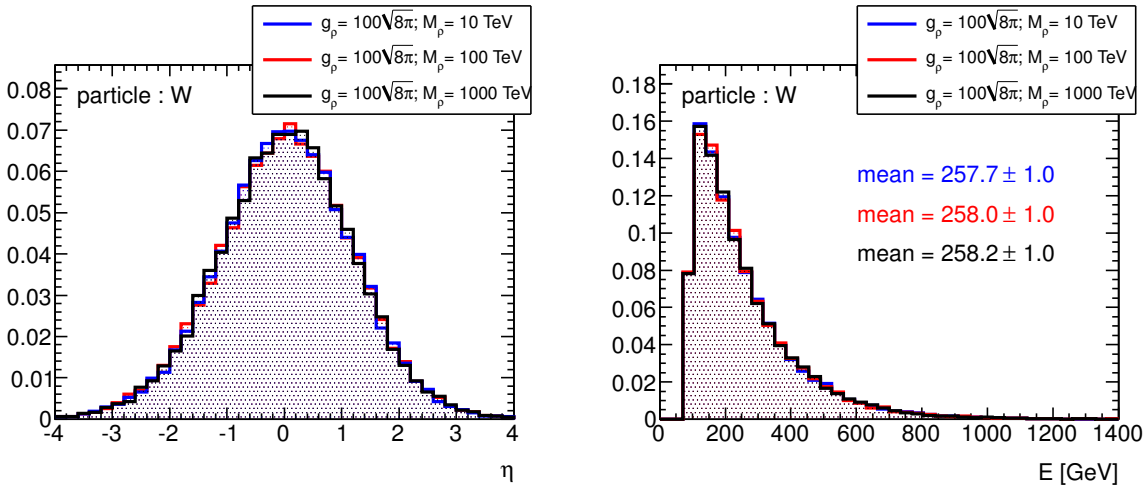
g_ρ= 100√8π; M_ρ= 10 TeV
g_ρ= 100√8π; M_ρ= 100 TeV
g_ρ= 100√8π; M_ρ= 1000 TeV
particle : W
η
E [GeV]
mean = 257.7 ± 1.0
mean = 258.0 ± 1.0
mean = 258.2 ± 1.0

(b)

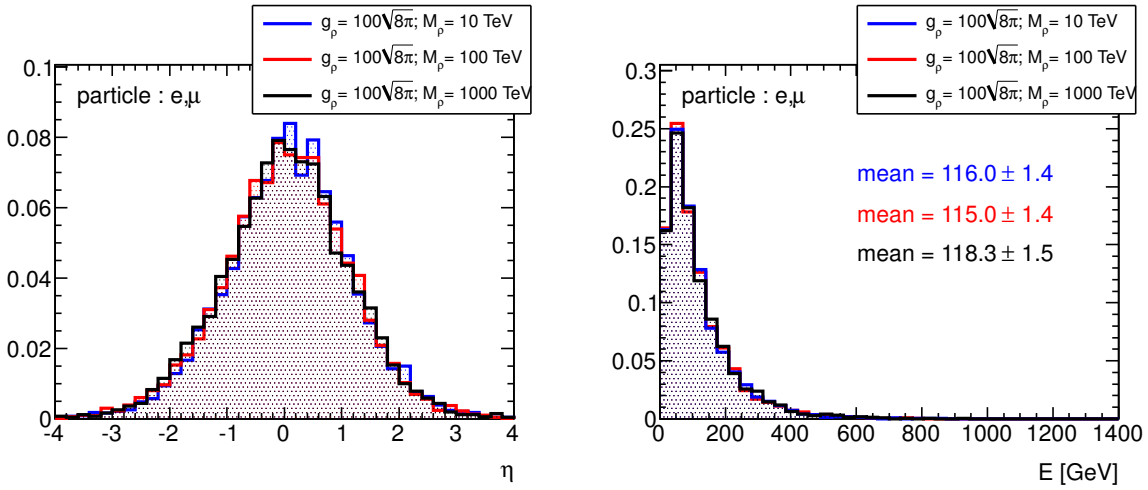
g_ρ= 100√8π; M_ρ= 10 TeV
g_ρ= 100√8π; M_ρ= 100 TeV
g_ρ= 100√8π; M_ρ= 1000 TeV
particle : e,μ
η
E [GeV]
mean = 116.0 ± 1.4
mean = 115.0 ± 1.4
mean = 118.3 ± 1.5

(c)

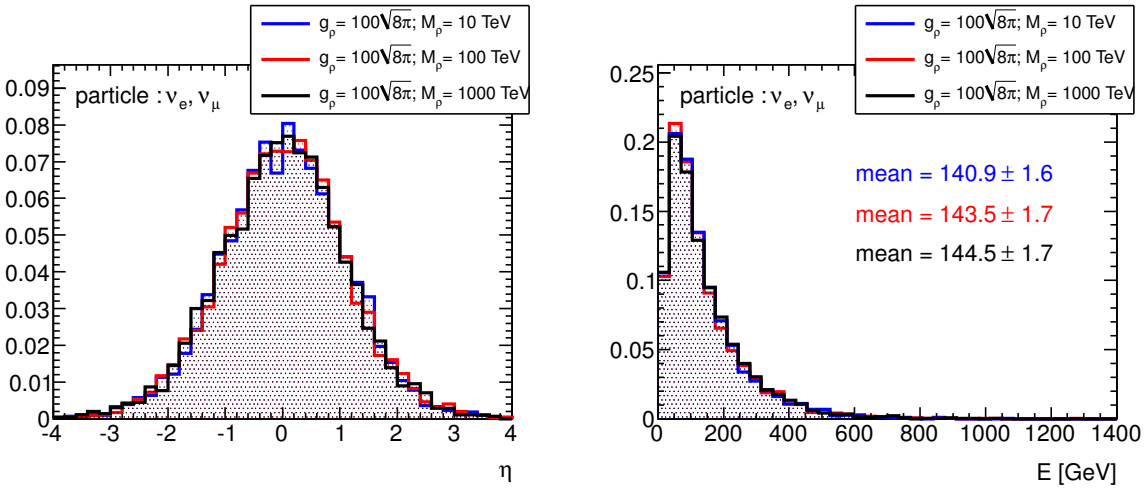

(d)

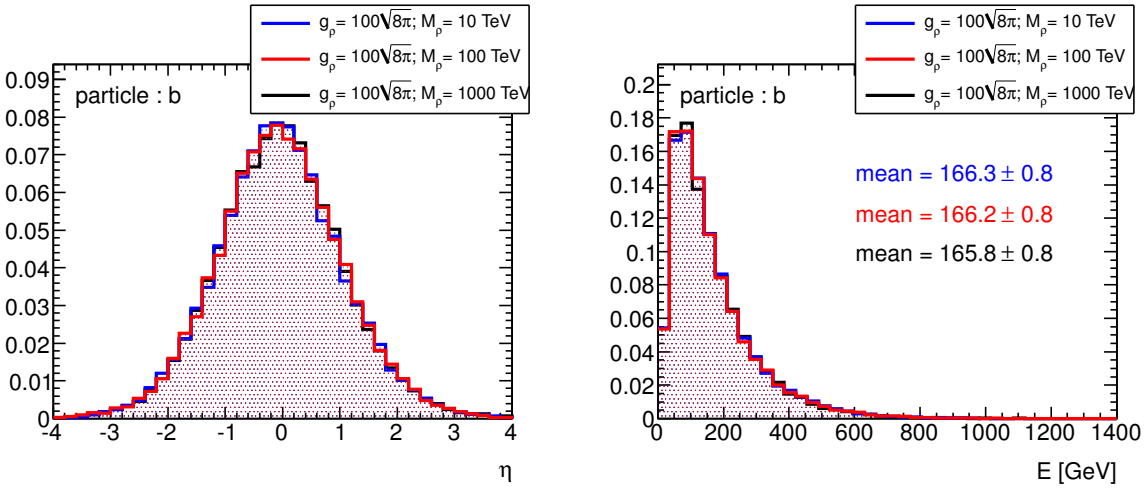

(e)

Figure A.1: Inclusive distributions of η and energy at parton level for top quarks (a), W bosons (b), electrons and muons (c), neutrinos (d) and b quarks (e) for the three different configurations studied.

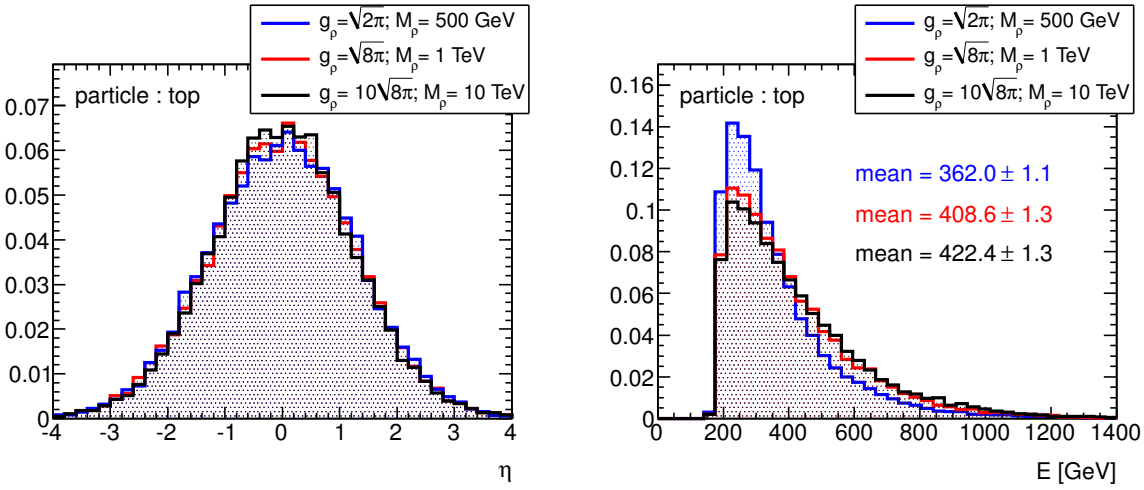
$g_\rho=\sqrt{2\pi}$; M_ρ= 500 GeV
$g_\rho=\sqrt{8\pi}$; M_ρ= 1 TeV
$g_\rho= 10\sqrt{8\pi}$; M_ρ= 10 TeV
particle : top
η
E [GeV]
mean = 362.0 ± 1.1
mean = 408.6 ± 1.3
mean = 422.4 ± 1.3

(a)

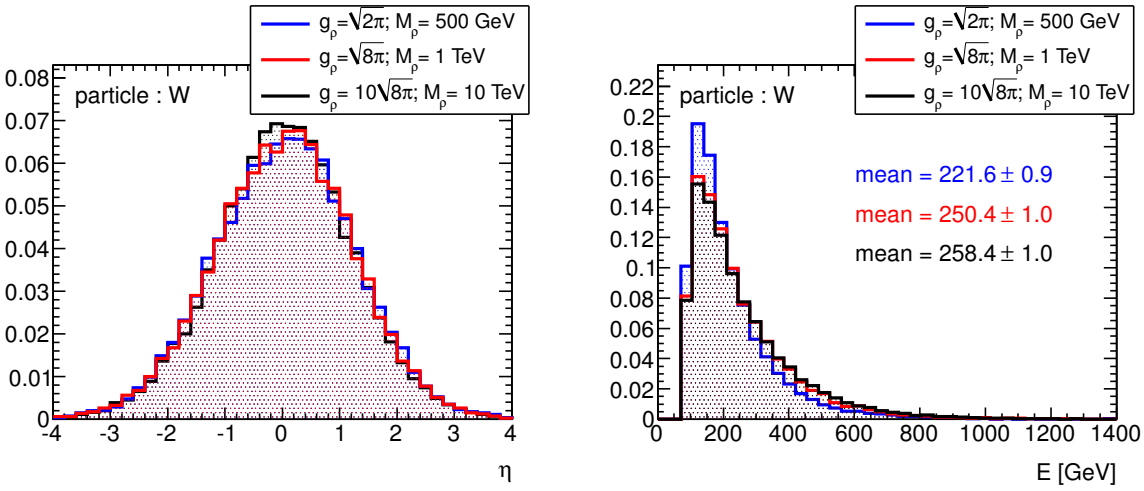
$g_\rho=\sqrt{2\pi}$; M_ρ= 500 GeV
$g_\rho=\sqrt{8\pi}$; M_ρ= 1 TeV
$g_\rho= 10\sqrt{8\pi}$; M_ρ= 10 TeV
particle : W
η
E [GeV]
mean = 221.6 ± 0.9
mean = 250.4 ± 1.0
mean = 258.4 ± 1.0

(b)

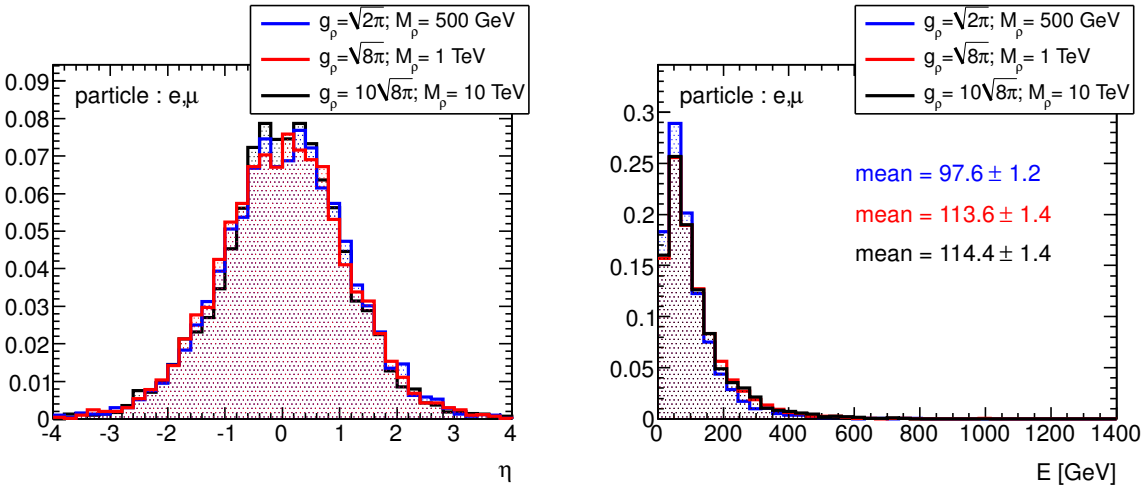
$g_\rho=\sqrt{2\pi}$; M_ρ= 500 GeV
$g_\rho=\sqrt{8\pi}$; M_ρ= 1 TeV
$g_\rho= 10\sqrt{8\pi}$; M_ρ= 10 TeV
particle : e,μ
η
E [GeV]
mean = 97.6 ± 1.2
mean = 113.6 ± 1.4
mean = 114.4 ± 1.4

(c)

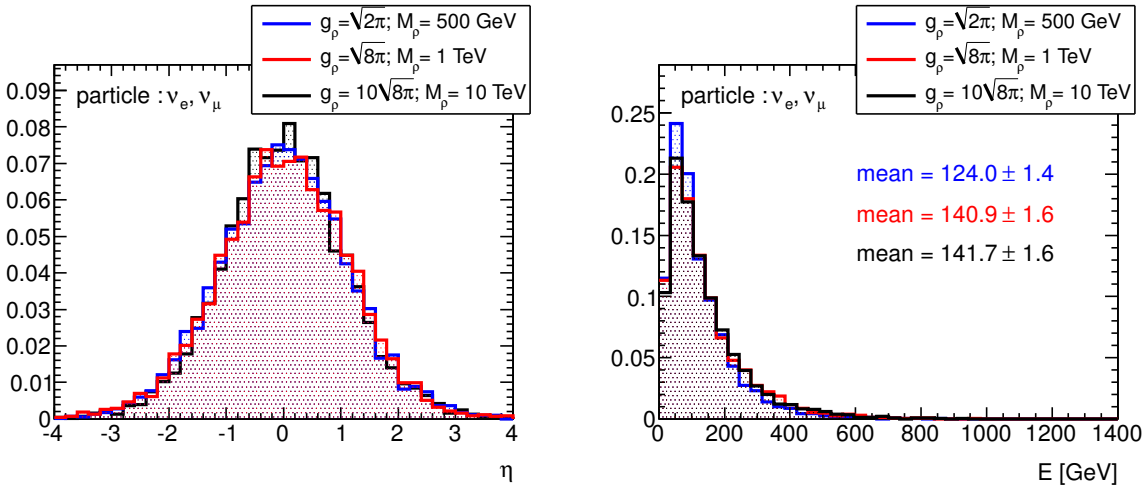

(d)

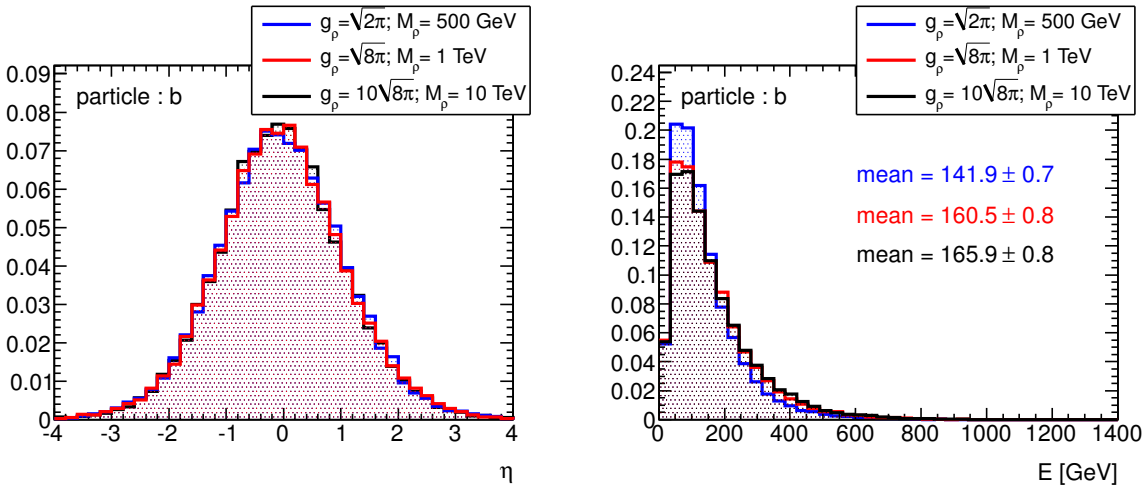

(e)

Figure A.2: Inclusive distributions of η and energy at parton level for top quarks (a), W bosons (b), electrons and muons (c), neutrinos (d) and b quarks (e) for ($g_\rho = \sqrt{2\pi}, M_\rho = 500$ GeV), ($g_\rho = \sqrt{8\pi}, M_\rho =$ 1 TeV) and ($g_\rho = 10\sqrt{8\pi}, M_\rho = 10$ TeV).

Appendix B

Systematic uncertainties used in the limit computation

B.1 Uncertainties affecting the Monte Carlo samples

The list of the systematic uncertainties affecting the Monte Carlo samples used for the limit computation on the four tops production cross-section at 7 (resp. 8) TeV can be found in Tables B.1, B.2 and B.3 (resp. B.4, B.5 and B.6) for the ee, $e\mu$ and $\mu\mu$ channels, respectively. In the tables, the name of the uncertainties follows the following notation:

- **BTagSF(b,c,l):** Uncertainties on the b-tagging, c-tagging and light-jets tagging scale factors.
- **EE(R,S):** Uncertainties on the electron energy resolution and electron energy scale.
- **JEFFSF:** Uncertainty on the jet efficiency scale factor.
- **JERSF:** Uncertainty on the jet energy resolution scale factor.
- **JES:** Uncertainty on jet energy scale.
- **JVFSF:** Uncertainty on the JVF scale factor.
- **Luminosity:** Uncertainty on the integrated luminosity.
- **MuER(ID,MS):** Uncertainty on the muon energy resolution coming from the inner detector (ID) and muon spectrometer (MS).
- **MuES:** Uncertainty on the muon energy scale.
- **PDF:** Uncertainty on the PDF.
- **SSW(id,rec,trg):** Uncertainty on the lepton scale factors of the same-sign pair coming from identification (id), reconstruction (rec) and trigger (trg).
- **XS:** Uncertainty on the cross-section production.

Uncertainty	4 tops C.I.	$t\bar{t}W(+jet)$	$t\bar{t}Z(+jet)$	$t\bar{t}WW$	$WWjj$	WZ/ZZ
BTagSFb	+4.9/-5.9	+7.3/-7.2	+4.6/-6.3	+7.3/-7.2	+1.5/-1.5	+1.5/-1.5
BTagSFc	+0.8/-0.6	+0.9/-0.9	+0.2/-0.2	+0.9/-0.9	+0.6/-0.8	+0.6/-0.8
BTagSFl	+0.0/-0.1	+0.7/-0.7	+0.4/-0.4	+0.7/-0.7	+19.2/-19.4	+19.2/-19.4
EER	+0.0/-0.3	+0.4/-0.0	+0.0/-0.1	+0.4/-0.0	+0.0/-0.0	+1.5/-1.2
EES	+0.3/-0.3	+1.6/-1.7	+1.5/-0.8	+1.6/-1.7	+0.0/-0.0	+0.1/-0.0
JEFFSF	+0.4/-0.4	+0.3/-0.4	+0.3/-0.4	+0.0/-0.1	+0.0/-0.0	+1.1/-1.2
JERSF	+2.9/-2.9	+0.3/-0.3	+5.5/-5.5	+0.3/-0.3	+4.0/-4.0	+4.0/-4.0
JES	+4.2/-1.4	+9.3/-10.4	+6.3/-7.7	+3.2/-8.1	+6.0/-6.0	+15.9/-14.4
JVFSF	+2.4/-3.0	+1.5/-1.9	+1.6/-1.9	+1.5/-1.9	+0.8/-1.1	+0.8/-1.1
Luminosity	+3.9/-3.9	+3.9/-3.9	+3.9/-3.9	+3.9/-3.9	+3.9/-3.9	+3.9/-3.9
MuERID	+0.3/-0.0	+0.0/-0.0	+0.0/-0.0	+0.0/-0.0	+0.0/-0.0	+0.0/-0.0
MuERMS	+0.3/-0.0	+0.0/-0.0	+0.0/-0.0	+0.0/-0.0	+0.0/-0.0	+0.0/-0.0
MuES	+0.4/-0.0	+0.0/-0.0	+0.0/-0.0	+0.0/-0.1	+0.0/-0.0	+0.0/-0.0
PDF	+1.0/-0.9	–	–	–	–	–
SSWid	+4.5/-4.4	+4.6/-4.5	+4.5/-4.4	+4.6/-4.5	+4.5/-4.4	+4.5/-4.4
SSWrec	+1.8/-1.8	+1.7/-1.7	+1.8/-1.8	+1.7/-1.7	+1.7/-1.7	+1.7/-1.7
SSWtrg	+0.9/-0.9	+0.5/-0.5	+0.1/-0.1	+0.5/-0.5	+1.0/-1.0	+1.0/-1.0
XS	+0.0/-0.0	+30.0/-30.0	+50.0/-50.0	+35.0/-24.0	+50.0/-50.0	+34.3/-34.3
Total	+9.8/-9.7	+32.9/-33.2	+51.3/-51.7	+36.5/-27.2	+54.4/-54.5	+43.1/-42.7

Table B.1: List of systematic uncertainties (in %) for each sample in the ee channel used in the limit computation at $\sqrt{s} = 7$ TeV.

Uncertainty	4 tops C.I.	$t\bar{t}W(+jet)$	$t\bar{t}Z(+jet)$	$t\bar{t}WW$	$WWjj$	WZ/ZZ
BTagSFb	+0.0/-0.9	+6.3/-7.8	+3.7/-4.6	+6.3/-7.8	+3.0/-3.0	+3.0/-3.0
BTagSFc	+0.1/-0.0	+0.2/-0.2	+0.4/-0.4	+0.2/-0.2	+9.4/-9.4	+9.4/-9.4
BTagSFl	+0.1/-0.1	+0.4/-0.4	+0.3/-0.4	+0.4/-0.4	+5.3/-5.4	+5.3/-5.4
EER	+0.0/-0.1	+0.0/-0.9	+0.0/-0.4	+0.0/-0.9	+7.7/-0.0	+7.7/-0.0
EES	+0.2/-0.0	+0.3/-1.1	+0.2/-0.3	+0.3/-1.1	+0.9/-0.1	+0.0/-0.0
JEFFSF	+0.0/-0.1	+0.0/-0.1	+0.1/-0.2	+0.1/-0.2	+0.0/-0.1	+0.3/-0.4
JERSF	+1.3/-1.3	+1.5/-1.5	+1.3/-1.3	+1.5/-1.5	+25.1/-25.1	+25.1/-25.1
JES	+0.8/-2.4	+8.1/-8.8	+10.8/-8.3	+9.7/-8.0	+6.3/-7.9	+13.4/-12.6
JVFSF	+2.4/-2.8	+1.5/-1.8	+1.5/-1.8	+1.5/-1.8	+0.8/-1.1	+0.8/-1.1
Luminosity	+3.9/-3.9	+3.9/-3.9	+3.9/-3.9	+3.9/-3.9	+3.9/-3.9	+3.9/-3.9
MuERID	+0.0/-0.1	+0.1/-0.0	+0.0/-0.1	+0.1/-0.0	+0.6/-0.0	+2.1/-0.0
MuERMS	+0.0/-0.1	+0.1/-0.0	+0.0/-0.1	+0.1/-0.0	+0.6/-0.0	+2.1/-0.0
MuES	+0.2/-0.2	+0.2/-0.2	+0.1/-0.1	+0.2/-0.2	+0.0/-0.1	+0.0/-0.0
PDF	+1.0/-0.9	–	–	–	–	–
SSWid	+3.0/-3.0	+3.0/-3.0	+3.0/-2.9	+3.0/-3.0	+3.0/-2.9	+3.0/-2.9
SSWrec	+1.2/-1.2	+1.2/-1.2	+1.3/-1.2	+1.2/-1.2	+1.2/-1.2	+1.2/-1.2
SSWtrg	+0.1/-0.1	+0.0/-0.0	+0.2/-0.2	+0.0/-0.0	+0.3/-0.3	+0.3/-0.3
XS	+0.0/-0.0	+30.0/-30.0	+50.0/-50.0	+35.0/-24.0	+50.0/-50.0	+34.3/-34.3
Total	+5.8/-6.4	+32.2/-32.7	+51.6/-51.2	+37.3/-27.1	+58.1/-57.8	+46.9/-46.0

Table B.2: List of systematic uncertainties (in %) for each sample in the $e\mu$ channel used in the limit computation at $\sqrt{s} = 7$ TeV.

Uncertainty	4 tops C.I.	$t\bar{t}W(+jet)$	$t\bar{t}Z(+jet)$	$t\bar{t}WW$	$WWjj$	WZ/ZZ
BTagSFb	+2.8/-3.3	+3.8/-5.5	+5.4/-6.1	+3.8/-5.5	+0.8/-0.8	+0.8/-0.8
BTagSFc	+0.4/-0.4	+0.2/-0.2	+0.6/-0.7	+0.2/-0.2	+0.1/-0.2	+0.1/-0.2
BTagSFl	+0.0/-0.0	+0.2/-0.2	+0.3/-0.3	+0.2/-0.2	+24.6/-24.9	+24.6/-24.9
EER	+0.0/-0.0	+0.0/-0.0	+0.0/-0.0	+0.0/-0.0	+0.0/-0.0	+0.0/-0.0
EES	+0.0/-0.0	+0.0/-0.1	+0.0/-0.0	+0.0/-0.0	+0.0/-0.0	+0.0/-0.0
JEFFSF	+0.2/-0.3	+0.0/-0.1	+0.6/-0.7	+0.1/-0.2	+0.0/-0.0	+0.4/-0.5
JERSF	+0.5/-0.5	+1.0/-1.0	+6.4/-6.4	+1.0/-1.0	+6.3/-6.3	+6.3/-6.3
JES	+0.0/-1.1	+8.1/-9.9	+5.4/-6.9	+5.1/-4.0	+0.5/-10.9	+6.0/-2.7
JVFSF	+2.2/-2.9	+1.5/-1.8	+1.4/-1.8	+1.5/-1.8	+1.2/-1.3	+1.2/-1.3
Luminosity	+3.9/-3.9	+3.9/-3.9	+3.9/-3.9	+3.9/-3.9	+3.9/-3.9	+3.9/-3.9
MuERID	+0.0/-0.0	+0.0/-0.0	+0.0/-0.9	+0.0/-0.0	+1.1/-1.1	+3.3/-0.6
MuERMS	+0.0/-0.0	+0.0/-0.0	+0.0/-0.9	+0.0/-0.0	+1.1/-1.1	+3.3/-0.6
MuES	+0.4/-0.4	+0.3/-0.3	+0.6/-0.6	+0.3/-0.3	+0.0/-0.0	+0.0/-0.0
PDF	+1.0/-0.9	–	–	–	–	–
SSWid	+1.5/-1.5	+1.5/-1.5	+1.5/-1.5	+1.5/-1.5	+1.5/-1.5	+1.5/-1.5
SSWrec	+0.7/-0.7	+0.7/-0.7	+0.7/-0.7	+0.7/-0.7	+0.7/-0.7	+0.7/-0.7
SSWtrg	+0.5/-0.5	+0.3/-0.4	+0.5/-0.5	+0.3/-0.4	+2.3/-2.2	+2.3/-2.2
XS	+0.0/-0.0	+30.0/-30.0	+50.0/-50.0	+35.0/-24.0	+50.0/-50.0	+34.3/-34.3
Total	+5.6/-6.2	+31.6/-32.4	+51.2/-51.5	+35.9/-25.4	+56.3/-57.5	+43.6/-43.2

Table B.3: List of systematic uncertainties (in %) for each sample in the $\mu\mu$ channel used in the limit computation at $\sqrt{s} = 7$ TeV.

	4 tops SM	4 tops C.I.	$t\bar{t}W(jet(s))$	$t\bar{t}Z(jet(s))$	$WWjj$	$t\bar{t}WW$	WZ/ZZ
BTagSFb	+6.2/-7.1	+0.0/-2.2	+19.1/-17.4	+15.6/-14.3	+0.0/+0.0	+16.9/-16.1	+0.0/+0.0
BTagSFc	+3.0/-2.7	+2.0/-1.9	+2.1/-2.2	+1.1/-0.5	+0.0/+0.0	+0.6/-0.8	+0.0/+0.0
BTagSFl	+0.8/-0.8	+0.1/-0.1	+0.9/-0.8	+0.3/-0.3	+0.0/+0.0	+0.3/-0.3	+0.0/+0.0
EER	+0.0/-0.4	+1.2/-0.0	+0.0/-1.0	+0.0/-0.0	+0.0/+0.0	+1.2/-0.0	+0.0/+0.0
EES	+0.0/-0.0	+0.0/-0.0	+0.0/-0.0	+0.0/-0.0	+0.0/+0.0	+0.0/-0.0	+0.0/+0.0
JEFFSF	+0.0/-0.0	+0.0/-0.0	+0.0/-0.0	+0.0/-0.0	+0.0/+0.0	+0.0/-0.0	+0.0/+0.0
JERSF	+2.2/-2.2	+1.1/-1.1	+2.6/-2.6	+5.2/-5.2	+0.0/+0.0	+2.7/-2.7	+0.0/+0.0
JES	+5.2/-7.8	+1.5/-2.8	+12.9/-12.0	+9.0/-26.1	+0.0/+0.0	+10.0/-9.4	+12.2/+0.0
JVFSF	+8.3/-7.0	+8.8/-7.4	+1.8/-2.2	+2.2/-2.3	+0.0/+0.0	+2.2/-2.3	+0.0/+0.0
Luminosity	+3.6/-3.6	+3.6/-3.6	+3.6/-3.6	+3.6/-3.6	+3.6/-3.6	+3.6/-3.6	+3.6/-3.6
MuERID	+0.0/-0.0	+0.0/-0.0	+0.0/-0.0	+0.0/-0.0	+0.0/+0.0	+0.0/-0.0	+0.0/+0.0
MuERMS	+0.0/-0.0	+0.0/-0.0	+0.0/-0.0	+0.0/-0.0	+0.0/+0.0	+0.0/-0.0	+0.0/+0.0
MuES	+0.0/-0.0	+0.0/-0.0	+0.0/-0.0	+0.0/-0.0	+0.0/+0.0	+0.0/-0.0	+0.0/+0.0
PDF	+1.0/-0.9	+1.0/-0.9	–	–	–	–	–
SSWid	+4.8/-4.7	+4.8/-4.7	+4.8/-4.7	+4.8/-4.7	+0.0/+0.0	+4.8/-4.7	+0.0/+0.0
SSWrec	+1.3/-1.3	+1.4/-1.3	+1.3/-1.3	+1.4/-1.4	+0.0/+0.0	+1.3/-1.3	+0.0/+0.0
SSWtrg	+0.0/-0.0	+0.5/-0.5	+0.5/-0.5	+0.2/-0.2	+0.0/+0.0	+0.2/-0.2	+0.0/+0.0
XS	–	–	+30.0/-30.0	+30.0/-30.0	+25.0/-25.0	+38.0/-26.0	+34.3/-34.3
Total	+13.6/-14.6	+11.2/-10.5	+38.5/-37.4	+36.0/-43.1	+25.3/-25.3	+43.4/-32.7	+36.6/-34.5

Table B.4: List of systematic uncertainties (in %) for each sample in the ee channel used in the limit computation at $\sqrt{s} = 8$ TeV.

	4 tops SM	4 tops C.I.	$t\bar{t}W(jet(s))$	$t\bar{t}Z(jet(s))$	$WWjj$	$t\bar{t}WW$	WZ/ZZ
BTagSFb	+8.4/-9.9	+2.7/-6.2	+20.9/-19.2	+18.3/-17.0	+0.0/-0.0	+15.8/-14.9	+13.5/-13.5
BTagSFc	+1.3/-1.3	+4.6/-5.3	+4.3/-4.9	+4.3/-3.2	+15.6/-15.6	+0.0/-0.9	+11.3/-13.4
BTagSFl	+0.3/-0.3	+0.0/-0.1	+1.2/-1.2	+1.5/-1.4	+22.6/-22.8	+0.8/-0.8	+0.6/-0.6
EER	+0.0/-0.1	+0.0/-0.0	+1.5/-0.0	+0.5/-1.2	+0.1/-0.1	+0.0/-0.5	+0.0/-0.0
EES	+0.0/-0.0	+0.0/-0.0	+0.0/-0.0	+0.0/-0.0	+0.0/-0.0	+0.0/-0.0	+0.0/-0.0
JEFFSF	+0.0/-0.0	+0.0/-0.0	+0.2/-0.2	+0.0/-0.0	+0.0/-0.0	+0.0/-0.0	+0.0/-0.0
JERSF	+0.2/-0.2	+1.2/-1.2	+0.2/-0.2	+4.9/-4.9	+0.1/-0.1	+4.1/-4.1	+100.0/-100.0
JES	+4.2/-7.1	+3.1/-3.3	+7.1/-8.0	+17.0/-12.8	+0.0/-0.1	+4.9/-11.2	+0.3/-0.2
JVFSF	+8.9/-7.5	+8.7/-7.4	+1.8/-2.1	+2.5/-2.5	+3.0/-2.6	+1.8/-2.2	+3.3/-2.7
Luminosity	+3.6/-3.6	+3.6/-3.6	+3.6/-3.6	+3.6/-3.6	+3.6/-3.6	+3.6/-3.6	+3.6/-3.6
MuERID	+0.0/-0.0	+0.2/-0.0	+0.4/-0.0	+0.0/-0.0	+0.0/-0.0	+0.0/-0.0	+0.0/-0.0
MuERMS	+0.0/-0.0	+0.2/-0.0	+0.4/-0.0	+0.0/-0.0	+0.0/-0.0	+0.0/-0.0	+0.0/-0.0
MuES	+0.0/-0.0	+0.0/-0.0	+0.0/-0.0	+0.0/-0.0	+0.0/-0.0	+0.0/-0.0	+0.0/-0.0
PDF	+1.0/-0.9	+1.0/-0.9	–	–	–	–	–
SSWid	+4.4/-4.3	+4.4/-4.3	+4.4/-4.3	+4.4/-4.3	+4.4/-4.3	+4.4/-4.3	+4.4/-4.3
SSWrec	+1.0/-1.0	+1.0/-1.0	+1.0/-1.0	+1.0/-1.0	+1.0/-1.0	+1.0/-1.0	+0.9/-0.9
SSWtrg	+1.1/-1.1	+0.9/-0.9	+1.8/-1.8	+1.7/-1.7	+2.4/-2.4	+0.3/-0.4	+2.1/-2.1
XS	–	–	+30.0/-30.0	+30.0/-30.0	+25.0/-25.0	+38.0/-26.0	+34.3/-34.3
Total	+14.3/-13.6	+12.3/-13.0	+38.1/-37.4	+40.1/-37.9	+37.8/-37.9	+42.1/-32.8	+107.4/-107.6

Table B.5: List of systematic uncertainties (in %) for each sample in the $e\mu$ channel used in the limit computation at $\sqrt{s} = 8$ TeV.

	4 tops SM	4 tops C.I.	$t\bar{t}W(jet(s))$	$t\bar{t}Z(jet(s))$	$WWjj$	$t\bar{t}WW$	WZ/ZZ
BTagSFb	+3.6/-6.9	+6.1/-7.7	+20.5/-19.0	+26.5/-23.4	+0.0/+0.0	+18.1/-16.5	+0.0/+0.0
BTagSFc	+4.0/-4.4	+3.3/-2.8	+0.4/-0.5	+5.3/-5.3	+0.0/+0.0	+1.0/-1.4	+0.0/+0.0
BTagSFl	+0.1/-0.1	+0.5/-0.5	+1.0/-1.0	+1.3/-1.4	+0.0/+0.0	+1.8/-1.8	+0.0/+0.0
EER	+0.0/-0.0	+0.0/-0.0	+0.0/-0.0	+0.0/-0.0	+0.0/+0.0	+0.0/-0.0	+0.0/+0.0
EES	+0.0/-0.0	+0.0/-0.0	+0.0/-0.0	+0.0/-0.0	+0.0/+0.0	+0.0/-0.0	+0.0/+0.0
JEFFSF	+0.0/-0.0	+0.0/-0.0	+0.1/-0.1	+0.0/-0.0	+0.0/+0.0	+1.6/-1.6	+0.0/+0.0
JERSF	+1.1/-1.1	+1.6/-1.6	+0.6/-0.6	+1.9/-1.9	+0.0/+0.0	+2.8/-2.8	+0.0/+0.0
JES	+2.5/-6.2	+0.0/-2.4	+8.6/-8.1	+10.9/-8.1	+0.0/+0.0	+8.2/-5.6	+0.0/+0.0
JVFSF	+9.2/-8.1	+9.2/-7.7	+1.7/-2.0	+3.2/-2.9	+0.0/+0.0	+1.9/-2.4	+0.0/+0.0
Luminosity	+3.6/-3.6	+3.6/-3.6	+3.6/-3.6	+3.6/-3.6	+3.6/-3.6	+3.6/-3.6	+3.6/-3.6
MuERID	+0.3/-0.0	+0.0/-0.0	+0.0/-0.0	+0.0/-0.0	+0.0/+0.0	+0.0/-0.0	+0.0/+0.0
MuERMS	+0.3/-0.0	+0.0/-0.0	+0.0/-0.0	+0.0/-0.0	+0.0/+0.0	+0.0/-0.0	+0.0/+0.0
MuES	+0.0/-0.0	+0.0/-0.0	+0.0/-0.0	+0.0/-0.0	+0.0/+0.0	+0.0/-0.0	+0.0/+0.0
PDF	1.0/-0.9	+1.0/-0.9	–	–	–	–	–
SSWid	+4.0/-4.0	+4.0/-4.0	+4.0/-4.0	+4.0/-4.0	+0.0/+0.0	+4.0/-4.0	+0.0/+0.0
SSWrec	+0.6/-0.6	+0.6/-0.6	+0.7/-0.7	+0.6/-0.6	+0.0/+0.0	+0.6/-0.6	+0.0/+0.0
SSWtrg	+2.4/-2.4	+2.1/-2.1	+2.1/-2.1	+1.9/-1.8	+0.0/+0.0	+2.4/-2.4	+0.0/+0.0
XS	–	–	+30.0/-30.0	+30.0/-30.0	+25.0/-25.0	+38.0/-26.0	+34.3/-34.3
Total	+12.6/-14.5	+13.0/-13.0	+37.9/-36.9	+42.4/-39.8	+25.3/-25.3	+43.5/-32.2	+34.5/-34.5

Table B.6: List of systematic uncertainties (in %) for each sample in the $\mu\mu$ channel used in the limit computation at $\sqrt{s} = 8$ TeV.

B.2 Uncertainties affecting the data-driven background

The systematic uncertainties affecting the data-driven background used for the limit computation at 7 (resp. 8) TeV are listed in Table B.7 (resp. B.8).

Sample	ee	$e\mu$	$\mu\mu$
Q Mis-id	+9.7/-11.8	+6.4/-12.8	–
Fakes	+50.0/-50.0	+40.0/-40.0	+30.0/-30.0

Table B.7: Systematic uncertainties (in %) affecting the data-driven background used for the limit computation for the three different channels in the analysis at $\sqrt{s} = 7$ TeV.

Sample	ee	$e\mu$	$\mu\mu$
Q Mis-id	+32.1/-32.0	+30.4/-30.3	–
Fakes	+30.0/-30.0	+30.0/-30.0	+30.0/-30.0

Table B.8: Systematic uncertainties (in %) affecting the data-driven background used for the limit computation for the three different channels in the analysis at $\sqrt{s} = 8$ TeV.

Appendix C

Kinematical variables after final selection

The distribution of some kinematical variables after the final selection at 7 (resp. 8) TeV are shown in Figures C.1, C.2 and C.3 (resp. C.4, C.5 and C.6) for the ee, $e\mu$ and $\mu\mu$ channel, respectively.

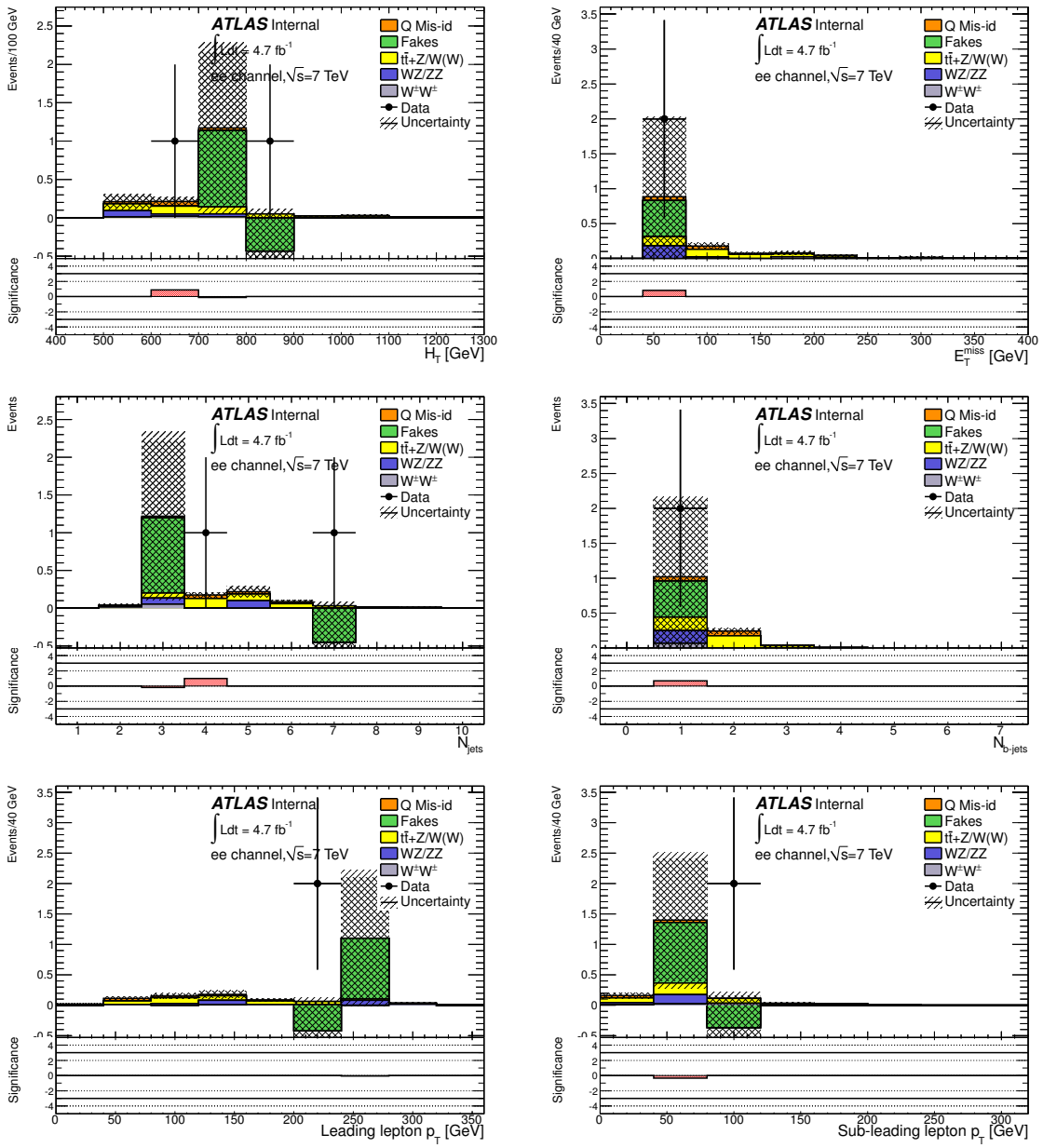

Figure C.1: Distribution of some kinematical variables for the data (points) and for the estimated background (histogram), after applying the final selection in the *ee* channel at $\sqrt{s} = 7$ TeV. The internal shaded areas correspond to the statistical uncertainties on the background while the external shaded areas correspond to the total uncertainties. For the Monte Carlo samples, systematic uncertainties include only the production cross section uncertainties.

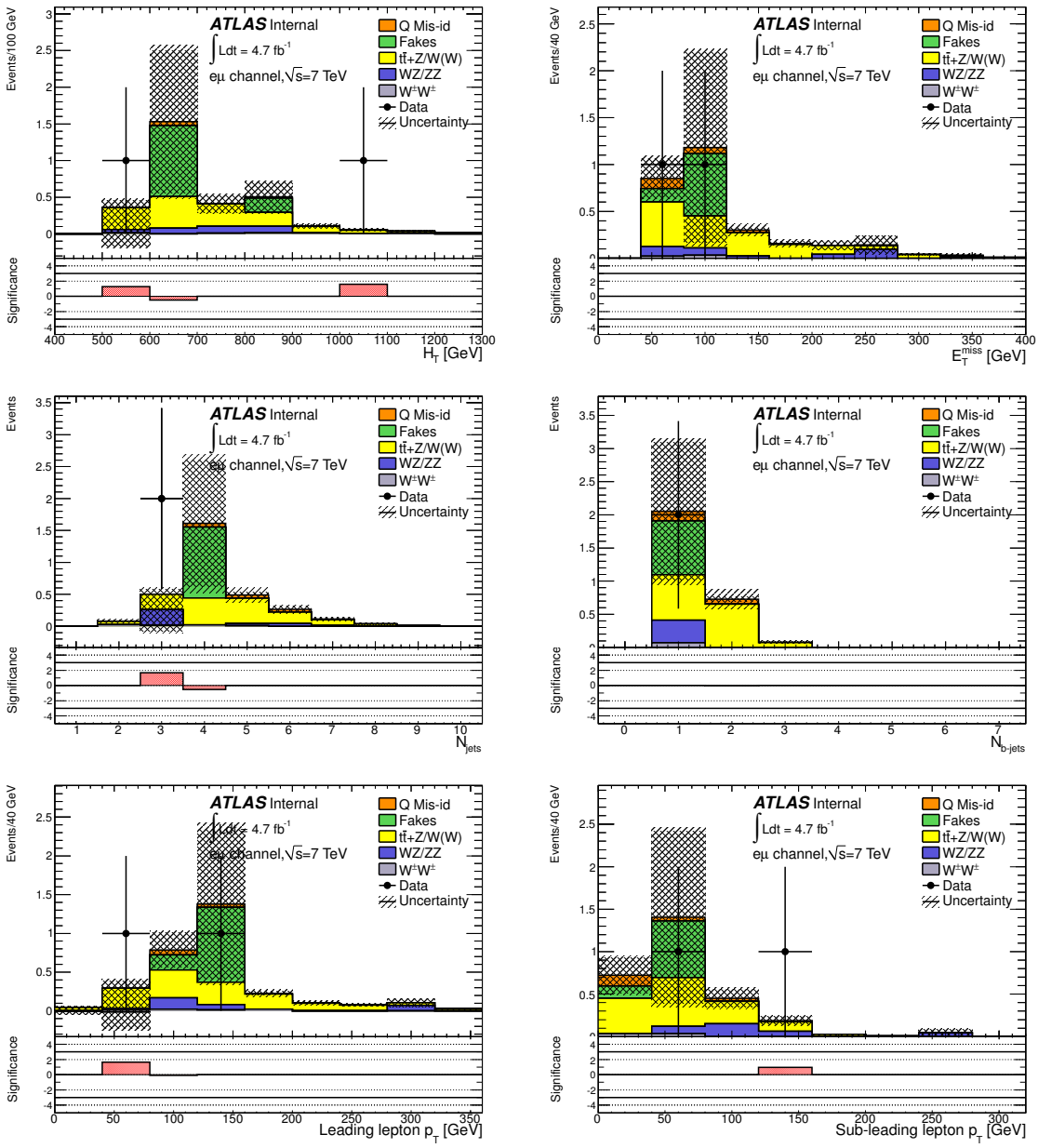

Figure C.2: Distribution of some kinematical variables for the data (points) and for the estimated background (histogram), after applying the final selection in the $e\mu$ channel at $\sqrt{s} = 7$ TeV. The internal shaded areas correspond to the statistical uncertainties on the background while the external shaded areas correspond to the total uncertainties. For the Monte Carlo samples, systematic uncertainties include only the production cross section uncertainties.

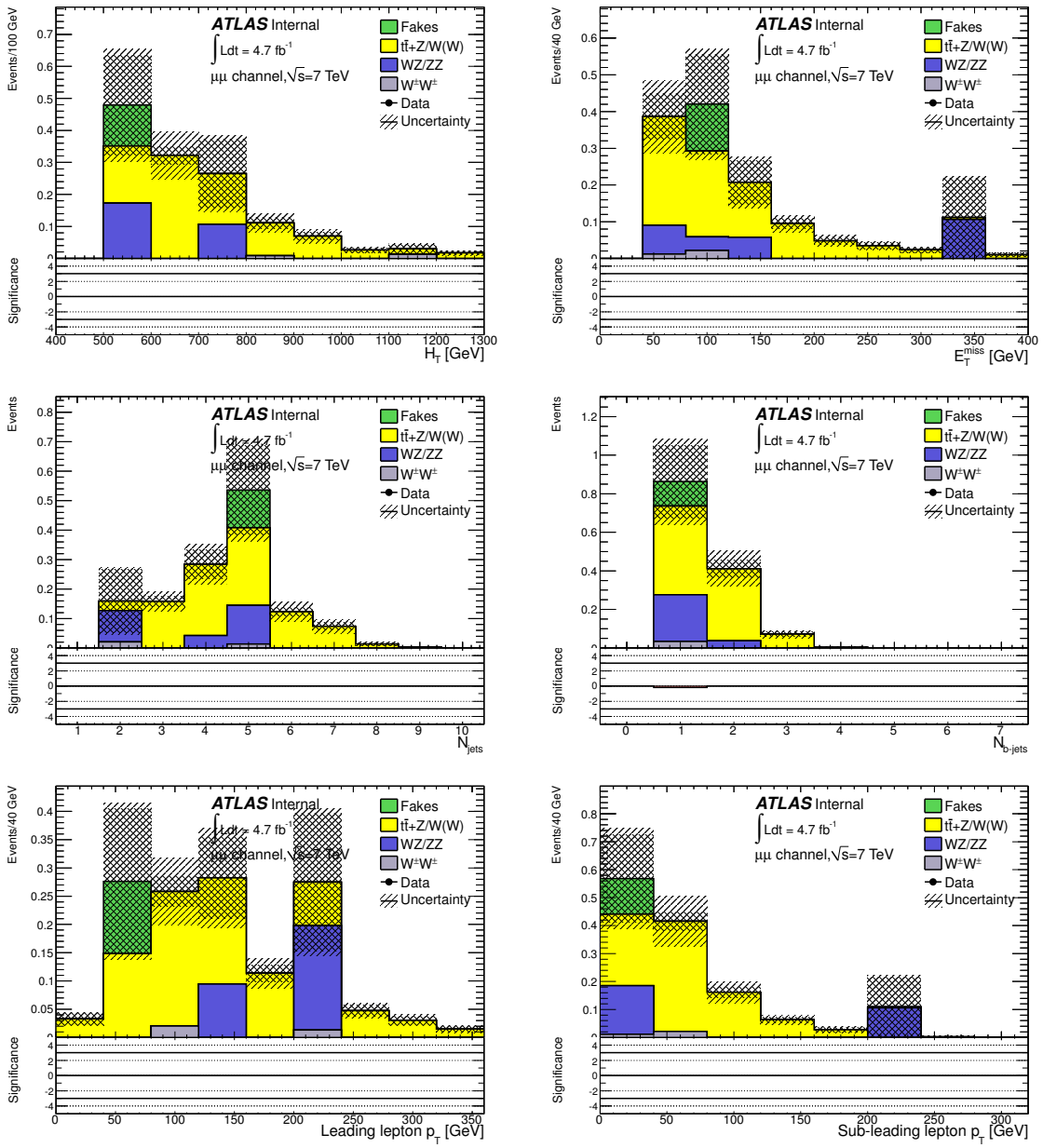

Figure C.3: Distribution of some kinematical variables for the data (points) and for the estimated background (histogram), after applying the final selection in the $\mu\mu$ channel at $\sqrt{s} = 7$ TeV. The internal shaded areas correspond to the statistical uncertainties on the background while the external shaded areas correspond to the total uncertainties. For the Monte Carlo samples, systematic uncertainties include only the production cross section uncertainties.

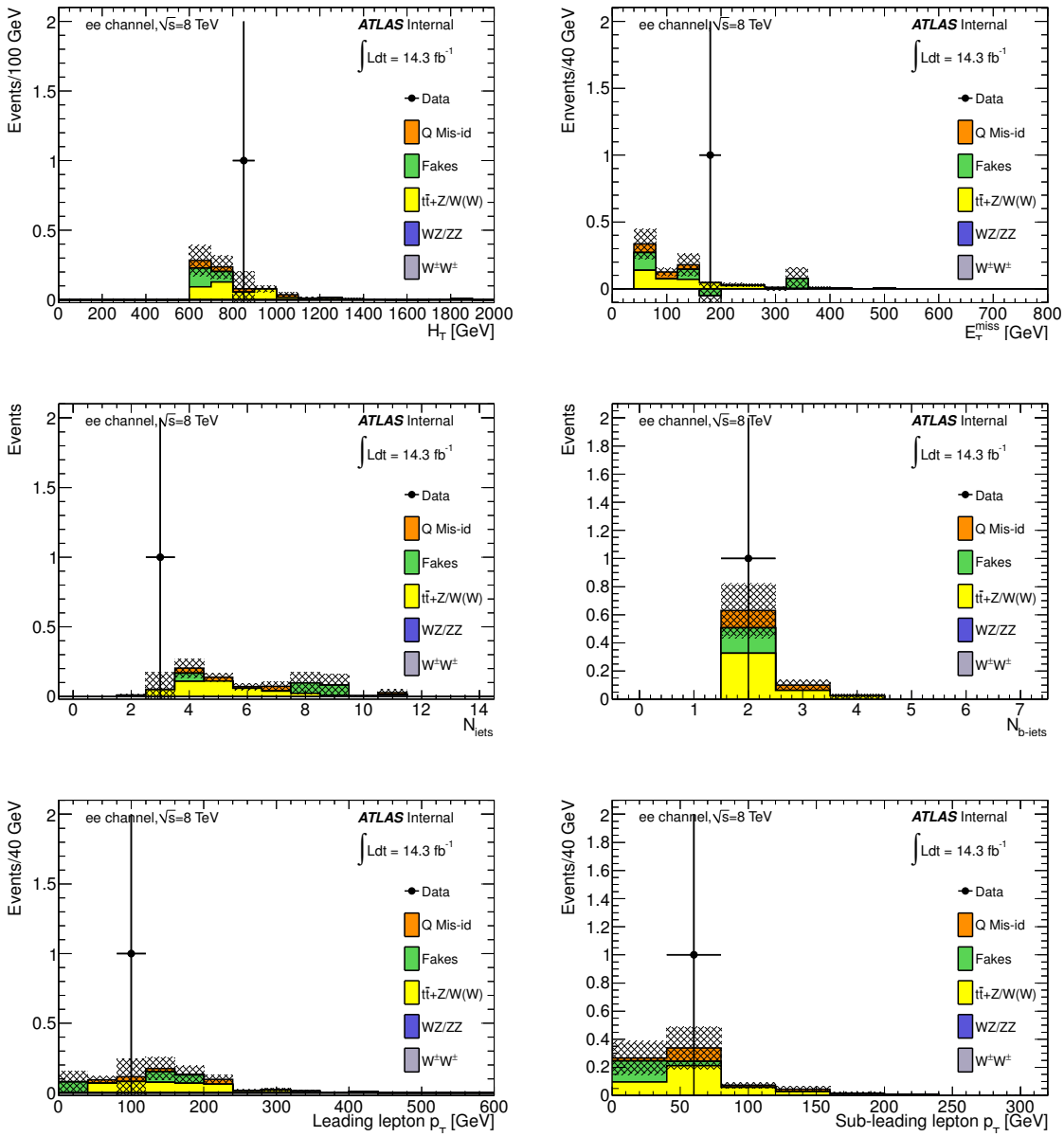

Figure C.4: Distribution of some kinematical variables for the data (points) and for the estimated background (histogram), after applying the final selection in the *ee* channel at $\sqrt{s} = 8$ TeV. The internal shaded areas correspond to the statistical uncertainties on the background while the external shaded areas correspond to the total uncertainties. For the Monte Carlo samples, systematic uncertainties include only the production cross section uncertainties.

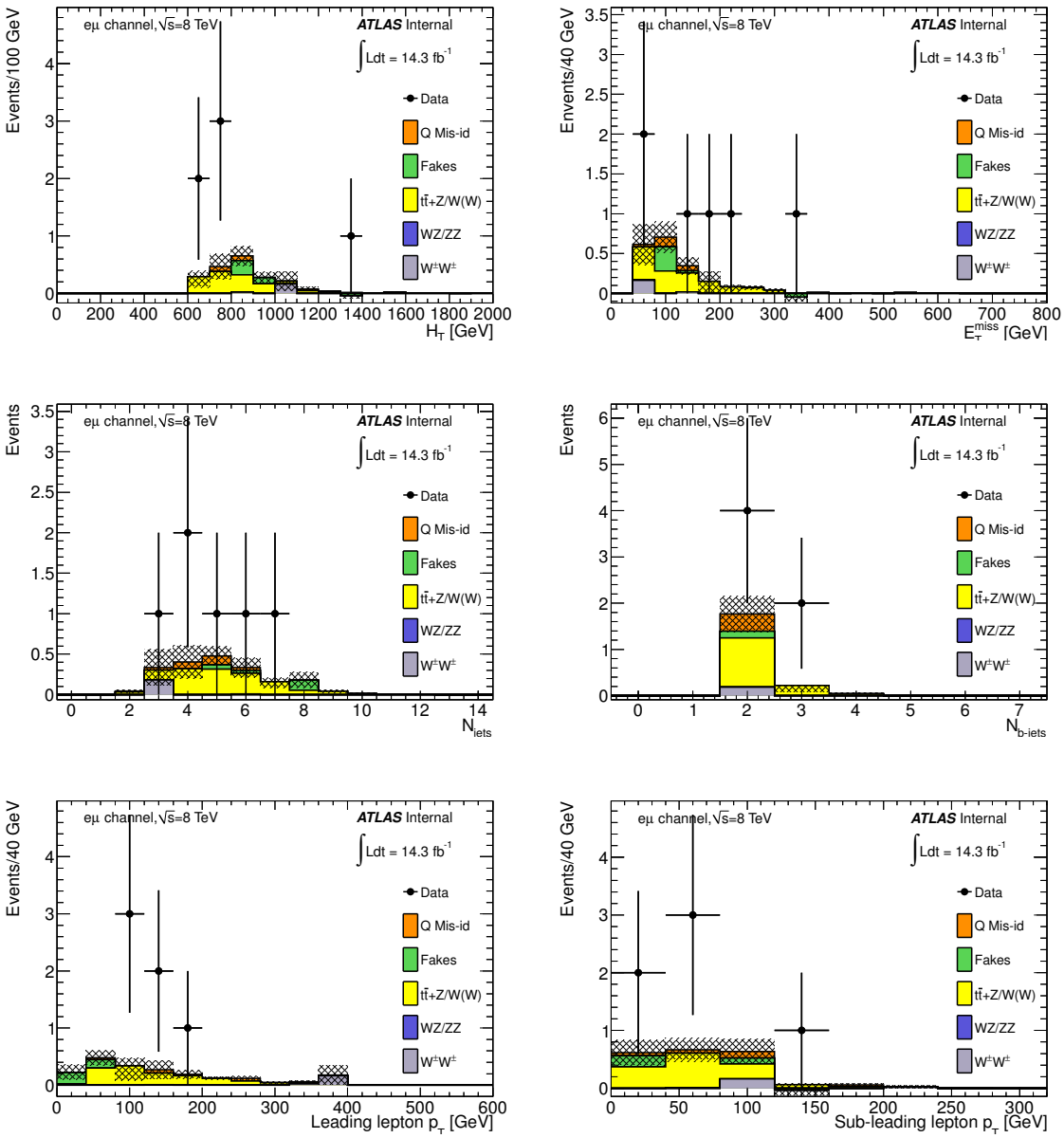

Figure C.5: Distribution of some kinematical variables for the data (points) and for the estimated background (histogram), after applying the final selection in the $e\mu$ channel at $\sqrt{s} = 8$ TeV. The internal shaded areas correspond to the statistical uncertainties on the background while the external shaded areas correspond to the total uncertainties. For the Monte Carlo samples, systematic uncertainties include only the production cross section uncertainties.

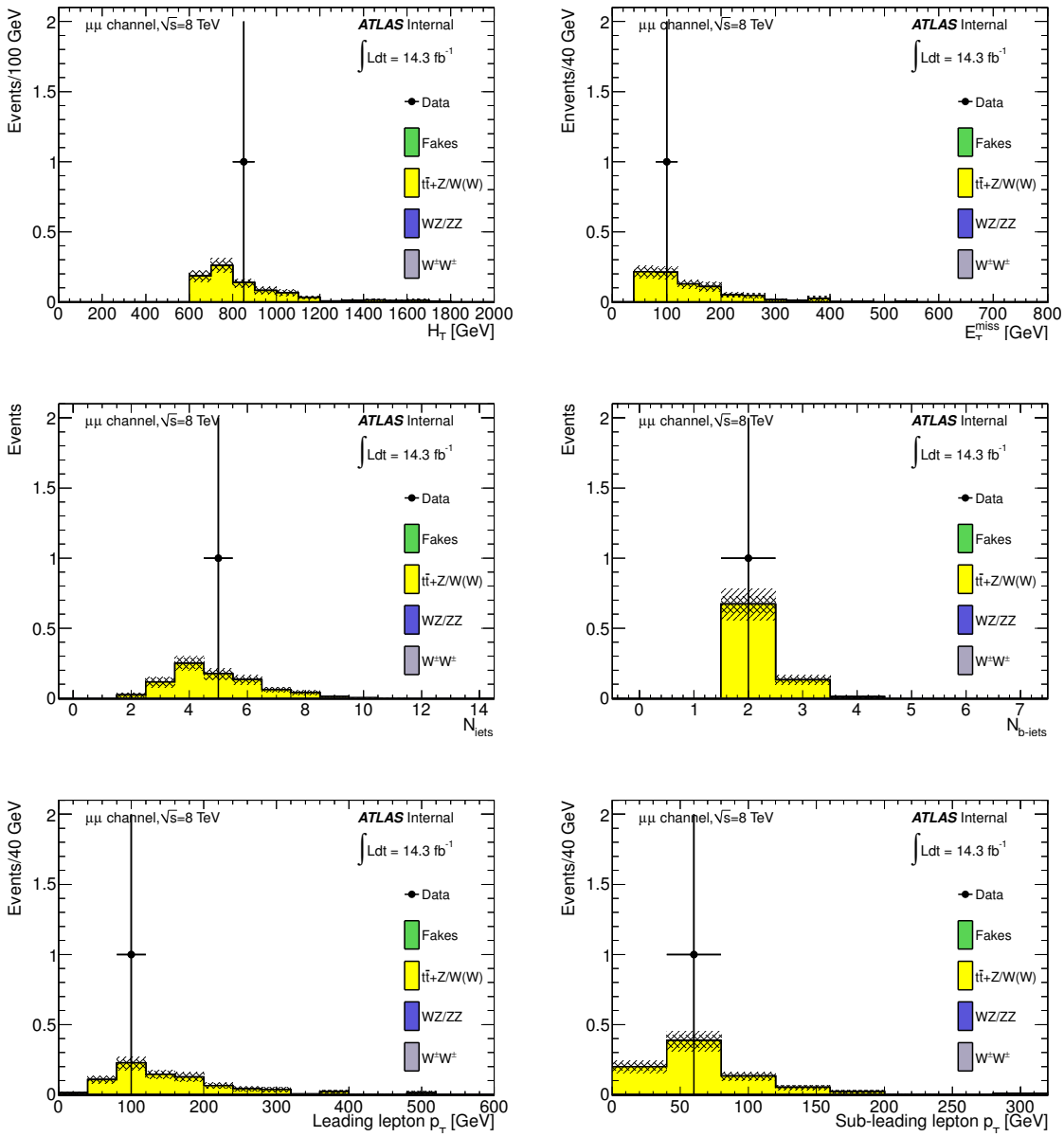

Figure C.6: Distribution of some kinematical variables for the data (points) and for the estimated background (histogram), after applying the final selection in the $\mu\mu$ channel at $\sqrt{s} = 8$ TeV. The internal shaded areas correspond to the statistical uncertainties on the background while the external shaded areas correspond to the total uncertainties. For the Monte Carlo samples, systematic uncertainties include only the production cross section uncertainties.

List of Figures

List of Tables

Bibliography

[1] P. Aurenche. The Standard Model of Particle Physics. arXiv:hep-ph/9712342 [hep-ph].

[2] G. Altarelli. The Standard Model of Particle Physics. arXiv:hep-ph/0510281 [hep-ph].

[3] L. Evans and P. Bryant. LHC Machine. *Journal of Instrumentation*, 3(08):S08001, 2008. http://stacks.iop.org/1748-0221/3/i=08/a=S08001.

[4] G. Aad *et al* – ATLAS Collaboration. The ATLAS Experiment at the CERN Large Hadron Collider. *JINST*, 3:S08003, 2008.

[5] S. Chatrchyan *et al* – CMS Collaboration. The CMS Experiment at the CERN LHC. *JINST*, 3:S08004, 2008.

[6] K. Cheung. Four Top Production and Electroweak Symmetry Breaking. arXiv:hep-ph/9507411 [hep-ph].

[7] M. Spira and J. D. Wells. Higgs Bosons Strongly Coupled to the Top Quark. *Nucl.Phys.*, B523:3–16, 1998, arXiv:hep-ph/9711410 [hep-ph].

[8] S. Jung and J. D. Wells. Low-scale warped extra dimension and its predilection for multiple top quarks. *JHEP*, 1011:001, 2010, arXiv:1008.0870 [hep-ph].

[9] G. Cacciapaglia, R. Chierici, A. Deandrea, L. Panizzi, S. Perries, *et al.* Four tops on the real projective plane at LHC. *JHEP*, 1110:042, 2011, arXiv:1107.4616 [hep-ph].

[10] A. Pomarol and J. Serra. Top Quark Compositeness: Feasibility and Implications. *Phys.Rev.*, D78:074026, 2008, arXiv:0806.3247 [hep-ph].

[11] K. Kumar, T. M. Tait, and R. Vega-Morales. Manifestations of Top Compositeness at Colliders. *JHEP*, 0905:022, 2009, arXiv:0901.3808 [hep-ph].

[12] G. L. Kane, E. Kuflik, R. Lu, and L. Wang. Top Channel for Early SUSY Discovery at the LHC. *Phys.Rev.*, D84:095004, 2011, arXiv:1101.1963 [hep-ph].

[13] C. Degrande, J.-M. Gerard, C. Grojean, F. Maltoni, and G. Servant. Non-resonant New Physics in Top Pair Production at Hadron Colliders. *JHEP*, 1103:125, 2011, arXiv:1010.6304 [hep-ph].

[14] S. Viret – LPC ATLAS Collaboration. LASER Monitoring System for the ATLAS Tile Calorimeter. *Nucl.Instrum.Meth.*, A617:120–122, 2010.

[15] D. Paredes and D. Calvet. Stability of the photodiodes and their electronics in the LASER system of the ATLAS Tile Calorimeter in 2011. Tech. Rep. ATL-TILECAL-INT-2012-006, CERN, Geneva, Sep, 2012.

[16] D. Paredes and D. Calvet. Stability of the photodiodes and their electronics in the LASER system of the ATLAS Tile Calorimeter in 2012 and 2013. Tech. Rep. ATL-COM-TILECAL-2013-028, CERN, Geneva, Jun, 2013.

[17] ATLAS Collaboration. Search for anomalous production of events with same-sign dileptons and b-jets in 14.3 fb^{-1} of pp collisions at $\sqrt{s} = 8$ tev with the ATLAS detector. Tech. Rep. ATLAS-CONF-2013-051, CERN, Geneva, May, 2013.

[18] ATLAS Collaboration. Search for exotic same-sign dilepton signatures (b' quark, $T_{5/3}$ and four top quarks production) in 4.7/fb of pp collisions at $\sqrt{s} = 7$ tev with the ATLAS detector. Tech. Rep. ATLAS-CONF-2012-130, CERN, Geneva, Sep, 2012.

[19] M. K. Gaillard, P. D. Grannis, and F. J. Sciulli. The Standard Model of Particle Physics. *Rev.Mod.Phys.*, 71:S96–S111, 1999, `arXiv:hep-ph/9812285 [hep-ph]`.

[20] F. Halzen and A. Martin, *Quarks & Leptons: An introductory course in modern particle physics*. John Wiley & Sons, New York, USA, 1984.

[21] D. Perkins, *Introduction to High Energy Physics*. Cambridge University Press, 2000. `http://books.google.fr/books?id=e63cNigcmOUC`.

[22] J. Beringer *et al* – Particle Data Group. Review of Particle Physics. *Phys. Rev. D*, 86:010001, Jul 2012. `http://link.aps.org/doi/10.1103/PhysRevD.86.010001`.

[23] Y. Fukuda *et al* – Super-Kamiokande Collaboration. Evidence for Oscillation of Atmospheric Neutrinos. *Phys. Rev. Lett.*, 81:1562–1567, Aug 1998. `http://link.aps.org/doi/10.1103/PhysRevLett.81.1562`.

[24] Y. Ashie *et al* – Super-Kamiokande Collaboration. Evidence for an oscillatory signature in atmospheric neutrino oscillation. *Phys.Rev.Lett.*, 93:101801, 2004, `arXiv:hep-ex/0404034 [hep-ex]`.

[25] S. Ahmed *et al* – SNO Collaboration. Measurement of the total active B-8 solar neutrino flux at the Sudbury Neutrino Observatory with enhanced neutral current sensitivity. *Phys.Rev.Lett.*, 92:181301, 2004, `arXiv:nucl-ex/0309004 [nucl-ex]`.

[26] K. Eguchi *et al* – KamLAND Collaboration. First results from KamLAND: Evidence for reactor anti-neutrino disappearance. *Phys.Rev.Lett.*, 90:021802, 2003, `arXiv:hep-ex/0212021 [hep-ex]`.

[27] M. Ahn *et al* – K2K Collaboration. Indications of neutrino oscillation in a 250 km long baseline experiment. *Phys.Rev.Lett.*, 90:041801, 2003, `arXiv:hep-ex/0212007 [hep-ex]`.

[28] G. Aad *et al* – ATLAS Collaboration. Observation of a new particle in the search for the Standard Model Higgs boson with the ATLAS detector at the LHC. *Phys.Lett.*, B716:1–29, 2012, arXiv:1207.7214 [hep-ex].

[29] S. Chatrchyan *et al* – CMS Collaboration. Observation of a new boson at a mass of 125 GeV with the CMS experiment at the LHC. *Phys.Lett.*, B716:30–61, 2012, arXiv:1207.7235 [hep-ex].

[30] H. D. Politzer. Reliable Perturbative Results for Strong Interactions?. *Phys.Rev.Lett.*, 30:1346–1349, 1973.

[31] H. D. Politzer. Asymptotic Freedom: An Approach to Strong Interactions. *Phys.Rept.*, 14:129–180, 1974.

[32] D. J. Gross and F. Wilczek. Asymptotically Free Gauge Theories. I. *Phys. Rev. D*, 8:3633–3652, Nov 1973. http://link.aps.org/doi/10.1103/PhysRevD.8.3633.

[33] D. Gross and F. Wilczek. Ultraviolet Behavior of Nonabelian Gauge Theories. *Phys.Rev.Lett.*, 30:1343–1346, 1973.

[34] S. Glashow. Partial Symmetries of Weak Interactions. *Nucl.Phys.*, 22:579–588, 1961.

[35] S. Weinberg. A Model of Leptons. *Phys. Rev. Lett.*, 19:1264–1266, Nov 1967. http://link.aps.org/doi/10.1103/PhysRevLett.19.1264.

[36] A. Salam. Weak and Electromagnetic Interactions. *Conf.Proc.*, C680519:367–377, 1968.

[37] P. W. Higgs. Spontaneous symmetry breakdown without massless bosons. *Physical Review*, 145(4):1156, 1966.

[38] P. Z. Skands. QCD for Collider Physics. arXiv:1104.2863 [hep-ph].

[39] G. P. Salam. Elements of QCD for hadron colliders. arXiv:1011.5131 [hep-ph].

[40] F. Englert and R. Brout. Broken Symmetry and the Mass of Gauge Vector Mesons. *Phys. Rev. Lett.*, 13:321–323, Aug 1964. http://link.aps.org/doi/10.1103/PhysRevLett.13.321.

[41] P. W. Higgs. Broken Symmetries and the Masses of Gauge Bosons. *Phys. Rev. Lett.*, 13:508–509, Oct 1964. http://link.aps.org/doi/10.1103/PhysRevLett.13.508.

[42] P. W. Anderson. Plasmons, Gauge Invariance, and Mass. *Phys. Rev.*, 130:439–442, Apr 1963. http://link.aps.org/doi/10.1103/PhysRev.130.439.

[43] L. Alvarez-Gaume and J. Ellis. Eyes on a prize particle. *Nature Physics*, 7(1):2 – 3, 2011.

[44] N. Cabibbo. Unitary Symmetry and Leptonic Decays. *Phys. Rev. Lett.*, 10:531–533, Jun 1963. http://link.aps.org/doi/10.1103/PhysRevLett.10.531.

[45] M. Kobayashi and T. Maskawa. CP-Violation in the Renormalizable Theory of Weak Interaction. *Progress of Theoretical Physics*, 49(2):652–657, 1973. http://ptp.ipap.jp/link?PTP/49/652/.

[46] Z. Maki, M. Nakagawa, and S. Sakata. Remarks on the unified model of elementary particles. *Prog.Theor.Phys.*, 28:870–880, 1962.

[47] B. Pontecorvo. Neutrino Experiments and the Problem of Conservation of Leptonic Charge. *Soviet Journal of Experimental and Theoretical Physics*, 26:984, May 1968.

[48] S. Abachi *et al* – D0 Collaboration. Observation of the top quark. *Phys. Rev. Lett.*, 74(14):2632–2637, April 1995. `http://link.aps.org/doi/10.1103/PhysRevLett.74.2632`.

[49] F. Abe *et al* – CDF Collaboration. Observation of top quark production in $\overline{p}p$ collisions with the collider detector at Fermilab. *Phys. Rev. Lett.*, 74(14):2626–2631, April 1995. `http://link.aps.org/doi/10.1103/PhysRevLett.74.2626`.

[50] Tevatron Electroweak Working Group, CDF Collaboration, D0 Collaboration. Combination of CDF and DO results on the mass of the top quark using up to 8.7 fb^{-1} at the Tevatron. `arXiv:1305.3929 [hep-ex]`.

[51] V. Barger, W.-Y. Keung, and B. Yencho. Triple-Top Signal of New Physics at the LHC. *Phys.Lett.*, B687:70–74, 2010, `arXiv:1001.0221 [hep-ph]`.

[52] G. Arnison *et al* – UA1 Collaboration. Experimental Observation of Isolated Large Transverse Energy Electrons with Associated Missing Energy at $\sqrt{s} = 540$ GeV. *Phys.Lett.*, B122:103–116, 1983.

[53] G. Arnison *et al* – UA1 Collaboration. Experimental Observation of Lepton Pairs of Invariant Mass Around 95-GeV/c^2 at the CERN SPS Collider. *Phys.Lett.*, B126:398–410, 1983.

[54] P. Ade *et al* – Planck Collaboration. Planck 2013 results. I. Overview of products and scientific results. `arXiv:1303.5062 [astro-ph.CO]`.

[55] V. Trimble. Existence and Nature of Dark Matter in the Universe. *Ann.Rev.Astron.Astrophys.*, 25:425–472, 1987.

[56] R. Durrer. What do we really know about Dark Energy?. *Phil.Trans.Roy.Soc.Lond.*, A369:5102–5114, 2011, `arXiv:1103.5331 [astro-ph.CO]`.

[57] J. Frieman, M. Turner, and D. Huterer. Dark Energy and the Accelerating Universe. *Ann.Rev.Astron.Astrophys.*, 46:385–432, 2008, `arXiv:0803.0982 [astro-ph]`.

[58] F. Stecker. The Matter-Antimatter Asymmetry of the Universe. `arXiv:hep-ph/0207323 [hep-ph]`.

[59] T. Hambye. CP Violation and the Matter-Antimatter Asymmetry of the Universe. *Comptes Rendus Physique*, 13:193–203, 2012.

[60] J. R. Ellis. Limits of the Standard Model. `arXiv:hep-ph/0211168 [hep-ph]`.

[61] L. Randall and R. Sundrum. A Large mass hierarchy from a small extra dimension. *Phys.Rev.Lett.*, 83:3370–3373, 1999, `arXiv:hep-ph/9905221 [hep-ph]`.

[62] H. Davoudiasl, J. Hewett, and T. Rizzo. Experimental probes of localized gravity: On and off the wall. *Phys.Rev.*, D63:075004, 2001, arXiv:hep-ph/0006041 [hep-ph].

[63] A. Pomarol. Gauge bosons in a five-dimensional theory with localized gravity. *Phys.Lett.*, B486:153–157, 2000, arXiv:hep-ph/9911294 [hep-ph].

[64] Y. Grossman and M. Neubert. Neutrino masses and mixings in nonfactorizable geometry. *Phys.Lett.*, B474:361–371, 2000, arXiv:hep-ph/9912408 [hep-ph].

[65] T. Gherghetta and A. Pomarol. Bulk fields and supersymmetry in a slice of AdS. *Nucl.Phys.*, B586:141–162, 2000, arXiv:hep-ph/0003129 [hep-ph].

[66] K. Agashe, A. Delgado, M. J. May, and R. Sundrum. RS1, custodial isospin and precision tests. *JHEP*, 0308:050, 2003, arXiv:hep-ph/0308036 [hep-ph].

[67] M. Guchait, F. Mahmoudi, and K. Sridhar. Associated production of a Kaluza-Klein excitation of a gluon with a $t\bar{t}$ pair at the LHC. *Phys.Lett.*, B666:347–351, 2008, arXiv:0710.2234 [hep-ph].

[68] A. Djouadi, G. Moreau, and R. K. Singh. Kaluza-Klein excitations of gauge bosons at the LHC. *Nucl.Phys.*, B797:1–26, 2008, arXiv:0706.4191 [hep-ph].

[69] M. Strassler. Generating a Fermion Mass Hierarchy in a Composite Supersymmetric Standard Model. *Phys.Lett.*, B376:119–126, 1996, arXiv:hep-ph/9510342 [hep-ph].

[70] A. E. Nelson and M. J. Strassler. A Realistic supersymmetric model with composite quarks. *Phys.Rev.*, D56:4226–4237, 1997, arXiv:hep-ph/9607362 [hep-ph].

[71] A. Delgado and T. M. Tait. A Fat Higgs with a Fat top. *JHEP*, 0507:023, 2005, arXiv:hep-ph/0504224 [hep-ph].

[72] B. Lillie, J. Shu, and T. M. Tait. Top Compositeness at the Tevatron and LHC. *JHEP*, 0804:087, 2008, arXiv:0712.3057 [hep-ph].

[73] A. Pomarol and J. Serra. Top quark compositeness: Feasibility and implications. *Phys. Rev. D*, 78:074026, Oct 2008. http://link.aps.org/doi/10.1103/PhysRevD.78.074026.

[74] M. Bona *et al* – UTfit Collaboration. Model-independent constraints on Δ F=2 operators and the scale of new physics. *JHEP*, 0803:049, 2008, arXiv:0707.0636 [hep-ph].

[75] H. Georgi. Generalized dimensional analysis. *Phys.Lett.*, B298:187–189, 1993, arXiv:hep-ph/9207278 [hep-ph].

[76] A. Manohar and H. Georgi. Chiral Quarks and the Nonrelativistic Quark Model. *Nucl.Phys.*, B234:189, 1984.

[77] H. Georgi, L. Kaplan, D. Morin, and A. Schenk. Effects of top quark compositeness. *Phys. Rev. D*, 51:3888–3894, Apr 1995. http://link.aps.org/doi/10.1103/PhysRevD.51.3888.

[78] G. Cacciapaglia, A. Deandrea, and J. Llodra-Perez. A Dark Matter candidate from Lorentz Invariance in 6D. *JHEP*, 1003:083, 2010, arXiv:0907.4993 [hep-ph].

[79] G. Cacciapaglia, A. Deandrea, and J. Llodra-Perez. The Universal Real Projective Plane: LHC phenomenology at one Loop. *JHEP*, 1110:146, 2011, arXiv:1104.3800 [hep-ph].

[80] T. Plehn and T. M. Tait. Seeking Sgluons. *J.Phys.*, G36:075001, 2009, arXiv:0810.3919 [hep-ph].

[81] S. Choi, M. Drees, J. Kalinowski, J. Kim, E. Popenda, *et al.* Color-Octet Scalars of N=2 Supersymmetry at the LHC. *Phys.Lett.*, B672:246–252, 2009, arXiv:0812.3586 [hep-ph].

[82] C. Kilic, T. Okui, and R. Sundrum. Vectorlike Confinement at the LHC. *JHEP*, 1002:018, 2010, arXiv:0906.0577 [hep-ph].

[83] C. Kilic, T. Okui, and R. Sundrum. Colored Resonances at the Tevatron: Phenomenology and Discovery Potential in Multijets. *JHEP*, 0807:038, 2008, arXiv:0802.2568 [hep-ph].

[84] G. Burdman, B. A. Dobrescu, and E. Ponton. Resonances from two universal extra dimensions. *Phys.Rev.*, D74:075008, 2006, arXiv:hep-ph/0601186 [hep-ph].

[85] S. Schumann, A. Renaud, and D. Zerwas. Hadronically decaying color-adjoint scalars at the LHC. *JHEP*, 1109:074, 2011, arXiv:1108.2957 [hep-ph].

[86] S. Calvet, B. Fuks, P. Gris, and L. Valery. Searching for sgluons in multitop events at a center-of-mass energy of 8 TeV. *JHEP*, 1304:043, 2013, arXiv:1212.3360 [hep-ph].

[87] R. Bailey and P. Collier. Standard Filling Schemes for Various LHC Operation Modes. Tech. Rep. LHC-PROJECT-NOTE-323, CERN, Geneva, Sep, 2003.

[88] K. Schindl. The Injector Chain for the LHC. Tech. Rep. CERN-PS-99-018-DI, CERN, Mar, 1999.

[89] A. Alves *et al* – LHCb Collaboration. The LHCb Detector at the LHC. *Journal of Instrumentation*, 3(08):S08005, 2008. http://stacks.iop.org/1748-0221/3/i=08/a=S08005.

[90] K. Aamodt *et al* – ALICE Collaboration. The ALICE Experiment at the CERN LHC. *Journal of Instrumentation*, 3(08):S08002, 2008. http://stacks.iop.org/1748-0221/3/i=08/a=S08002.

[91] G. Anelli *et al* – TOTEM Collaboration. The TOTEM Experiment at the CERN Large Hadron Collider. *JINST*, 3:S08007, 2008.

[92] O. Adriani *et al* – LHCf Collaboration. The LHCf Detector at the CERN Large Hadron Collider. *Journal of Instrumentation*, 3(08):S08006, 2008. http://stacks.iop.org/1748-0221/3/i=08/a=S08006.

[93] J. Pinfold, R. Soluk, Y. Yao, S. Cecchini, G. Giacomelli, M. Giorgini, L. Patrizii, G. Sirri, D. H. Lacarrére, K. Kinoshita, J. Jakubek, M. Platkevic, S. Pospísil, Z. Vykydal, T. Hott, A. Houdayer, C. Leroy, J. Swain, D. Felea, D. Hasegan, G. E. Pavalas, and V. Popa. Technical Design Report of the MoEDAL Experiment. Tech. Rep. CERN-LHCC-2009-006. MoEDAL-TDR-001, CERN, Geneva, Jun, 2009.

[94] ATLAS Collaboration, *ATLAS inner detector: Technical Design Report, 1.* Technical Design Report ATLAS. CERN, Geneva, 1997.

[95] ATLAS Collaboration, *ATLAS inner detector: Technical Design Report, 2.* Technical Design Report ATLAS. CERN, Geneva, 1997.

[96] V. I. Martinez Outschoorn and J. Guimaraes da Costa, *Measurement of the Charge Asymmetry of W Bosons Produced in pp Collisions at $\sqrt{s}$ = 7 TeV with the ATLAS Detector.* PhD thesis, Harvard U., Cambridge, MA, USA, 2011. Presented 19 May 2011.

[97] N. Wermes and G. Hallewel, *ATLAS pixel detector: Technical Design Report.* Technical Design Report ATLAS. CERN, Geneva, 1998.

[98] I. Perić, L. Blanquart, G. Comes, P. Denes, K. Einsweiler, P. Fischer, E. Mandelli, and G. Meddeler. The FEI3 readout chip for the ATLAS pixel detector. *Nuclear Instruments and Methods in Physics Research Section A: Accelerators, Spectrometers, Detectors and Associated Equipment*, 565(1):178 – 187, 2006. http://www.sciencedirect.com/science/article/pii/S0168900206007649. Proceedings of the International Workshop on Semiconductor Pixel Detectors for Particles and Imaging.

[99] G. Aad *et al* – ATLAS Collaboration. ATLAS Pixel Detector Electronics and Sensors. *Journal of Instrumentation*, 3(07):P07007, 2008. http://stacks.iop.org/1748-0221/3/i=07/a=P07007.

[100] Y. Unno. ATLAS silicon microstrip detector system (SCT). *Nuclear Instruments and Methods in Physics Research Section A: Accelerators, Spectrometers, Detectors and Associated Equipment*, 511(1-2):58 – 63, 2003. http://www.sciencedirect.com/science/article/pii/S0168900203017510. Proceedings of the 11th International Workshop on Vertex Detectors.

[101] J. R. Pater. The ATLAS SemiConductor Tracker operation and performance. *Journal of Instrumentation*, 7(04):C04001, 2012. http://stacks.iop.org/1748-0221/7/i=04/a=C04001.

[102] F. Campabadal, C. Fleta, M. Key, M. Lozano, C. Martinez, *et al.* Design and performance of the ABCD3TA ASIC for readout of silicon strip detectors in the ATLAS semiconductor tracker. *Nuclear Instruments and Methods in Physics Research Section A: Accelerators, Spectrometers, Detectors and Associated Equipment*, 552(3):292 – 328, 2005. http://www.sciencedirect.com/science/article/pii/S0168900205013926.

[103] S. D'Auria. The ATLAS semiconductor tracker: operations and performance. Tech. Rep. ATL-INDET-PROC-2012-027, CERN, Geneva, Nov, 2012.

[104] E. Abat *et al.* The ATLAS TRT Barrel Detector. *Journal of Instrumentation*, 3(02):P02014, 2008. http://stacks.iop.org/1748-0221/3/i=02/a=P02014.

[105] E. Abat *et al.* The ATLAS TRT end-cap detectors. *Journal of Instrumentation*, 3(10):P10003, 2008. http://stacks.iop.org/1748-0221/3/i=10/a=P10003.

[106] ATLAS Collaboration, *ATLAS calorimeter performance: Technical Design Report.* Technical Design Report ATLAS. CERN, Geneva, 1996.

[107] ATLAS Collaboration, *ATLAS detector and physics performance: Technical Design Report, 1.* Technical Design Report ATLAS. CERN, Geneva, 1999. Electronic version not available.

[108] ATLAS Collaboration, *ATLAS liquid-argon calorimeter: Technical Design Report.* Technical Design Report ATLAS. CERN, Geneva, 1996.

[109] ATLAS Collaboration, *ATLAS tile calorimeter: Technical Design Report.* Technical Design Report ATLAS. CERN, Geneva, 1996.

[110] E. A. Starchenko, G. Blanchot, M. Bosman, M. Cavalli-Sforza, A. N. Karyukhin, S. Kopikov, A. Myagkov, M. Nessi, A. Shalimov, N. A. Shalanda, M. Soldatov, A. Solodkov, A. Soloviev, V. M. Tsoupko-Sitnikov, and A. Zaitsev. Cesium Monitoring System for ATLAS Tile Hadron Calorimeter. Tech. Rep. ATL-TILECAL-2002-003, CERN, Geneva, Feb, 2002.

[111] K. J. Anderson, M. H. Hurwitz, I. Jen-La Plante, J. E. Pilcher, and R. Teuscher. Performance and Calibration of the Tilecal Fast Readout Using the Charge Injection System. Tech. Rep. ATL-TILECAL-INT-2008-002, CERN, Geneva, Mar, 2008.

[112] European Organization for Nuclear Research (Ginebra), *ATLAS Muon Spectrometer: Technical Design Report.* ATLAS technical design report. CERN, 1997. `http://books.google.fr/books?id=Re-SPQAACAAJ`.

[113] G. Aad *et al* – ATLAS Collaboration. Expected Performance of the ATLAS Experiment - Detector, Trigger and Physics. `arXiv:0901.0512 [hep-ex]`.

[114] A. G. Brandt. ATLAS Forward Detectors. Tech. Rep. ATL-LUM-PROC-2010-003, CERN, Geneva, Jul, 2010.

[115] G. Aad *et al* – ATLAS Collaboration. Luminosity Determination in pp Collisions at $\sqrt{s} = 7$ TeV Using the ATLAS Detector at the LHC. *Eur.Phys.J.*, C71:1630, 2011, `arXiv:1101.2185 [hep-ex]`.

[116] S. Ask. Status of the Forward Physics Projects in ATLAS. `arXiv:0706.0644 [hep-ex]`.

[117] C. Gabaldon. Performance of the ATLAS Trigger System. *Journal of Instrumentation*, 7(01):C01092, 2012. `http://stacks.iop.org/1748-0221/7/i=01/a=C01092`.

[118] S. Kama. Evolution of the Trigger and Data Acquisition System in the ATLAS experiment. Tech. Rep. ATL-DAQ-PROC-2012-061, CERN, Geneva, Nov, 2012.

[119] M. Elsing, L. Goossens, A. Nairz, and G. Negri. The ATLAS Tier-0: Overview and Operational Experience. *Journal of Physics: Conference Series*, 219(7):072011, 2010. `http://stacks.iop.org/1742-6596/219/i=7/a=072011`.

[120] M. Branco, D. Cameron, B. Gaidioz, V. Garonne, B. Koblitz, M. Lassnig, R. Rocha, P. Salgado, and T. Wenaus. Managing ATLAS data on a petabyte-scale with DQ2. *Journal of Physics: Conference Series*, 119(6):062017, 2008. `http://stacks.iop.org/1742-6596/119/i=6/a=062017`.

[121] C. Eck, J. Knobloch, L. Robertson, I. Bird, K. Bos, N. Brook, D. Dullmann, I. Fisk, D. Foster, B. Gibbard, C. Grandi, F. Grey, J. Harvey, A. Heiss, F. Hemmer, S. Jarp, R. Jones, D. Kelsey, M. Lamanna, H. Marten, P. Mato-Vila, F. Ould-Saada, B. Panzer-Steindel, L. Perini, Y. Schutz, U. Schwickerath, J. Shiers, and T. Wenaus, *LHC computing Grid: Technical Design Report. Version 1.06 (20 Jun 2005)*. Technical Design Report LCG. CERN, Geneva, 2005.

[122] Z. J. Ajaltouni, F. Badaud, N. Bouhemaid, P. Brette, M. Brossard, R. Chadelas, J. Chevaleyre, M. Crouau, F. Daudon, J. Dugne, F. Durand, C. Fayard, G. Lentignac, S. Mayade, B. Michel, G. Montarou, G. S. Muanza, J. Nigon, D. Pallin, F. Pozzobon, S. Poirot, E. Sahuc, R. Saigne, G. Savinel, L. Says, F. Vazeille, and D. Vincent. The tilecal laser monitoring. Tech. Rep. ATL-TILECAL-94-039. ATL-L-PN-39, CERN, Geneva, Dec, 1994.

[123] A. Bamberger, J. Lehmann, D. Schäcke, and M. Wülker. Calibration of the ZEUS calorimeter. *Nuclear Instruments and Methods in Physics Research Section A: Accelerators, Spectrometers, Detectors and Associated Equipment*, 277(1):46 – 55, 1989. `http://www.sciencedirect.com/science/article/pii/0168900289905342`.

[124] T. Golling, H. Hayward, P. Onyisi, H. Stelzer, and P. Waller. The ATLAS data quality defect database system. *The European Physical Journal C*, 72(4):1–6, 2012. `http://dx.doi.org/10.1140/epjc/s10052-012-1960-y`.

[125] ATLAS Collaboration. Luminosity Determination in *pp* Collisions at $\sqrt{s} = 7$ TeV using the ATLAS Detector in 2011. Tech. Rep. ATLAS-CONF-2011-116, CERN, Geneva, Aug, 2011.

[126] J. Pumplin, D. Stump, J. Huston, H. Lai, P. M. Nadolsky, *et al.* New generation of parton distributions with uncertainties from global QCD analysis. *JHEP*, 0207:012, 2002, `arXiv:hep-ph/0201195 [hep-ph]`.

[127] A. Martin, W. Stirling, R. Thorne, and G. Watt. Parton distributions for the LHC. *Eur.Phys.J.*, C63:189–285, 2009, `arXiv:0901.0002 [hep-ph]`.

[128] M. Guzzi, P. Nadolsky, E. Berger, H.-L. Lai, F. Olness, *et al.* CT10 parton distributions and other developments in the global QCD analysis. `arXiv:1101.0561 [hep-ph]`.

[129] Geant4 Collaboration. Geant4: a simulation toolkit. *Nuclear Instruments and Methods in Physics Research Section A: Accelerators, Spectrometers, Detectors and Associated Equipment*, 506(3):250 – 303, 2003. `http://www.sciencedirect.com/science/article/pii/S0168900203013688`.

[130] E. Richter-Was, D. Froidevaux, and L. Poggioli. ATLFAST 2.0 a fast simulation package for ATLAS. Tech. Rep. ATL-PHYS-98-131, CERN, Geneva, Nov, 1998.

[131] J. Alwall, M. Herquet, F. Maltoni, O. Mattelaer, and T. Stelzer. MadGraph 5 : Going Beyond. *JHEP*, 1106:128, 2011, `arXiv:1106.0522 [hep-ph]`.

[132] T. Sjostrand, S. Mrenna, and P. Z. Skands. PYTHIA 6.4 Physics and Manual. *JHEP*, 0605:026, 2006, `arXiv:hep-ph/0603175 [hep-ph]`.

[133] T. Sjostrand, S. Mrenna, and P. Z. Skands. A Brief Introduction to PYTHIA 8.1. *Comput.Phys.Commun.*, 178:852–867, 2008, arXiv:0710.3820 [hep-ph].

[134] M. L. Mangano, M. Moretti, F. Piccinini, R. Pittau, and A. D. Polosa. ALPGEN, a generator for hard multiparton processes in hadronic collisions. *JHEP*, 0307:001, 2003, arXiv:hep-ph/0206293 [hep-ph].

[135] G. Corcella, I. Knowles, G. Marchesini, S. Moretti, K. Odagiri, *et al.* HERWIG 6: An Event generator for hadron emission reactions with interfering gluons (including supersymmetric processes). *JHEP*, 0101:010, 2001, arXiv:hep-ph/0011363 [hep-ph].

[136] J. Butterworth, J. R. Forshaw, and M. Seymour. Multiparton interactions in photoproduction at HERA. *Z.Phys.*, C72:637–646, 1996, arXiv:hep-ph/9601371 [hep-ph].

[137] T. Gleisberg, S. Hoeche, F. Krauss, M. Schonherr, S. Schumann, *et al.* Event generation with SHERPA 1.1. *JHEP*, 0902:007, 2009, arXiv:0811.4622 [hep-ph].

[138] S. Frixione and B. R. Webber. Matching NLO QCD computations and parton shower simulations. *JHEP*, 0206:029, 2002, arXiv:hep-ph/0204244 [hep-ph].

[139] J. Alwall, P. Demin, S. de Visscher, R. Frederix, M. Herquet, *et al.* MadGraph/MadEvent v4: The New Web Generation. *JHEP*, 0709:028, 2007, arXiv:0706.2334 [hep-ph].

[140] J. M. Campbell and R. K. Ellis. $t\bar{t}W^{\pm}$ production and decay at NLO. *JHEP*, 1207:052, 2012, arXiv:1204.5678 [hep-ph].

[141] M. Garzelli, A. Kardos, C. Papadopoulos, and Z. Trocsanyi. Z^0 - boson production in association with a top anti-top pair at NLO accuracy with parton shower effects. *Phys.Rev.*, D85:074022, 2012, arXiv:1111.1444 [hep-ph].

[142] M. Cacciari, G. P. Salam, and G. Soyez. The Anti-k(t) jet clustering algorithm. *JHEP*, 0804:063, 2008, arXiv:0802.1189 [hep-ph].

[143] G. Aad *et al* – ATLAS Collaboration. Jet energy measurement with the ATLAS detector in proton-proton collisions at $\sqrt{s} = 7$ TeV. arXiv:1112.6426 [hep-ex].

[144] ATLAS Collaboration. Measurement of the b-tag efficiency in a sample of jets containing muons with 5 fb^{-1} of data from the atlas detector. Tech. Rep. ATLAS-CONF-2012-043, CERN, Geneva, Mar, 2012.

[145] G. Aad *et al* – ATLAS Collaboration. Electron performance measurements with the ATLAS detector using the 2010 LHC proton-proton collision data. *Eur.Phys.J.*, C72:1909, 2012, arXiv:1110.3174 [hep-ex].

[146] ATLAS Collaboration. Muon reconstruction efficiency in reprocessed 2010 LHC proton-proton collision data recorded with the ATLAS detector. Tech. Rep. ATLAS-CONF-2011-063, CERN, Geneva, Apr, 2011.

[147] G. Aad *et al* – ATLAS Collaboration. Performance of Missing Transverse Momentum Reconstruction in Proton-Proton Collisions at 7 TeV with ATLAS. *Eur.Phys.J.*, C72:1844, 2012, arXiv:1108.5602 [hep-ex].

[148] L. Gauthier, A.-I. Etienvre, and G. Servant, *Etudes dans le canal avec deux leptons de même signe de la physique du top au-delà du Modèle Standard*. PhD thesis, U. Paris-Sud 11, Dept. Phys., Orsay, Sep, 2012. Presented 14 Sep 2012.

[149] G. Aad *et al* – Atlas Collaboration. Measurement of the top quark-pair production cross section with ATLAS in pp collisions at $\sqrt{s} = 7$ TeV. *Eur.Phys.J.*, C71:1577, 2011, `arXiv:1012.1792 [hep-ex]`.

[150] T. Theveneaux-Pelzer and F. Derue, *Études sur la reconstruction des électrons et mesure de la section efficace de production de paires de quarks top dans les canaux dileptoniques dans l'expérience ATLAS auprès du LHC*. PhD thesis, LPNHE, Paris, 2012. Presented 02 Jul 2012.

[151] A. Alonso, O. Smirnova, and A. Torsten, *Transition Radiation Tracker calibration, searches beyond the Standard Model and multiparticle correlations in ATLAS*. PhD thesis, Lund U., Apr, 2012. Presented 20 May 2012.

[152] T. Junk. Confidence level computation for combining searches with small statistics. *Nucl.Instrum.Meth.*, A434:435–443, 1999, `arXiv:hep-ex/9902006 [hep-ex]`.

[153] A. L. Read. Presentation of search results: The CL(s) technique. *J.Phys.*, G28:2693–2704, 2002.

[154] J. M. Campbell and R. K. Ellis. $t\bar{t}W^{\pm}$ production and decay at NLO. *JHEP*, 1207:052, 2012, `arXiv:1204.5678 [hep-ph]`.

[155] M. Garzelli, A. Kardos, C. Papadopoulos, and Z. Trocsanyi. $t\bar{t}W^{\pm}$ and $t\bar{t}Z$ Hadroproduction at NLO accuracy in QCD with Parton Shower and Hadronization effects. *JHEP*, 1211:056, 2012, `arXiv:1208.2665 [hep-ph]`.

[156] D. Bourilkov, R. C. Group, and M. R. Whalley. LHAPDF: PDF use from the Tevatron to the LHC. `arXiv:hep-ph/0605240 [hep-ph]`.